Aston University
Birmingham

DOCTORAL THESIS

# Multiphase modelling of the characteristics of close coupled gas atomization

Nicola Zeoli

# *Multiphase Modelling of the Characteristics of Close Coupled Gas atomization*

Nicola Zeoli
Doctor of Philosophy

ASTON UNIVERSITY
June 2011

Aston University

# Multiphase Modelling of the Characteristics of Close Coupled Gas atomization

Nicola Zeoli
Doctor of Philosophy

June 2011

## Thesis summary

Notwithstanding the high demand of metal powder for automotive and High Tech applications, there are still many unclear aspects of the production process. Only recently has supercomputer performance made possible numerical investigation of such phenomena. This thesis focuses on the modelling aspects of primary and secondary atomization. Initially two-dimensional analysis is carried out to investigate the influence of flow parameters (reservoir pressure and gas temperature principally) and nozzle geometry on final powder yielding. Among the different types, close coupled atomizers have the best performance in terms of cost and narrow size distribution. An isentropic contoured nozzle is introduced to minimize the gas flow losses through shock cells: the results demonstrate that it outperformed the standard converging-diverging slit nozzle. Furthermore the utilization of hot gas gave a promising outcome: the powder size distribution is narrowed and the gas consumption reduced. In the second part of the thesis, the interaction of liquid metal and high speed gas near the feeding tube exit was studied. Both axisymmetric and non-axisymmetric geometries were simulated using a 3D approach. The filming mechanism was detected only for very small metal flow rates (typically obtained in laboratory scale atomizers). When the melt flow increased, the liquid core overtook the adverse gas flow and entered in the high speed wake directly: in this case the disruption is driven by sinusoidal surface waves. The process is characterized by fluctuating values of liquid volumes entering the domain that are monitored only as a time average rate: it is far from industrial robustness and capability concept. The non-axisymmetric geometry promoted the splitting of the initial stream into four cores, smaller in diameter and easier to atomize. Finally a new atomization design based on the lesson learned from previous cases simulation is presented.

***Keywords:*** *aerospike atomization nozzle, melt atomization, 3D multiphase modelling, primary and secondary break up.*

## Acknowledgments

I would like to express my deepest gratitude to my supervisor, Dr Sai Gu: his guide and continuous encouragement determined the quality of the present analysis. I am also grateful to Professor Roger Kettle and Dr Greg Swadener who supported my research in the last two years. Special thanks to the friends and colleagues Spyros Kamnis and Konstantinos Papadikis for their comments and enthusiasm. Iam also indebted to BSA Metal Powder, Aston University, EPSRC and Powdermatrix for the financial support. Finally it is my pleasure to express thanks to my family for the strong sustain received throughout my studies.

***TABLE OF CONTENT***

## *LIST OF FIGURES*

### *Chapter 1*



### *Chapter 2*



### *Chapter 3*

***Chapter 4***

### *Chapter 5*



### *Appendix A*



## *LIST OF TABLES*

### *Chapter 3*



### *Chapter 4*

***Chapter 5***



## *NOMECLATURE*

A: oscillation amplitude
$B_0$, $B_1$: constants for KH model
Cb, CF Ck, Cd: constants for TAB model
dp: droplet radius
f: fraction of solidified melt
H: melt latent heat of fusion
$K_g$: gas thermal conductivity
Pr: Prandtl number
$r_P$: diameter of parent droplet
R: diameter of child droplet
Re: Reynolds number
t: time
$t_b$: break-up time
tn: time step n
T: droplet temperature
$T_g$: gas temperature
urel: relative velocity between gas and droplet
Z: Ohnesorge number = $\nu(\rho/\sigma\ dp)$
X: displacement of the droplet equator
Y: non-dimensional value for the displacement of the droplet equator
yn: y value at tn;
We: Weber number

### *Greek letters*

$\Gamma$ : Taylor number = Z(We0.5)
$\Lambda$: wavelength of disturbance
$\mu_l$: liquid viscosity
$\varrho_g$: gas flow density
$\varrho_l$: melt density
$\sigma$: surface tension of the fluid droplet
$\omega$: oscillation frequency
$\Omega$: growth rate of the wavelength

### *Subscript*

l: liquid
g: gas
s: solid
p: particles
vel: velocity

**Publications:**

N. Zeoli, S. Gu, S. Kamnis, Numerical simulation of in-flight particle oxidation during thermal spraying, Computers and Chemical Engineering, volume 32, pp 1661-1668, 2008;

N. Zeoli, S. Gu, Computational validation of an isentropic plug nozzle design for gas atomisation, Computational Materials Science, Volume 42, pp 245-258, 2008;

N. Zeoli, S. Gu, S. Kamnis, Numerical modelling of metal droplet cooling and solidification, International Journal of Heat and Mass Transfer, Volume 51, pp 4121-4131, 2008;

S. Kamnis, S. Gu, N. Zeoli, Mathematical modelling of Inconel 718 particles in HVOF thermal spraying, Surface & Coatings Technology, Volume 202, pp 2715-2724, 2008;

N. Zeoli, S. Gu, Computational simulation of metal droplet break-up, cooling and solidification during gas atomization, Computational Materials Science, Volume 43, pp 268-278, 2008;

N. Zeoli, S. Gu, Numerical modelling of droplet break-up for gas atomisation, Computational Materials Science, Volume 38, pp 282–292, 2006;

# CHAPTER 1

## INTRODUCTION

Metal powders represent a small part of metal market compare to cast and wrought material. Powder metallurgy processes like sintering, isostatic pressing (hot or cold) and injection moulding provided special solutions (not achievable with standard material) to market niches. Due to the high cost, powder material is mainly a choice, rather than an alternative. The quantity of powder (aluminum, copper, iron, steel) produced worldwide is 1.3 million tons per year, in the form of particles from 0.001 to 1 mm diameter. Particles can have different shapes: spherical, flake like and irregular granules. Despite the rapid development of surface technology over the last decade, the methods of producing metal powders have not changed significantly and are subdivided into three main categories: chemical, mechanical and physical. Figure 1.1 reports the powder application field as a function of size. The chemical methods rely on the decomposition of metal compound or the precipitation from solution. Mechanical powders are obtained by milling or grinding machining to remove small chips from the bars. In physical atomization the liquid metal stream is pulverized by high speed fluid jet (water or gas).

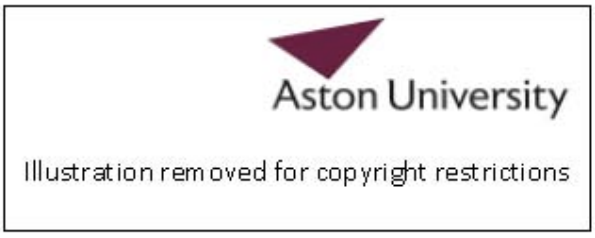


**Figure 1.1: application of powder as function of size [1]**

## 1.1 Overview of melt atomization process

New applications and emerging surface technologies from industry demand high quality powders with reduced diameter, narrow size distributions and purity. This has put greater technical and financial constraints on the production techniques of metal powders. Water atomization is relatively less expensive than gas atomization and is used for metals with easily reducible oxides: a water jet coming from discrete nozzles systems (or annular slit) is directed toward the melt stream that is disrupted into several droplets. The particles are quenched and reach the bottom of the tower where the metal powder is collected, filtered and dried. The particle shape is extremely irregular because of the fast cooling rate ($10^4$ - $10^6$ K/s) and the yielding presents broad size distribution (10 - 1000 μm)[2]. The rapid cooling means removal of macrosegregation and reduction of microsegregation that lead to an overall refinement of the microstructure. Sometimes, to avoid oxidation of steel containing Chromium and Manganese, oil is used instead of water.

However processes like MIM and thermal spray coating require very regular shape (close to spherical) and gas atomization is mandatory. Quenching effect in gas atomization are considerably less (cooling rate $10^3$ -$10^5$ K/s)[2] so that droplets have more time to spheroidize before solidification. Depending on the specific media, irregular-shaped particles could still be produced: gases with smaller and lighter molecules have higher thermal conductivity because the molecules move faster without colliding each others. Consequently, Hydrogen and Helium molecules have a greater heat transfer coefficient compared to Nitrogen and Argon. The gas metal atomization (GMA) process has been widely employed as an effective method to produce fine spherical metal powders. The principle of high pressure gas atomization (HPGA) is to transfer kinetic energy from a high-speed gas jet to a liquid metal stream. The rapidly accelerated liquid becomes unstable and breaks into ligaments that are successively atomized (due to the aerodynamic force arising from the velocity difference between fluid and metal drops) into the jet wake. The particles produced in this process undergo in-flight solidification and are collected as metal powder.

The most widely deployed processes in gas atomization practice are close-coupled (sometimes called confined) and free-fall atomization [1-3]. The difference between these two technologies is where the gas and melt jets meet: figure 1.2 gives an overview of the main characteristics of the two systems. The gas exit is confined to the melt delivery tube in close-coupled atomization while, in free-fall atomization, a distance varying from 10 cm

to 30 cm is placed between the exit of the melt feeding tube and the gas exit, which allows the melt flow downward in quiescent air before the high velocity gas impacts and disrupt it. The close-coupled atomization is more favourable for the production of fine powders with smaller configuration despite the drawbacks such as backflow and freeze-off that normally do not occur in free-fall atomization. It has been proved that the short distance between the gas jet and the metal melt enhances a closer interaction within the two-phase flow and consequently achieves a better break-up of liquid phase [7-8].


**Figure 1.2: free-fall and close coupled gas atomization [2]**

Molten metal is poured into the atomization chamber from the tundish through a ceramic feeding tube where a high pressure gas jet comes into contact with the melt. When the melt stream enters the gas wake formed at the feeding tube tip, it immediately forms either a complete film that moves radially outward or (depending on the gas to melt mass flow rate ratio) takes a fountain shape. The gas used for atomization influences the droplet rate of cooling: lighter gas (like He) has an increased heat capacity, thermal conductivity and heat transfer coefficient and generates faster cooling. As will be discussed in detail in the next chapters, the low pressure recirculating zone formed at the base of the feeding tube pushes the gas against the melt exit: this mechanism is responsible for the horizontal acceleration of the melt towards the external edge of the ceramic tube. A considerable portion of primary break-up takes place when the melt comes into contact with the supersonic expanded gas on the outer edge of the feeding tube. It is important to notice that using a faster, lower viscosity gas (He) increases the shearing force on the interface between gas and liquid thus producing a finer droplet distribution.

The design of gas nozzle is critical, considering the atomization principle that the melt stream needs to obtain as much kinetic energy as possible from the high-speed gas jet. Up to now, two different gas nozzles are widely used for close-coupled atomization, namely annular-slit and discrete-jet nozzle. The annular-slit nozzle is an annular slot surrounding the melt feeding tube while the discrete-jet nozzle is made of a number of discrete holes. The annular-slit nozzles are commonly used by industry because of their superior performance in comparison to the discrete-jet nozzles[4]. Therefore, annular-slit nozzles are the basic framework of this research. In order to make the process more clear, figure 1.3 gives a description of the equipment used in a typical gas atomization plant.

Close coupled gas atomization is characterized by the low control of particles size: such a inefficiency means extremely costly process. Furthermore the raw powder diameters range from 1 to 250 μm while manufacturing processes require only a limited fraction (see figure 1.1). The process optimization means yield with narrow sizes range and mean diameter lower than 10 μm. This study investigates the atomization phenomena to identify (and control) the process parameters.


**Figure 1.3: typical gas atomization plant [4]**

## 1.2 Terminology

This section provides the definition of common quantities used to determine drop size. The Volume Median Diameter (VMD, also denoted as $D_{V50}$) determines the diameter for which half of the spray volume is made up of smaller droplets. Sauter Mean Diameter (SMD) defines the ratio of total spray volume to total surface area of all the droplets[9]:

$$SMD = \frac{\sum_i d_i^3}{\sum_i d_i^2} = D_{32} \tag{1.1}$$

The Volume Mean Diameter ($D_{30}$) is the averaged drop size considering the total spray volume:

$$D_{30} = \left( \frac{1}{N} \sum_i d_i^3 \right)^{1/3} \tag{1.2}$$

where N is the number of particles in the spray

## 1.3 CFD introduction

The set of relations describing fluid dynamics was obtained more than a century ago but the analytical solution of this partial differential equations system exists only for a limited number of flows (far away from most real cases). Numerical solution (approximated!) techniques were also well known but only the increasing performance of computers made effective their use for engineering analysis. Computational fluid dynamics (CFD) deals with the solution of Navier-Stokes equations on computers. The basic concept behind CFD is the discretization (in space and time) of the differential equations into an algebraic system.

Iterative methods are preferred to direct solver because less time/resources consuming. Real flows involve phenomena for which the exact equations are not not available and the use of models is necessary.

Fluent is a commercial solver (finite volume discretization scheme) able to simulate several steady and unsteady flows, including multiphase and turbulent ones. A wide range of boundary conditions are available and the user has the opportunity to implement his own models loading user defined function: the complete array of flow variables is accessible for each cell. Due to its flexibility it has been chosen to develop the current study.

The advantages of using CFD are the relative low cost compared to experiments (imagine to built up an engine to evaluate new blade shape) and the possibility to switch quickly boundary conditions during optimization investigation. The accuracy of the simulation could be, theoretically, always improved reducing the portion of region analysed (introducing more cells in the domain = grid refinement) or decreasing the time step. However fine grid and small time steps mean high computational power and calculation period. The assumptions included in the models and the iterative methods errors require a critical analysis of the results: just running a commercial code is useless if not associated with physical discussion and interpretation. User skills are still necessary to avoid colour pictures album. An exhaustive introduction to CFD can be found in [10-11].

**References**

[1] Capus M. Joseph, Metal Powders: A Global Survey of Production, Applications and Markets to 2010, Elsevier Science, Oxford, 2005;

[2] Liu Huimin, Science and Engineering of Droplets - Fundamentals and Applications, William Andrew Publishing, New York, 2000;

[3] Neikov D. Oleg et al.,Handbook of Non-Ferrous Metal Powders - Technologies and Applications, Elsevier, Oxford, 2009;

[4] S. P. Mates, G. S. Settles, A study of liquid metal atomization using close-coupled nozzles, part 1: gas dynamic behavior, Atomization and Sprays, Volume 15, pp.19-40, 2005;

[5] S. P. Mates, G. S. Settles, A study of liquid metal atomization using close-coupled nozzles, part 2: atomization behavior, Atomization and Sprays, Volume 15, pp. 41-60, 2005;

[6] M. Miskovicovà, M. Fedorcàkovà, V. Bodàk, Properties and microstructure of high speed steel powders produced under rapid solidification conditions, Journal de Physique, Volume 3, pp 153-156, 1993 ;

[7] A. Yule, J.J. Dunkley, Atomization of Metals, Oxford University Press, Oxford, 1994;

[8] R. Ünal, M. Aydın, High Efficient Metal Powder Production by Gas Atomisation Process, Materials science forum, Volumes 534 - 536, pp 57 - 60, 2007;

[9] York, J. L., Stubbs, H. F., and Tek, M. R., The Mechanism of Disintegration of Liquid Sheet, Trans. ASME, Volume 75, pp 1279–1286, 1953;

[10] J.H. Ferziger, M. Peric, Computational methods for fluid dynamics, Springer 2002;

[11] C. Hirsch, Numerical computation of internal and external flows, Butterworth-Heinemann, 2007;

# CHAPTER 2

## LITERATURE REVIEW

The literature review reported in this chapter is subdivided into experimental and numerical categories. This is also the way in which the analyses on the subject were developed. At the beginning the computing power and mathematical models were very poor, so that experiments were the only investigation tool. Later, as modeling activity became more sophisticated, the interest of many researchers went in this direction, also because the extreme condition in the gas atomization process (high temperature, high pressure and high frequency) make difficult to understand and visualize the physics involved (ex. Recirculation zone, primary break up, melt instability).

### 2.1 Principles of jet disintegration

The atomization process involves a bulk liquid that is disrupted into many particles (also called dispersed phase) under the action of an external force exerted by the surrounding medium (continuous phase). The surface tension keeps the liquid in the geometry of minimum energy and the viscosity acts against shape modification. When the aerodynamic force overcomes the resisting component the core break up takes place. The shape of the liquid column is determined by the equilibrium of disruptive and cohesive forces. As the expanded gas reaches the liquid surface, it experiences perturbations and eventually oscillates: when the momentum of the gas reaches a certain level, the oscillations become unstable and the melt breaks-up (this stage is called *primary break-up*). The particles formed by initial breakup undergo further atomization steps (called *secondary break-up*) until the formation of a fine powder plume. A pioneering analysis to model the liquid jet disintegration was performed by Dombrowski and Johns [1]. As illustrated in figure 2.1, they distinguished three steps in the atomization of the liquid stream coming out from a planar slit nozzle.

Initially, the waves grow quickly denoting the instability on the liquid surface until the longitudinal elements detach from the core. The ligaments move downstream and deform into cylindrical bodies that successively disintegrate (according to capillary instability) and, driven by surface tension, become drops. Successively Bradley introduced a more refined

model [2,3]: he considered a horizontal liquid sheet with zero velocity, over which compressible gas was flowing parallel with uniform velocity.

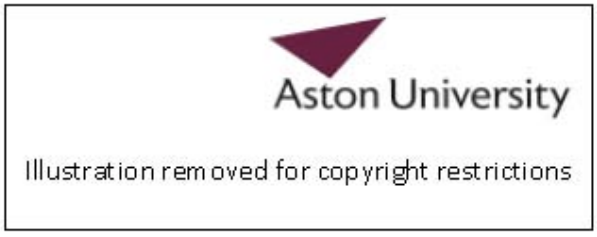


**Figure 2.1: aerodynamic atomization model of planar liquid stream [1]**

The critical wave number $k_{max}$ (related to the fastest growing amplitude) was obtained by quadratic equation as a function of liquid kinematic viscosity, liquid/gas interface energy, gas Mach number and fluid densities. The diameter of the ligaments was modeled as:

$$d_l = \frac{2\pi\varepsilon}{k_{\max}} \tag{2.1}$$

where ε has a constant value (≈0.25, obtained by Bradley for air atomization of water [2]). The diameter of droplets produced during primary atomization is given by:

$$d_{child} = \frac{2.95\sigma_l}{Lv_{gs}^2\rho_g} \tag{2.2}$$

where L is a dimensionless parameter (function of Mach number), $v_{gs}$ the gas sonic velocity, $\sigma_l$ liquid surface tension and $\rho_g$ the gas density. The comparison with the experiments conducted by See [4] shows that the model predictions match the measured data within a factor of 2. Notwithstanding its simplicity, Bradley model does not consider relevant parameters of the process such as gas to melt flow ratio, liquid viscosity and nozzle geometry. Rao et al [5] demonstrated that ε depends on atomization angle and nozzle diamenter. Furthermore, the initial assumption is that the melt and gas flow parallel while usually the gas velocity has a component normal to the melt surface: many aspects of primary breakup remain undisclosed and numerical simulations offer the possibility to gain

additional detail on the subject. Even if primary atomization determines the initial spray composition, it is the secondary atomization stage that finalizes the powder size distribution. The deformable liquid bubble is destabilized by the aerodynamic force generated by the relative velocity with respect to the surrounding gas. As for primary break-up the surface tension and liquid viscosity tackle the disruption: the former has a stabilizing effect while the latter dumps unstable perturbation. The force distribution on the droplet surface changes with time due to interface deformation. When the aerodynamic force overtakes the internal resistance the particle is disrupted into smaller droplets: the process continues until the balance of the forces is attained. The droplet size, at which equilibrium is reached, determines the *critical diameter*. There are different atomization modes that depend on the fluid's physical properties (density, viscosity, surface tension) and flow organization around the particle. According to Hinze [6] there are three possible break-up modes:

1) The droplet becomes oblate and successively deforms into a torus that is stretched and breaks in smaller particles. This is the case of drops experiencing aerodynamic pressure or viscous stresses in parallel flow ;
2) The droplet shape becomes elongated with thread shape and successively breaks-up. This condition takes place in Couette flow;
3) Protuberances are released and successively detached from the droplet surface due to deformations occurring within chaotic flow.


**Figure 2.2: break-up modes for secondary atomization [7]**

Bubbles present different reaction depending on the acceleration type. When the particles go through steady acceleration, they are gradually flattened and then pulled to form bag like shape.

The instability on the bag layer causes the disruption into child drops with diameters one order of magnitudesmaller than the parents. This model is called *bag break-up*. In case the particles experience sudden acceleration (i.e. impulsive exposition to high speed flow), a liquid sheet is pulled out from the external surface in the gas direction. Successively small filaments of melt are removed from the sheet and atomized. This is termed *shear break-up*. Figure 2.2 shows a comparison of the two mechanisms.

The bag break up resembles the Kelvin-Helmholtz instability features, while shear break-up is associated with the Rayleigh–Taylor instability. The main criteria to determine atomization is based on Weber number (defined as $We = \frac{\rho_g u_{rel}^2 d_p}{\sigma_l}$). Hsiang and Faeth [8] showed that the critical We value is given by the following equation:

$$We_{cri} = 12(1 + 1.077Z^a) \tag{2.3}$$

where the Ohnesorge number (Z) is equal to $\frac{\mu_l}{\rho_l \sigma_l d_l}$ and the exponent "a" varies in the range from 1.6 to 1.64. It is evident that for Z smaller than 0.1 the critical Weber number is practically constant, as reported in figure 2.3. Multimode break-up includes parachute break-up, chaotic break-up and bag break-up [9]. The characteristic timescale involved in the atomization process is:

$$t^* = \frac{d_0}{u_{rel}} \sqrt{\frac{\rho_l}{\rho_g}} \tag{2.4}$$

Hsiang [8] quantified the deformation time before breakup in $1.6t^*$: during shape modification the particle drag coefficient undergoes significant variation. Computational implementation of break-up models will be presented in chapter 3.

The absence of a general theory on droplet formation mechanism led to the development of empirical correlation based on the process parameters and liquid properties. Standard liquids such as water or fuel have been analyzed extensively while publications on melts are still limited. Most of the formulae available to describe size distribution of metal droplets originate from experimental observation and theoretical models on powder already

solidified. One of the first attempts to predict particle size distribution was done by Lubanska [10] and worked out the following equation:

$$d_{50,3} = K\left[\left(1+\frac{M_m}{M_g}\right)\frac{\upsilon_m}{\upsilon_g}\cdot\frac{1}{We}\right]^{1/2} D_m \qquad (2.5)$$


**Figure 2.3: break-up regimes for droplet deformation and secondary atomization [8]**

This empirical correlation was defined for the free fall nozzle configuration, but is considered as a reference for all the atomization types because it includes (at the correct order) all the relevant parameters involved in the melt disruption process. The constant K accounts for the different nozzle geometry and, in the Lubanska model, ranges between 40 and 80: recent investigations [11-12] proved that higher values could also be necessary (112 - 140). The reduction of melt stream diameter ($D_m$) promotes finer powder production: this can be achieved by reducing the feeding tube hole. $M_m/M_g$ stands for the dependency on melt to Gas Mass flow Ratio (i.e. 1/GMR –define GMR). In other words the reduction of liquid metal rate and/or the enhancement of gas flux would shift the resulting powder yield toward smaller sizes. The Weber number is proportional to the square of the relative

velocity between gas and droplet: this means that the fastest gas would generate finer powder. Melt viscosity $\upsilon_m$ acts as an antagonist force to the break up. Lubanska rearranged the Wigg's [13] correlation according to the atomization results of many low melting point alloys (Sn, Fe, Al, Cu), steel and wax (see figure 2.4). When Rao et al [5] applied (2.1) for the results obtained using nozzles of different diameters and apex angle it failed to match the experimental data.


**Figure 2.4: mean particle sizes distribution, Lubanska correlation [10]**

Further investigations provided modified a Lubanska correlation [14-15] and an atomization model based on Raleigh's instability [2,3], but none of those has a general character. Further it has to be noted that such models were developed for subsonic flow, while the majority of modern atomizers run at supersonic conditions. An exhaustive overview on mean and median particle size is given by Liu [16]: empirical and semi-empirical equations are correlated to the operating condition, nozzle design and liquid properties. The thermophysical properties of gas and melt have a direct effect on droplet size because they determine the heat exchange. Putimtsev [17] analyzed melt atomization using air, nitrogen, argon and helium and observed that low density, low thermal conductivity, and high viscosity gas produces finer powder: the reason is that when the heat exchange is reduced the particle remains above the solidification temperature for a longer time, enhancing the in-flight atomization period/path. On the contrary, metals with

high thermal conductivity and low thermal capacity solidify quickly and inhibit the secondary break up (denoted by the presence of many large droplets in the resulting powder yield. Melt overheating (100 K above melting point) is a common practice in industry in order to extend the atomization zone. However very slow cooling rate could introduce additional issues related to the sticking phenomena: within a dense cloud of drops, it is extremely easy to collide and generate satellite aggregation. Also gas chemistry can affect the particles shape: the formation of oxide layer (i.e. external skin) preserves ligaments from further disruption [18]. For this reason inert gases are preferably used and oxygen blending is avoided.

## 2.2 Experimental investigations

In 1948, Thompson [19] performed the earliest detailed study of Aluminium close coupled atomization. He analyzed the influence that the process parameters such as gas pressure, metal temperature and metal flow rate have on powder sizes, testing different nozzle configurations. However it was only during 1980s, due to the increasing interest in powder microstructure and unique properties, that the research activity expanded.

Couper and Singer [20] investigated the operational gas pressure to find the "critical point" pressure that guarantees sub ambient condition at melt tip: the purpose was to avoid melt backflow and freeze-off arising because of high pressure in the recirculation bubble. For a typical nozzle design, it was found that the critical point is reached for a stagnation pressure in the range 900-1200 psig (62-83 bar ). Results show a correlation between stagnation pressure and local pressure at the melt stream exit: they suggested that the break up process is linked to the presence of sub ambient pressure at the feeding tube exit. However such values for operating pressure result in wide pattern subsonic flow with poor atomization performance. Ayers and Anderson [21] made an overview of the applications and production processes for powder with very small sizes (<10μm). The different processes were subdivided according to the different physical principles they involve. The correlation between stagnation pressure and particle diameter distribution was confirmed: the best yield was found in correspondence to the stagnation pressure that minimizes the static pressure at melt exit orifice. Unal [22] investigated the 2014 Aluminium powder production with a close coupled nozzle using three different gases: nitrogen, argon and helium. Different combinations of stagnation pressure, gas to melt flow rate ratio and melt superheating temperature were tested. The finest powder was produced by Helium with

median size in the range 14.6 -18.5 μm while the coarsest result was obtained with Argon (21-37 μm). Nitrogen yielded intermediate median diameters. Alloy temperature over 825 °C had only a slightly influence on particle size reduction and this is the effect of lower surface tension and viscosity of the melt. However, temperatures below 775 °C may cause early solidification that leads to the break up vanishing. A pressure of 1.56 MPa proved to be the most appropriate for atomization via nitrogen: higher pressure means gas waste while lower pressure produces partially atomized flakes. The mean particle diameter was directly proportional to the square root of melt flow rate and powder sizes were fitted by a log-normal distribution: broadening of size range was directly correlated to the increase of liquid alloy flow rate. Successive analyses were performed by Unal [23] on confined nozzle at supersonic condition, using Schlieren photography of gas only flow. The wave pattern corresponding to a 1.56 MPa stagnation pressure was deeply affected by feeding tube length: long protrusion promoted an expansion fan so that the jet undergoes subsonic condition a few diameter away from the tip. Longer supersonic plumes were associated with shorter protrusion and with shock formation at the delivery tube tip. The supersonic plume is a measure of process efficiency: the nozzles with more extended supersonic jet had better performance in terms of fine powder. A methodology based on the method of characteristic was presented in order to define atomization condition as a function of nozzle geometry and to determine the optimal feeding tube protrusion to achieve the longest supersonic plume.

Miller et al. [24] introduced a new method to calculate the melt flow rate: they demonstrated that the aspiration pressure is not the only parameter governing liquid motion during atomization. The new model is based on the force balance and momentum conservation at the border between melt and gas. Successively, Miller et al. [25] made a comparison between axisymmetric and non axisymmetric nozzle geometry. The results show that the yield of fine powder is improved by the use of a non axisymmetric configuration. The explanation of better performance relies on the split of the main metal core into multiple streams of reduced diameter. It was believed that non axisymmetric nozzle force the melt outward in the high velocity gas zone by means of privileged roads. Clear evidence was the plume broadening.

An alternative improvement to the atomization mechanism was suggested by Strauss [26]: considering that the disruption process is mainly driven by aerodynamic force (that is proportional to relative velocity between gas and droplet), it was evident that an increase in

gas velocity could bring some benefit. However, instead of boosting atomization pressure, the author investigated the use of preheated gas. Trial tests were run in a laboratory scale close coupled atomizer with converging slit nozzle geometry. The mean particle size reduction correlated well with gas temperature increase. However, even if the mean diameter was reduced, the minimum achievable diameter remains almost unchanged for different gas temperatures: it seems that operating gas temperature affects only the bigger droplets. In any case introduction of hot gas reduce the running expenses because of its lower mass consumption. A new parameter was introduced, the normalized gas energy rate, that is the gas kinetic energy normalized by the melt mass flow: compared to the gas to melt mass flow ratio, this parameter contains more process parameters (gas velocity, mass flow rate and energy) and give a better correlation with experimental data. In successive studies, Strauss [27] showed that pressure at the tip does not result in a clear index. He did not find a successful correlation between tip pressure measured for gas only flow and melt flow during atomization. Aspiration pressure was not even correlated to mean particle diameter, while gas to melt flow rate ratio proved a clear link with resulting particle sizes but only over a reduced operating range. The normalized gas energy rate was confirmed to be a distinctive term to predict powder characteristics for wide combinations of working parameters.

Ting et al. [28] tested the atomization process at two specific operating conditions, open and closed wake, to evaluate their effect on the yield. Closed wake means that the recirculating bubble under the nozzle tip is not affected by the surrounding zone because of a normal shock (also called Mach disk) that acts as a shield. For the specific geometry considered, Mach disk arises at about 4.9 MPa. The powder obtained on atomizing at lower pressure had bigger sizes but gave a better result in terms of gas consumption because the gas to melt flow rate ratio was lower. The use of stagnation pressure just above the closed wake stage produced a pulsating behaviour of the melt: the explanation given by the authors is that when the melt enters into the recirculation volume, the Mach disk disappears (in other words, the shock pattern is opened by the melt). A sudden change in shock structure causes a pressure increase at the melt exit orifice so that the melt flow reduces and the Mack disk is created again. This phenomenon seems to improve the melt filming on the nozzle tip and was addressed as the main reason for the finer powder produced. Figure 2.5 reports the proposed atomization model.


**Figure 2.5: closed wake atomization model**

Further understanding about melt oscillating behaviour during supersonic atomization was obtained by Ting e al. [29], recording the atomization of 304L stainless steel with high-speed film footage (10 000 frames per second). The examined nozzle consists of 18 convergent holes around a 9.5mm pouring tube. The images captured were digitalized and the amount of pixels containing melt was used as input data for the discrete Fourier transform. The derived spectrum showed many peaks with higher amplitude in the low frequency range. The dominant low frequency peaks revealed fluctuation of melt in the recirculation zone. Splitting the analysis to the different regions of the atomizer, it was evident that the zone further downstream, where the secondary atomization takes place, was dominated by high frequency. A singular peak was found in the high frequency spectrum: the authors explained this as the effect of aero-acoustic noise (known also as screech tones of nozzle at off design condition). However considering the attenuation that ultrasounds experience in the far field, it seems unlikely that their energy may affect the break-up process: further studies are necessary to verify this issue. An analysis on the

aspiration at the feeding tube tip was done by Cui et al. [30]. Converging and converging-diverging nozzle geometries were tested at different atomization conditions. The converging nozzle resulted in greater sensitivity to gas pressure, protrusion length and taper angle but was able to create sub ambient pressure also with short feeding tube, avoiding dynamic energy loss coming from jet impact and deflection.

Very interesting results were found by Unal [31] testing the performance of a new close coupled nozzle, with discrete converging-diverging nozzles. Increasing the operating gas pressure the melt flow rate was reduced while in the past it was expected to increase, because of the lower pressure at the tip. The melt atomized with higher gas pressure produced finer powder: improvement in droplet size cannot be explained only with the higher kinetic energy given to the gas by pressure boost but the variation in gas to melt mass flow ratio also has to be considered. Feeding tube length has a complex influence. Three different protrusions were tested 5, 10 and 15 mm: while 5 and 15 mm configurations had similar trends for aspiration pressure, the 10mm had a more unstable behaviour. Figure 2.6 shows the test facility and relative results.

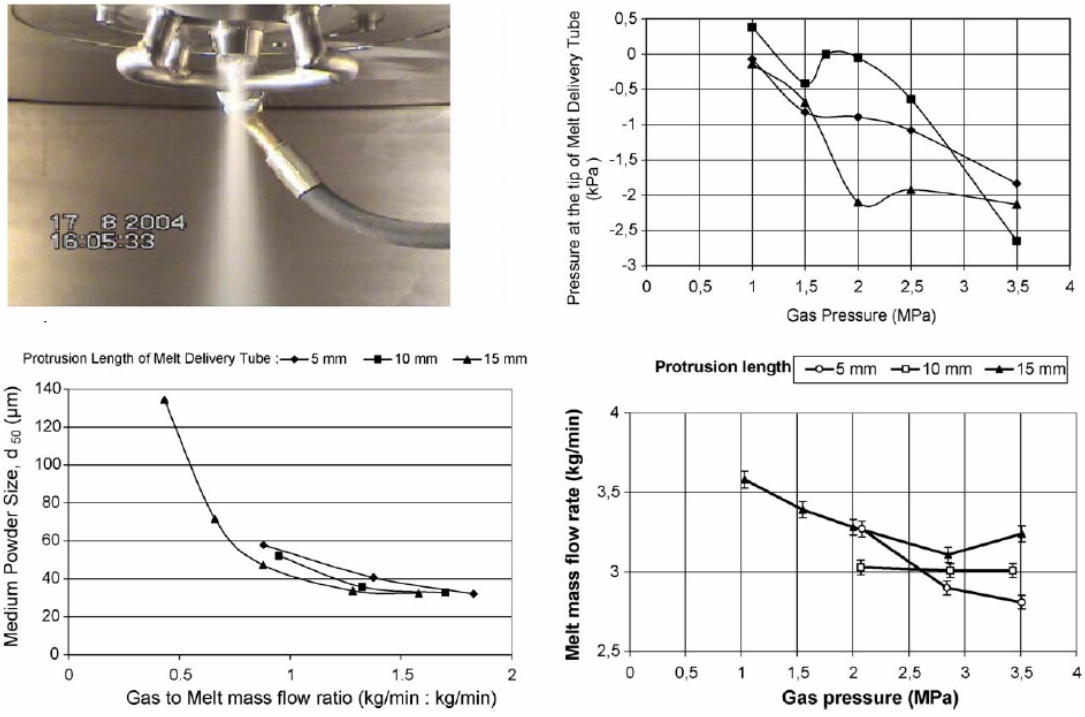


**Figure 2.6: Unal test facility and results**

Mates at al. [32] investigated four different converging nozzle geometries, three with discrete numbers of nozzles and one with an annular slit. Axial Pitot pressure

measurements have been used to evaluate the relationships between geometry, supersonic jet length and dynamic pressure. Process images proved that droplet breakup is driven by the dynamic pressure but it is not confined to the nozzle tip region: the atomization continues far away from the pouring tube exit, so that the distance over which dynamic pressure is kept at high level also plays an important role. Long supersonic jets with large dynamic pressure improve the interaction between melt and gas, producing finer droplets. Pressure profiles demonstrated that the increase in operating pressure corresponded to a longer supersonic plume due to the higher momentum given to the flow. The formation of normal shock had a dramatic effect on the slit nozzle jet extension that decayed much faster than before Mach disk formation. It is evidence that the turbulent mixing rate is increased by the presence of normal shock. On the contrary, no relevant effects were noticed when normal shock took place in discrete jets configurations. The annular nozzle produced the longest supersonic jet with the higher dynamic pressure over the examined pressure range: in fact, due to the smaller jet surface (for the same throat area, annulus requires smaller perimeter than discrete holes) the diffusion of momentum by turbulent mixing is reduced.

A comprehensive overview on close coupled gas atomization was published by Mates and Settles [33-34]. They analyzed the characteristics of gas only flow and related performance during metal atomization for both converging and converging diverging nozzles. According to their results, the jet plume was almost the same for the two configurations: the only difference was at the lower end of the investigated pressure range (≈ 1,4 MPa), where the converging-diverging nozzle has almost a double supersonic length. The explanation is that, even if the converging flow is underexpanded, it does not form normal shock, but just oblique shocks that do not have deep impact on plume decay. As explained in [35], a Mach disk forms only when the underexpanded jet has a certain Mach number. At higher stagnation pressure ratio (>55) a closed wake phenomenon arises: Schlieren images captured during these tests have proven that, when melt enters the domain the wake is opened and remain in this condition. It was concluded that wake closure does not affect the investigation: a pulsating mechanism may develop for special operating configurations, but it looks an improbable operating mode. Increasing the operating pressure ratio from 14 to 55, the jet length underwent a two to fourfold increase, while the maximum dynamic pressure on the centreline showed modest increase.

The microsecond exposure Schlieren images clearly identify primary break up close to the nozzle tip and secondary break up far away, up to 10 nozzle diameters from melt exit. Large unatomized droplets were visible downstream in the jet core, while fine particles exist in the outer region at the same distance: this means that mass loading is a relevant phenomenon. The strength of core gas is weakened by the carried particles, causing reduction in the atomization attitude. Figure 2.7 presents a sketch of the situation. Melt filming under the delivery tube tip is absent, while the dominant primary break up is fountain like.


**Figure 2.7: microsecond Schlieren exposure with interpretative sketch on mass loading phenomenon [34]**

The shock flow pattern was deeply affected by the presence of melt: the waves that, in gas only flow, cross through the jet core and form large shock diamond cells are reflected before they reach the core zone, forming smaller diamond cells. This may lead to subsonic velocity for a long distance in the central jet region. There was no noticeable difference in powder sizes produced by the two geometries at higher operating pressure, where the supersonic jet plumes were similar. The gas to melt flow ratio played an important role in determining supersonic jet length and its decay. Particle size distribution showed a high dependence on high velocity distribution away from the nozzle tip rather than on the particular flow pattern at melt exit. Similar yields were achievable with different nozzle geometries when the process parameters (stagnation pressure and gas to melt flow ratio)

were approximately the same. Application of visualization methods was presented by Ridder et al. [36]: high speed photography and laser scattering techniques were used to determine the particle formation mechanism and their size. This provided insight into process understanding so that an efficient feedback system could be developed to control the atomization process. Ziesenis et al. [37] introduced the phase Doppler anemometry as an investigation tool for the atomization process. This non intrusive measurement method gave the possibility to analyze not only particle diameter and velocity, but also the local mass flux of the spray cone.

New processes were introduced in the recent with the aim of decreasing the yielded particle sizes and maintaining them in a narrow range. Lagutkin et al. [38] proposed a pressurized centrifugal nozzle for the melt: liquid metal leaves the nozzle as a hollow cone and is further atomized as in the free fall configuration. In this way, the melt prefilming is ensured and the primary breakup is more efficient. Strong dependency of powder sizes on gas to melt mass flow ratio was noted. The initial results were encouraging but comparison with standard processes at similar conditions was not reported. Furthermore, the crucible needs to be pressurized: this means a more complex system with higher cost.

## 2.3 Numerical investigations

Espina et al. [39] solved the two-dimensional flow field using the method of characteristic (MOC), a widespread tool for compressible flow analysis. The solution was able to predict the pressure at the melt exit as interaction of first shock structure with the delivery tube side corner. The results were interesting even if, due to the absence of 3D effects, they were only an approximation. Due to the inviscid flow assumption, the kinetic dissipation of the viscous flow is not taken into account by MOC: boundary layer effects cannot be reproduced. A similar approach was used by Unal [40] using the two-dimensional wave theory to establish a correlation for aspiration pressure based on the relative position of pouring tube respect to the shock pattern of underexpanded jet. The accuracy of such methods was very low and only the main aspects could be captured. Computational fluid dynamics represented a strong improvement as an of investigation tool and over time overcame the previous models.

In 1992 Piomelli [41] solved the averaged Navier-Stokes equations to describe the gas-only flow in different close coupled atomization nozzles. The computational field was subdivided into two blocks: the first included the annular gas inlet and the second the area

above the feeding tube. The results were able to show the influence of stagnation pressure, turbulence and taper angle on the developed flowfield. It was found that turbulence has a deep impact on the jet evolution. Further, separation arose on the side surface of feeding tube: the author argued that when the build up and solidification of melt around the tip reaches the feeding tube orifice this lead to the interruption of liquid metal stream (freeze-off). The gas-only flow field and its interaction with discrete particles was modeled by Figliola et al. [42]. The equations describing the fluid motion were solved numerically: the Baldwin-Lomax two equations model was used to account for the turbulent effect. The computational two-dimensional domain extended axially over5 feeding tube diameters and radially over 2 diameters. Grid resolution was 96 x 56 nodes (in radial and axial direction), too coarse to capture the complex physics involved. However the particles' heat transfer was predicted using a Lagrangian representation to calculate their path. The comparison with experiments showed that the results were not accurate: the discrepancy was an effect of the two dimensional approach used to model an axisymmetric domain. However, using such results, they proposed a very interesting primary break-up mechanism that produced a liquid sheet with umbrella shape. A more advanced numerical simulation was performed by Mi et al. [43]: the high pressure gas atomizer gas-only flow pattern was investigated to evaluate the influence of high speed gas on molten metal atomization. Possible correlations between stagnation pressure, flow pattern and near tip condition were analyzed. The gas nozzle consisted of an annular convergent slit with 45° taper angle. Due to the symmetric geometry the computational domain was a two-dimensional axial section, with constant pressure on the far field boundary and axisymmetric condition along the axis. The extension was 6 melt tip diameters in the axial direction and 1 diameter in the radial one: it was discretized with 400 cells axially and 75 cells radially. The grid spacing was not uniform in order to have a finer grid in the zone where steeper gradients (boundary layer, shocks, recirculation) for flow properties (temperature, velocity, density) were expected. The turbulent model adopted was the standard k-ε. Mach disk arouse for stagnation pressure around 3 MPa. Increasing the stagnation pressure, this moves downstream and became stronger. Pressure gradient was found along the delivery tube tip and its strength was proportional to stagnation pressure. The liquid metal entering the domain should be forced radially outward by this gradient, enabling the formation of the thin layer of filming process. A difference between experimental and numerical results can be noticed for the aspiration pressure and mach disk location: apparently the reason was that simulated

geometry had a slit nozzle while the experimental configuration had discrete holes. However, good agreement was found in terms of the trend of results. Successively, Mi et al. [44] did a parametric study of the influence of geometric parameters on gas flow field. The grid and model employed were the same for the previous research. Longer protrusion of feeding tube into the domain caused smaller pressure gradients on the tip meaning a more uniform pressure distribution, limiting the filming mechanism. On the other hand, shorter tip protrusion created higher pressure at the melt exit, destabilizing the process. Also the taper angle influenced the aspiration pressure: a straight feeding tube surface developed deeper subambient pressure when compared with a geometry having a taper angle >0, but, at the same time, had a smaller pressure gradient at the tip. A tradeoff between protrusion and taper angle was recommended, in order to have good aspiration (for process stability) with sufficient melt driving force (powder size refinement due to more effective primary break-up).

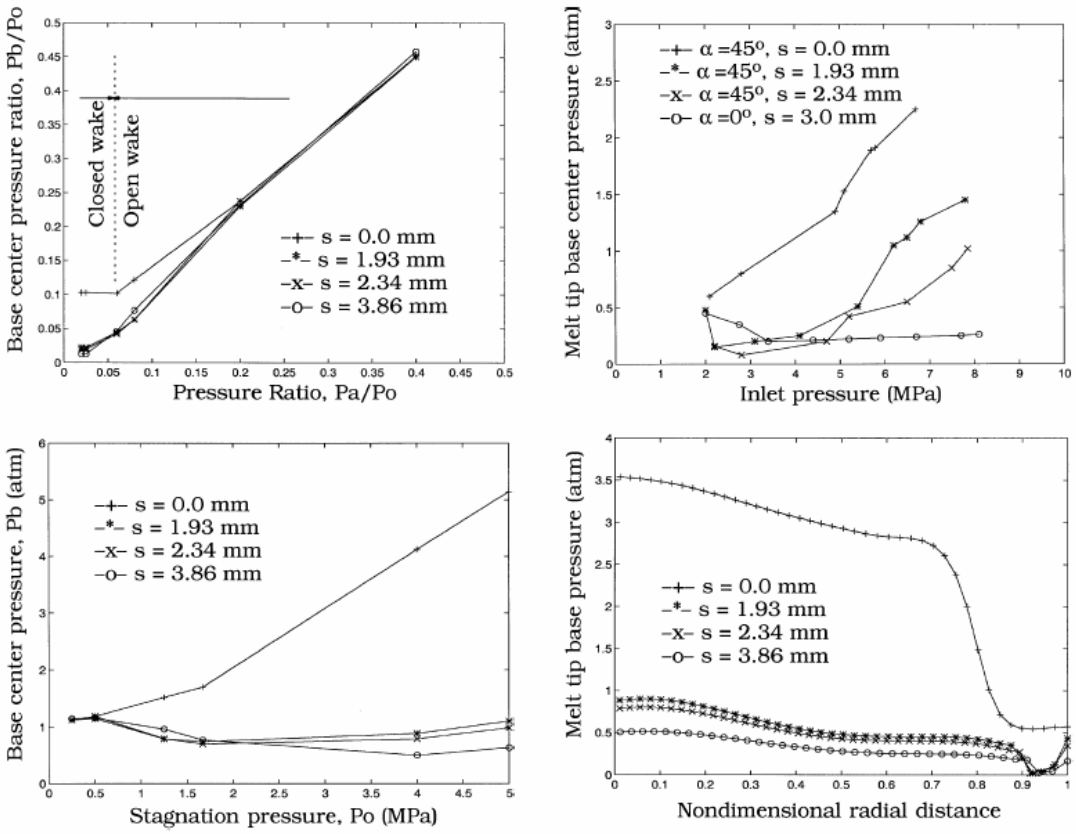


**Figure 2.8 base centre pressure and melt tip base pressure correlations**

Figure 2.8 shows the relationship found. Many numerical analyses were executed at the National Institute of Standard and Technology (NIST) [45-47] to predict the gas-only flow in close coupled atomizer using a converging slit nozzle. The computational domain was

subdivided in three blocks containing 73 000 cells. The domain extended axially 7,35 feeding tube diameters and radially 5 diameters. The turbulent model employed was a modified k-ε version. The boundary conditions were symmetry along the axys and constant pressure on the outer edge of the domain. Different stagnation pressures were used in the simulations and the results of aspiration pressures were compared to the experimental data: the discrepancy was around 10-20%. This was the result of poor accuracy in the prediction of flow field inside the recirculation bubble, principally due to the lack of a turbulence model. Premature flow separation was noticed on the external surface of the delivery tube: as already found by Piomelli in 1992, the low pressure that exists in the separated zone sucks part of the melt at the delivery tube tip that because of cold expanded gas freezes (see figure 2.9 for schematic sketch). The accumulation of solidified melt changes the shape of the delivery tube and sometimes brings a premature end to atomization. In order to avoid this issue, the choice of the longer feeding tube that does not present separation was proposed as a design guideline for new nozzles.

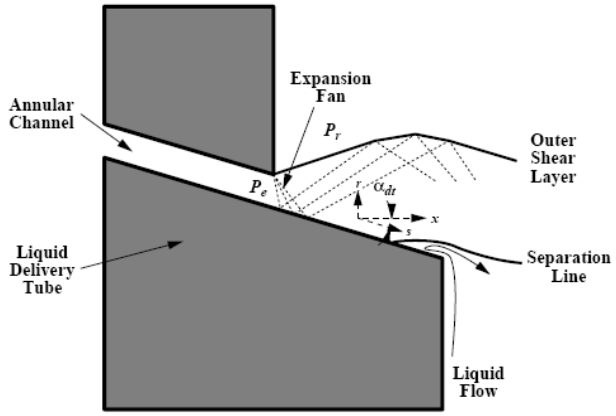


**Figure 2.9: sketch of flow separation on feeding tube surface**

The simulation with preheated gas showed that, doubling the temperature the momentum of the gas jet is reduced by 29%. The hot gas also separated earlier on the liquid delivery tube. Also the jet spreading rate is reduced and resulted 32% reduction when measured 4 diameters from the tip. The injection of liquid metal was modelled introducing hot gases with high momentum (to have the same momentum of melt stream). The additional fluid pushed downstream the existing recirculation zone. The reattachment point remained in the same position, so that the recirculating bubble became shorter and reduced the surface area: this means less area for momentum exchange thus a deceleration of internal flow. Detailed investigation on the recirculation zone was carried out by Xu e al.[48] on a converging slit nozzle with 45° taper angle. The tip pressure is the results of two opposite

mechanisms: entrainment of recirculating gas in the high speed axial jet and backflow from the jet into the recirculating bubble at the reattachment point. The entrainment is the effect of viscous shearing along the internal jet surface: this is proportional to the velocity of separated gas. The reattachment point acts as a barrier against the upstream gas, that has to spend its axial momentum to overcome it, otherwise also turning into a backflow. When the operating pressure increases, velocity and jet momentum also increase, reducing the amount of gas unable to prevail over the reattachment point. In this condition, the formation of sub atmospheric pressure at the nozzle tip is facilitated. The study confirmed a correlation between tip pressure feeding tube protrusion and stagnation pressure. The authors concluded that a certain protrusion is essential to guarantee a stable aspiration pressure at the liquid exit orifice. Ridder et al [49] analyzed the influence of two pour tube shapes on flow field structures. The first one presented straight surface and discrete nozzles with taper angle >0, while in the second geometry the feeding tube surface matched the taper angles of the discharge holes. Imagines from Schlieren tests and numerical simulations showed that the angle discontinuity caused a longer recirculation zone. Furthermore, the discontinuity aroused a strong shock wave, that reduced both energy and momentum contained in the jet. The authors suspected that this could lead to a poor performance during atomization. Ting et al. [50] simulated half of the central cross section of an annular slit nozzle with 45° taper angle. The domain was 50 mm long and 15 mm lwide, with symmetry boundary condition along the axis and open boundary on the domain border. 6 different operating pressures were analyzed, ranging from 0,69 to 7,58 MPa. The gas used was argon and the turbulence model was the well known Reynold Stress. Recirculation zone and shock pattern were analyzed in detail. During the open wake condition, the reattachment point moved downstream. A secondary recirculation zone was revealed in the closed wake condition, behind the Mach disk: this was bounded by two high pressure points. The values of pressure in those points are much higher than in the first recirculation zone and than the stagnation pressure predicted for all open wake conditions. The authors hypothesized that, when the melt enters the domain, the Mach disk disappears and the pulsating mechanism arises, as explained in [10]. Czish et al. [51] gave an example of how CFD can be used as a design tooling. A new system was developed for the atomization of a viscous melt. The idea was to improve the efficiency and decrease the sizes of yielded particles, increasing the specific surface energy of the melt before atomization. A rotating disk spread out thin melt film that is then atomized by high

speed gas. Numerical simulations were used to derive the optimum condition to achieve the maximum gas momentum acting on the liquid film against the atomization nozzle direction. The experiment showed that the minimum mass median particle size achievable is 210µm. Future developments to improve these results are ongoing. Figure 2.10 shows the principle of this new process.

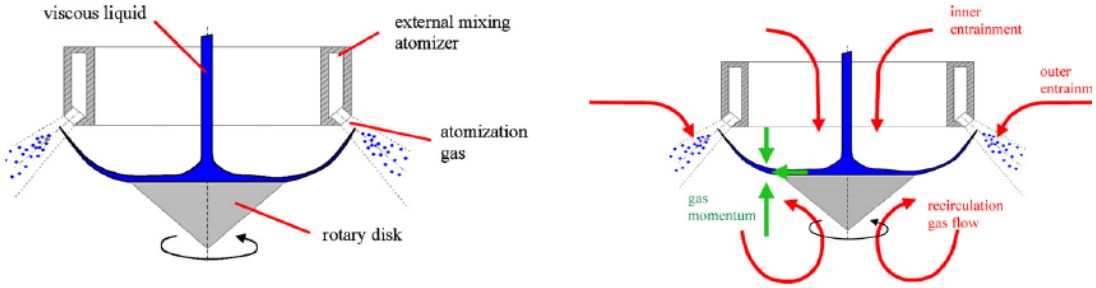


**Figure 2.10: gas atomization with rotating disk**

## 2.4 Multiphase flow

In the recent decades, many analyses focused on modelling the interaction of melt and gas. This is a typical multiphase problem, similar to fuel atomization. The most advanced model is the VOF (Volume Of Fluid) that considers the two fluids (gas and melt) as immiscible, solves a single set of momentum equations and tracks the volume fraction of each of the fluids throughout the domain. However in order to model a droplet with sufficient accuracy, it has to contain at least ten grid cells on the diameter: this means that, for a 20µm droplet, the grid size should be 2µm and a 2D domain of 20 x 5 cm should contain 25 x $10^8$ cells. This is beyond the current computing power. Usually, to overcome the computing power limitation the second phase is modeled as a discrete phase: droplet trajectory is obtained by integrating the Newton law in a Lagrangian reference frame (also called Lagrangian approach). Both models will be detailed in chapter 3 and 4.

Kuntz and Payne [52] developed the first numerical model to predict particle size distributions in a close-coupled gas metal atomizer (probably the best study on this subject so far). The gas flow field and the melt stream were decoupled. 2D Gas only flow was simulated using the INCA solver. The axisymmetric computational domain extended 0.10 m radially and 0.30 m axially and was discretized by 52893 nodes. The simulated gas is argon at 5.5 MPa: the exit condition of the converging slit is Mach 1 (choked flow), but then the gas accelerates up to Mach 6 in the atomization chamber. Turbulence was simulated according to the Baldwin Barth one equation model due to converging issue

with k-ε (see appendix A.2.4). In this research, they followed a decoupled approach to the problem by modeling the gas-only flow first and then using a particle disruption-tracking algorithm to calculate the resulting particle size distribution. The melt stream is calculated separately using a set of equations implemented by the authors: this code uses the gas flow path as entering data to predict the melt path. The atomization process is subdivided into three steps: film formation at nozzle tip, primary break up of liquid sheet and secondary break up of big droplets. The break up model is strongly affected by the material properties, and has to be tuned for the specific melt atomized.

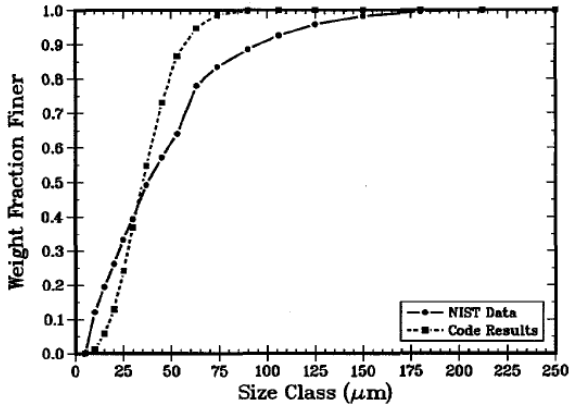


**Figure 2.11: cumulative size distribution**

As shown in figure 2.11 the predicted results were in trend with the experimental data. The discrepancy, in terms of size range (narrower in the simulation), is due basically to the absence in the model of collision and coalescence. It has to be noted that the uncoupled solution does not permit consideration of the droplet presence in the gas flow solution: this means that momentum/energy exchange is only one way (gas to droplet) and the flow field is unaffected by phenomena such as mass loading illustrated by Mates.

Li et al. [53] developed a two dimensional model to analyze momentum and thermal behavior of atomized droplets of γ-TiAl. The velocity flow field was not resolved but was modelled with an equation matching previous experimental data. Droplet path was predicted with a Lagrangian approach. The primary and secondary break up was not modelled and droplets of different sizes were modelled to reproduce the cone spray at different locations. Velocity, temperature, flight time, cooling rate and solidification behaviour during in-flight condition were evaluated against distance and elapsed time from the injection point. The solidification model used includes cooling in the liquid state, undercooling, recalescence, segregated solidification, peritectic solidification and cooling in

the solid state. Influence of radial distance, axial distance and droplet diameter were disclosed. Results on droplet cooling are reported in figure 2.12.


**Figure 2.12: droplet cooling [53]**

Grant et al [54-56] modeled numerically the in-flight dynamic and thermal histories of gas atomized droplets versus the distance during spray forming. It was found that the particle path and thermal history is deeply affected by droplet diameters and distribution as well as by momentum exchange with the gas phase. The mass mean droplet diameter was modeled as a function of melt delivery nozzle diameter, fluid properties, gas velocity and metal flow rate (Lubanska correlation). An analytical expression for solid fraction inside the droplet was deduced as a function of gas velocity, molten alloy super heat above the liquidus axial distance and melt flow rate. The basic assumption was that the average thermal history of droplet could represent the thermal behavior of the full spray. It was also assumed that the droplet diameter, representative of the average thermal history, was affected by the process parameters as the mass mean droplet diameter. The constants included in the equation were determined in a fitting process, by multiple linear regression, to the results previously obtained with full model.

Underhill et al [57] performed a 2D numerical simulation on a converging slit nozzle using nitrogen gas. Grid spacing was irregular to account for high gradients. The atomization process was not modeled and groups of droplets were injected in the atomization zone.

Shapes and sizes of the droplets vary according to Rosin-Rammler distribution. A FORTRAN code was used to post process droplet trajectory and temperature. As expected the cooling rate was higher for smaller droplets. The results were in good agreement with experimental data.

Hattel et al. [58-59] developed a mathematical model to describe particles cooling during spray forming. Also in this case the atomization is not simulated and the cooling process is subdivided into four stages: liquid cooling, undercooling/recalescence, solidification, solid cooling. The gas temperature is not the result of previous tests or empirical but is the result of heat balance inside the computational cell: this is the first model that introduce the droplet effect on the gas phase. The results confirm that bigger droplet shift downstream the solidification point: the reason is that, when the diameter increases, the heat exchange coefficient decreases. The droplet inside the particle is assumed uniform (lumped assumption).The cooling ability of three different gases were tested and argon showed the best performance. Results are reported in figure 2.13. In the second part of the study, accuracy and applicability of the numerical model were tested, comparing experimental and calculated results from the atomization of 12Cr–Mo–V steel. The effects of undercooling and melt/gas ratio on solidification process were analyzed. Undercooling phenomena affect the recalescence step but do not influence the overall solid fraction. Furthermore the undercooling level decreases with increasing particle size. Higher gas/melt ratios push forward the solidification point: the explanation is that when more gas is introduced in the domain, the gas velocity field increases in value and consequently the particle velocity increases, so, even if the droplet solidification time reduces, the traveled distance increases. The droplet cooling rate resulted in good agreement with the experimental data.

Bergmann et al [60] introduced a mathematical model to describe the cooling and solidification of in flight alloy particles. The solidification process involves the same stages as the one developed by Li, but the flowfield was solved numerically and source/sink terms in the equation describing fluid motion (Navier-Stokes) account for gas momentum/energy exchange with the droplets. Uniform temperature was assumed inside the droplet. Results show strict dependency of droplet cooling on flight path and gas to metal mass flow ratio. In-flight temperature and solid fraction variations at different gas to metal ratio for a 85 μm droplet is reported in figure 2.14.


**Figure 2.13: particle solid fraction as function of distance [58]**

Similar analyses were carried on also by Shukla et al.[61], Mahesh et al. [62] and Johnson [63] focusing on the droplet microstructure as a consequence of fast solidification. Only recently, has the attention of researchers concentrated on modelling melt behaviour during break up.


**Figure 2.14 In-flight temperature and solid fraction at different gas to metal ratio for 85 μm droplet[60]**

In 2002, Markus et al [64] investigated the primary disintegration process in a free-fall atomizer. The surface perturbation and growth bring the liquid metal jet to break-up. Experiments were conducted on water, tin and steel atomized by air. Linear stability analysis was performed on a viscous liquid jet discharged by a round nozzle into an inviscid gas phase. Increases in gas velocity cause an increase in the maximum wave growth that instead decreases when the liquid surface tension augments.


**Figure 2.15: wave characteristic of different waves [64]**

Lower growth rate values mean that more energy (higher relative velocities) is required to atomize. The linear stability analysis fails for large grow rate values: in this case, initial conditions, that usually are unknown, may have a strong impact. The instability modes are superimposed and a combination of spiral with helical form matches the experimental results.


**Figure 2.16: algorithm flow-chart [65]**

Antipas [65] presented a model for primary and secondary break up, termed Surface Wave Formation. The algorithm relies on the principles that break up involves an array of sinusoidal waves growing on the liquid surface: the fastest growing wave is then responsible for the motion of the liquid surface. The flow chart of the algorithm is reported in figure 2.16. The only forces that the model assumes acting on the ligaments when they collapse, are the gas inertial force and the liquid surface tension. The cylindrical globules that were detached by the melt stream became spherical under the action of surface tension. Predicted results presented a good agreement with the experiment.


**Figure 2.17: primary break up sequence [66]**

A direct numerical simulation was conducted by Tong et al. [66] for the first time on a close coupled atomizer. A front tracking formulation has been used to investigate the dynamic interaction between two interpenetrating fluids. A equispaced 2D grid, made up of 501 x 502 nodes was used for calculations. The highest Mach number that the nozzle could achieve was 1 so that both gas and quiescent gas are considered incompressible (this seems an unlikely assumption, because chocked flow may expand to Mach much higher than 1). Strong hydrodynamic interaction was found between gas and melt: the peak pressure location varies before and after the melt stream. Pressure and velocity fields are extremely irregular in both axial and radial directions. The creation of the stagnation point has a completely different mechanism when the melt stream enters the domain. The predictions showed also that the process is very unsteady, so that steady state simulations are not appropriate. Figure 2.17 reports the sequence of modelled primary break up.

## 2.5 Supersonic Base flow

Numerous research efforts have focused on the analysis of the flow behind an axisymmetric body. The near wake region (also termed base flow) was investigated experimentally theoretically and recently also numerically. Initially, the studies considered the subsonic case and only lately the development of new investigation tools switched research interest to the supersonic case. Wind tunnel experiments had to face the issue related to model holding system: the interaction between incoming fluid and the support could considerably affect the flow-field behind the base. Chapman [67] clamped the body with lateral rods while Donaldson [68] connected the rear face to a support sting. Successively Dayman [69] introduced wires to hold the model as sketched in figure 2.18. However none of the systems allowed disturbance-free measurements: the presence of sting affected the base pressure while the wires influenced the separated wake. Additional disturbances were caused by intrusive measurement devices (Pitot tube and hot wire probe) and by the upstream interaction of the turbulent boundary layer with the tunnel surface.
The exponential growth of disturbance throughout the flow field denotes absolute instability. Free flight experiments do not present such inconveniences but are quite expensive. Furthermore the conditions around the in-flight object are difficult to control and test reproducibility is almost impossible.


**Figure 2.18: wire support system used in wind gallery test by Dayman [69]**

Gaviglio et al. [70] carried out a detailed investigation on the near wake occurring in supersonic base flow: a sketch of the flow configuration is given in figure 2.19. The authors analyzed the effect of compressibility and anisotropy on the production of turbulent kinetic energy and found that a negative production occurs within the expansion zone.

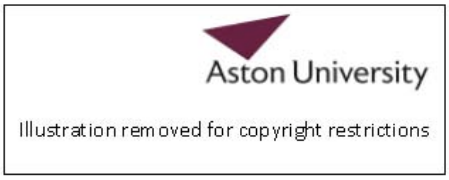


**Figure 2.19: flow field sketch [70]**

During the experiments performed at the University of Illinois at Urbana Champaign, Dutton et al. [71-73] supported the model with a forward sting: a supersonic blowdown wind tunnel was properly designed for the analysis of cylindrical body base flow. Compared to the other approaches, the forward sting presented lowest influence. Velocity components, turbulent kinetic energy and Reynolds shear stress contour were presented interpolating the data measured by means of LDV (Laser Doppler velocimetry). The planar laser sheet Mie scattering technique was implemented to visualize the development of the separating boundary layer. The "undisturbed" approaching flow was at Mach = 2.46. The results showed the existence of two separate zones in the free shear layer: an outer zone where the compressibility dumps turbulent fluctuation and an inner region where

turbulence activity is promoted by the close interaction between coherent structures (present in the shear layer) and the slow flow in the recirculating zone.

The presence of large coherent structures in the wakes of subsonic flow has been widely discussed and proved in the literature: Aschenbach [74] analyzed the flow behind a sphere at Mach <1 and confirmed the presence of two vortex shedding modes. On the contrary, the understanding of vortices dynamic behavior in the near wake of axisymmetric supersonic flow is still low. Qualitative evidence of the existence of large organized structures was given by Demetriades [75-76]: he studied the turbulence characteristic in the wake produced by Mach 3 flow over an axisymmetric slender body. Even if the data were measured in the far wake, the amplitude spectra had two peaks at low frequencies denoting the presence of coherent structures. In 1962 Morkovin [77] formulated the hypothesis that the direct effect of density fluctuation on turbulence (in near wall flow) is small when the root mean square of fluctuation is small compared to absolute density: recently So et al. [78] proved its validity also for a turbulent field. The best definition of coherent structure was probably given by Hussain [79]: "a connected turbulent fluid mass with instantaneously phase-correlated vorticity over its spatial extent". Papamoschou et al. [80] observed that large scale structures become less organized as convective Mach increases: the absence of organization was visible on both side and plan view. A possible explanation of the chaotic pattern was the coexistence of two- and three- dimensionalities in the flow.

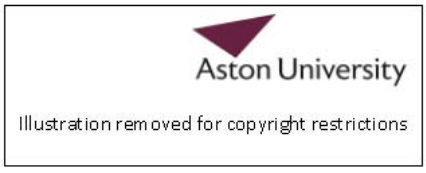


**Figure 2.20: coherent structures identification by means of Q isocontours method [81]**

Finally, visual proof of vortex structures in axisymmetric base flow was given [71-73] and their sizes were comparable to shear layer thickness. Sandberg et al. [81] made a great contribution to evaluating axisymmetric wake instabilities: direct numerical simulation (DNS) was used to identify coherent structure, as shown in figure 2.20. Numerical investigation was conducted on different circumferential domain sizes in order to exclude

the azimuthal/helical modes. Helical structures were detected close to annular boundary layer separation and many longitudinal structures were localized within recirculating flow. The vortices experience strong stretching and move toward hairpin configuration which promote instability and consequently small scale production.


**Figure 2.21: shear layer instability [82]**

A zonal detached eddy simulation (ZDES) was implemented by Simon et al [82] to simulate compressible axisymmetric shear layer for Reynolds number close to 2.9 x $10^6$ and 2.46 Mach (as per Dutton experiments). The domain is subdivided into 20.7 million cells and the physical time step 2 x $10^{-7}$ s. It was found that the flow includes a broad range of time scales covering free shear layer and recirculating flow features.

The Baroclinic torque and the vortex stretching terms in the vorticity transport equation were of the same order. The recirculation zones showed a global motion around their mean position. Significant displacement for supersonic flow was detected also by Humble [83].

**Figure 2.22: recirculation zone instability [83]**

Despite the impressive simulation carried out by Simon, difficulties still remain in the numerical solution of problems that include confined boundary layer, free shear layer and shock interaction.


**Figure 2.23: a) pressure distribution on plug shell [85]; b) pressure distribution on plug tip [86]**

Theoretically the best approach to simulating turbulent phenomena is DNS. This does not introduce any kind of filtering or averaging of governing equations and resolves all the scales in the flow. Small scales are produced by inertial forces and consumed by viscous one: when Reynolds number increases, the viscous effect becomes weaker and the formation of small scales is enhanced. However direct numerical simulation is extremely heavy and requires huge computational power: today it is limited to simple geometry and relatively small Reynolds number ($< 10^5$). In order to reduce the scales amount, an ensemble averaging is operated on the Navier-Stokes equations: this approach is termed RANS (Reynolds averaged Navier Stokes). The terms generated by equation non-linearity has to be modeled: over the years several models have been developed and a clear overview is given in [84]. The standard RANS model does not perform very well on separated flow: as reported in figure 2.23 the model failed to capture all the scales in the wake. The large eddy simulation (LES) model represents a more "elegant" tool to model turbulence [87]: the averaging is replaced by a filtering operation. The large coherent structures are solved while the small scales are modeled through a subgrid model. The results are extremely promising but the computational requirements are still very high for real scale analysis Fureby et al [88] performed LES simulation of axisymmetric baseflow: they considered the standard case of Dutton. The grid had 1.4 million cells and it extended axially 10 base diameters and radially 6 diameters. Reynolds number was $2.86 \times 10^6$. The results matched closely the experimentally measured pressure and velocity field. Kawai [89] conducted a computational study on supersonic base flow using a hybrid turbulence model: RANS near the wall boundary and LES in the rest of the domain. The flow properties were the same as for the Fureby case. The hybrid model showed good capability in reproducing the unsteadiness of the flow: shear layer roll-up is given in figure 2.24. The grid resolution requirements close to the solid boundary are considerably less than in LES because RANS can act upon a coarser mesh. In 2007, de Feo et al. [90] presented the analysis of supersonic base flow with a different RANS model implemented in the software FLUENT: the Reynolds stress model (RSM) gave results comparable with LES simulation even though the computing effort was much lower. RSM represents a good trade-off in terms of computational resources and quality: it will be described in Appendix A and used as a base model in this study.


**Figure 2.24: side view of vorticity magnitude [89]**

## 2.6 Melt flow

The liquid stream in free fall and close coupled configuration can be modelled according to the Bernoulli equation:

$$p + \rho g y + \frac{\rho u^2}{2} = const. \tag{2.6}$$

Considering the path of a liquid metal parcel from the tundish surface to the feeding tube orifice, the exit velocity is:

$$u_{exit} = \sqrt{2\left(\frac{\Delta P}{\rho_l} + g\Delta h\right)} \tag{2.7}$$

Where ΔP stands for static pressure difference and Δh is the metallostatic height of the melt. A reference value for ΔP is 0.15 atm while Δh ranges between 0 cm and 25 cm: according to those values the two factors have the same weight on the exit velocity (≈ 1.4 ÷ 3 m/s). It is clear that the aspiration pressure exsisting close to the melt exit plays a very important role, and it acts as a valve limiting the flow rate. As mentioned above, the quantity of liquid that enters the domain (i.e. GMR) has a strong impact on the final powder quality, so it is extremely important to understand/predict the pressure distribution near the ceramic nozzle tip during atomization.

## 2.7 Aim and objectives of the project

The literature review showed that only few aspects of close coupled atomization have been modelled and understood successfully: even if the parameters that govern the phenomena

have been pointed out, their interaction and influence on the break-up phenomena must be determined.

The 2D axisymmetric geometry is the basic approach to simulate gas only flow. Furthermore the turbulence models used show significant limitation with steep expansion, wall bounded domain and flow anisotropy. Because of this, the starting point of the thesis was the investigation of 2D axisymmetric domain: instead of the classical k-ε approach, the turbulence is modelled with the RSM scheme to overcome the limitation experienced by previous analysis on compressible shear layer. Initially the gas only flow is modelled to define supersonic plume length and shocks localization. Droplet interaction with the gas jet has not been modelled before in the same domain as well as droplet atomization and non Newtonian cooling. In order to correlate the process parameters and powder characteristics, the atomization process is modelled by user defined function (udf) implemented in the main solver Fluent: multiphase flow is investigated injecting a discrete phase (Lagrangian approach, sink/source in the momentum and energy equation to couple gas and drops) and modelling infligth secondary break up of liquid particles generated during primary atomization (not modelled but determined according to Markus results [62]). With the aim of improving the energy/momentum transfer between gas and liquid, the isentropic plug nozzle has been designed: longer penetration of thesupersonic zone in the wake has been indicated as the target by the research community. Three different gas temperatures are investigated as potential gain in top speed and reduction in nitrogen consumption.

A specific solidification model for binary alloy was also implemented to provide an example of diagnostic tool for real industrial case able to run beyond the simplified assumption. The cooling rate of metal droplet is a key factor in the design of atomization facility: when the solidification path is longer than tower height, mushy droplets will stick on the wall with consequent shut down of the operation to clean the equipment (very high cost for industrial scale unit!).

The atomization phenomena is extremely difficult to visualize due to the chaotic behaviour, metal temperature and jet high speed: primary break up physics remains mostly unrevealed. The Lagrangian approach is very light computationally speaking, but is not appropriate to reproduce the melt core entering the domain: for such reasons, the Volume of Fluid model was introduced in chapter 4. Moreover, 3D analysis was chosen to capture the instability phenomena that rule the early disruption stage (flow unsteadiness is limited

by axisymmetric model constraint). The metal stream for isentropic plug nozzle and non-axisymmetric nozzle is reproduced and the key characteristics of primary break-up are evinced. The results showed the absence of thin liquid sheet (the most favourable condition for primary breakup) formation near to the plug tip: it means that new nozzle configurations are necessary. Conclusions are summarized in chapter 6. Appendices A and B report the equations describing the flows and the implemented udf. Figure 2.25 summarizes the roadmap of the thesis while Figure 2.26 presents the planned timescales chart.

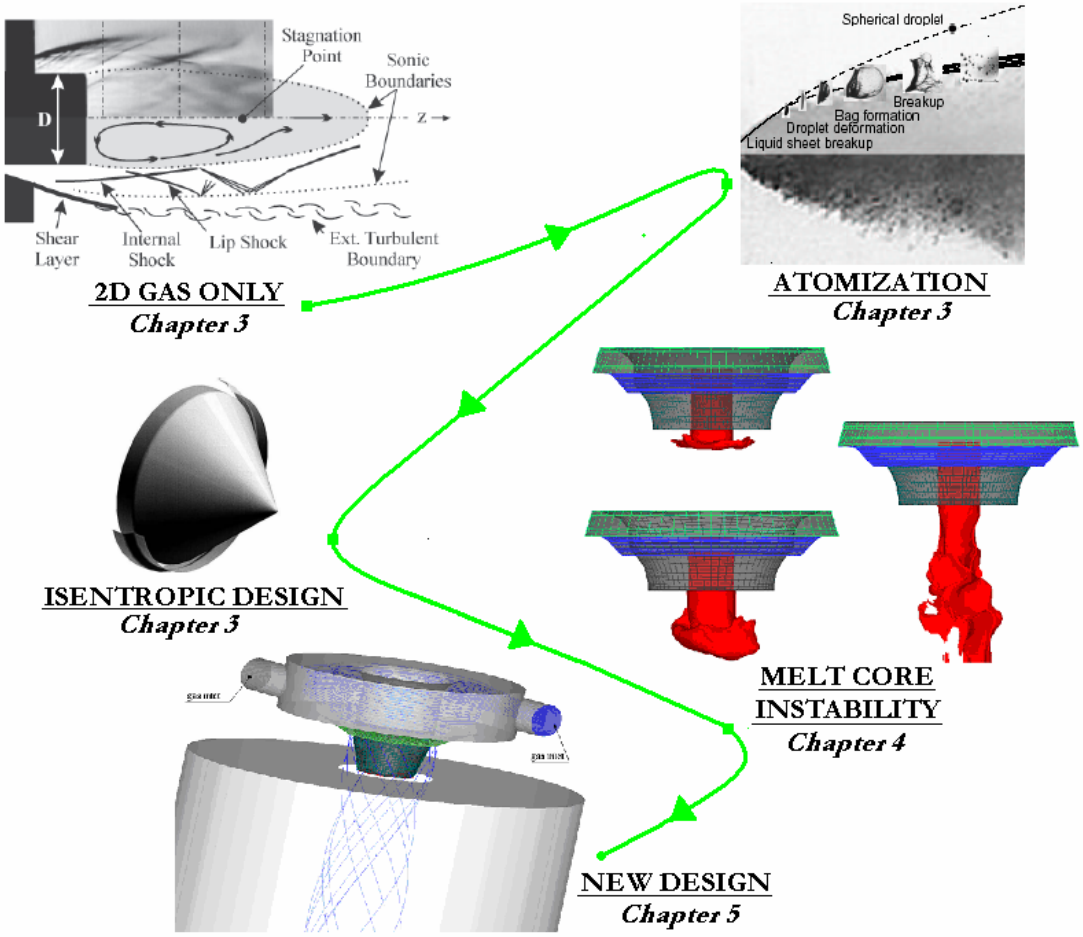


**Figure 2.25: thesis roadmap**

The use of CFD helps to understand and control the industrial process that is usually presented as a "black art": fine tuning of the atomization operations relaying on the experience more than process specifications. As for other disciplines (turbomachinery, heat exchanger, etc.), optimization using reliable models will be cheaper than the trial and error methods used up to now.

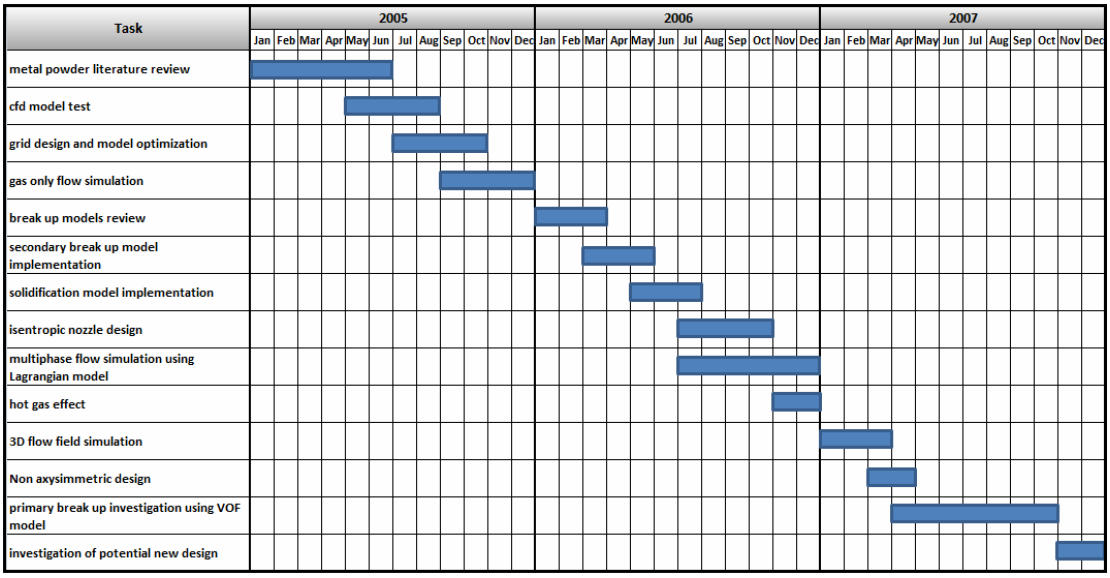


**Figure 2.26: thesis GANTT**

Finally the purposes of this investigation can be summarized as follows:

- Improve the methodology for gas atomization analysis;
- Determine the influence of operating (pressure, temperature) and geometrical parameters on the gas flow;
- Determine the effects of the melt presence in the flow field;Analyze the three-dimensional multiphase flow field to determine the primary break-up performance;
- Give recommendations for the design of an innovative atomization tower.

## References

[1] N. Dombrowski, W.R. Johns, The aerodynamic instability and disintegration of viscous liquid sheet, Chem. Eng. Sci. 18, pp. 203–214, 1963.

[2] D. Bradley, On the Atomization of Liquids by High-Velocity Gases, J. Phys. D: Appl. Phys., Volume 6, pp 1724 – 1736, 1973;

[3] D. Bradley, On the Atomization of a Liquid by High-Velocity Gases - II, J. Phys. D: Appl. Phys., Volume 6, pp 2267-2272, 1973;

[4] J. B. See, G. H. Johnston, Interactions between Nitrogen Jets and Liquid Lead and Tin Streams, Powder Technol., Volume 21, pp 119-133, 1978;

[5] K. P. Rao, S. P. Mehrotra, Effect of Process Variables on Atomization of Metals and Alloys, Modern Developments in Powder Metallurgy, Principles and Processes MPIF and APMI International, Princeton, NJ, USA, Volume 12, pp.113-130, 1981;

[6] J. O. Hinze, Fundamentals of the Hydrodynamic Mechanism of Splitting in Dispersion Processes, AIChE J., Volume 1, pp 289-295, 1955;

[7] A.J. Yule, J.J. Dunkley, Atomization of Melts, Clarendon Press, Oxford, 1994;

[8] L.P. Hsiang, G.M. Faeth, Near-limit drop deformation and secondary breakup, Int. J. Multiphase Flow, Volume 18, pp. 635-652, 1992;

[9] S. A. Krzeczkowski, Measurement of Liquid Droplet Disintegration Mechanisms, Int. J. Multiphase Flow, Volume 6, pp 227-239, 1980;

[10] H. Lubanska, Correction of Spray Ring Data for Gas Atomization of Liquid Metals, Journal of Metals, pp 45 – 49, 1970;

[11] Kramer, C., Die Kompaktierungsrate beim Sprühkompaktieren von Gauß-förmigen Deposits, Dissertation, University of Breme, 1997;

[12] J. Tillwick, Einsatz der PDA-Messtechnik zur Charakterisierung des Spru□hkompaktierprozesses bei der Zersta□ubung von Metallschmelzen, University of Breme, 1999;

[13] L. D. Wigg, Drop-Size Predictions for Twin Fluid Atomizers, J. Inst.Fuel, Volume 27, pp. 500-505, 1964;

[14] S.P. Mehrotra: Mathematical Modelling of Gas Atomization Process for Metal Powder Production, Part 1, Powder Metallurgy International, Volume 13, pp 80 – 84, 1981;

[15] S.P. Mehrotra: Mathematical Modelling of Gas Atomization Process for Metal Powder Production, Part 2, Powder Metallurgy International, Volume 13, pp 132-135, 1981;

[16] H. Liu, Science and Engineering of Droplets: Fundamentals and Applications, William Andrew Publ., Norwich, USA , 2000;

[17] B. N. Putimtsev, Effect of the Thermophysical Properties of Gases and Molten Metals on the Properties of Atomized Powders, Sov. Powder Metall. Met. Ceram., pp 171-175, 1972;

[18] J. B. See, G. H. Johnston, Interactions between Nitrogen Jets and Liquid Lead and Tin Streams, Powder Technol., pp 119-133, 1978;

[19] J. S. Thompson, A Study of Process Variables in the Production of Aluminium Powder by Atomization, J. Inst. Metal., Volume 74, pp. 101–132, 1948;

[20] M. J. Couper, R. F. Singer, Rapidly Solidified Aluminium Alloy Powder Produced by Optimization of the Gas Atomization Technique, Proc. Int'l. Conf. Rapidly Quenched Metals, pp. 1737-174, 1984;

[21] J. D. Ayers, I.E. Anderson, Very Fine Metal Powders, J. of Metals, Volume 37, pp. 16-21, 1985;

[22] A. Unal, Effect of processing variables on particle size in gas atomization of rapidly solidified aluminium powders, Materials Science and Technology Volume 3, pp. 1029-1039, 1987;

[23] A. Unal, Influence of gas flow on performance of "Confined" atomization nozzles, Journal Metallurgical and Materials Transactions B Volume 20, Number 6 Category, pp. 833-843, 1989;

[24] R. S. Miller, S. A Miller, S. D Savkar, D. P Mourer, Two phase flow model for the close-coupled atomization of metals, International journal of powder metallurgy, Volume 32, pp. 341-352, 1996;

[25] S.A. Miller, R.S. Miller, D.P. Mourer, R.W. Christensen, High yield, nonaxisymmetric atomization of nickel base superalloys International journal of powder metallurgy, Volume 33, pp. 37-50, 1997;

[26] J.T. Strauss, Hotter gas increase atomization efficiency, Metal Powder Report, Volume 54, 1999;

[27] J. Strauss, Improvements in Close-Coupled Atomization: An Empirical Approach, proceedings of TMS annual meeting in Nashville, Tennessee, pp. 83-94, 2000;

[28] J. Ting, M. W. Peretti, W. B. Eisen, The effect of wake-closure phenomenon on gas atomization performance, Materials Science and Engineering A, Volume 326, pp. 110-121, 2002;

[29] J. Ting, J. Connorb, S. Ridder, High-speed cinematography of gas-metal atomization, Materials Science and Engineering A, Volume 390, pp. 452-460, 2005;

[30] C. Cui, F. Cao, Q. Li, Formation mechanism of the pressure zone at the tip of the melt delivery tube during the spray forming process, Journal of Materials Processing Technology, Volume 137, pp. 5-9, 2003;

[31] R. Unal, The influence of the pressure formation at the tip of the melt delivery tube on tin powder size and gas/melt ratio in gas atomization method, Journal of Materials Processing Technology, Volume 180, pp. 291–295, 2006;

[32] S.P. Mates, S.D. Ridder, F.S. Biancaniello, Comparison of the supersonic length and dynamic pressure characteristics of discrete-jet and annular close-coupled nozzles used to produce fine metal powders, proceedings of TMS annual meeting in Nashville, Tennessee, pp. 71-81, 2000;

[33] S. P. Mates, G. S. Settles, A study of liquid metal atomization using close-coupled nozzles, part 1: gas dynamic behavior, Atomization and Sprays, Volume 15, pp.19-40, 2005;

[34] S. P. Mates, G. S. Settles, A study of liquid metal atomization using close-coupled nozzles, part 2: atomization behaviour, Atomization and Sprays, Volume 15, pp. 41-60, 2005;

[35] R. Courant, K.O. Friedrichs, Supersonic Flow and Shock Waves, Springer, 1999;

[36] S.D. Ridder, F.S. Biancaniello, Process Control During High Pressure Atomization, Mat. Sci. Eng. Volume 98, pp 47- 51, 1988;

[37] J. Ziesenis, J. Tillwick, M. Krauss, V. Uhlenwinkel, Analysis of. molten metal atomization process using modified phase-doppler-anemometry, proceedings of TMS annual meeting in Nashville, Tennessee, pp. 61-70, 2000;

[38] S. Lagutkin, L. Achelis, S. Sheikhaliev, V. Uhlenwinkel, V. Srivastava, Atomization process for metal powder, Materials science & engineering. A383,pp. 1-6, 2004;

[39] P. I. Espina, S. D. Ridder, F. S. Biancaniello, G. E. Mattingly, Analysis of the Aspiration Phenomena in a Close-Coupled Inert Gas Atomizer, Characterization & Diagnostics of Ceramics & Metal Particulate Processing (ed. E. J. Lavernia, H. Henein, and I. Anderson), TMS, pp. 49-62, 1989;

[40] A. Unal, Gas Flow in Atomization Nozzles; Physical Chemistry of Powder Metals: Production and Processing (ed. W. M. Small), TMS, pp. 201-228, 1989;

[41] U. Piomelli, Numerical Solution of the Viscous Flow in an Atomization Die, NIST/Industrial Consortium on Intelligent Processing of Rapidly Solidified Metal Powders by Inert Gas Atomization, First Annual Report, pp. 15-25, 1992;

[42] R. S. Figliola, I. E. Anderson, Characterization of High Pressure Gas Atomization Flow Fields, Computational and Numerical Techniques in Powder Metallurgy (ed. D. Madam, I. Anderson, W. Frazier, P. Kumar, and M. McKimpson), TMS, pp. 29-39, 1993;

[43] J. Mi, R. S. Figliola, I. E. Anderson, A numerical simulation of gas flow field effects on high pressure gas atomization due to operating pressure variation, Materials Science and Engineering A, Volume 208, pp. 20-29, 1996;

[44] J. Mi, R. S. Figliola, I. E. Anderson, A numerical simulation of gas flow field effects on high pressure gas atomization due to melt tip geometry variation, Metallurgical and material Transaction B, Volume 28B, pp. 935-941, 1997;

[45] P. I. Espina, U. Piomelli, G. E. Mattingly, A Numerical Investigation of the Compressible Flow Field Produced in an Annular Jet, Close-Coupled, Gas Metal

Atomizer, Computational and Numerical Techniques in Powder Metallurgy, ed. D. S. Madan, I. E. Anderson, and W. E. Frazier, (Warrendale, PA: TMS), pp. 41-53, 1993;

[46] P. I. Espina, U. Piomelli, Study of the Gas Jet in a Close-Coupled Gas-Metal Atomizer, AIAA 98-0959, pp. 1-12; 1998;

[47] P. I. Espina, U. Piomelli, Numerical Simulation of the Gas Flow in Gas-Metal Atomizers, Proceedings of FEDSM'98, ASME Fluids Engineering Division Summer Meeting, Washington DC, pp. 1-11, 1998;

[48] Q. Xu, D.cheng, G. Trapaga, E.J. lavernia, fundamental fluid dynamics during liquid metal atomization, proceedings of TMS annual meeting in Nashville, Tennessee, pp. 37-48, 2000;

[49] S.D. Ridder, A.Johnson, P.I.Espina, F.S. Biancaniello, G.J. DelCorso, Optimization of an annular jet commercial gas-metal Atomizer, proceedings of TMS annual meeting in Nashville, Tennessee, pp. 51-61, 2000;

[50] J. Ting, I.E. Anderson, A computational fluid dynamics (CFD) investigation of the wake closure phenomenon, Materials Science and Engineering: A Volume 379, pp. 264-276, 2004;

[51] C. Czisch, u. Fritsching, Atomizer design for viscous-melt atomization, Material science and Engineering A, volume 477, pp. 21-25, 2008;

[52] D. W Kuntz, J. L. Payne, Simulation of Powder Metal Fabrication with High Pressure Gas Atomization, Advances in Powder Metallurgy and Particulate Materials, Part 1: Powder Production and Characterization (ed. M. Phillips and J. Porter), pp. 63-78, 1995;

[53] B. Li, X. Liang, J. C. Earthman and E. J. Lavernia, Two dimensional modelling of momentum and thermal behaviour during spray atomization of γ-TiAl, Acta Materialia Volume 44, Issue 6, pp. 2409-2420, 1996;

[54] P. S. Grant, B. Cantor, L. Katgerman Modelling of droplet dynamic and thermal histories during spray forming—I. Individual droplet behaviour, Acta Metallurgica et Materialia, Volume 41, Issue 11, pp 3097-3108, 1993;

[55] P. S. Grant, B. Cantor, L. Katgerman, Modelling of droplet dynamic and thermal histories during spray forming—II. Effect of process parameters, Acta Metallurgica et Materialia, Volume 41, Issue 11, pp 3097-3108, 1993;

[56] P.S. Grant, B. Cantor, Modelling of droplet dynamic and thermal histories during spray forming—III. Analysis of spray solid fraction, Acta Metallurgica et Materialia Volume 43, Issue 3, pp. 913-921, 1995;

[57] R.P. Underhill, P.S. Grant, B. Cantor, D.J. Bryant, Modelling of droplet behaviour during spray forming using FLUENT, , Int. J. Non-Equilibrium Processing, Volume 10, pp. 201-216, 1997;

[58] J H Hattel, N H Pryds, J Thorborg and P Ottosen, A quasi-stationary numerical model of atomized metal droplets. I: Model formulation, Modelling Simul. Mater. Sci. Eng. Volume 7, pp. 413–430, 1999;

[59] N H Pryds, J H Hattel and J Thorborg, A quasi-stationary numerical model of atomized metal droplets. II: Prediction and assessment Modelling Simul. Mater. Sci. Eng., Volume 7, pp. 431–446, 1999;

[60] D. Bergmann, U. Fritsching, K. Bauckhagem, A mathematical model for cooling and rapid solidification of molten metal droplets, International Journal of Thermal Sciences Volume 39, Issue 1, pp. 53-62, 2000;

[61] P. Shukla, R K Mandal, S N Ojha, Non-equilibrium solidification of undercooled droplets during atomization process, Bull. Mater. Sci., Volume 24, No. 5, pp. 547–554, 2001;

[62] N. S. Mahesh, Johnson Mendonca, M. K. Muralidhara, B. K. Muralidhara, C. Ramachandra, Modelling of droplet dynamic and thermal behaviour during spray deposition, Bull. Mater. Sci., Volume 26, No. 3, pp. 355–364, 2003;

[63] S. B. Johnson, J.P. Delplanque, Y. Lin, Y. Zhou, E. J. Lavernia, K. M. McHugh, Numerical Simulation and Experimental Characterization of a Binary Aluminium Alloy Spray - Application to the Spray Rolling process, TMS 2005 - 134th Annual Meeting & Exhibition, San Francisco, 2005;

[64] S. Markus, U. Fritsching, K. Bauckhage, Jet break up of liquid metal in twin fluid atomisation, Materials Science and Engineering A326, pp. 122–133, 2002;

[65] G.S.E. Antipas, Modelling of the break up mechanism in gas atomization of liquid metals. Part I: The surface wave formation model, Computational Materials Science, Volume 35, Issue 4, pp. 416-422, 2006;

[66] M. Tong, D. J. Browne, Direct numerical simulation of melt–gas hydrodynamic interactions during the early stage of atomization of liquid intermetallic, Journal of materials processing technology, Volume 202, pp. 419–427, 2008;

[67] D. R. Chapman, An analysis of base pressure at supersonic velocities and comparison with experiments, NACA Rep. 1051 (National Advisory Committee for Aeronautics), 1951;

[68] I. Donaldson, The effect of sting supports on the base pressure of a blunt-based body in a supersonic stream, Aeronautical Quarterly Volume 6, pp 221-229, 1955;

[69] B. Dayman, Support interference effect on the supersonic wake, AIAA J., Volume 8, pp 1921-1923, 1963;

[70] J. Gaviglio, J.P. Dussauge, J.F. Debieve, and A. Favre, Behavior of a turbulent flow, strongly out of equilibrium at supersonic speeds, the physics of fluids, Volume 20, pp 179-192, 1977;

[71] J. L. Herrin, J. C. Dutton, Supersonic base flow experiments in the near wake of a cylindrical afterbody, AIAA J., Volume 32, pp 77-83, 1994;

[72] J. L. Herrin, J. C. Dutton, Effect of a rapid expansion on the development of compressible free shear layers, Phys. Fluids, Volume 7, pp 159-171, 1995;

[73] J. L. Herrin, J. C. Dutton, The turbulence structure of a reattaching axisymmetric compressible free shear layer, Phys. Fluids, Volume 9, pp 3502-3512, 1997;

[74] E. Aschenbach, Vortex shedding from spheres, J. Fluid Mech., Volume 62, pp 209-, 1974;

[75] A. Demetriades, Turbulence front structure of an axisymmetric compressible wake, J. Fluid Mech., Volume 34, pp 465-480, 1968;

[76] A. Demetriades, Turbulence measurements in an axisymmetric compressible wake, Phys. Fluids, Volume 11, pp 1841-1852, 1968

[77] M.V. Morkovin, Effects of compressibility on turbulent flows, Mécanique de la Turbulence, CNRS Paris, pp. 367–380, 1962 ;

[78] R. M. C. So, T. B. Gatski, T. P. Sommer, Morkovin Hypothesis and the Modeling of Wall-Bounded Compressible Turbulent Flows, AIAA Journal, volume 36, pp 1583-1592, 1998;

[79] A. K. M. F. Hussain, Coherent structures and turbulence, J. Fluid Mech., Volume 173, pp 303-356, 1986;

[80] D. Papamoschou, A. Bunyajitradulya, Evolution of large eddies in compressible shear layers, Phys. Fluids, Volume 9, pp 756-765, 1996;

[81] R. D. Sandberg, H. F. Fasel, Numerical Investigation of Transitional Supersonic Axisymmetric Wakes, J. Fluid Mech. Volume 563, pp 1-41, 2006

[82] F. Simon, S. Deck, P. Guillen, P. Sagaut and A. Merlen, Numerical simulation of the compressible mixing layer past an axisymmetric trailing edge, J. Fluid Mech., Volume 591, pp 215-253, 2007;

[83] R.A. Humble, F.Scarano, B.W.van Oudheusden, Unsteady planar base flow investigation using particle image velocimetry and proper orthogonal decomposition, 44th AIAA Aerospace Sciences Meeting and Exhibit, Nevada, 2006;

[84] S. B. Pope, Turbulent Flows, Cambridge University Press, U.K., 2000;

[85] R. Schwane, G. Hagemann, P. Reijasse, Plug nozzles: Assessment of prediction methods for flow features and engine performance, AIAA Paper 2002-0585, 2002;

[86] R. Benay, P. Servel, Two-Equation k-σ Turbulence Model: Application to a Supersonic Base Flow, AIAA Journal, Volume 39, pp 407-416, 2001;

[87] M. Lesieur, O. Metais, P. Comte, Large-Eddy Simulations of Turbulence, Cambridge University Press, 2005;

[88] C. Fureby, K. Kupiainen, Large-Eddy Simulation of Supersonic Axisymmetric Baseflow, Turbulent Shear Flow Phenomena (TSFP3), Japan, 2003;

[89] S. Kawai, K. Fujii K, Computational Study of a Supersonic Base Flow Using Hybrid. Turbulence Methodology, AIAA Journal, Volume 43, pp 1265-1275, 2005;

[90] D. M. de Feo, S.T. Shaw, Turbulence Modeling and Supersonic Base Flows,45th AIAA Aerospace Sciences Meeting and Exhibit Nevada, 2007.

# CHAPTER 3

## TWO DIMENSIONAL GAS ATOMIZATION MODELING

The break-up model is implemented in a closed coupled HPGA (High Pressure Gas Atomization) environment, where the metal jet is poured into the atomization chamber from the tundish through a ceramic feed tube. A high pressure gas jet comes into contact with the melt on the feed tube tip and breaks the melt stream into micro size droplets. The gas field is generated with a commercial CFD code, FLUENT™. In the computational domain, gas and melt are treated as separate gas and liquid spray phases. The equations that describe the liquid phase motion are solved in a Lagrangian frame and the effects of the liquid phase on the gas flow field are included by introducing source terms in the Navier-Stokes equations. The liquid spray is treated as a number of parcels that contain a given number of droplets with the same mass, momentum and physical properties. The HPGA nozzles operate at the reservoir pressure of 11 atmospheric pressures at the gas inlet. The fluid is nitrogen, modelled as compressible gas with ideal gas law for density. The break-up and the cooling model described in sections 3.2 and in 3.5 are integrated with the gas flow field through a user defined function (UDF) code. Section 3.4 presents the results of particle laden flow for the isentropic plug nozzle geometry and the effect of hot gas on the atomization efficiency.

### 3.1 Flowfield description

According to the models described in chapter 2 and before describing the physics of the atomization process, a detailed description of the flow field is given. Due to the rotational symmetry of this set-up, a 2-D simulation is performed on one half of an axial section of the atomizer chamber. The computational domain is based on a conventional HPGA nozzle, namely converging-diverging slit nozzle (CDSN) as depicted in figure 3.1.

Recirculating flows do not respect the basic assumptions of wall functions (see appendix A.2.7): for this reason, all the simulations in this thesis have been performed resolving the boundary layer. A laminar sublayer solution is computationally intensive, because a very fine mesh is requested near the non slip surface. According to the inner layer subdivision, the viscous sublayer occupies the region where $y+ < 5$. Although the near-wall modeling approach is computationally more expensive because of the increasing cell quantity, it is more appropriate for complex flows including separation, reattachment points and re-

circulation flows, where the bounded flow effects are not captured by the classical logarithmic laws of walls.

An initial structured grid (≈ 30.000 cells) is deployed and local refinement is achieved in the zones of high pressure gradients and near the wall until the solution becomes mesh independent and the boundary cells centroids are located in the viscous sublayer. The Reynolds-stress turbulence model is used due to its superiority in capturing flows with rapid variations in the mean flow: as shown in appendix A.2.3, for this turbulent model the transport equations are solved for all Reynolds stresses $\langle u_i u_j \rangle$ and for the dissipation ε, therefore the turbulent-viscosity hypothesis is not needed, eliminating one of the major defects of the two equation k-ε model.

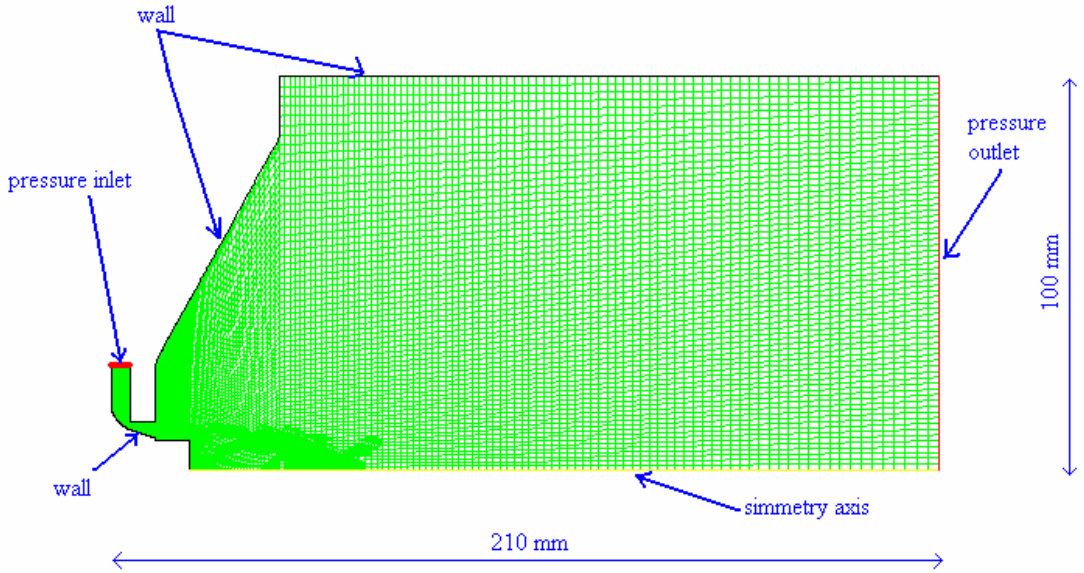


**Figure 3.1: computational domain for converging diverging slit nozzle**

### 3.1.1 Gas flow dynamics

The simulation starts with the calculation of gas flow before the melt is injected. The velocity flow field is showed in Figure 3.2. A series of shocks present from the supersonic jet is consistent with the theoretical descriptions of compressible flow and high-speed jets in the literature [1].

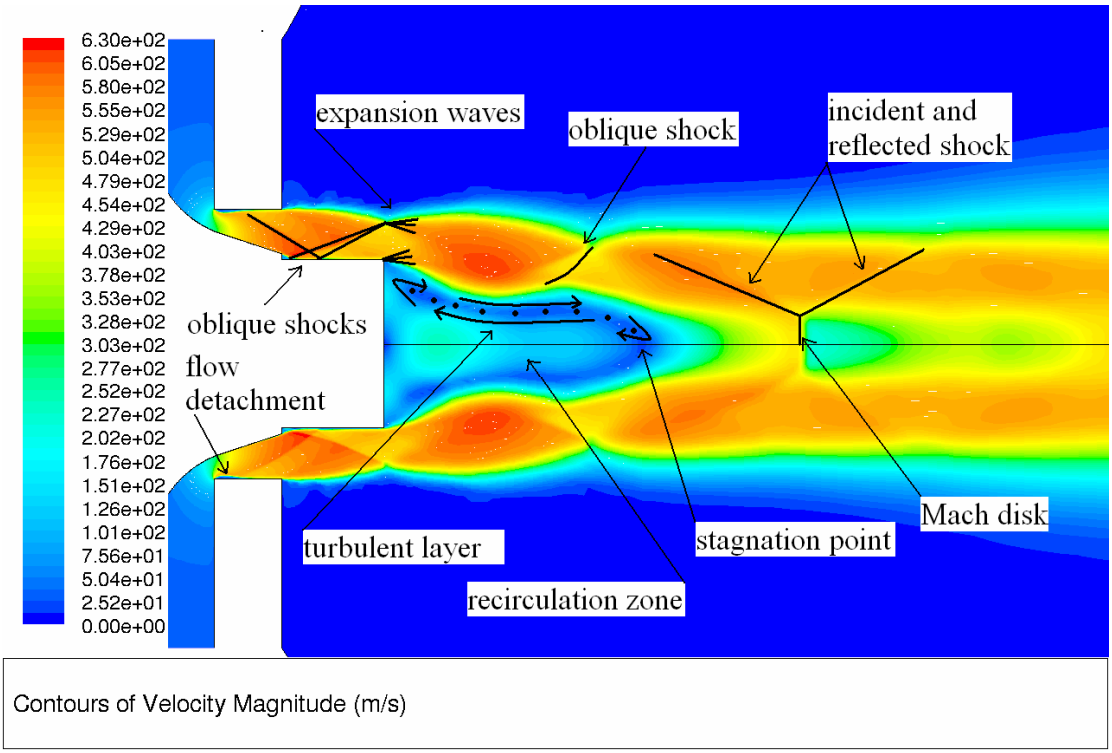


**Figure 3.2: velocity flow field in central upstream region of model in Fig. 3.1**

The gas flow field is the driving force of the atomization process and it is important to have good insights of the flow dynamics. As the high pressure gas enters the nozzle, the sharp angle with the nozzle causes a detachment of the flow from the wall and a recirculation flow is generated around the corner of the throat. An oblique shock is formed inside the nozzle and reflected by the outer surface of the feeding tube. At the exit, the gas flow expands through a series of Prandtl-Meyer expansion waves and recompression shocks to match the atmospheric pressure inside the atomization chamber and the high velocity gas continuously overshoots the equilibrium position as the external layer of the jet communicates with the jet core by sound/pressure waves, which are slower than the supersonic flow. The gas flow separation at the end of the melt tube generates a recirculation vortex under the melt exit hole. The recirculation zone is distinguished from the high velocity gas with the sonic lines. The gas flow in the centre of the recirculation zone moves toward the feeding tube and turns outward radially as it moves close to the tip. When the gas flow comes into contact with the sonic boundary, it is pushed inward and flows downstream. Inside the recirculation zone, a turbulent layer separates upstream and downstream flows, which is consistent with the experimental observation [2]. At the end of this recirculation zone there is a stagnation front, where the gas velocity falls to around zero (as quantitatively shown by the linear velocity diagram in Figure 3.3). About 15 mm

behind the stagnation point there is a mach disk (normal shock) corresponding to the velocity drop in the curve.

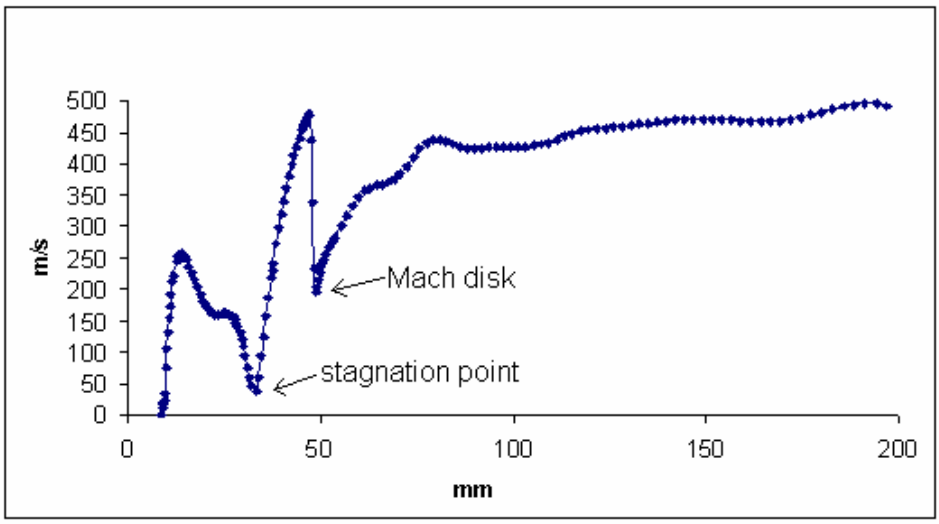


**Figure 3.3: axial velocity plot**

In order to show the decay of velocity in the jets plume, the radial profiles are plotted in figure 3.4. Four sections are chosen along the centreline, namely 7.5, 15, 70 and 150 mm. Near the melt inlet (7.5 mm), the flow is still in the centre, slightly outwards is a small recirculation flow, then a sudden surge of velocity within the supersonic jet region and further outwards is steady ambient air. A short distance from the melt inlet (15 mm), substantial recirculation flow develops in the centre, further outwards is the supersonic jet region and the ambient air. In the middle of the domain (70 mm), the high velocity profile is developed in the centre while the supersonic jet moves towards the centreline and the maximum velocity has been retained. Close to the end of the domain (150 mm), relatively high velocity remains in the centre and a more spreading outwards.

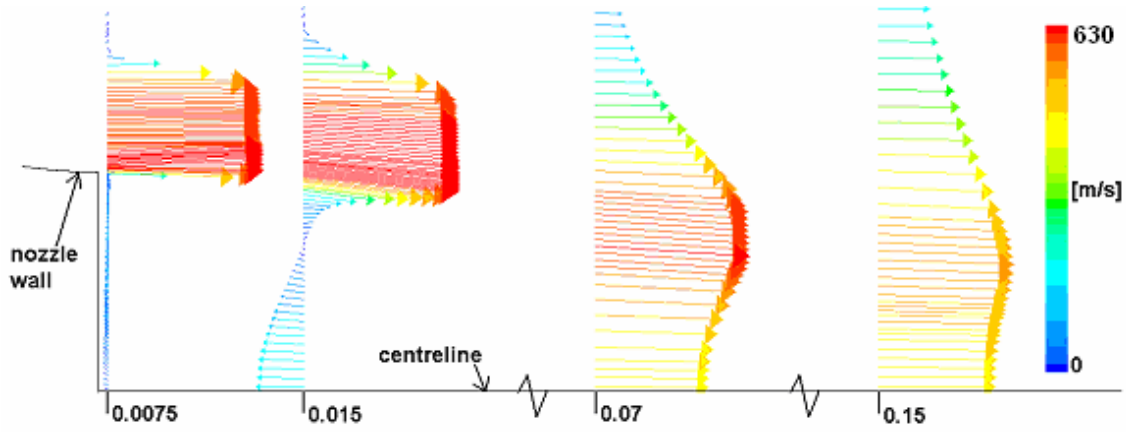


**Figure 3.4: radial velocity vector plot**

It is known that a large amount of energy would be dissipated through shocks [3] and, as a result, the gas jet would lose its momentum faster. It is expected that a more sustainable high speed jet would enhance/prolong the energy transfer between the gas and melt phase and give rise to more efficient atomization. Therefore, it is beneficial to have a shock free/reduction nozzle to improve the gas atomization. The issue of design optimization will be addressed in the section 3.4.

## 3.2 Atomization models

In order to reproduce numerically the gas atomization physics it was necessary to implement a model for the melt break up. Experiments and instabilities theories demonstrate that the atomization process is composed of primary and secondary fragmentations. It can be reasonably assumed that the melt stream becomes an assembly of large droplets after primary break-up and further transforms to fine droplets with secondary break-up. This analysis is focused on the formation of fine droplets and only the secondary break-up mechanism is considered. The mechanism of primary break-up is out of the scope of this chapter.

Secondary atomisation has been described with a wide range of break-up theories [4]. In a HPGA, there is a large velocity gradient between the gas and melt phases. Therefore, the secondary atomization of liquid elements can be best described by the fragmentation theory [5], which summarizes the atomisation patterns as a number of break-up modes. The theoretical description of atomisation processes is schematically illustrated in Figure 3.5.


**Figure 3.5: Secondary droplet atomization [6]**

The secondary break-up starts with a droplet stretched towards a flat disk. During the bag break-up, the flat disk is under an outward force which blows the droplet disk to a thin membrane and finally the membrane bursts into numerous fine droplets. During the

stripping break-up, the force turns inwards and the membrane is stripped at the edges to form fine droplets. When the relative velocity between gas and liquid phase is extremely high, it is also possible to have a third mode of secondary atomization, called catastrophic mode in which droplets are elongated and then broken due to the theory of Rayleigh instability. The main parameter related to break-up physics is the Weber number, defined as:

$$We = \frac{\rho_g u_{rel}^2 d_p}{\sigma} \tag{3.1}$$

For a better representation of the physical break-up mechanism, it is important to consider the dynamic interaction between the melt and gas phases. Physics study [6] demonstrates that the droplet goes through a deformation time before starting to break as aerodynamic forces act on the droplet. The deformation time is named as break-up time $t_b$, which is varied according to different numerical break-up models.

In this study, a self-written secondary atomization code [Appendix B] is developed to include both the Weber number and the break-up time into the break-up mechanism. The most widely used numerical models for break-up simulation are the Taylor Analogy Break-up (TAB)[7] and Kelvin-Helmotz (KH) instability break-up [8] models. Despite various modified versions being proposed, the TAB and KH are still the most robust models available. It is known that the TAB model works better in the bag break-up mode (usually for 12 < We < 40-100) and the KH model gives good agreement with experimental data in the stripping and even catastrophic break-up (80 < We < 800).. Even if both models are available in Fluent, it is not possible to use both of them at the same time: for this reason it was implemented by the author a new function that applies TAB equations when We < 80 and KH at higher Weber values. The solidification model was not available in Fluent for the discrete phase: phase change and cooling equations were solved as subroutine in the break up user defined function [Appendix B].

### 3.2.1 TAB model

This model treats the oscillation of distorting droplets with the analogy of a spring-mass system. The restoring force of the spring is represented by the surface tension, while the external force is replaced by aerodynamic force. The liquid viscosity represents the damping forces. Letting $y = \frac{x}{C_b r}$ the governing equation is:

$$\ddot{y} = \frac{C_F}{C_b}\frac{\rho_g}{\rho_l}\frac{u^2}{r^2} - \frac{C_k \sigma}{\rho_l r^3} y - \frac{C_d u_l}{\rho_l r^2}\dot{y} \tag{3.2}$$

The break-up occurs only if y > 1. The values of constant $C_b$, $C_F$, $C_k$ and $C_d$ are determined by comparing experimental and theoretical results. First, the relative velocities of each parcel are calculated with respect to the surrounding gas velocity. The second step is to calculate We and the frequency ω defined as:

$$\omega^2 = C_K \frac{\sigma}{\rho_l r^3} - \left(\frac{C_d \mu_l}{2\rho_l r^2}\right)^2 \tag{3.3}$$

At this point the oscillation amplitude can be calculated as:

$$A^2 = \left(y^n - \frac{We}{12}\right)^2 + \left(\frac{\dot{y}^n}{\omega}\right)^2 \tag{3.4}$$

The break-up condition is:

$$A + \frac{We}{12} \geq 1 \tag{3.5}$$

The break-up time $t_b$ is estimated assuming that the drop oscillation is undamped for its first period (that is true for very small droplets) and is the smallest root greater than $t^n$ of the equation:

$$\frac{We}{12} + A\cos\left[\omega\left(t - t^n\right) + \phi\right] = 1 \tag{3.6}$$

where

$$\cos\phi = \frac{y^n - \frac{We}{12}}{A} \quad \text{and} \quad \sin\phi = -\frac{\dot{y}^n}{A\omega} \tag{3.7}$$

the size of the product droplet is related to the break-up time via an exponential expression:

$$r = \frac{d_p}{2} * \text{decayfactor} \tag{3.8}$$

where decay factor is a function of the parent droplet life time until the break-up condition is reached.

### 3.2.2 KH model

This model takes into account the fastest growing disturbance on the surface of the droplet, which is most likely to result in break-up. The wavelength of this disturbance is:

$$\Lambda = \frac{9.02\left(1+0.45Z^{0.5}\right)\left(1+0.4\Gamma^{0.7}\right)}{\left(1+0.87We^{1.67}\right)^{0.6}}d_p \tag{3.9}$$

The growth rate of the wavelength is:

$$\Omega = \frac{\left(0.34+0.38We^{1.5}\right)}{\left(1+Z\right)\left(1+1.4\Gamma^{0.6}\right)}\left(\frac{\sigma}{\rho_l d_p^3}\right)^{0.5} \tag{3.10}$$

The droplets radius r resulting from atomization is proportional to the wavelength of the fastest-growing unstable surface wave:

$$r = B_0\Lambda \tag{3.11}$$

$B_0$ is a model constant equal to 0.61 based on the Reitz analysis. The break-up time $t_b$ is given by:

$$t_b = \frac{3.726B_1 a}{\Omega\Lambda} \tag{3.12}$$

$B_1$ must be regarded as an adjustable model constant, with a different value in each break-up regime: in the Reitz analysis it is assumed that $B_1 = 10$. To model the stretching and thinning mechanism of "child" droplets pinching from the "parent" droplet, the diameter evolution law is:

$$\frac{dr_p}{dt} = \frac{r_p - r}{t_b} \tag{3.13}$$

Further the parent droplet diameter reduction will take place only after the mass removed reaches three percent of its mass.

### 3.2.3 Droplet tracking model

Droplet trajectory is obtained by integrating the Newton law in a Lagrangian reference frame. The law (for unity of mass) projection on the x reference axis is given by:

$$\frac{\partial u_p}{\partial t} = F_D\left(u-u_p\right)+\frac{g_x\left(\rho_p-\rho\right)}{\rho_p}+F_x \tag{3.14}$$

where $u_p$ is the velocity of the particle, u is the velocity of fluid around the particle, $g_x$ is the x component of gravitational acceleration, $\rho_p$ is the droplet density and $\rho$ is the fluid density. On the right hand side of the equation, the first term is drag force, the second is gravity and the third is additional acceleration. For the drag force, the expression for the coefficient $F_D$ is:

$$F_D = \frac{18\mu}{\rho_p d_p^2}\frac{C_D\,\mathrm{Re}}{24} \tag{3.15}$$

$C_D$ is the drag coefficient, $\mu$ is the first coefficient of molecular viscosity of the fluid and Re is the Reynolds number:

$$\mathrm{Re} = \frac{\rho D_p \left| \left(u_p - u\right) \right|}{\mu} \tag{3.16}$$

The drag coefficient for liquid droplet is given by:

$$C_D = a_1 + \frac{a_2}{\mathrm{Re}} + \frac{a_3}{\mathrm{Re}^2} \tag{3.17}$$

where $a_1$, $a_2$, $a_3$ remain constant over a range of several orders of magnitude [9].

The additional force is expressed as:

$$F_x = \frac{1}{2}\frac{\rho}{\rho_p}\frac{d}{dt}\left(u - u_p\right) + \frac{\rho}{\rho_p} u_p \frac{\partial u}{\partial x} \tag{3.18}$$

The first term is a "virtual mass" force that accounts for the acceleration of the fluid surrounding the particle and the second term is a pressure gradient that is due to the "local" pressure gradient in the fluid surrounding the particle. The virtual mass is important when $\rho > \rho_p$, so, in our simulation, it has weak influence.

### 3.2.4 Droplet solidification

The solidification is considered according to the theory of Newtonian cooling that describes the droplet temperature as remaining constant during solidification as a result of latent heat of fusion. The radiation heat transfer mode is not included in the droplet model. The fraction of melt solidified is given by the equation:

$$\frac{df}{dt} = \frac{6K_g}{H\rho_l d_p^2}\left(T - T_g\right)\left(2 + 0.6\,\mathrm{Re}^{0.5}\,\mathrm{Pr}^{0.33}\right) \tag{3.19}$$

As a first analysis this simplified mechanism has been implemented, while, in paragraph 3.5, a more sophisticated model will be used for the analysis of droplet solidification.

## 3.3 Atomization simulations

The equations that describe the liquid phase motion are solved in a Lagrangian frame and the effects of the liquid phase on the gas flow field are included by introducing source terms in the Navier-Stokes equations. The liquid spray is treated as a number of parcels that contain a given number of droplets with the same mass, momentum and physical properties as described in Table 1. In all simulations, the melt (properties in Table 3.1) superheat at the pouring stage is 100 K and the gas to melt mass flow rate ratio is

approximately 1.1. The experimental study [10] indicates that the droplets emerging at the exit after primary break-up is about 10-100% of the melt nozzle diameter. Therefore, based on the melt nozzle of 6-mm diameter, droplets of 1mm, 3mm and 5 mm are injected. The HPGA nozzles operate at the reservoir pressure of 11 atmospheres at the gas inlet. The fluid is nitrogen, modelled as compressible gas with ideal gas law for density and the gas constants given in Table 3.2.

| | |
|---|---|
| H latent heat [J/kg] | 250000 |
| C solid [J/kg-K] | 723 |
| C liquid [J/kg-K] | 825 |
| density [kg/m3] | 7700 |
| melting temperature [K] | 1790 |
| Thermal cond. [W/m-K] | 16.3 |

**Table 3.1: Metal melt properties**

| | |
|---|---|
| C [J/kg-K] | 1040.67 |
| Thermal cond. [W/m-K] | 0.0242 |
| Viscosity [kg/m-s] | 1.663 e-05 |
| Molecular weight [kg/kgmol] | 28.0134 |

**Table 3.2: Nitrogen properties**

The droplet and atomization model is based on the following assumptions:

- The droplets and powder particles are spherical;
- The solidification takes place according to the theory of Newtonian cooling as the Biot number for the simulated particles is smaller than 0.1;
- The powder particles are composed of pure metal;
- The radiation heat transfer mode is not included;

Simulation schemes are summarized in the Table 3.3

| | |
|---|---|
| Solver | Segregated |
| Time | Unsteady |
| Flow model | Multiphase – coupled discrete phase |
| Turbulence model | RSM |

**Table 3.3: simulation schemes**

The detailed geometric change of droplets is demonstrated in Figs. 3.6 – 3.8. It is evident that all the droplets undergo a continuous break-up with rapid reduction of their geometries.

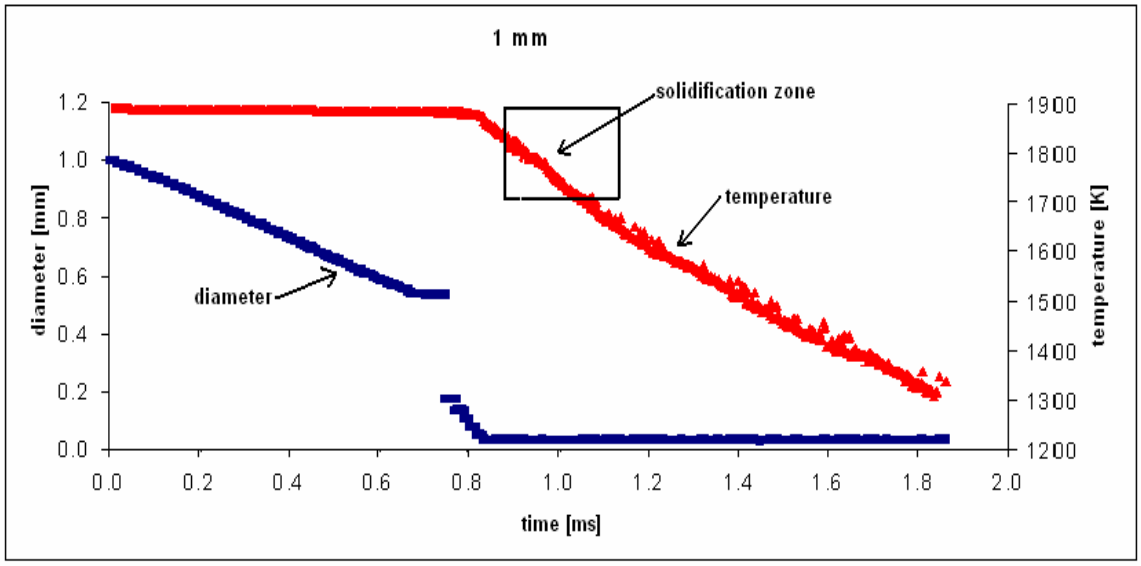


**(a) Throughout the domain**

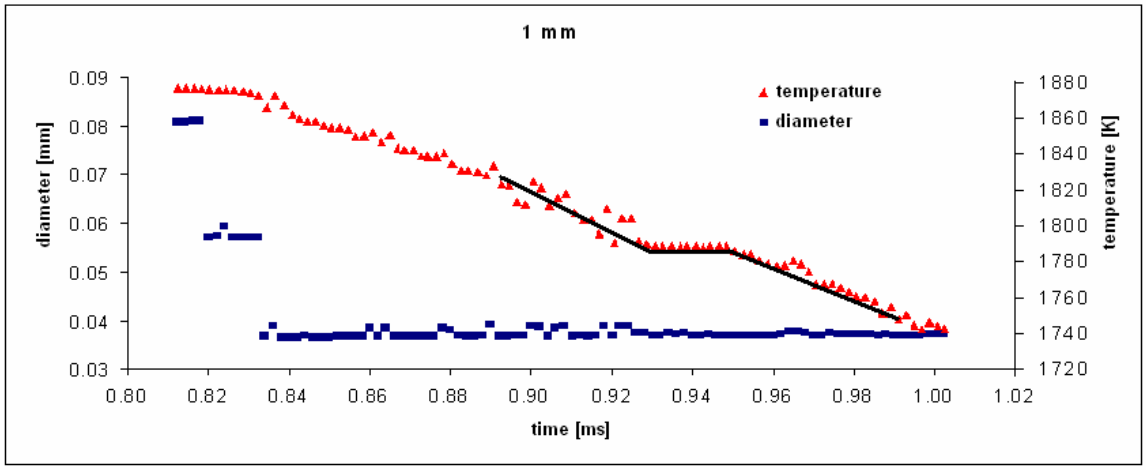


**(b) Within solidification zone**

**Figure 3.6: 1mm droplet diameter and temperature history**

The continuation of break-up is dependent on the initial droplet size: the droplets with initial diameter of 1 mm stop the break-up at 0.83 ms and become stable in the rest of the domain; the break-up prolongs to 3.55 ms for the 3 mm diameter droplets and the break-up continues almost throughout the domain and stops just in front of the exit for the large 5 mm diameter droplets. In contrast to the geometric change, the droplets are able to retain their high temperature in the early stage of atomization despite rapid break-up as shown in Figs. 3.6 – 3.8. The droplet temperatures only start to drop rapidly when they are reduced to very fine sizes. In that case, the heat within the fine droplets evaporates into the cold surrounding swiftly, which triggers the solidification and brings the break-up process to an end.

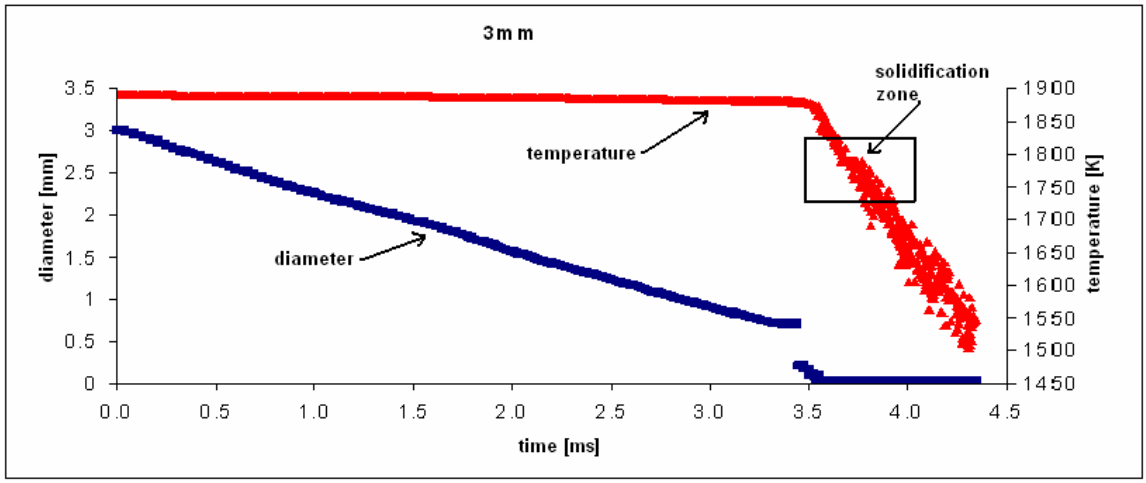


**(a) Throughout the domain**

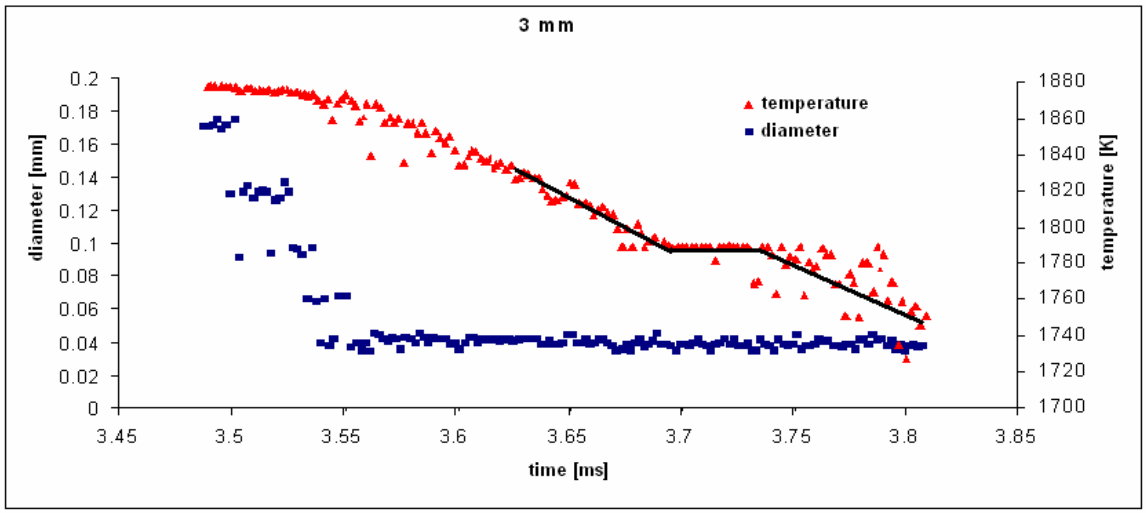


**(b) Within solidification zone**

**Figure 3.7: 3mm droplet diameter and temperature history**

By comparing the droplet size and temperature plots, it is evident that the droplet size becomes stable from the solidification zone onwards. The blow-up images of the solidification zone in Figs. 3.6b and 3.7b illustrate that the droplet temperatures remain constant during the solidification as the result of the latent heat phenomenon and continues to decline afterwards. It is not possible to have a detailed solidification result

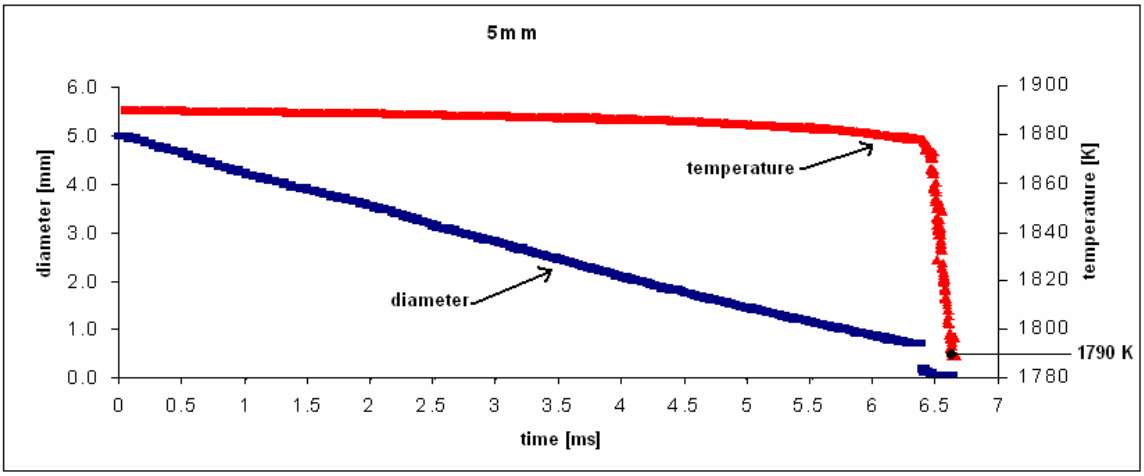


**Figure 3.8: 5mm droplet diameter and temperature history**

for the 5 mm droplet, as solidification takes place almost at the exit and completes outside the current computational domain. The droplet velocity history is shown in Figure 3.9. It is apparent that small droplets accelerate quicker, reach higher speed at the exit and have shorter dwell time within the domain.

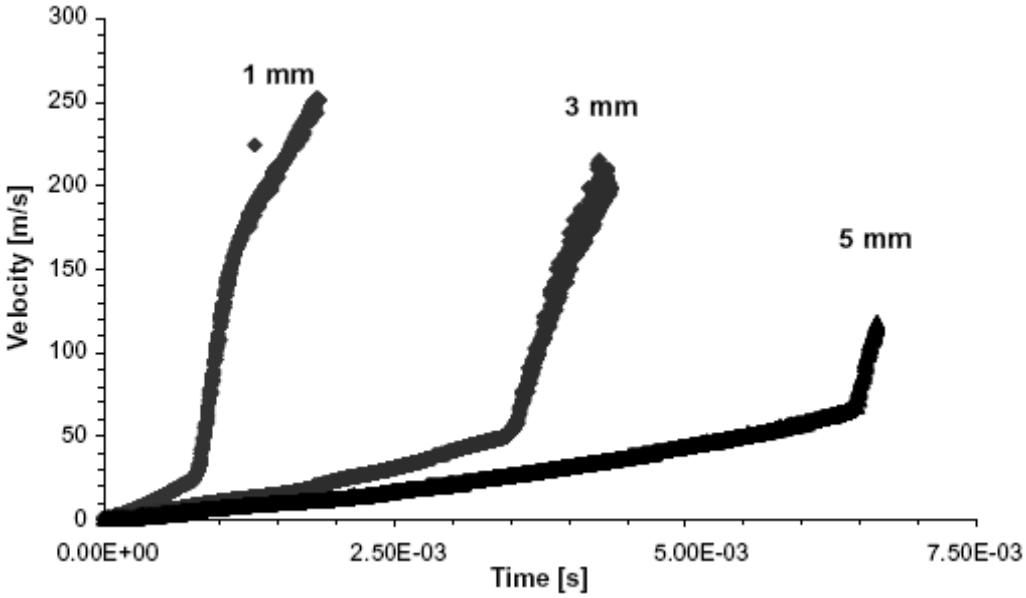


**Figure 3.9: 5mm droplet velocity history**

## 3.4 Isentropic plug nozzle (IPN) design

The design of gas nozzle has not been explored extensively in the context of HPGA. A new concept of gas nozzle is analyzed, serving the purpose of improved expansion from the supersonic gas jet, effectively reduction of shock generation and preservation of energy within the gas plume for the melt atomisation. The new annular-slit nozzle aims to generate an isentropic supersonic jet and is named as plug nozzle. The design of the plug nozzle is based on the method developed by Angelino [11]. This kind of nozzle is commonly used in aircraft and missile propulsion systems. The principle of the plug nozzle is schematically shown in Figure 3.10.

The presence of a sonic line AB at the nozzle throat, and a velocity vector inclined by the Prandtl-Meyer angle (for the design exhaust conditions) with respect to the axis direction are assumed. Furthermore, all the characteristics are straight as the two that limit the expansion fan. The surface area associated with a characteristic is given by the expression:

$$S = 2\pi \frac{e_A + e_l}{2} \frac{e_A - e_l}{\sin\alpha} \tag{3.20}$$

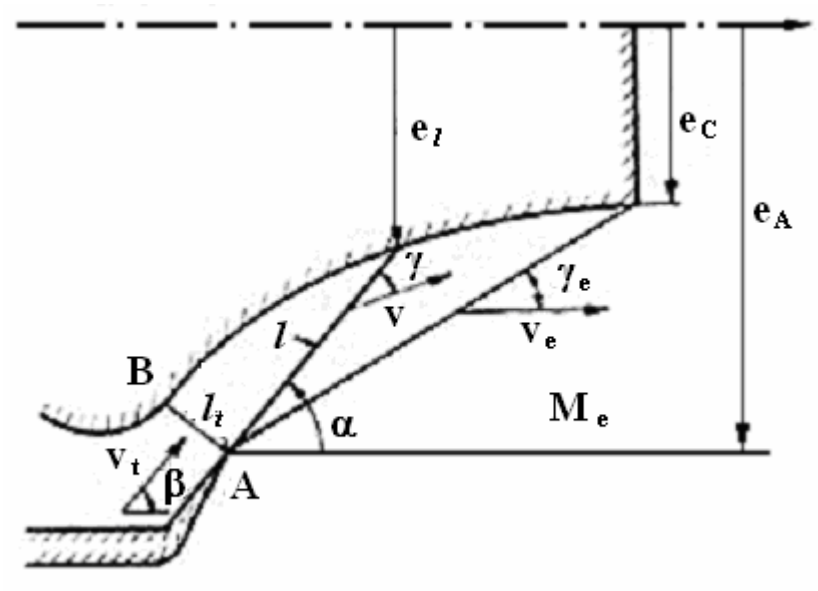


**Figure 3.10: annular plug nozzle [11]**

Due to the inclination μ of the velocity vector, the area normal to the velocity is:

$$A = S\sin\mu = \frac{\pi\left(e_A^2 - e_l^{\,2}\right)}{M\sin\alpha} \tag{3.21}$$

The characteristic length $l$ between the nozzle lip and the nozzle contour is:

$$l = \frac{e_A - e_l}{\sin\alpha} \tag{3.22}$$

The area at the exit of the nozzle is:

$$A_e = \pi\left(e_A^2 - e_c^2\right) \tag{3.23}$$

From equation (3.22) e (3.23) we obtain the relation for the length of the characteristic:

$$l = \frac{e_A - \left[e_A^2 - \left(AM \sin\alpha / \pi\right)\right]^{0.5}}{\sin\alpha} \tag{3.24}$$

The nozzle contour given in the parametric form is:

$$l = \frac{e_A - \left[e_A^2 - \left(AM \sin\alpha / \pi\right)\right]^{0.5}}{\sin\alpha}$$
$$\alpha = \beta_e - \phi(M) - \gamma(M) \tag{3.25}$$

where M is the Mach number, and varies between 1 and the exit design value.

### 3.4.1 Comparison of CDSN and IPN

The isentropic nozzle, designed by the author according to the theory of previous paragraph, has been investigated using the same approach as for the CDSN. Prandtl-Meyer expansion waves are still present in the flowfield (Figure 3.11) but no shocks are visible with the IPN.

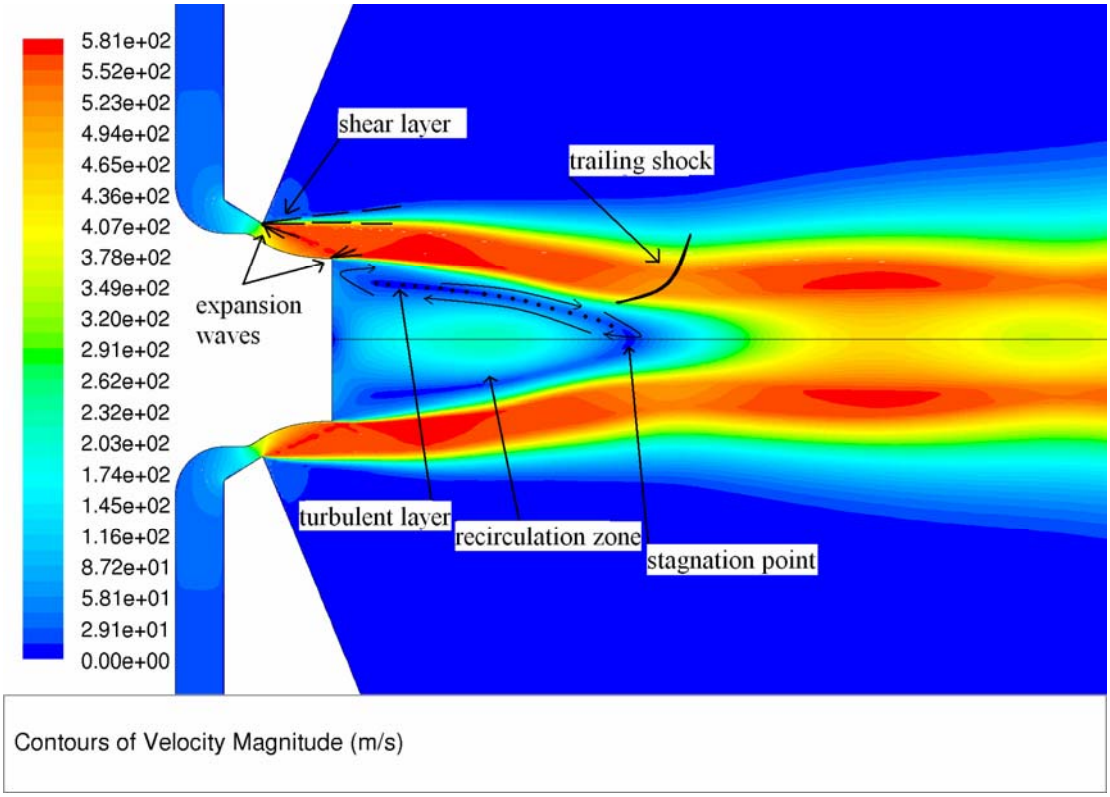


**Figure 3.11: plug nozzle velocity flow field**

Although the results clearly demonstrate that the IPN generates a more stable supersonic jet, it is not possible to completely eliminate the trailing shocks, which are due to the truncated nozzle body (see chapter 4).

A turbulent layer is available inside the recirculation zone (that results well longer than for CDSN), while the mach disk no longer exists in such a geometry. The comparison of radial velocity at 6 different stages is illustrated in figure 3.12.

As expected the profile of the IPN reaches a higher value of velocity in the central zone of the simulated domain (0.1-0.15 m). It must be noted that the higher values of velocity are not on the axis but at a certain distance from it and this is true both for IPN and CDSN.

Using the same approach presented in paragraph 3.3, particles of 1, 3 and 5 mm were injected into the IPN geometry: the particle distributions at the exit of domain are plotted in Figure 3.13. The benefit of such an IPN design is apparent across all the droplet sizes: the particle range is narrowed from over 30 μm by the CDSN to 20 μm by the IPN for 1 mm droplets; the mean particle is reduced from 40 μm by the CDSN to 30 μm by the IPN for 3 mm droplets.

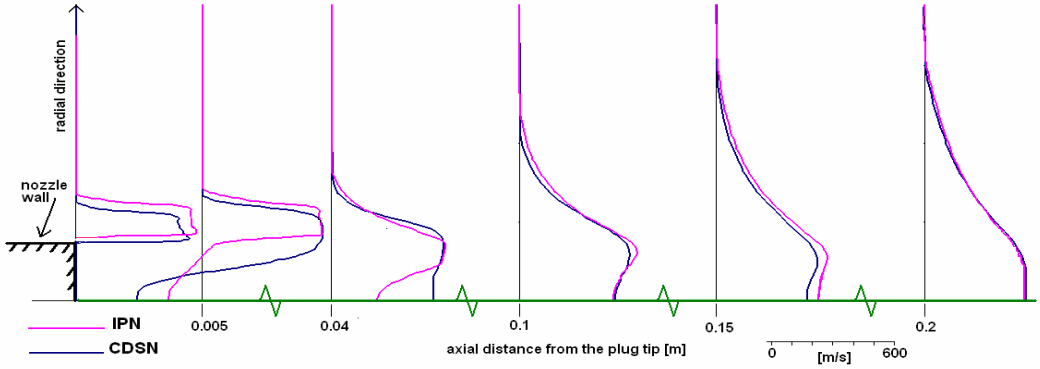


**Figure 3.12: radial velocity profile**

It is evident that the new IPN has the ability to generate finer powders and improve the yield of powder production.

## 3.4.2 Effect of gas temperature

There are reports of using hot gas to improve the yield of powder production in HPGA [12]. This is based on the principle that hot gas will prolong the heat transfer between the melt and gas phases, slow down the solidification of droplets, enhance the transfer of kinetic energy from the gas phase and allow the droplet break-up to proceed further. To evaluate such a practice quantitatively, the incoming gas flow is given three temperature variations, namely

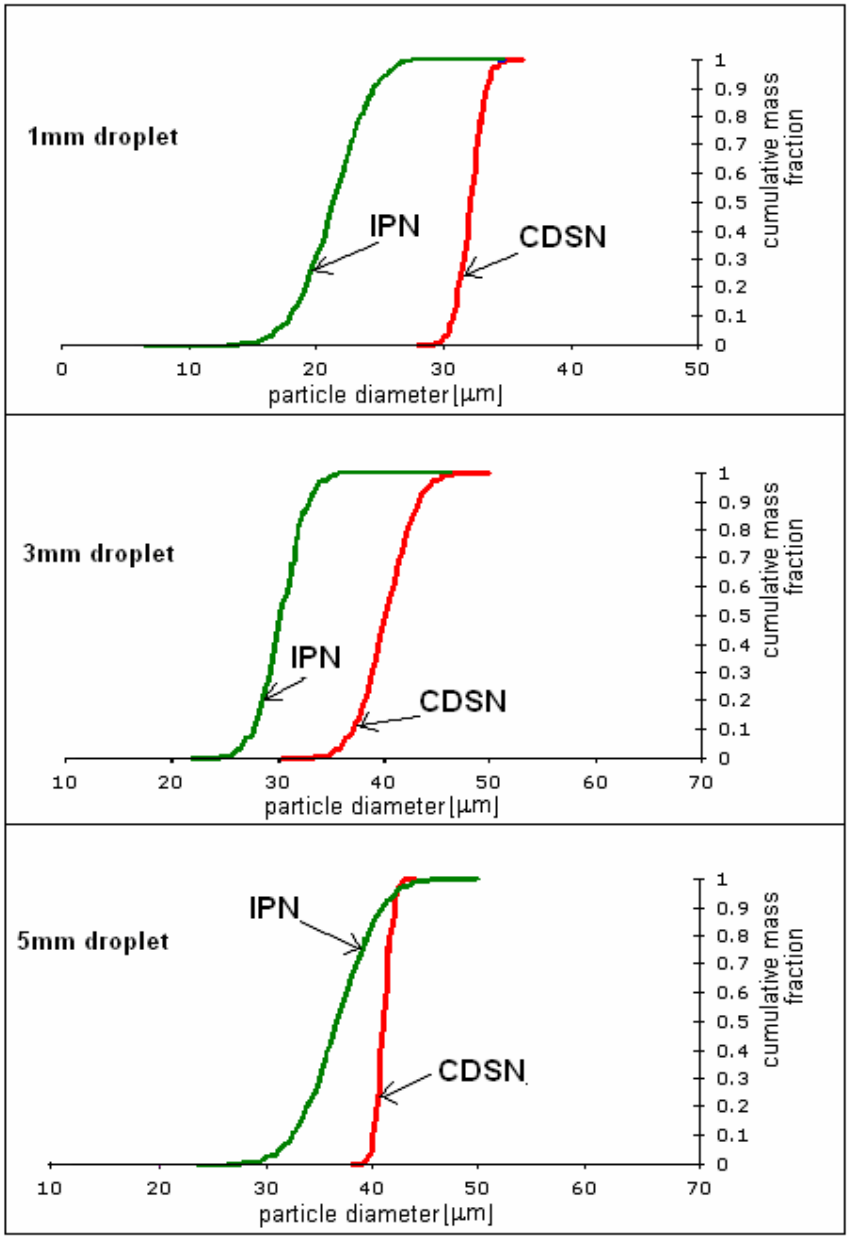


**Figure 3.13: powder size distribution**

300, 400 and 500 K, while the reservoir pressure is always 11 atm. The velocity variations along the centreline of the atomization chamber (IPN geometry) for the different operating gas temperatures are plotted in Figure 3.14. As expected, the flow velocity throughput responds positively to the incoming gas flow temperature while the general flow patterns are similar among those gas flows. The velocity oscillation behaviour is due to the fact that the trailing shock is still present in the IPN design as explained before.

The centreline plots indicate that the velocity increases as the flow develops along the centreline without any sign of decline, which contradicts the common knowledge of supersonic jets. The velocity contour plots demonstrate that the supersonic jets from the nozzle maintain their momentum and decline slightly along the core; the jets move towards

the centreline and finally merge at a certain far point downstream. The flow has very low velocity at the front of the centreline and gradually speeds up by mixing with the incoming supersonic jets.

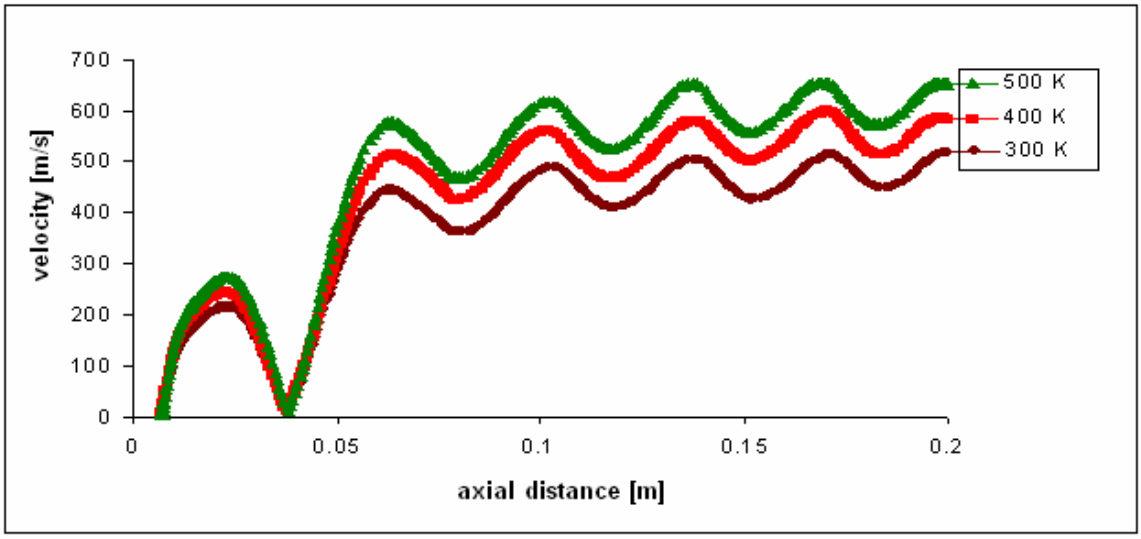


**Figure 3.14: comparison axial velocity plot**

Figure 3.15 reports the gas velocity versus the radial direction at axial distances of 7.5, 15, 70 and 150 mm. The level of the first section is the same as that of melt exit. At 15 mm, the presence of a recirculation zone, with a velocity ranging between 170 and 225 m/s is evident in the left side of the curve. Furthermore, the gas jet velocity has a value not much different from the previous section and close to the higher velocity.

It should be noted that an increase of 200K in the gas temperature gives more than 160 m/s improvement of velocity with a 22.4% saving of gas as listed in Table 3.4. It is known that gas consumption makes a major contribute to cost for HPGA. For the metal powder industry such a significant reduction of gas consumption with improvement of momentum output will be very beneficial to commercial scale production.

| Gas temperature [K] | 300 | 400 | 500 |
|---|---|---|---|
| Mass flow rate [kg/s] | 0.29 | 0.25 | 0.225 |

**Table 3.4: gas mass flow rate**

Figure 3.16 gives the mean distribution of atomized droplets diameter at the exit of the domain. For the 1 mm particles, there is no sensible difference in the distribution size at 500 K and 400 K: the 500 K distribution fits the 400K distribution.

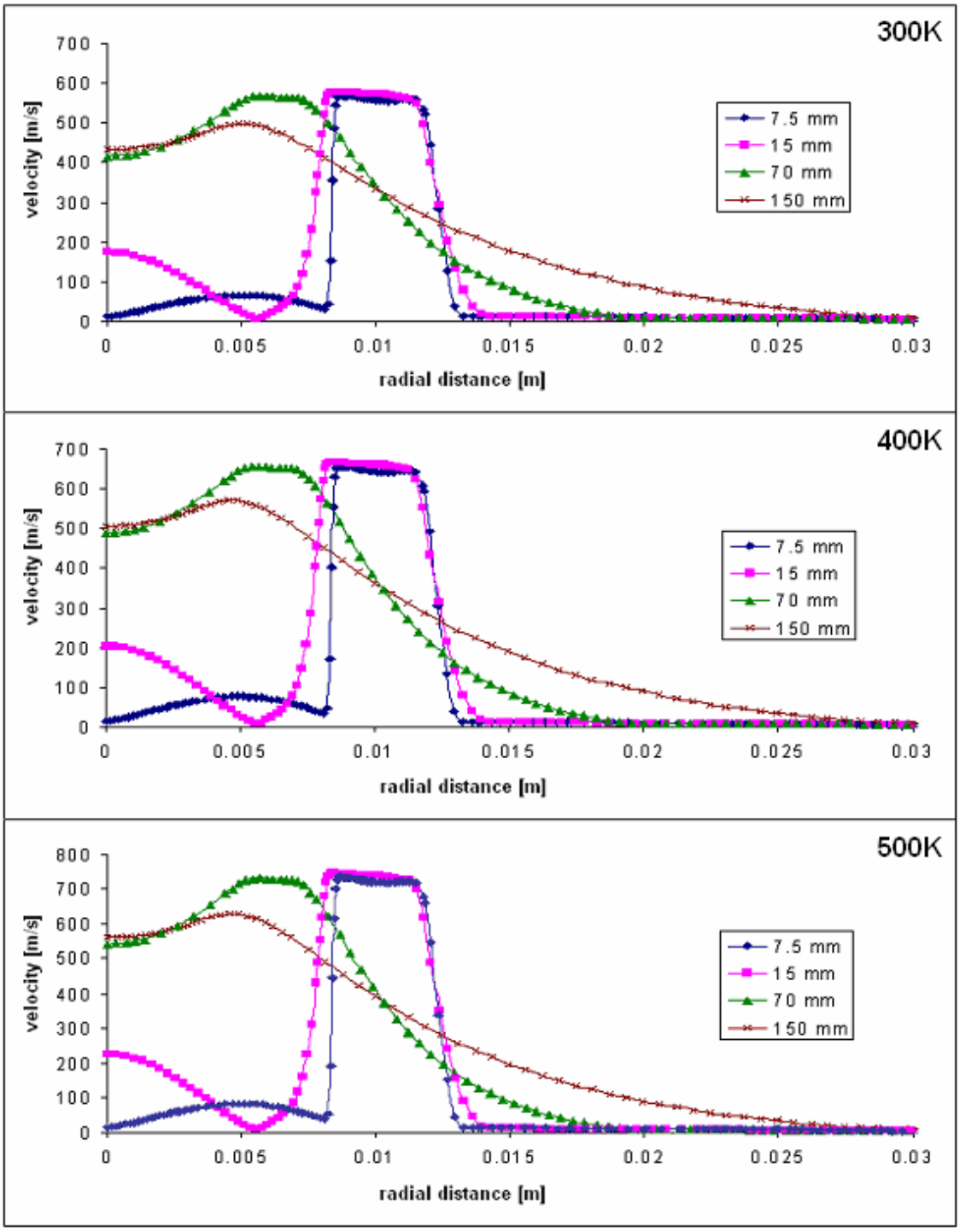


**Figure 3.15: radial velocity plot at 7.5mm 15mm 70mm and 150mm sections for 300K, 400K and 500K**

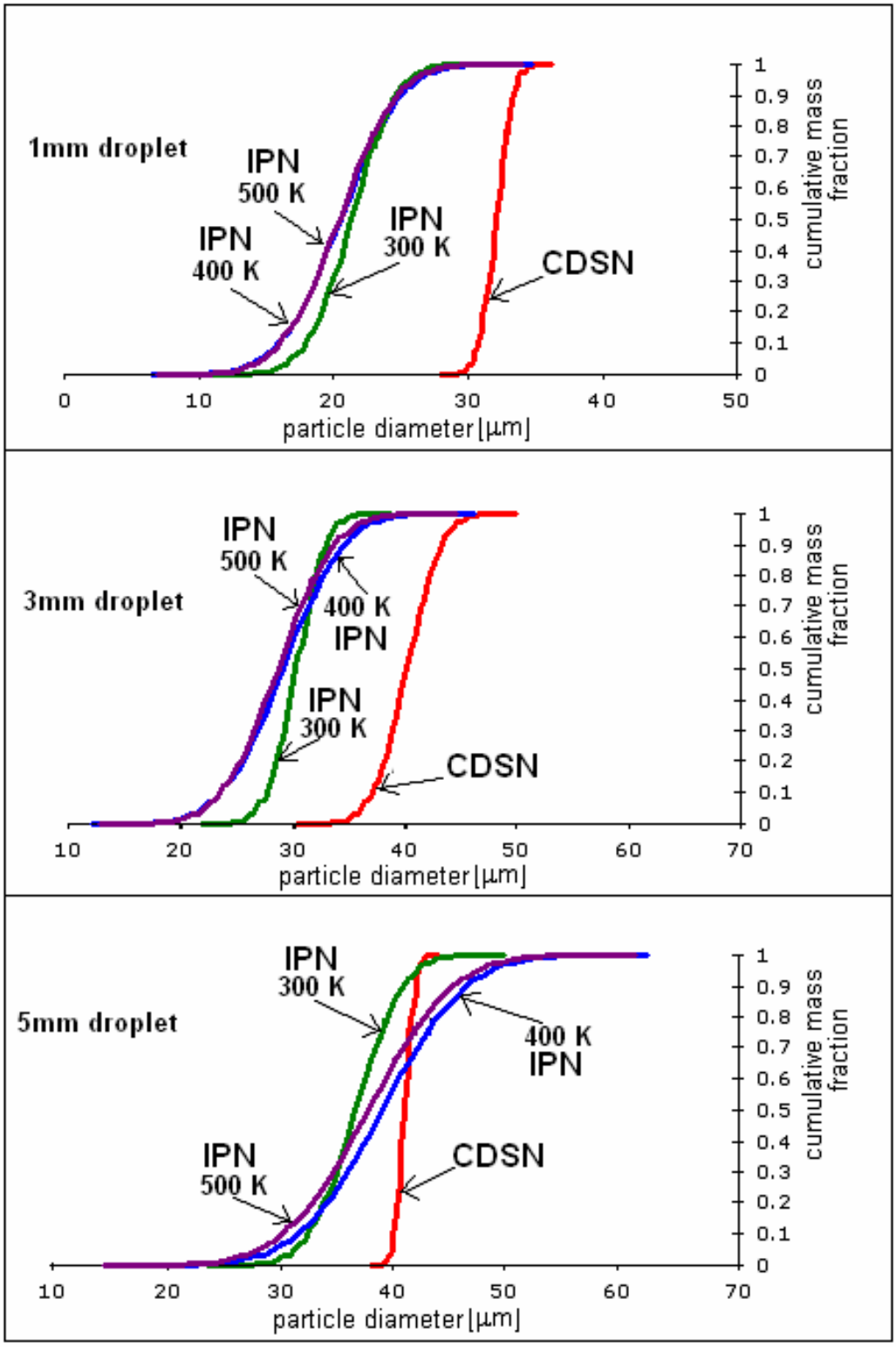


**Figure 3.16: powder size distribution**

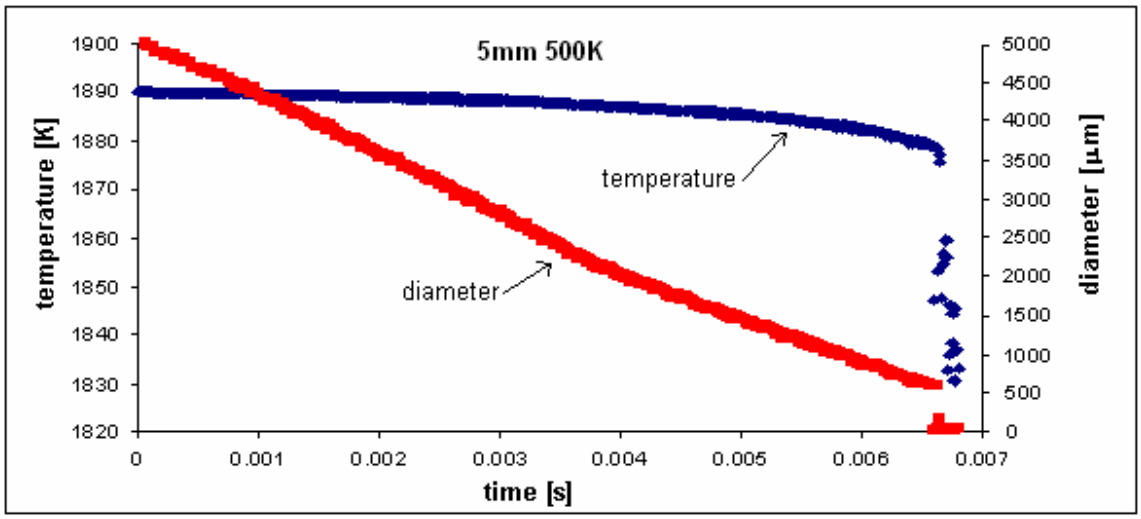


**Figure 3.17: droplet diameter and temperature history**

In any case, the production of the IPN is finer than the CDSN geometry, as shown for all the diameters considered. For 3mm droplets, when the temperature increases, the distribution moves towards smaller diameters. When the larger droplets are atomized with hot gas they show a larger range for the particle sizes produced: while an increase is achieved in the final product for the diameter smaller than 35 µm, at the same time the yielding with size bigger than 40 µm increases.

The increase of bigger droplets in the hot gas results is due to the incomplete atomization of droplets at the end of the simulated domain. In fact, looking at the figure 3.17, the temperature of the liquid metal is above 1790 K i.e. the solidification temperature. The results demonstrate that the IPN design and increased gas temperature generally improve in-flight droplet dynamics; the benefit is more substantial for big droplets, which need a greater extent of fragmentation with slower solidification and demand more energy input from the gas phase.

## 3.5 Refined droplet cooling model

The cooling process for a metal droplet in an environment similar to gas atomization has been best described by Bergmann [13]. The high cooling rate experienced by the atomized droplets is far away from the equilibrium and Newtonian model is not appropriate. A complete transformation from liquid droplet to solid particle includes: cooling in the liquid state, undercooling, recalescence, initial segregated solidification, peritectic transformation, further segregated solidification and cooling in the solid state. In order to have a more accurate model, we will integrate this scheme into the break-up algorithm that we

implemented. An accurate representation of the cooling process needs to include all the sub-processes which will be described respectively.

### 3.5.1 Cooling in liquid state

When droplets are just formed after they break away from the melt stream, the droplets are superheated with temperature above the liquidus temperature $T_L$. As the liquid droplets are cooled down by the surrounding gas, the heat exchange as a result of convection and radiation can be described as [14]:

$$c_{pl}\frac{dT_p}{dt}=\frac{6h}{\rho_p D}(T_p-T_g)-\frac{6\varepsilon\sigma}{\rho_p D}(T_p^4-T_w^4) \tag{3.20}$$

where $c_{pl}$ is the specific heat of the material in the liquid state, h is the convection heat exchange coefficient, D is the diameter of the droplet, the droplet material density, $T_p$ is the particle temperature, $T_g$ is the temperature of the gas around the droplet, $T_w$ is the wall temperature, $\varepsilon$ is the emissivity and $\sigma$ is the Stefan-Boltzmann constant.

### 3.5.2 Undercooling

Equation (3.20) is valid for droplet in the liquid state when droplets develop from superheated to liquidus temperature and further progress to nucleation temperature. The period from liquidus to nucleation temperature is called undercooling. In the context of high pressure gas atomisation, droplets are surrounded by a large volume of cold gas. The extensive heat exchange between hot droplets and cold surrounding gas gives rise to undercooling of the droplets. It is known that undercooling is a function of the cooling rate and droplet diameter. Despite the fact that droplets are subject to temperature below $T_L$ during undercooling, solidification will not start until the nucleation temperature $T_N$ is reached. In this cooling model, heterogeneous nucleation is considered for the droplets, due to the fact that the major portion of powder particles generated by gas atomisation is over 20 $\mu$m, in which range heterogeneous nucleation occurs. The nucleation temperature is obtained as:

$$T_N=T_L-\Delta T_{het} \tag{3.21}$$

The heterogeneous undercooling $\Delta T_{het}$ can be calculated according to the experimental data [15] as:

$$\Delta T_{het}=\Delta T_{\hom}\exp(-2.2\times10^{12}V) \tag{3.22}$$

According to the nucleation theory [16], the maximum homogeneous undercooling $\Delta T_{\text{hom}}$ for a droplet can be evaluated from

$$\Delta T_{\text{hom}}^2 = \frac{16\pi\sigma_m^3\Omega^2 T_L^2}{3k(T_L - \Delta T_{\text{hom}})H_f^2 \ln(10^{44} V \frac{\Delta T_{\text{hom}}}{\dot{T}})} \tag{3.23}$$

$H_f$ is the latent heat of fusion, $\sigma_m$ is the solid-liquid interface energy, $\Omega$ is the atomic volume of the material, k is the Boltzmann's constant; V is the particle volume and $\dot{T}$ the cooling rate.

### 3.5.3 Recalescence

Once the droplet temperature reaches the nucleation temperature, solidification starts to progress and the droplets are no longer in a complete liquid state. In this case, Equation (3.20) is no longer valid. After nucleation, there is a sudden surge of droplet temperature, due to the release of the latent heat of fusion. This phenomenon is called recalescence. This period ends when the added internal heat source from the latent heat of fusion is balanced by the rate of heat exchange with the surrounding gas. Now, the heat exchange including convection and radiation is expressed as:

$$H_f \frac{df}{dt} = \frac{6h}{\rho_p D}(T_p - T_g) + \frac{6\varepsilon\sigma}{\rho_p D}(T_p^4 - T_w^4) \tag{3.24}$$

The growth rate of solid phase can be modelled with the expression:

$$\frac{df}{dt} = \frac{R(T_L - T_p)}{D} \tag{3.25}$$

The temperature at the end of recalescence $T_r$ (Tp at end of recalescence) can be found by introducing equations (3.24) in (3.25):

$$H_f \frac{R(T_L - T_r)}{D} = \frac{6h}{\rho_p D}(T_r - T_g) + \frac{6\varepsilon\sigma}{\rho_p D}(T_r^4 - T_w^4) \tag{3.26}$$

### 3.5.4 Segregated solidification

Solidification continues to progress within the droplet after the recalescence. Two segregated solidifications have been identified for alloy droplets, namely initial and further segregated solidifications. The initial segregated solidification takes place after recalescence while the further segregated solidification occurs after a peritectic transformation. Both segregated solidifications work on the same principle and the droplet temperature decreases as the solidification processes. The heat exchange can be expressed as:

$$\frac{dT_p}{dt}[c_{pl}(1-f)+c_{ps}f-H_f\frac{df}{dT_p}]=\frac{6h}{\rho_p D}(T_p-T_g)+\frac{6\varepsilon\sigma}{\rho_p D}(T_p^4-T_w^4) \tag{3.27}$$

where $c_{ps}$ is the specific heat of the material in the solid state and f is the solid fraction inside the droplet. According to Scheil's theory [17] the solid fraction during segregation can be modelled as:

$$f=1-(1-f_r)\left(\frac{T_M-T_p}{T_M-T_L}\right)^{\frac{1}{k_e-1}} \tag{3.28}$$

$T_M$ is a reference temperature and $f_r$ is the solid fraction at the end of recalescence. Derivation of (3.28) gives the rate of change of f with temperature as:

$$\frac{df}{dT_p}=\frac{1-f_r}{(k_e-1)(T_M-T_L)}\left(\frac{T_M-T_p}{T_M-T_L}\right)^{\frac{2-k_e}{k_e-1}} \tag{3.29}$$

### 3.5.5 Peritectic transformation

The droplet temperature declines during the initial segregated solidification, but solidification within the droplet continues to progress at a constant temperature once the peritectic temperature is reached. The energy equation can be expressed as:

$$H_f\frac{df}{dt}=\frac{6h}{\rho_p D}(T_p-T_g)+\frac{6\varepsilon\sigma}{\rho_p D}(T_p^4-T_w^4) \tag{3.30}$$

Peritectic solidification ends when the composition of the remaining liquid reaches the appropriate concentration. The solid fraction at the end of the peritectic transformation can be found by lever rule (according to the phase diagram):

$$f_{per}=\frac{0.494-c_0}{0.494-0.473}=0.67 \quad (for\ c_0=0.48) \tag{3.31}$$

### 3.5.6 Cooling in solid state

The droplet is not fully solidified after the peritectic solidification and further segregated solidification finally turns the droplet to a complete solid particle. As the droplet is still much hotter than the surrounding gas, the heat exchange for the solid particle can be expressed as:

$$c_{ps}\frac{dT_p}{dt}=\frac{6h}{\rho_p D}(T_p-T_g)-\frac{6\varepsilon\sigma}{\rho_p D}(T_p^4-T_w^4) \tag{3.32}$$

The convective heat transfer coefficient h is calculated by the widely used correlation of Ranz and Marshall [18]:

$$h = \frac{k_g}{D}(2 + 0.6\sqrt{\mathrm{Re}}\sqrt[3]{\mathrm{Pr}}) \tag{3.33}$$

$k_g$ is the gas thermal conductivity, Re the Reynolds number $\frac{\rho_g D(v_g - v_p)}{\mu_g}$, Pr the Prandtl number $\frac{c_{pg}\mu_g}{k_g}$ and $\mu_g$ is the molecular viscosity of the gas

### 3.5.7 Results for the cooling model

Four simulations cases are preformed as listed in Table 3.5. In Case a), 3 mm droplets are injected at the corner of the feeding tube. The simulation generates the baseline results described here. Due to the over performing results, the IPN geometry has been used for all the cases.

| Simulation Cases | Droplet Size at Injection (diameter-mm) | Location | Droplet Size at exit of domain (diameter - μm) |
|---|---|---|---|
| Case a) | 3 | Feeding tube corner | 82 |
| Case b) | 5 | Feeding tube corner | 152 |
| Case c) | 1 | Feeding tube corner | 22 |
| Case d) | 5 | Stagnation point | 213 |

**Table 3.5 Simulation Cases performed**

The convective heat transfer coefficient (CHTC) h is a function of both droplet diameter and the relative velocity between gas and droplet phases. CHTC increases as droplet diameter decreases and responses positively to the increase of the relative velocity.

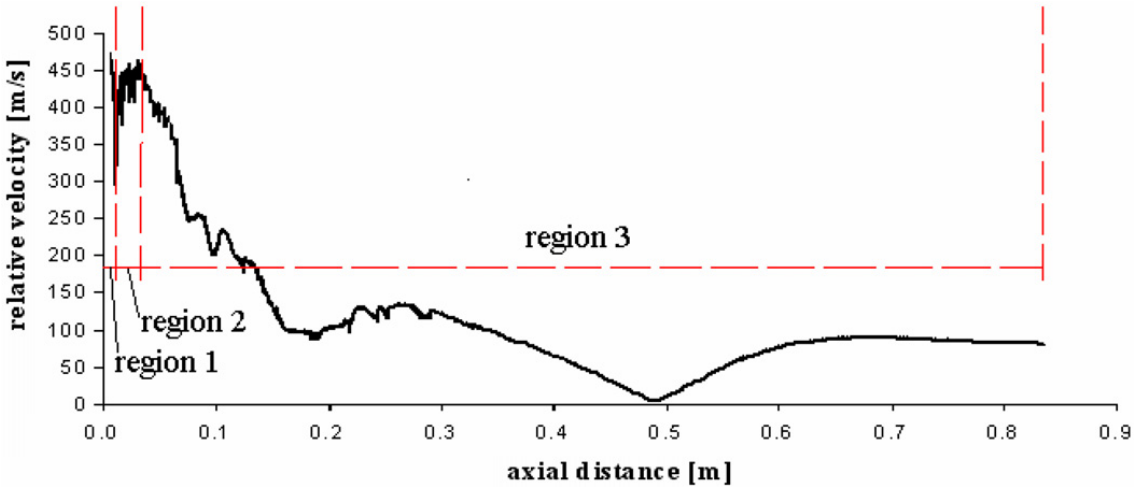


**Figure 3.18 Relative velocity profile from Droplet A**

As the droplets are injected into the domain, they are accelerated by expanded nitrogen and undergo the atomization process. Figure 3.18 shows the behaviour of the relative velocity between gas and droplet. At the beginning, the droplets are accelerated as they come into

contact with the external surface of the nitrogen jet. Subsequently the relative velocity decreases, as shown in Region 1.

When the drops pass through the external mixing layer (region between expanded nitrogen and quiet air) and enter the jet core, the relative velocity suddenly increases as shown in Region 2. After this, the relative velocity decreases as the carrying gas accelerates the droplets further, as shown in Region 3. For the droplet diameters as depicted in Figure 3.19, the droplet size declines rapidly in Regions 1 and 2 and reaches a stable size in Region 3.

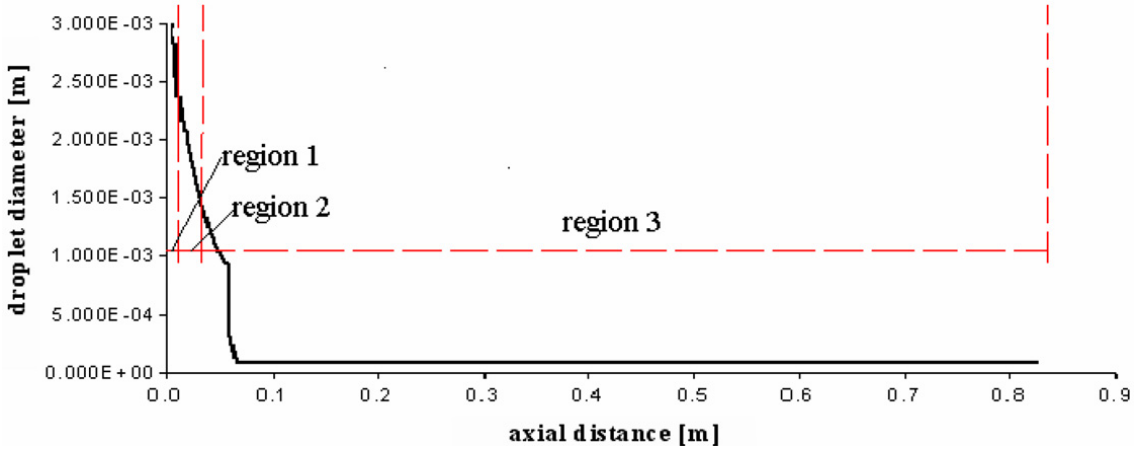


**Figure 3.19 Change of particle size from Droplet A**

The combined effects on CHTC are shown in Figure 3.20. CHTC starts at a low value, due to the large droplet size, it increases steadily in regions 1 and 2, followed by a surge in Region 3 as both relative velocity and droplet size decrease rapidly. CHTC peaks when the droplets stop to breakup further. From that point on, CHTC develops accordingly to the relative velocity as the droplet size remains constant. CHTC declines to a minimum as the relative velocity drops toward zero (transition from acceleration to deceleration). In the final part, CHTC gradually increases with increasing relative velocity. Throughout the entire simulation domain, the CHTC is very high (>$10^3$ W/m$^2$K). The predicted value and development are consistent with the simulation results given in [19]. The minimum value is achieved after a distance of 0,5 m from the tip and the variation becomes very smooth after the spike. Peak value is almost 50% lower than in [19]: this is due to the atomization that generates child droplets far from the high gas speed at the tip, while in [19] the droplets are injected as powder from the beginning and atomization process is not modelled.

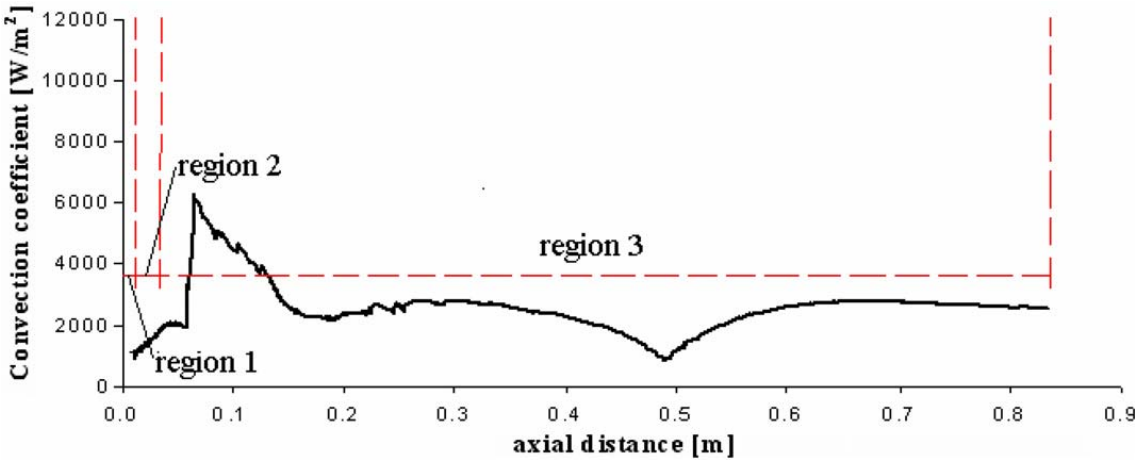


**Figure 3.20 Change of particle size from Droplet A**

Figure 3.21 summarizes the thermal history and solidification. The temperature of the particle starts to decline gradually at the beginning in an almost linear fashion. At the point P1, when the particle starts to break down to a smaller size, two scenarios occurs: one is that the smaller particle accelerates much faster and the second is that the heat transfer rate is much faster with smaller droplets. Both effects will lead to a rapid decline in particle temperature and the trend continues until it reaches the nucleation temperature (1550 K) P2, where the solidification takes place: for a 3mm droplet this value is strongly affected by undercooling phenomena. At this stage, the recalescence produced a fast rise in temperature. This is due to the fact that the external cooling of the drop (convection) is not able to remove the heat released in the interior, is associated with a fast increase of solid fraction. At the end of recalescence, almost 70% of the particle is solid, P3. After recalescence, solidification is very slow: the droplet leaves the simulated domain before being fully solidified (90%). Low solidification rate and high particle velocity mean a long atomization tower.

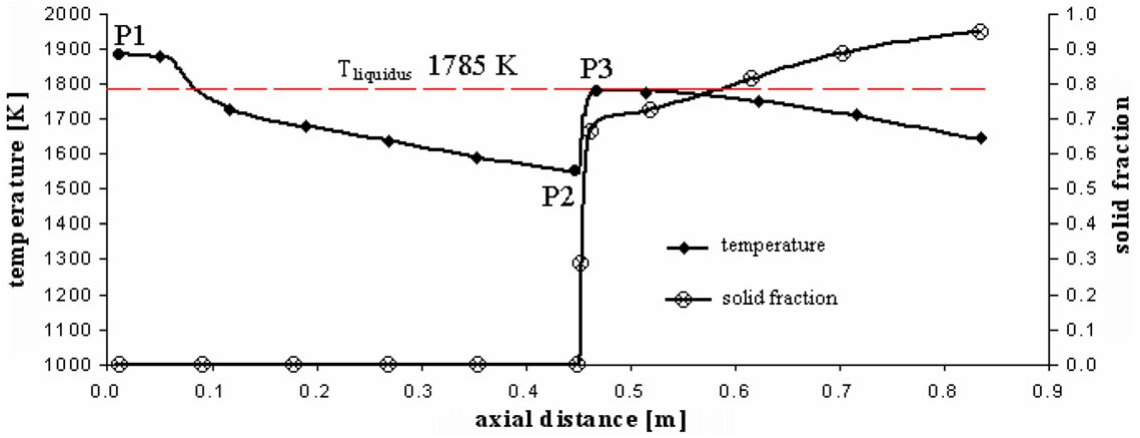


**Figure 3.21 Particle temperature and solidification profile Droplet A**

In order to quantify the effects of droplet size on thermal behaviour, two additional sizes of droplets are injected at the corner of the feeding tube, namely 5 and 1 mm diameters. The relative velocity profiles among these three droplets have similar shapes (they undergo almost identical stages) as plotted in figure 3.22. The droplet sizes are shown in Figure 3.23. For CHTC, the general trends among those droplets are similar. However, the smaller droplet size, the higher is the CHTC achieved.

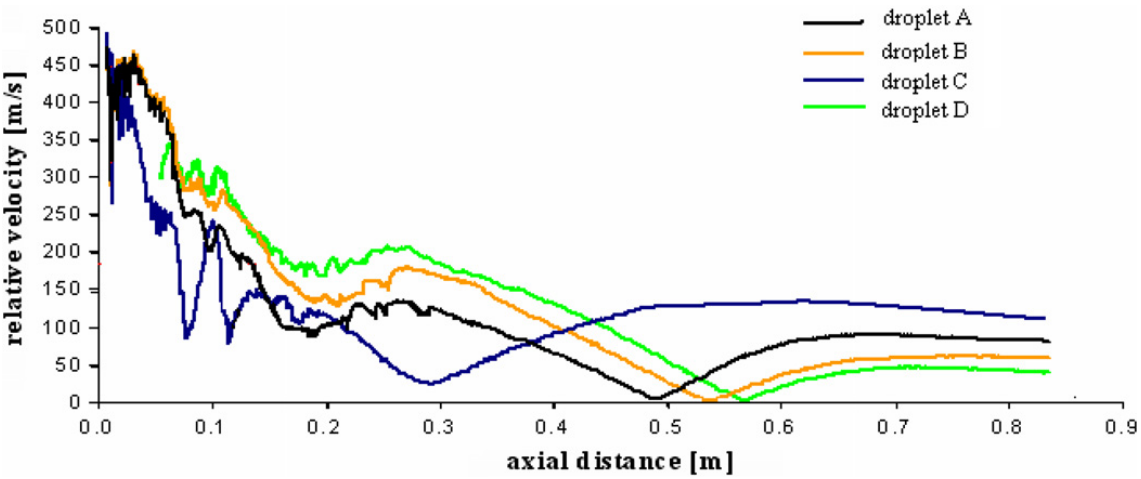


**Figure 3.22: Relative velocity profile from droplets A - D**

The temperature and solid fraction plots in figures 3.24 and 3.25 show that, for the small droplets produced in the atomization case c) the solidification process is completed during the recalescence. In fact, as stated in [20], when the nucleation undercooling is greater than the hypercooling limit ($H_f/C_p$), solidification is complete during recalescence. In this simulation the hypercooling limit is about 328 K while the undercooling experienced by the droplet is around 420 K: a similar value has been predicted in [21]. For the other two cases (due to the higher diameter), undercooling is not present.

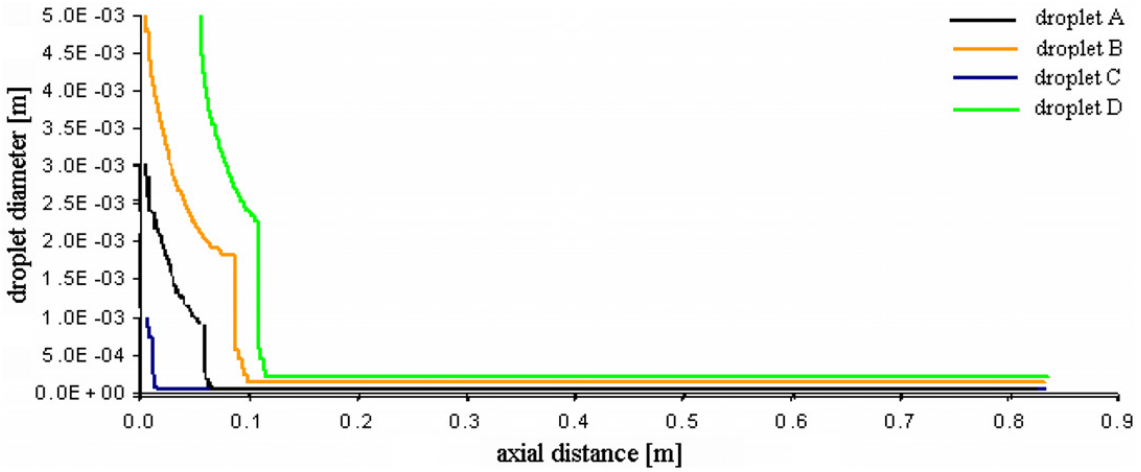


**Figure 3.23: Change of particle diameter from Droplets A - D.**

According to experimental observation on similar systems [2], small droplets are seen at the corner of the melt feeding tube and large droplets appear flowing down from the recirculation zone. It is believed that prefilming will push the melt along the radius of the feeding tube and generate small droplets at the corner. The droplets flowing down directly from the feeding tube have not gone through the pre-filming and large droplets are formed as a result after the recirculation zone. In this analysis, large droplets with initial diameter of 5 mm are released after the recirculation (Droplet D). The comparisons between the after recirculation and corner injections are shown in Figs. 3.22–25.

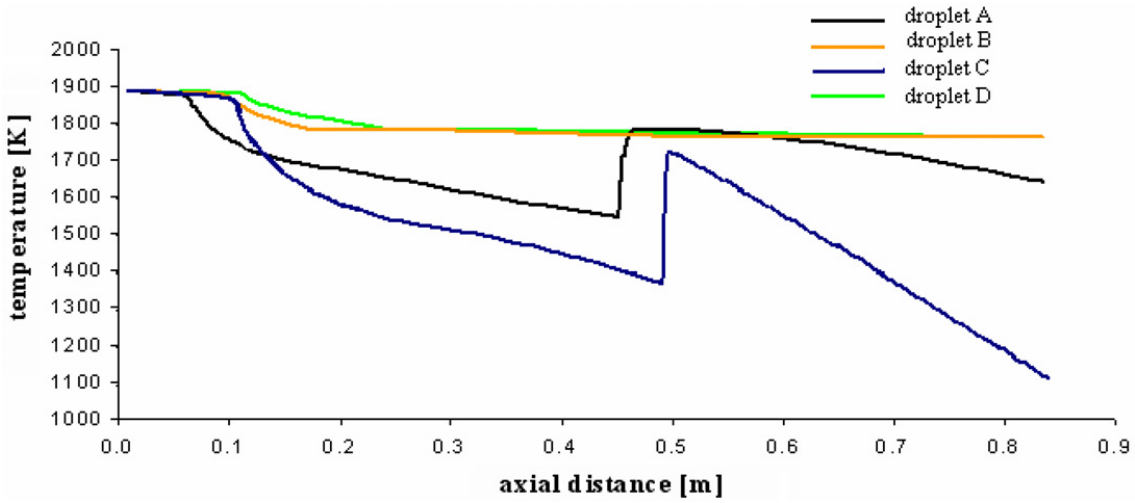


**Figure 3.24: Temperature profiles from Droplets A, B, C andD.**

In the case of the same droplet size (Droplets B and D), the profiles of their variables throughout the domain are very similar apart from a shift of displacement (10 cm).

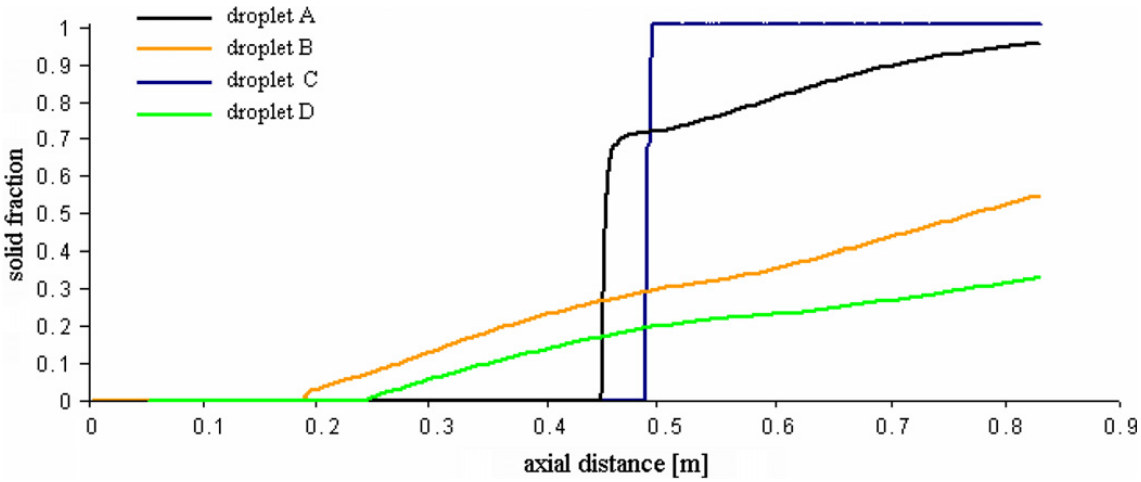


**Figure 3.25: Solid fraction profiles from Droplets A, B, C andD.**

These results indicate that the atomization and solidification processes of droplets are closely related to inflight distance rather than their initial locations in the gas flow.

It needs to be pointed out that, the use of 5 mm droplets at both locations is only for quantitative comparison. In reality, smaller droplets emerge from the corner of the feeding tube as a result of prefilming and large droplets flow down from the recirculation zone. Therefore, droplets from the corner are expected to be atomized and solidified in a greater extent than droplets from the recirculation zone.

## 3.6 Chapter 3 summary

This chapter was focused on the 2D analysis of the close coupled atomizer. The implementation of secondary break up model gave the possibility to simulate the in-flight behavior of second phase (liquid metal) droplets. The isentropic nozzle design is characterized by the absence of oblique shocks in the flow field: the energy previously wasted by shocks structures is available to be transferred at the droplet through aerodynamic interaction. The combination of heated reservoir gas and isentropic nozzle shows promising results in terms of powder size reduction and narrow diameter distribution.

Detailed carbon steel solidification has been implemented to provide an example of solidification with high cooling rate. Simulations showed that the size reduction considerably affects the cooling rate and consequently determines the path length before solidification. The possibility of tracking the droplet evolution allows the designer to choose or verify the atomization tower length very quickly for several operational conditions (i.e. gas reservoir pressure, gas temperature and gas type) and geometries. In order to overcome model limitations like droplets merging in the atomized plume and primary break up atomization, additional researches are necessary.

**References**

[1] J. D. Anderson, Modern Compressible Flow, McGraw-Hill 2004;

[2] S.P. Mates, G.S. Settles, A study of liquid metal atomization using close-coupled nozzles, part 1-2, Atomization and Sprays, Volume 15, pp 19-59, 2005;

[3] R. Courant, K.O. Friedrichs, Supersonic Flow and Shock Waves, Springer, 1999;

[4] S.S. Sadhal, P.S. Ayyaswamy, J.N. Chung, Transport Phenomena with Drops and Bubbles, Springer, Berlin, 1997;

[5] G. Antipas, C. Lekakou, P. Tsakiropoulos, The break-up of melt streams by high pressure gases in spray forming, Proc. 2nd International Conference on Spray Forming ICSF-2, Swansea, 1993;

[6] C.S. Lee, R.D. Reitz, Effect of liquid properties on the breakup mechanism of high speed liquid drops, Atomization and Sprays, Volume 11, pp 1-19, 2001;

[7] P.J. O'Rourke and A.A. Amsden, The Tab Method for Numerical Calculation of Spray Droplet Breakup, SAE Technical Paper. 872089, 1987;

[8] Rolf D. Reitz,Modeling atomization processes in high-pressure vaporizing sprays, Atomisation and Spray Technology, Volume 3, pp. 309-337, 1987;

[9] A.J.Alexander, S.A.Morsi: An investigation of particle trajectories in two-phase flow systems, J. Fluid Mech., pp 193-208, 1972;.

[10] S. Markus, U. Fritsching, K. Bauckhage, Jet break up of liquid metal in twin fluid atomisation, Materials Science and Engineering A , Volume 326, pp 122-133, 2002;

[11] G. Angelino, Approximate Method for Plug Nozzle Design, AIAA Journal, Volume 2, pp 1834-1835, 1964;

[12] W.G. Hopkins, Hot Gas Atomisation, PM2001, Nice, 2001;

[13] D. Bergmann, U. Fritsching, K. Bauckhage, A mathematical model for cooling and rapid solidification of molten metal droplets, Int. J. Therm. Sci., Volume 39, pp 53-62, 2000;

[14] J. H. Lienhard IV, J. H. Lienhard V, A Heat Transfer Textbook, Phlogiston Press Cambridge Massachusetts, 2004;

[15] P. Mathur, D. Apelian and A. Lawley, Acta metall. mater., Volume 37, pp 429-450, 1989;

[16] J. P. Hirth, Metal. Trans. 9A, pp 401, 1978;

[17] E. Scheil, Zeitschrif fur Metallkunde, Volume 34, pp 70, 1942;

[18] W.E. Ranz, W.R. Marshall, Chem. Engg. Prog., Volume 48, pp 141-146, 1952;

[19] J.P. Delplanque, E.J. Lavernia, R.H. Rangel, Analysis of in-flight oxidation during reactive spray atomization and deposition processing of aluminium, Journal of heat transfer Vol.122, pp 126-133, 2000;

[20] B.Cantor, Microstructure development during rapid solidification, Proceedings of the 22nd Risø International Symposium on Materials Science, Roskilde, Denmark pp 483-493, 2001;

[21] B. Li, X. Liang, J.C. Earthman, E.J. Lavernia, Acta Materialia, Volume 44, pp 2409-2420, 1996.

# CHAPTER 4

## Three-Dimensional Characteristics of the Unsteady Atomization Nozzle Flowfield

In terms of physical phenomena, the flow in the atomization nozzle can be described as an internal and external expansion around a truncated plug. Axisymmetric flow due to aerospike nozzle has been investigated since the second half of the last century, in the pioneering work carried out in [1]. Numerical and experimental analyses were conducted in order to verify the feasibility and to evaluate the performance of the aerodynamic spike nozzle. The aim of the research was to provide a thrust chamber with an efficient expansion while, at the same time, being light, small and easy to cool: an annular nozzle was a good solution. Of course, those are the requirements for missile propulsion or, in general, ballistic systems. However the structure of the plug nozzle base flow is the principle of the close coupled atomization process. The "road map" for aerospace researchers points to the reduction of drag due to base pressure distribution, while metal powder production is more interested in drag control. In fact, as explained in the previous chapter, the pressure in the recirculation area plays a key role in melt atomization: lower drag means higher pressure at the nozzle tip and the possibility of backflow with associated freeze-off. Reduction in base pressure (drag increase) improves the atomization stability, but, at the same time, reduces the melt filming. this research has been oriented to point out the crucial mechanisms that determine the wake characteristics (shape, pressure/velocity/temperature distribution, vortex interaction).

## 4.1 Base Flow Description

The supersonic flowfield at the rear shoulder of an axisymmetric blunt based body represents one of the most complicated problems of fluid dynamics [2]. An approaching viscous layer experiences isentropic expansion through a series of Mach waves (Prandtl-Meyer expansion fan) around the sharp corner, resulting in a free shear layer, which separates the supersonic stream from the subsonic recirculation zone below (see figure 4.1). As the slip layer reaches the centreline, it coalesces ("neck") and turns toward the axial direction by means of recompression shock waves. The wake neck region is characterized by momentum deficit (defect in velocity profile): the momentum balance on the control volume surrounding the body indicates that there is a net force acting on the object, which is responsible for drag. For a better understanding, it is useful to highlight four main

aspects of the base flow: expansion around the corner, free shear layer, recirculation and recompression in the wake neck. When the boundary layer approaches the corner, it interacts with the expansion fan in order to generate distorted Prandtl-Meyer waves: due to the hyperbolic character of supersonic equations, the upstream flow cannot be informed (information travels at the speed of sound) of the change in pressure so that it presents a steep change. The flow around the corner is characterized by high viscosity and is often referred to as Stokes-like flow. At the end of the expansion, the flow reaches a pressure lower than the one in the recirculation volume: in order to match the base pressure a shock is formed ("lip shock"). As shown in the experimental investigation [3], the lip shock shape is influenced by both Mach and Reynolds numbers. Higher Mach number results in stronger lip shock (due to the higher overexpansion) so that the interaction with the trailing shock becomes more effective: for very high Mach and low Reynolds values, they merge into a continuous shock, while, for low Mach, they can be clearly distinguished. Figure 4.2 shows the basic changes in the shock pattern for different Mach and Reynolds ranges [3]. The presence of strong vorticity transmits momentum around the corner: this means a delay in the boundary layer separation. Many experimental works detected the separation point on the base and not at the trailing edge [3]. The free shear layer originating from boundary layer

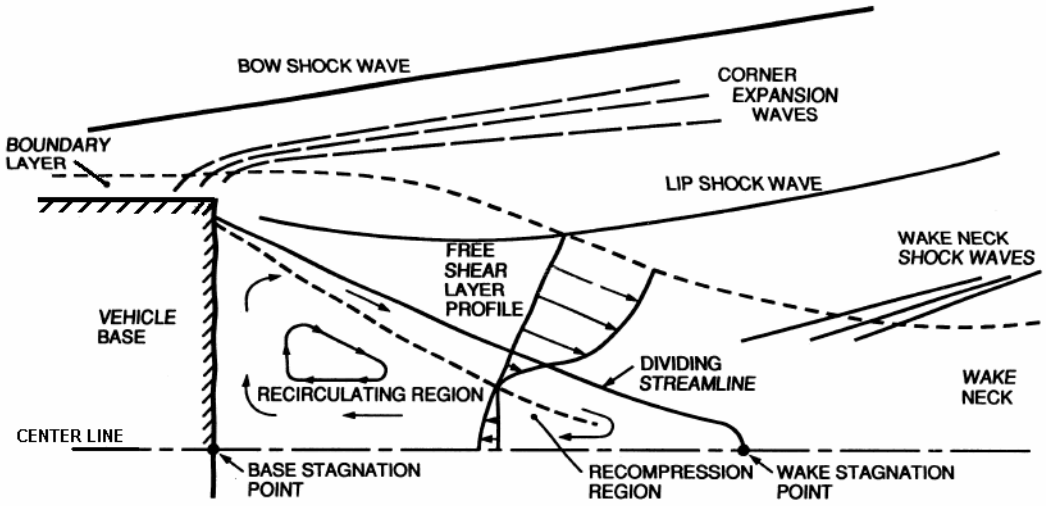


**Figure 4.1: base flow field, partially reproduced from [4].**

separation is characterized by the peak of shear stress along its centre and zero shear stress on the limiting surface (due to the zero velocity derivatives): because of the absence of a viscous sublayer (like in the boundary layer) the energy exchange is entirely regulated by free turbulence. A fraction of the fluid recirculating in the toroidal base vortex is entrapped in the free shear layer as a result of shear stresses action: the dividing streamline marks the

border between this portion of the fluid and the one belonging to the boundary layer. According to [5], the flow in the recirculation zone is relatively slow so that the static pressure does not present significant variation and can be approximated as a constant value: in this specific contest, it makes sense to speak about base pressure.

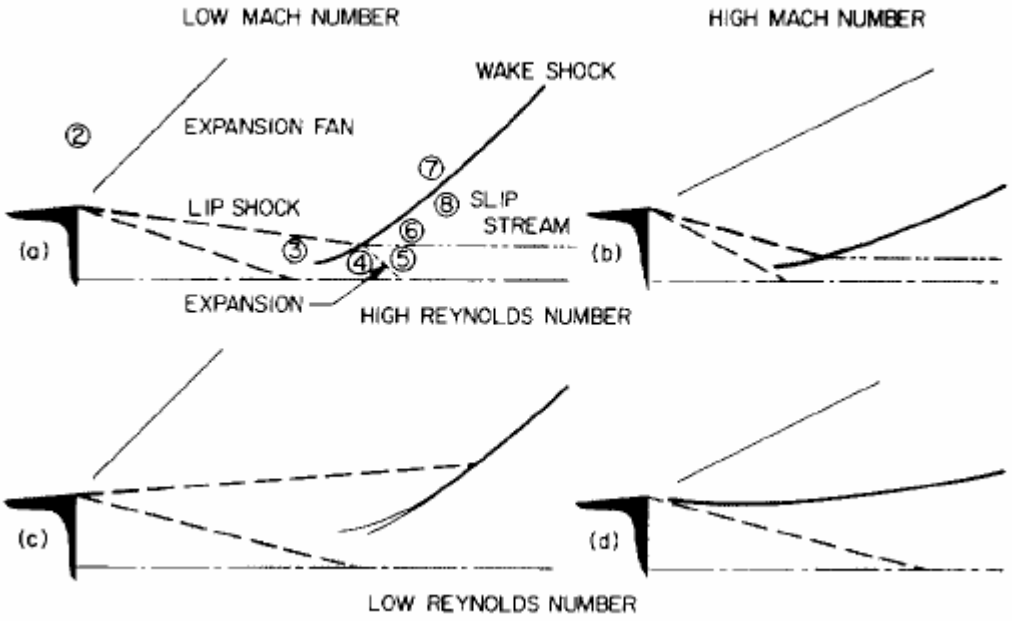


**Figure 4.2: Mach and Reynolds number influence on the shock pattern, reproduced from [3].**

The end of the recirculation is marked by the reattachment process: when the shear layer collapses in the wake neck, a stagnation point is determined. The turbulent/laminar nature of the shear layer affects the location of the neck: the growing rate of its thickness determines where the merging process takes place. The experiments conducted by Pui and Gartshore [6] confirmed that an increase in stream turbulence causes higher shear layer growth rate and amplifies Reynolds stresses. At the reattachment location the flow experiences an adverse pressure gradient: a gradual recompression is determined by the weak (~ isentropic) compression waves that merge generating the tail shock.

### 4.1.1 Wake closure

The wake closure phenomenon is commonly referred to as the condition at which the recirculation region is insensitive to ambient conditions: in other words, the base pressure is not affected by changes in the surrounding area. A closed wake represents the design operating condition for rocket propulsion systems and is associated with high pressure ratio (reservoir pressure or combustion chamber pressure over stagnation pressure). On the contrary, when the separated region is sensitive to the environment, the flow is labeled

as open wake and appears unsteady in nature. Many researchers have investigated this particular flowfield aspect in linear and axisymmetric plug nozzles. Sule and Mueller [7] showed the relation between pressure ratio and plug length: a shorter plug needs lower pressure ratio to generate a closed wake. Ruf ad McConnaughey [8] reported the notable shock features involved in the transition between open and closed wake. A dominant feature in the closed state is the so called "Mach disc" (sometimes Mach Stem): this structure has been documented in the exhaust jet of a converging-diverging Bell nozzle [9] (underexpanded and overexpanded flow) and a truncated plug nozzle [10].

## 4.2 Simulated grid and boundary conditions

In order to evaluate the effect of the above-mentioned phenomena on the gas flow behind the gas atomization nozzle, the simulations are carried out on two different geometries as represented in figure 4.3. The plug nozzle is the same as that analyzed with the 2D axisymmetric model and will be used to evaluate the performance of the 2D approach.

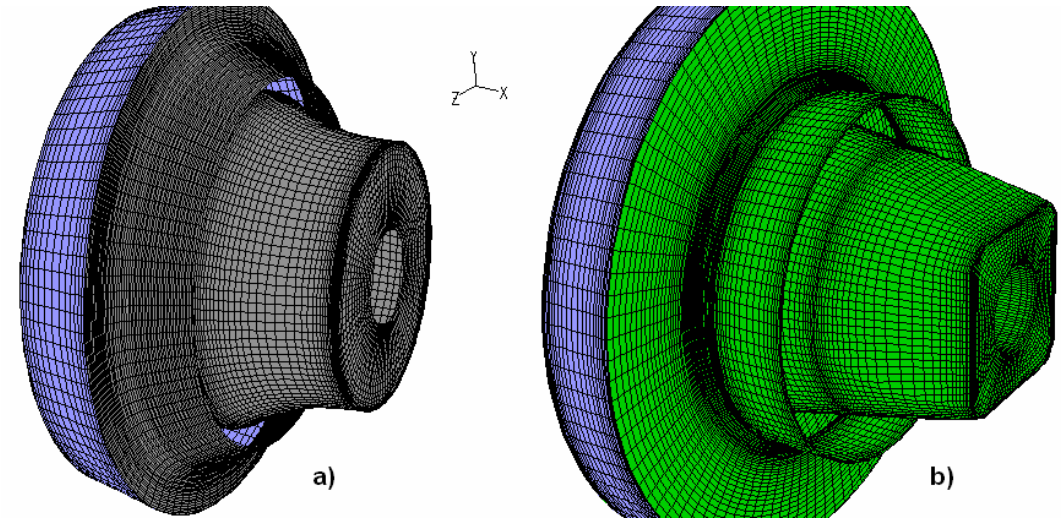


**Figure 4.3: geometry of simulated nozzle a) isentropic plug nozzle, b) nonaxisymmetric plug nozzle.**

The non axisymmetric geometry has been introduced by Miller [11] and can be simulated only with a 3D model: according to the experimental test executed by Miller, it seems to outperform the axisymmetric geometry. The non axisymmetric nozzle is characterized by the transition from circular to square cross-section: the planes on the boattail surface guide the high speed gas toward the melt. Nozzle neck section has the same dimensions of IPN to ensure the same gas flow rate. The pouring channel has the same diameter for both geometries. Grid resolution is extremely important to resolve properly the flowfield features: grid nodes must be clustered in the region of high flow variable gradients. This means that the specific flowfield being solved affected the choice of node location: shock

zone, the boundary layer and baseflow region demand finer meshing than the far away volume. The spacing near the wall is several orders of magnitude smaller than in the freestream: the cell distance from the plug wall (figure 4.4) was chosen to achieve $y^+<5$ (necessary to capture the effects of the inner portion of viscous layer and to properly reproduce the flow condition before tip expansion, see appendix A.2.7).

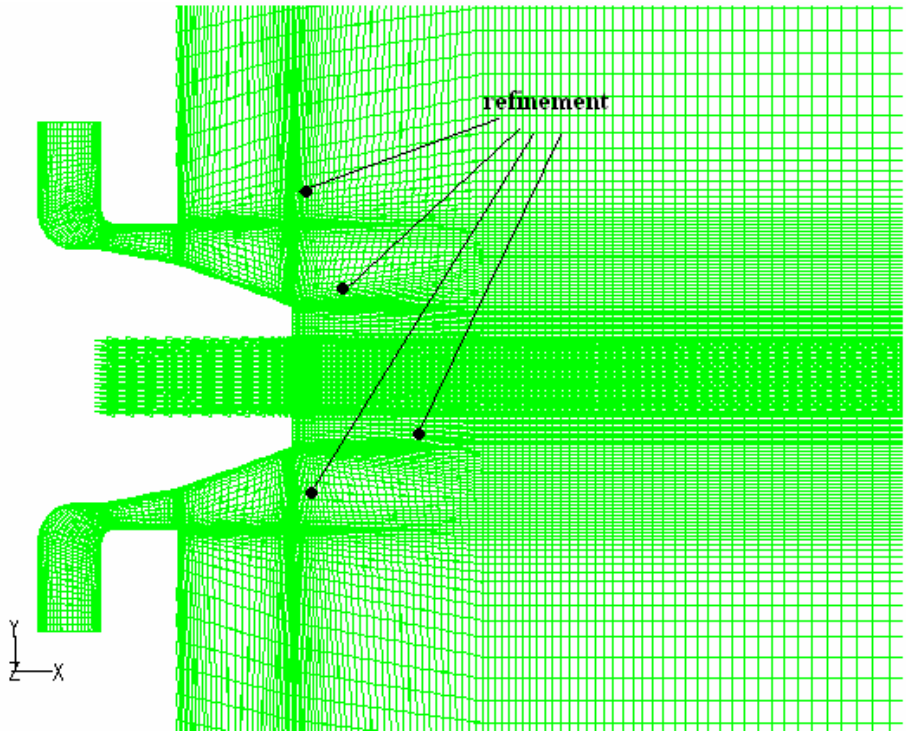


**Figure 4.4: side view of computational domain and mesh for nonaxisymmetric plug nozzle**

The overall grid has 125 nodes in the flow direction and 90 in radial direction. A surface boundary layer was placed on the plug wall with 5 points in 45 μm. The clustering towards the wall and in the expansion/shock area is evident. In both cases the grid size is 1.200.000 cells and the typology is structured. Grid refinements are performed using hanging node method in order to reach a tradeoff between computational resources and accuracy of the solution. Wall refinement was concluded when $y^+$ value approched 5, while in the rest of the domain the adaption cycle continued up to when further refinement did not provide significant changes (i.e. grid sensitivity). Three different boundary conditions were used in the simulation of compressible turbulent flow: pressure inlet, pressure outlet and wall. Unfortunately, very few experimental data are available for supersonic flow in such geometries: one of the main difficulties relies on measuring turbulence quantities in compressible viscous flow and then understanding the meaning of the collected data. Furthermore, all the simulations performed in the last 15 years on axisymmetric base flow have been validated with the experiment of Herrin and Dutton [12]: a milestone for the

investigation of supersonic mixing layer past an axisymmetric body but far away from the aerospike nozzle configuration. Nevertheless, qualitative features like base pressure distribution and recirculation region length will be used as simulation quality indices: most turbulent models fail to reproduce the pressure distribution in the recirculating flow due to the fact that they were developed for incompressible and non not separated conditions. the computational model and the grid shape used in this thesis represent the best trade off achievable with the computational power available during the research. .

## 4.3 Plug nozzle analysis

The simulations results have been subdivided into two macro categories, steady and unsteady, with the aim of distinguishing what can be captured with extended exposure systems (Schlieren images are an example of time averaged images) and intrinsically time dependent phenomena (like coherent structure in the wake or shedding features). 2D axisymmetric scheme "force" the solution (flow field) to be symmetric along the axis: unstable effects are deleted by the superposition of symmetric condition on flow variables.

### 4.3.1 Steady flow

In this section the steady state results (computed with the RSM turbulence model) are analyzed. Flow structure in the near wake zone of an axisymmetric plug nozzle is represented in figure 4.5. The high pressure gas leaves the annular throat and expands in still air around the isentropic contoured ceramic plug. The scenario is much more complicated than the standard base flow problem: in fact it is modelled using an incoming steady flow over a cylinder without involving nozzle expansion and shocks pattern. Table 4.1 summarizes the simulation schemes.

| | |
|---|---|
| Solver | Segregated |
| Geometry | 3D – isentropic plug nozzle |
| Time | Steady |
| Flow model | Single phase (without melt) |
| Turbulence model | RSM |

**Table 4.1: simulation schemes**

The first expansion fan is centred at the outer edge of the throat "A". The plug design ensures that the pressure at location "B" matches closely the chamber condition: this is the reason why the deflection of the gas stream toward the atomizer axis is not prominent.

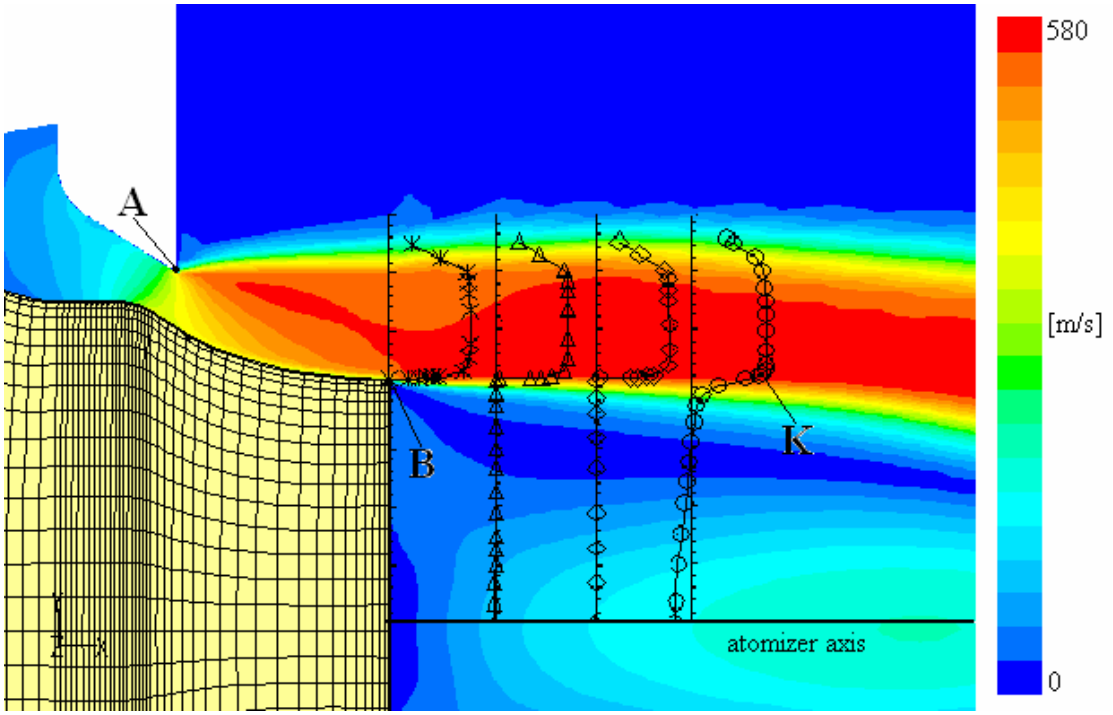


**Figure 4.5: velocity contour plot for steady state simulation**

The normalized streamwise velocity profiles taken at four different locations show a kink (marked as "K" in the last one). The steep gradient in the profile characterizes the rapidly expanded shear layer, denoting the presence of an interface between the viscous sublayer and the remaining part of the approaching boundary layer. The expansion level experienced by fluid parcels in the boundary layer that approaches separation at "B" is inversely proportional to their distance from the wall: this means that the inner stratum of free shear layer suffers higher disturbance. This explains why the outer part of the free shear layer just convects the frozen turbulence while, at the inner edge, there is sensible turbulent activity that engulfs fluid from the recirculation bubble by means of large scale eddies. Equivalent considerations can be done for the expansion at location A. The yellow and green zones, around the gas stream core in figure 4.5, mark the mixing region (initially very thin and becoming thicker as the distance from the plug tip increases). The nitrogen pressure decreases through the expansion fan at "A" from 12 atm to chamber condition, while at B it expands to a sub-atmospheric condition. The extended flow field is given in Figure 4.6: this shows the velocity contours on a symmetry plane of the simulated domain. The structures are similar to the 2D results: the trailing edge shock displays the truncation on the ideal plug and the recirculation zone appears wider than in the two-dimensional grid.

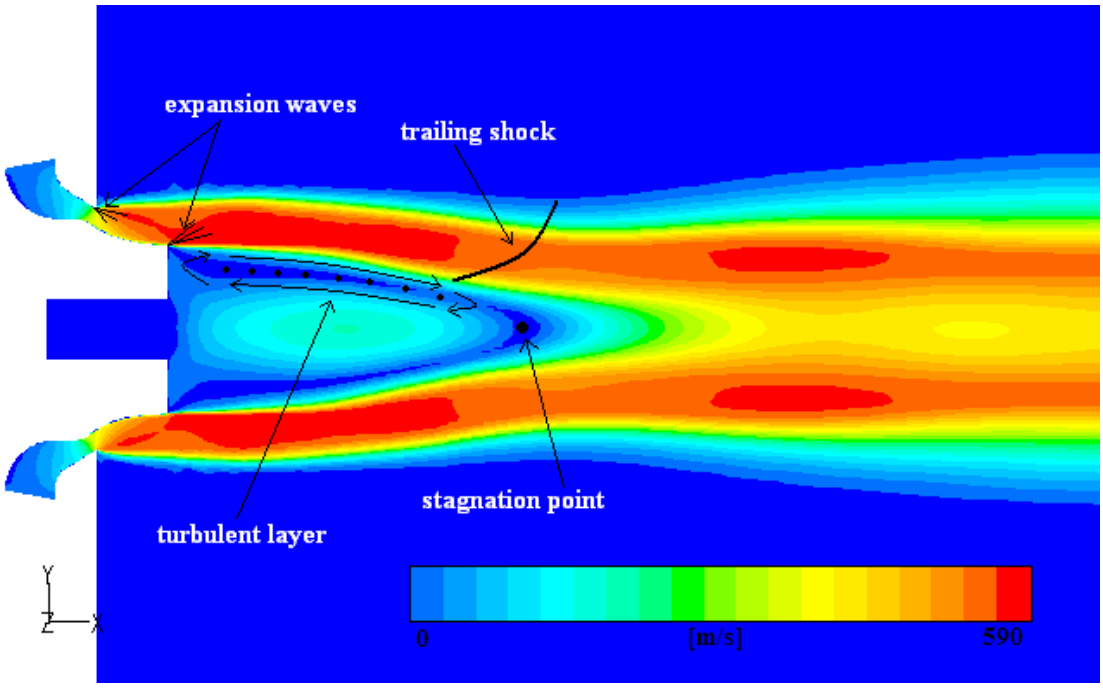


**Figure 4.6: velocity contour on a symmetry plane**

The wake flow after the stagnation point shows that jet core velocity remains well under the maximum speed achieved in the border until the exit of the simulated domain. The mixing region on the jet periphery becomes wider in the wake: this means that the free shear layer subtracts momentum from the high speed gas (negative effect on atomization potential). In order to reduce such phenomena, it would be reasonable to design a nozzle with reduced diameter at the plug truncation point. Axial velocity plot ($U_{axial}$) to mean flow velocity at the separation point ($U_S$) ratio is given in figure 4.7, together with 2D results.

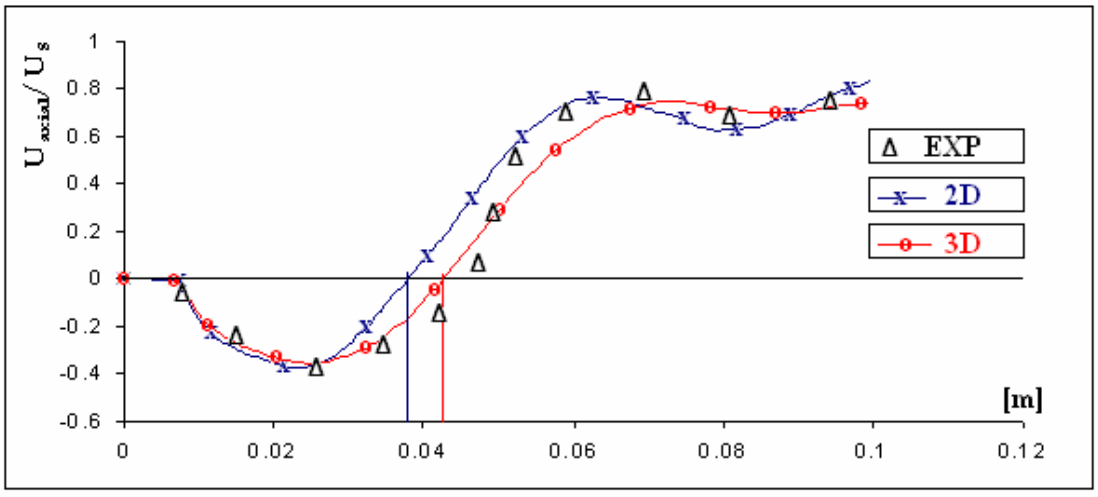


**Figure 4.7: comparison of mean axial velocity along the domain axis between 2D and 3D simulation**

The curves have the same shape: the small differences in recirculation length and velocity ramp-up relate to the two dimensional numerical model simplifications (in 3D vortices

stretch other vortices while in two dimensions they only move around each other's without changing strength).

The recirculation extension is about 4.2 times (0,035/0,0084) the base radius ($R_b$) and the peak reverse velocity is 0.38 $U_S$, positioned downstream compared to the recirculation bubble centre (at $x/R_b$ = 2.25). The 3D results fits pretty well the experimental data (less than 2% difference): the rear stagnation point is shifted upstream because the spreading rate of turbulent shear layer has been slightly overpredicted by the turbulent model. It is important to remember that the recirculation length is also affected by the lip shock presence that influence the turning rate of free shear layer. Herrin and Dutton [12] found a recirculation length of 2.65 base radii, considerably smaller than our result. However, the boundary conditions were different: Herrin used for the analysis (cylindrical sting with radius 31,75 mm) an approaching free stream with Mach 2.46 and Reynolds number $2.86*10^6$ while, in our case, Mach = 2,27 and Reynolds = $8*10^5$. Furthermore the shock pattern of an expanding plug nozzle presents more structures than simple supersonic flow past an axisymmetric body.

Figure 4.8 shows in detail isovalue Mach lines around the separation corners. The lines at the shroud end spread quickly in the still air, while they remain packed after the plug tip because of the presence of lip shock. The recirculating fluid is far away from the sonic condition. As described by the plot in figure 4.9, within all the bubble there exists a subsonic condition with peak Mach value = 0.64.

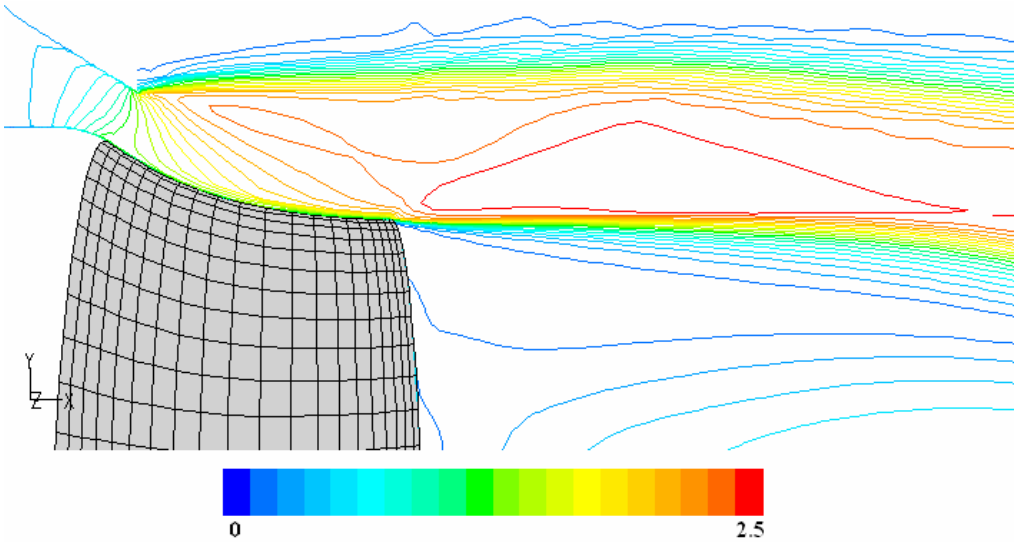


**Figure 4.8: isovalue Mach lines in base region**

The supersonic length extends in the wake outside the simulated domain, reaching the maximum value (≈1.6) close to the reattachment point: experimental measurement [13] on

a similar geometry with slightly higher operating pressure (14 atm) found Mach crest value = 2.

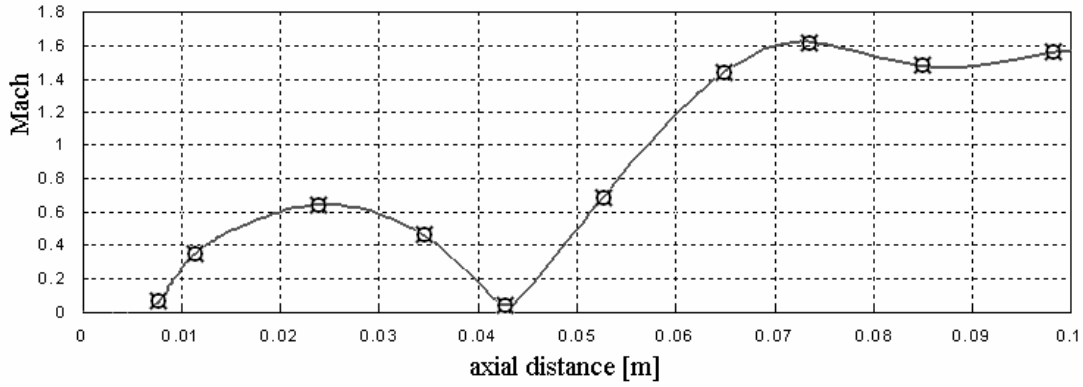


**Figure 4.9: Mach plot along domain axis**

Axial velocity contours are presented in figure 4.10. The initial part of the free shear layer is characterized by the presence of very closely spaced isovalue lines that denote sharp gradients of axial velocity component: this agrees with experimental findings. The spreading rate of the contour lines on the periphery of the shear layer is higher compared to the internal ones that diverge slowly moving downstream. This is a confirmation of the two layers development in the free shear layer: the outer (with reference to jet core) one with high turbulence content grows quickly capturing fluid from the adjacent region.

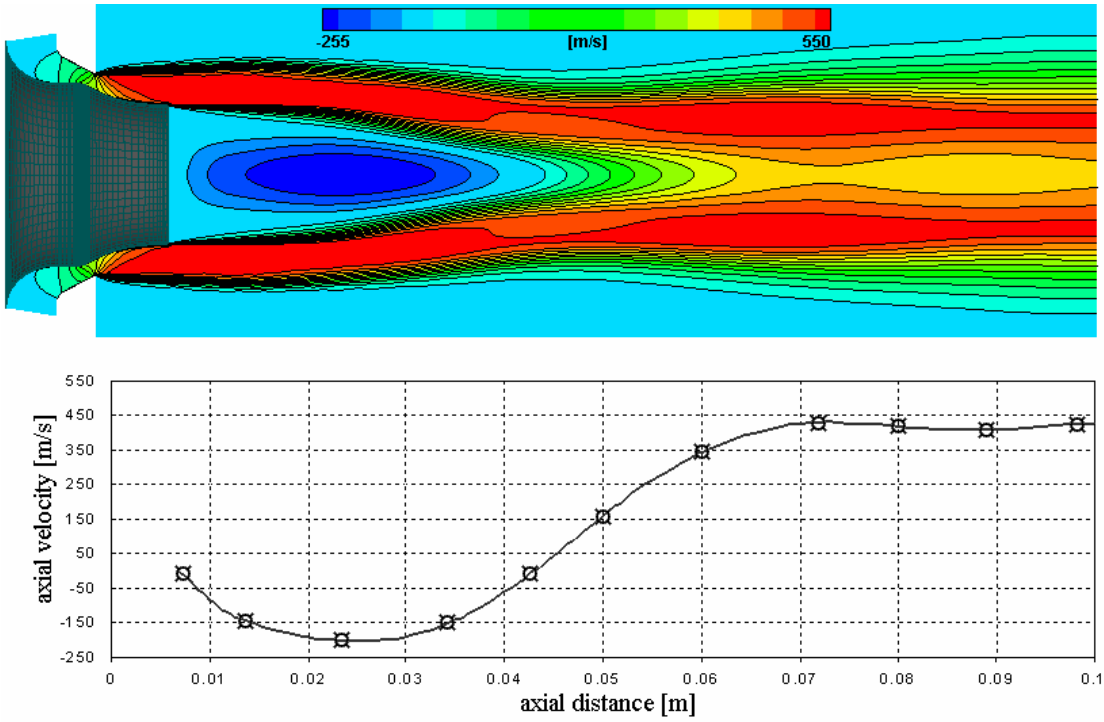


**Figure 4.10: axial velocity component behind plug separation**

Close to the reattachment point the inner layer is overtaken in the flow wake. Even if the gas undergoes steep acceleration on the chamber axis after reattachment, contour levels

demonstrate that velocity defects between fastest zone and chamber axis still exist at the domain exit. In other words, after 6 base diameters, full velocity recover in the wake did not happen.

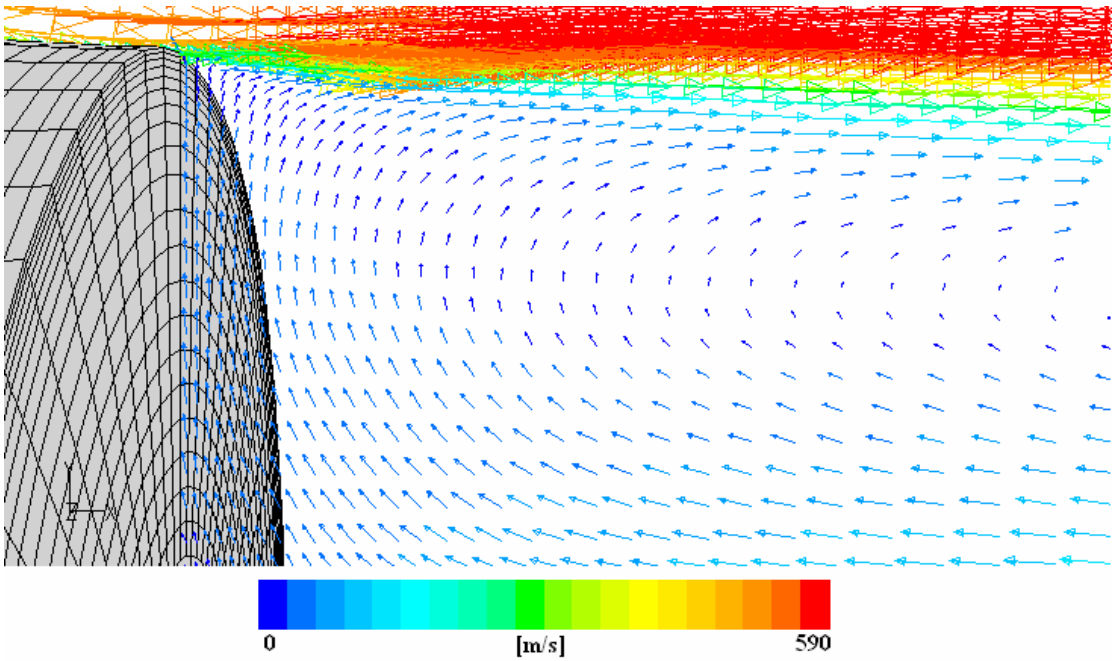


**Figure 4.11: velocity vector in base region**

Velocity vectors distribution on the symmetry plane is given in figure 4.11. Very slow fluid is situated adjacent to the base. As the blue vectors reach the expanded gas on the corner there is an abrupt colour change that marks the contact with the shear layer. It is important to notice that part of the fluid turns away from the wall and remains in the turbulent layer inside the bubble.

In order to have a better understanding of axial velocity recovery, velocity profiles at 4 different locations (at axial distance 0.01 m, 0.02 m, 0.05 m and 0.08 m respectively) are plotted in figure 4.12. The plots for 0.01 m and 0.02 m denote the presence of negative values close to the axis due to the presence of recirculating flow. At 0.05 m, the external diameter of the high speed jet is smaller because the shear layer moved toward the axis to reattach, but there is still a gap of 400 m/s between the fastest gas and jet core. On the last image, the recovery is not fully completed even if the maximum velocity zone is quite close to the axis. The high speed gas layer became significantly thicker moving downward due to the mixing activity of turbulence.

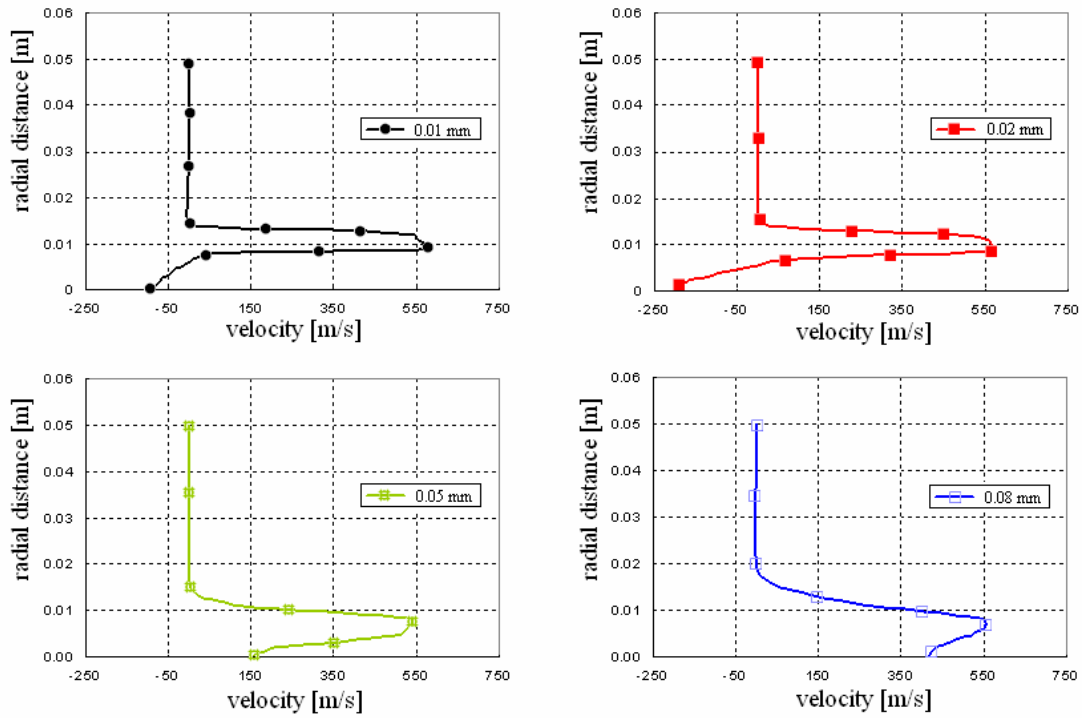


**Figure 4.12: axial velocity profiles at different locations**

Figure 4.13 shows the pressure contours and pressure plot along the domain axis. As expected, a large and reasonably constant sub-atmospheric zone is located within the separated region.

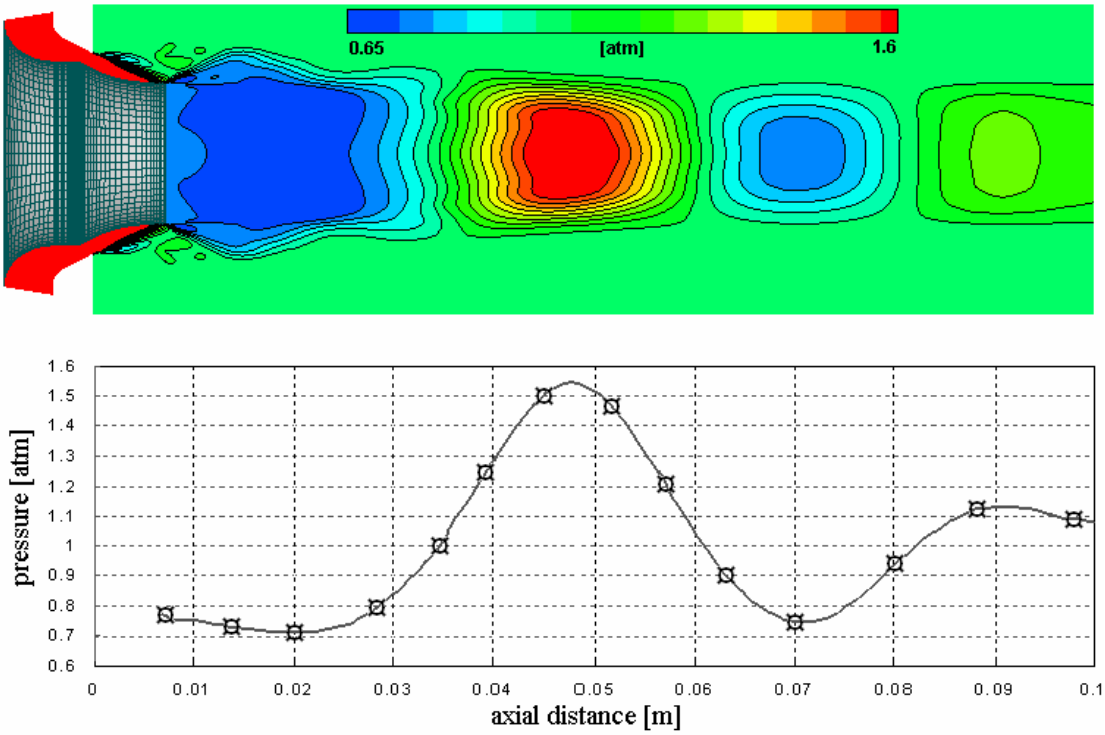


**Figure 4.13: pressure distribution behind plug separation**

Values such as 0,78 atm are commonly registered for a similar nozzle geometry: Settles and Mates [13] measured the tip pressure for a converging-diverging nozzle at different operating conditions and they found the plot in figure 4.14. The discrepancy between the predicted 0,78 atm and the measured 0,85 atm related to the different extension of melt delivery tube. In the simulated domain, the tube length is 7,2 mm while, in [13], it was 5 mm: as explained in chapter 2, the increase in protrusion length is associated with a tip pressure decrease. The prediction of flat pressure distribution along the chamber axis within a large part of the recirculating bubble is commonly observed for the base flow problem. The downstream part of the recirculation zone presents a pressure increase (caused by the trailing shock that occurs when the high speed streamlines approach the domain axis and realign) and reaches the maximum value at the reattachment point. A second shock cell is visible into the domain but the strength is severely reduced and the chamber pressure is almost reached. The clustered isovalue lines near the plug and shroud tip indicate the presence of a strong pressure gradient (Prandtl Mayer expansion) that is reflected by the outer free jet boundary as compression waves merge together in the envelope shock.

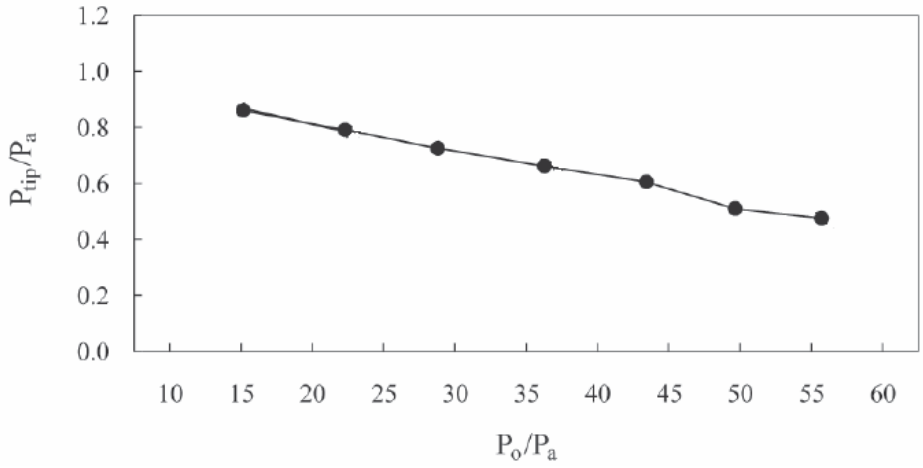


**Figure 4.14: pressure measured on the delivery tube tip**

Figure 4.15 represents the static pressure distribution across the base. The maximum value is registered on the inner diameter, where the recirculating flow stagnates, while the lower pressure insists near the base corner. The rising pressure at the outer diameter is the result of severe curvature experienced by the streamlines in this zone: as the low speed recirculating gas that moves outward reaches the high speed gas, it is entrapped in the shear layer and it turns more than 90 degrees so that the pressure near the corner is higher. The peak on inner diameter is a direct consequence of melt feeding hole presence. The pressure radial gradient is a driving force in the melt filming mechanism: a high pressure gradient would favourite outward movement of the liquid.

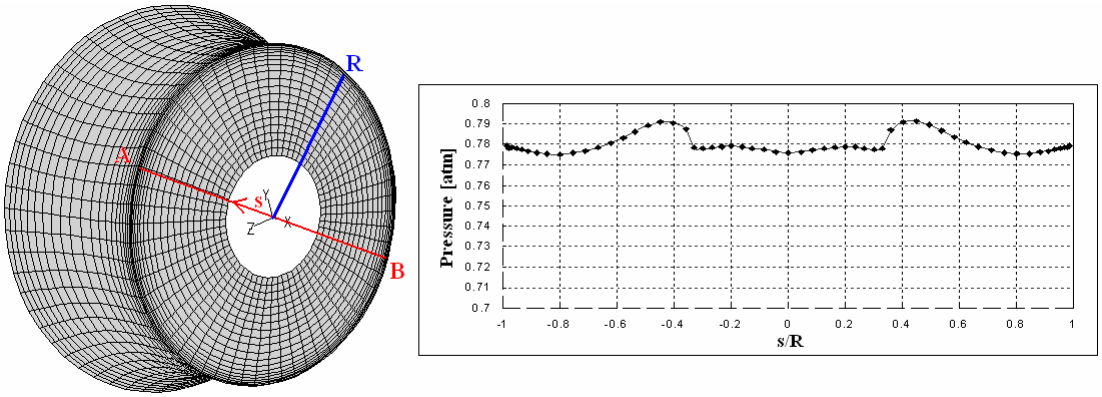


**Figure 4.15: base pressure distribution for isentropic plug nozzles**

As anticipated in chapter 2, radial gradient is improved by short feeding tube protrusion and high taper angle that, on the other hand, increase base pressure and may generate melt backflow with consequent freeze off: most of the time, the filming attitude is avoided in industrial application to run a more stable process. Herrin and Dutton [12] experimental analysis showed that time averaged base pressure for supersonic axisymmetric base flow is almost constant along the radius (3% variation). The predicted profile for the isentropic plug nozzle exhibits smooth variation (2,6%). Turbulence model plays a very important role to capture correctly the recirculating flow. In fact two equations models overpredict the turbulent kinetic energy before the separation (turbulent viscosity $\nu_t \infty k^2/\varepsilon$) so that the free shear layer is diffused (i.e. increased growth rate) and tilts faster versus the axis. The resulting recirculation bubble would be shorter and the backward velocity higher with a consequent unrealistic strong pressure at the base centre (stagnation point). The RSM used in this simulation is also based on averaged turbulent quantity but it is not affected by turbulent viscosity issue and Reynolds stresses are not aligned with the strain rate(isotropic assumption. LES model would be the most appropriate for time depending solution due to the intrinsic dynamic behaviour, and will be introduced in the paragraph 4.5. In order to complete the overview of flow characteristics, temperature contours are given in figure 4.16. Expanded gases reach very low temperature (≈135K) that increases the cooling rate of atomized droplets.

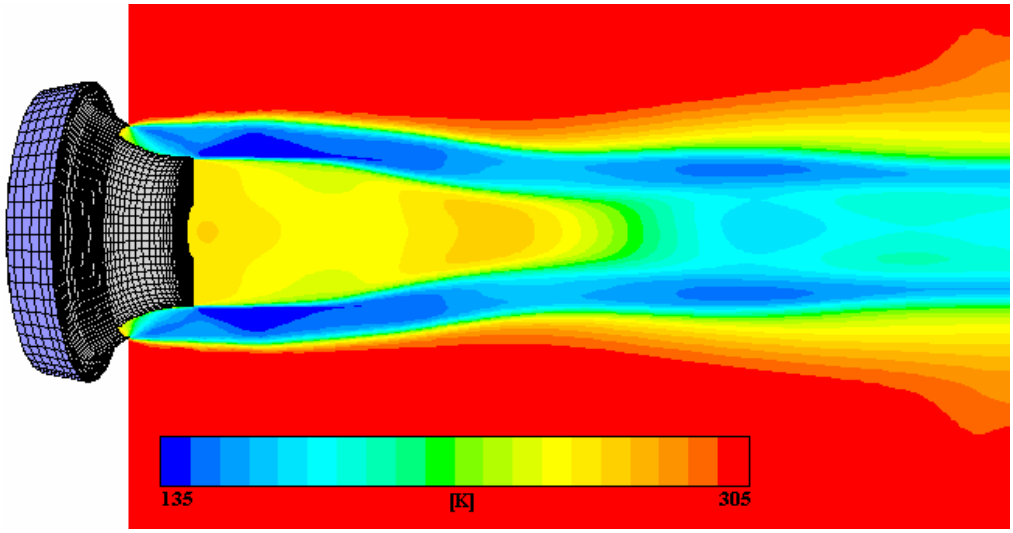


**Figure 4.16: temperature contours for isentropic plug nozzles**

The last part of the steady state analysis has been dedicated to evaluation of the influence of the reservoir pressure on the flow field. Many studies in the past focused on this topic but many aspects are still open and the proof is that most of the current analyses concern the impact of closed wake (mach disc presence) or open wake on the atomization process. Three different pressure levels were simulated: 16 atm, 20 atm and 30 atm.

The velocity flow fields for all the cases are shown in figure 4.17. The isentropic nozzle was designed for 12 atm, so clearly it works off-design in an underexpanded condition. Despite the 150% higher pressure the peak velocity increases by less than 23% and only near the plug. Most of the additional energy is lost in the strong shocks behind the base: this means that no particular benefit could be expected in the secondary atomization process. Basically 16 atm and 20 atm present the same characteristics as the baseline case (12 atm). The simulation result for 30 atm gives a nozzle operating in closed wake condition: a second recirculation zone arises while the primary zone becomes very short and thin. A comparison between the different recirculating bubbles is plotted in figure 4.18.

| Reservoir pressure [atm] | Mass flux [kg/s] |
|---|---|
| 12 | 0.33 |
| 16 | 0.44 |
| 20 | 0.545 |
| 30 | 0.82 |

**Table 4.2: gas mass flow for different reservoir pressure**

Gas mass flux details are summarized in table 4.2. Up to 20 atm, the reattachment point is shifted toward the end of the domain and the peak of reverse velocity increase is proportional to the free stream condition, close to 40% of its value.

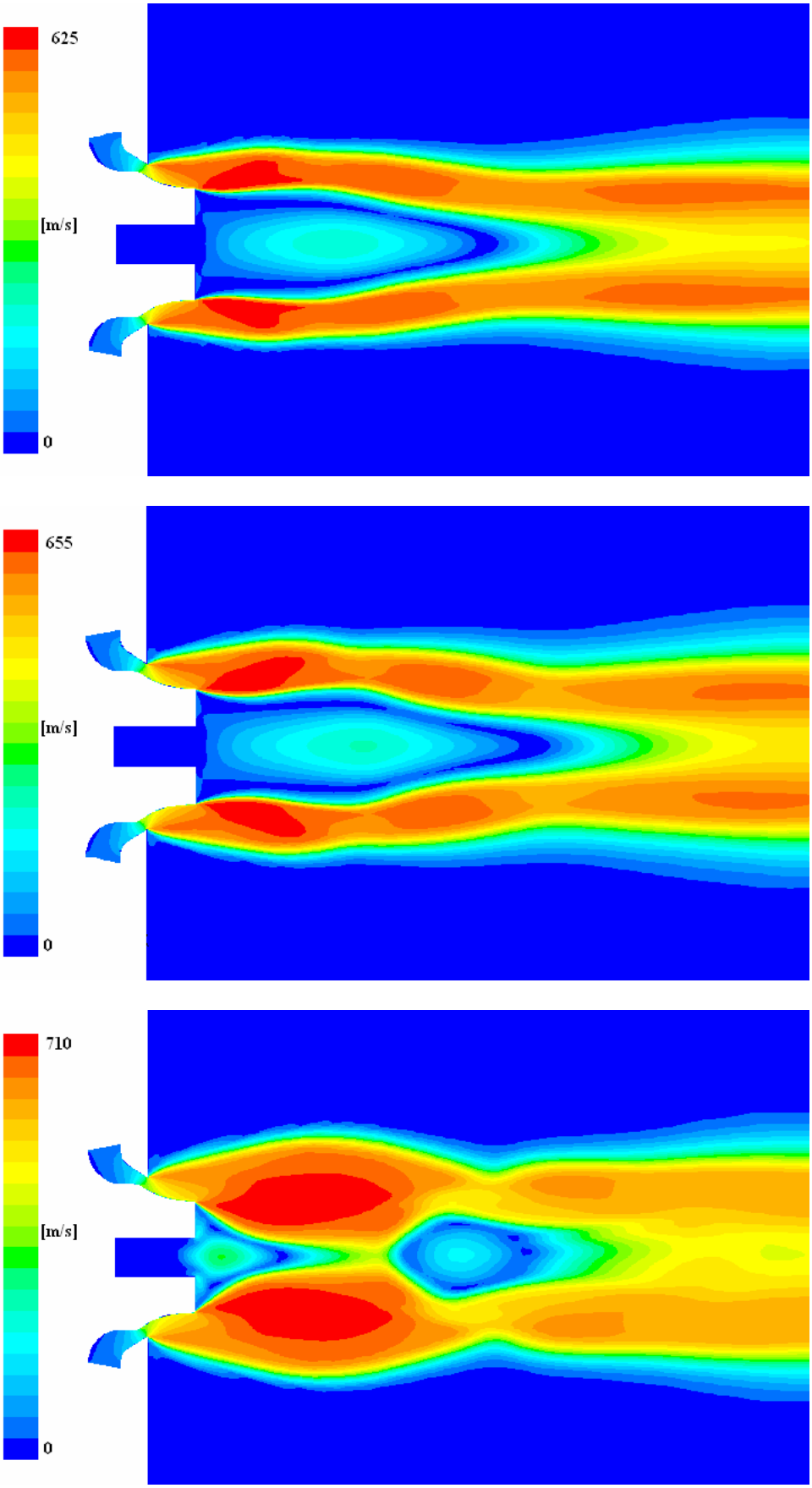


**Figure 4.17: velocity flow pattern for different reservoir pressure: a) 16 atm, b) 20 atm, c) 30 atm**

The presence of normal shock at 30 atm divided into two non communicating parts the recirculating volume. A smaller bubble could improve the primary atomization performance, however the scientific community is still arguing as to the existence of a closed wake after the melt enters the domain. Multiphase flow simulation in chapter 4.5 will give more insights on the subject.

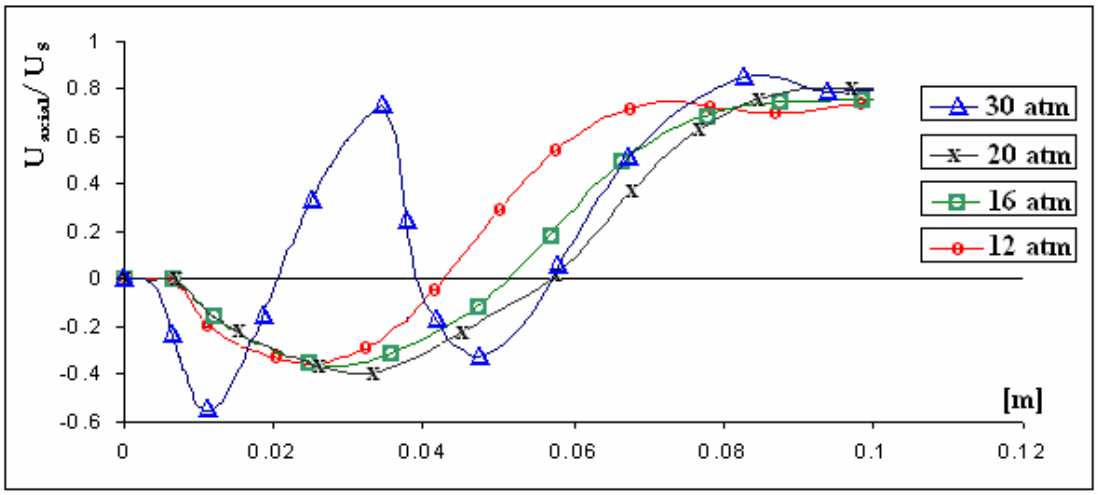


**Figure 4.18: comparison of mean axial velocity along the domain centreline for increased manifold pressure**

It is extremely important to analyze the effect of manifold pressure variation on the pressure distribution along the centreline. From an overall point of view, the consequence of the increase in operating pressure is a flow with higher Mach. With the exception of the 30 atm case (because it experiences wake closure), this correspond to a longer recirculation zone. This means that the high pressure zone (reattachment) moves downstream, as shown in figure 4.18. It could be concluded that the backflow becomes larger and weaker, so that the pressure rises up. This is not true: as shown in figure 4.19, the pressure along the axis decreases for increasing Mach, because higher operating pressures induce strong circulating flow.

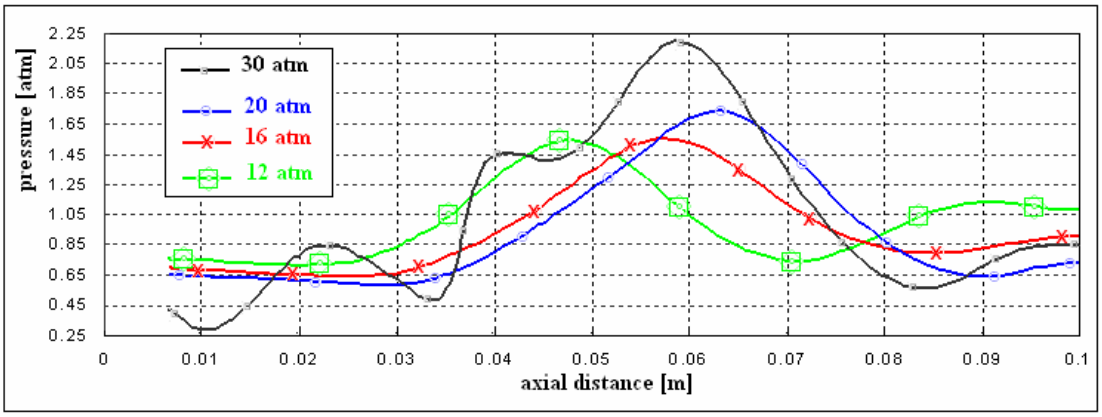


**Figure 4.19: comparison of pressure along the domain centreline**

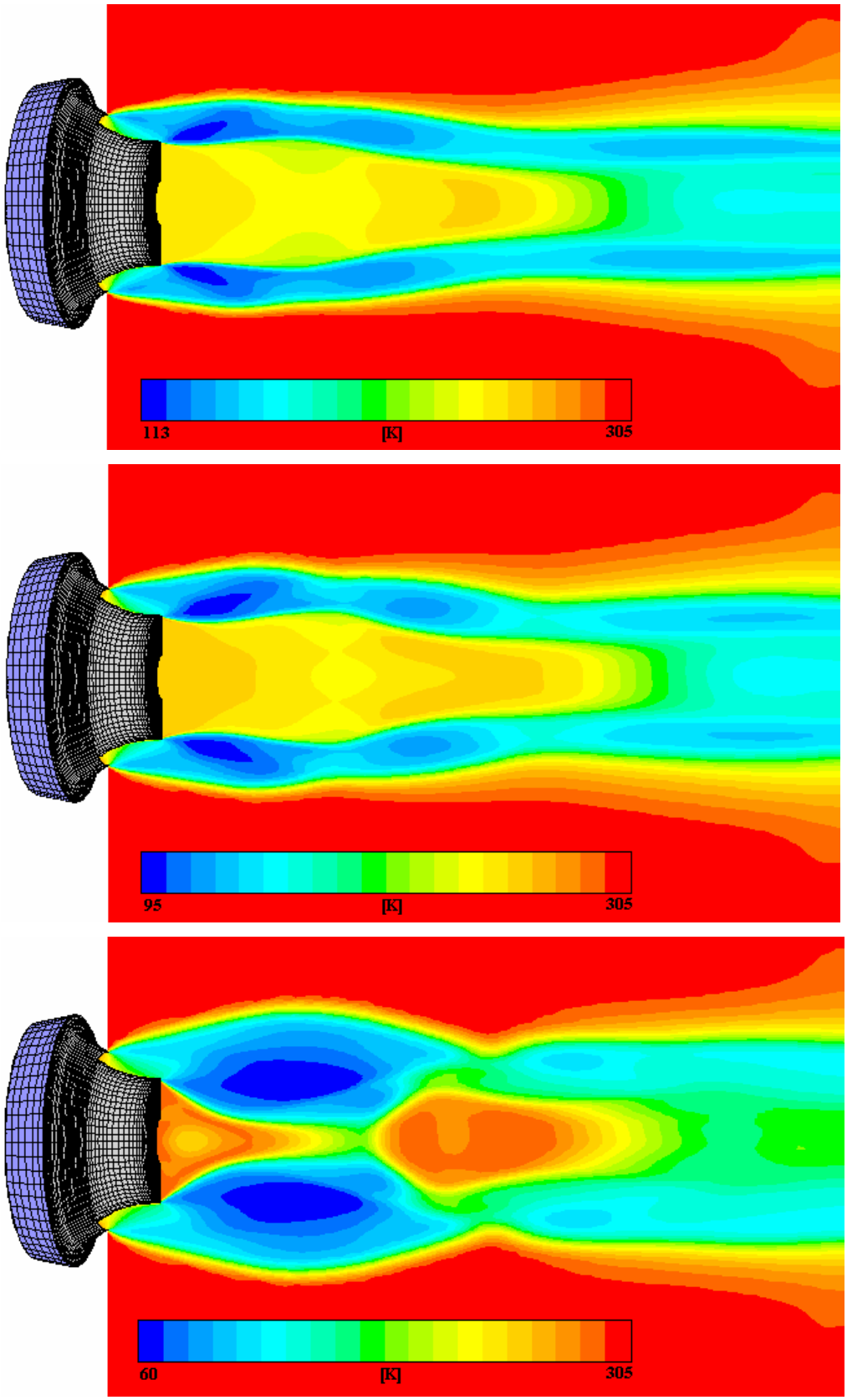


**Figure 4.20: temperature contours for different reservoir pressure: a) 16 atm, b) 20 atm, c) 30 atm**

Before the abrupt change due to the formation of a normal shock cell, the pressure within the separated flow decreases toward an asymptotic value. Finally figure 4.20 shows the

temperature evolution: higher expansion means lower temperature. For the 30 atm case, the temperature reaches 60K: this means that not only the atomization process is influenced by the higher momentum but also the droplet cooling rate and metallic structure are affected.

## 4.4 Nonaxisymmetric plug nozzle analysis

The use of a 3D simulation made it possible to investigate a nonaxysimmetric geometry. Figure 4.21 shows the characteristics of the velocity flow field. The presence of a non axisymmetric tail is still clearly detectable at the end of the simulated domain, where the velocity defect presents quatrefoil shape. Steady simulation is performed using the same parameter mentioned for the IPN in the previous paragraph.

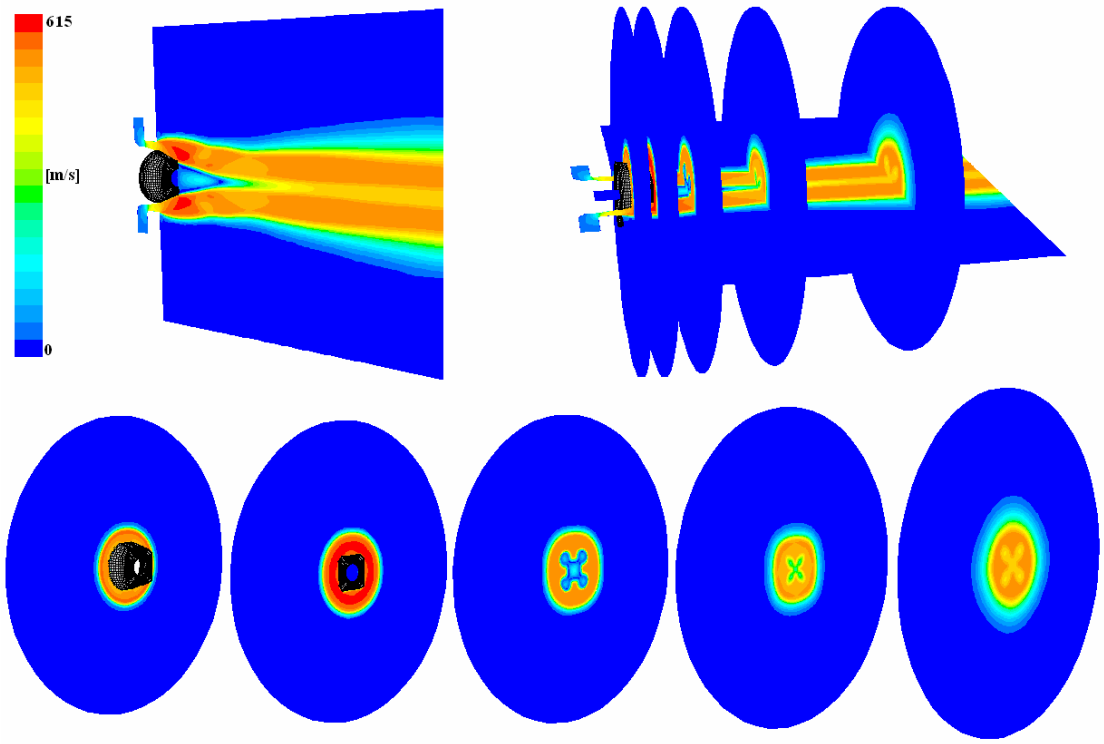


**Figure 4.21: velocity contour evolution**

The peak velocity is 6% higher than the isentropic plug (compared at the same operating pressure, 12 atm) denoting underexpanded jet behaviour. The expanded gas reaches the maximum velocity close to the end of the plug. The external side of the jet is axisymmetric and does not seem to be affected by plug geometry. Looking at the axial velocity contour in figure 4.22, it is evident that the recirculation zone is totally different compared to the isentropic counterpart. First of all, the shape is not like an hourglass but it is similar to a pyramid with quatrefoil section. Further the length is significantly reduced, less than 20 mm instead of 40 mm. The reattachment point moved closer to the feeding tube tip: this

could affect the length of liquid jet core, forcing its disruption near to the exit hole. The maximum negative speed in the recirculation bubble is 18% lower than in the axisymmetric configuration. The inner velocity on the axis wake is comparable with the previous case, close to 450 m/s, but it is reached at a shorter distance from the plug (55 mm instead of 60mm) indicating faster transfer of momentum for atomization purpose.

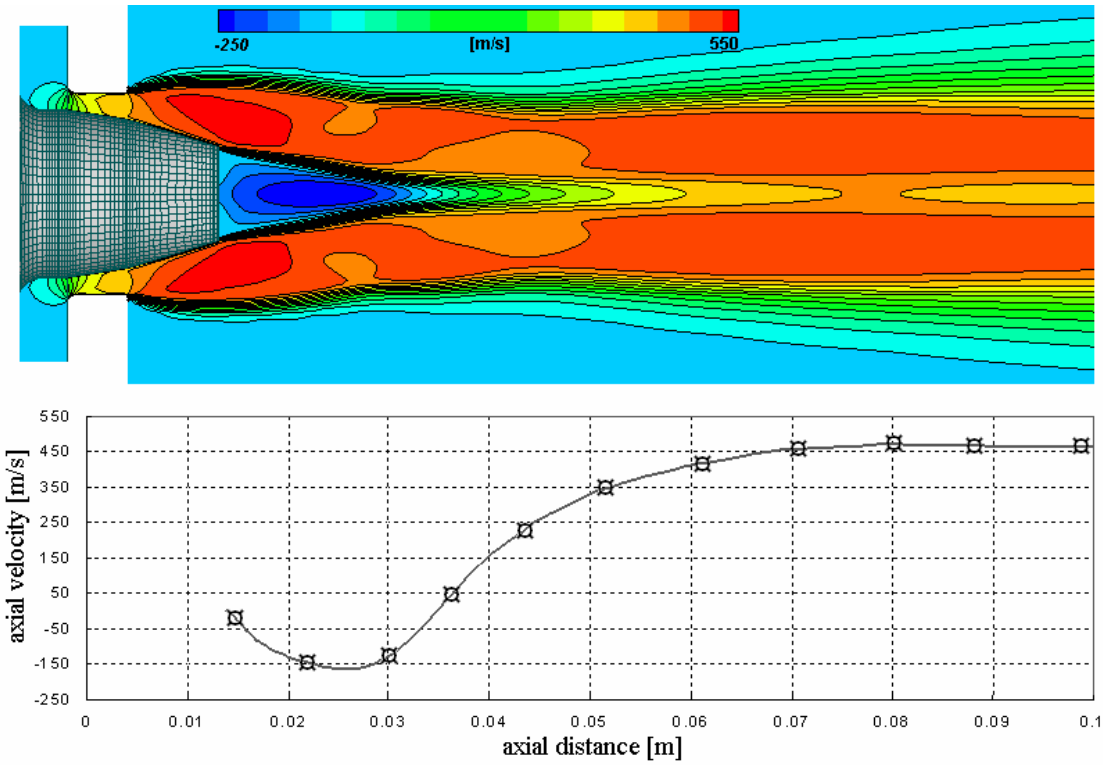


**Figure 4.22: axial velocity component behind plug separation**

The packed isovalue lines at the nozzle exit denote a steep velocity gradient in the initial portion of the shear layer. The spreading rate is analogous to the isentropic plug: it is initially smooth and then becomes large in the wake, where the supersonic effect is weaker.

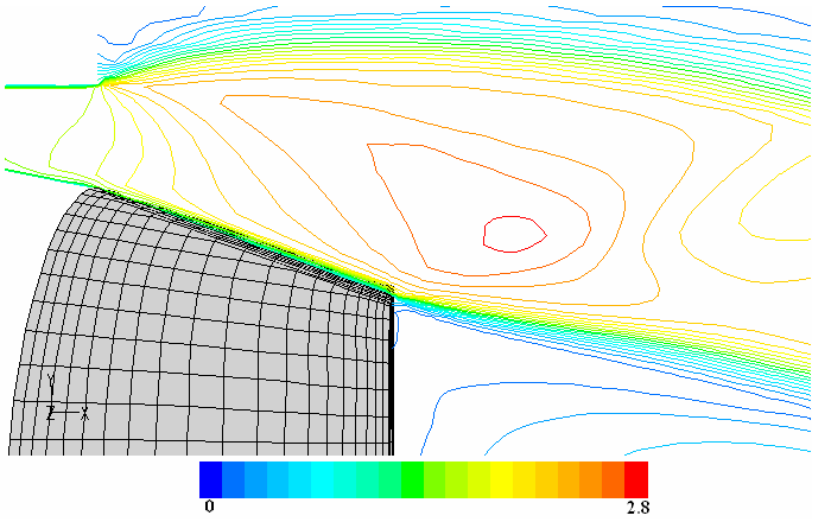


**Figure 4.23: Mach isovalue lines in base region**

A blow up of the isovalue Mach lines is reported in figure 4.23. The lines at the shroud end spread quickly in the still air. Surprisingly, also the lines departing from the tail edge do not remain packed: this means that there is no lip shock influence. Also in this case the recirculating fluid is far away from the sonic condition: as plotted in figure 4.24, the peak Mach value = 0.5.

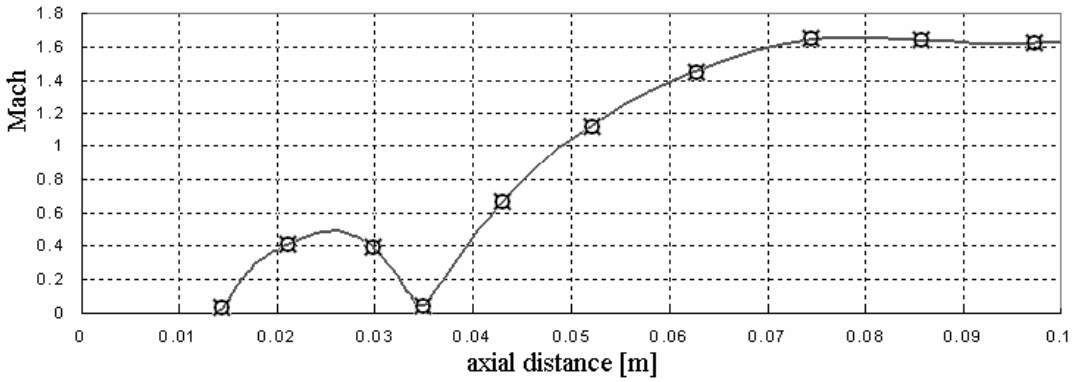


**Figure 4.24: Mach plot along domain axis**

The supersonic length extends in the wake outside the simulated domain, reaching the maximum value (≈1.6) close to the reattachment point, as for the axisymmetric geometry.

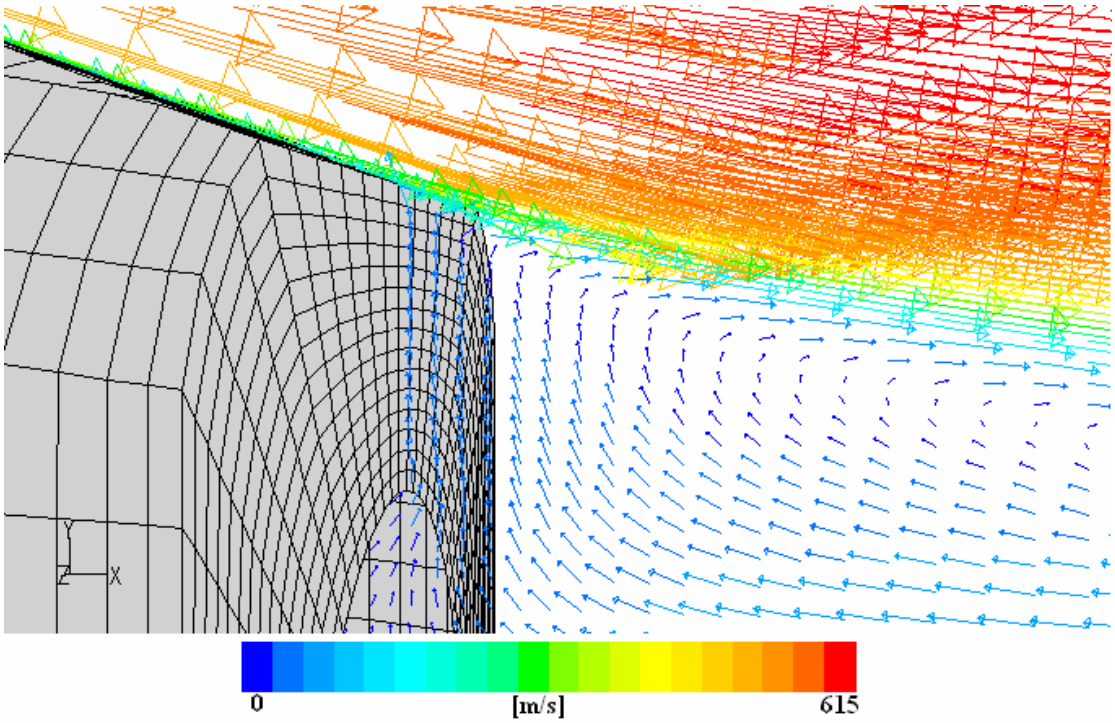


**Figure 4.25: velocity vector in base region**

Velocity vector organization close to the base edge is illustrated in figure 4.25: the turning angle is higher than 90 degrees and, immediately, the fluid parcel is accelerated by the incoming nitrogen. The radial path is considerable smaller than the isentropic case.

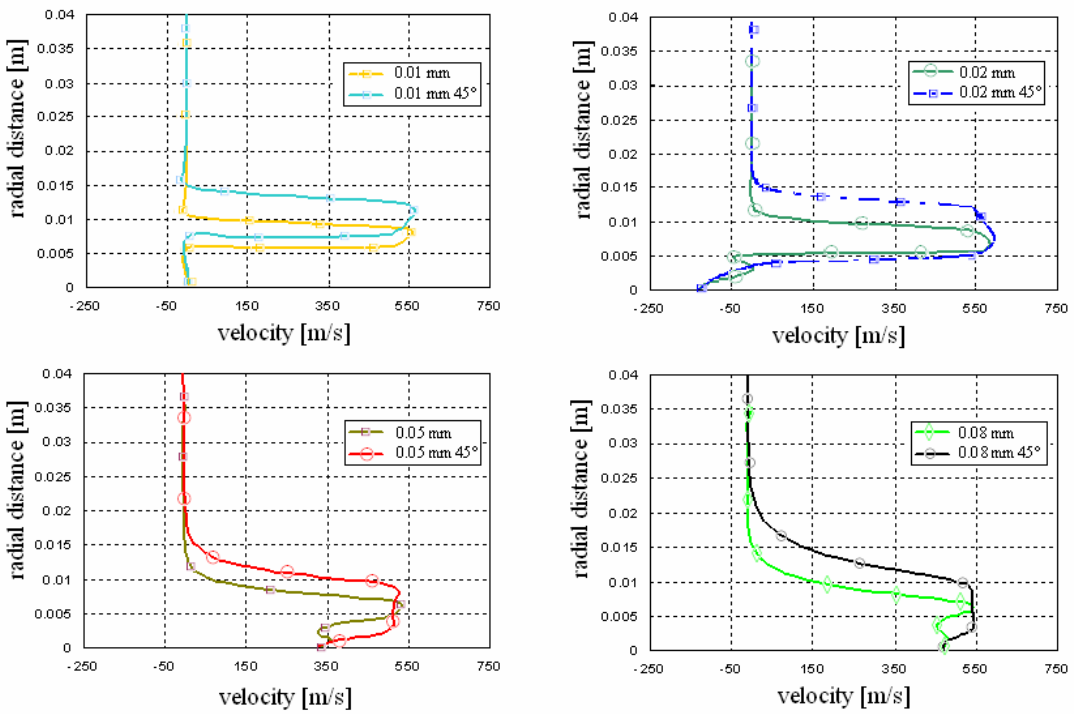


**Figure 4.26: axial velocity profile at different location**

Due to the particular shape of the nozzle, two planes have been considered to analyze the velocity profiles: the first is the symmetry plane while the second is obtained by rotating the symmetry plane by 45 degrees around the chamber axis.

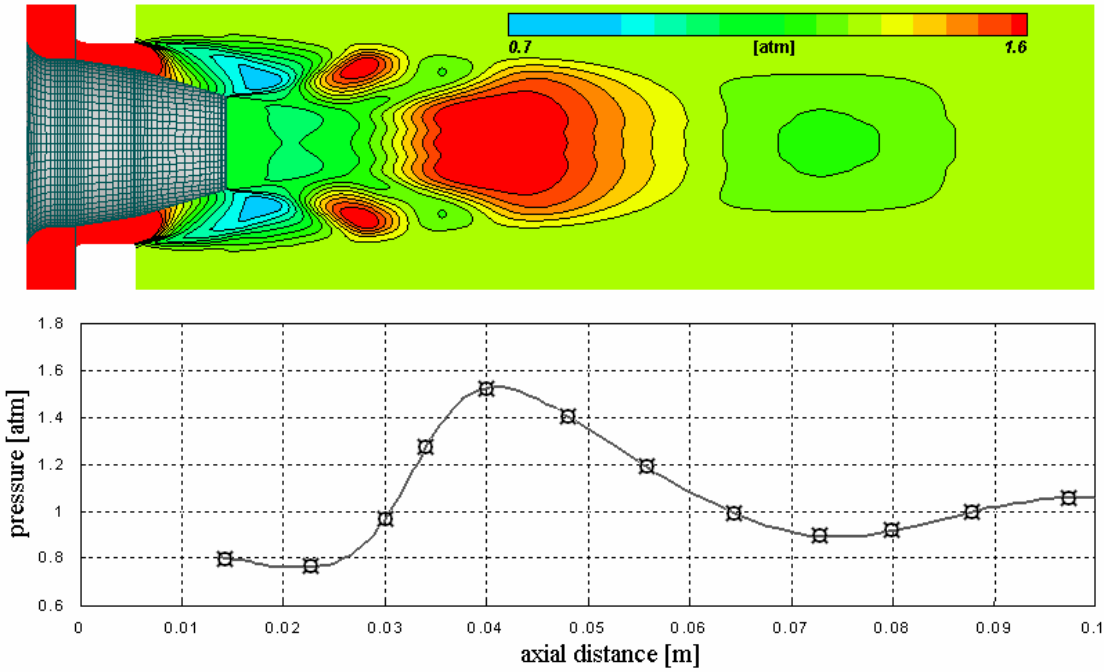


**Figure 4.27: pressure distribution behind plug separation**

Figure 4.26 presents the results at the different sections: for all the cases, the high speed layer on the 45 degree plane is thicker denoting higher spreading rate of the mixing layer. Peak velocity and velocity defect are almost identical on the two planes and resemble the

isentropic case in terms of values.Pressure contours and their plot along the domain axis are presented in figure 4.27. The pressure distribution within the recirculating flow is reasonably flat and this match experimental observation. The maximum pressure reached at the stagnation point is about 1.55 atm (as for the axisymmetric geometry), while the second shock cell is absent (or very weak) because the gas matches atmospheric condition at the domain exit.

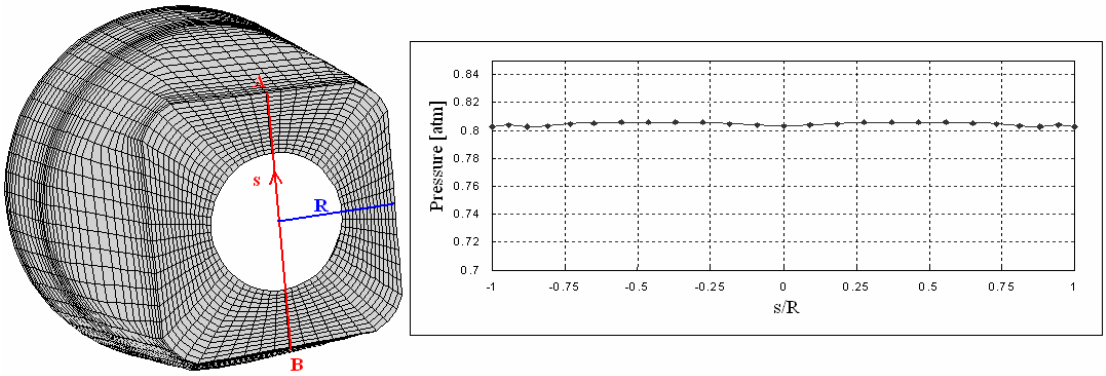


**Figure 4.28: base pressure distribution for nonaxisymmetric plug nozzles**

Figure 4.28 presents the pressure distribution on the plug base: it is almost flat but slightly higher than that for the axisymmetric plug shown in figure 4.15. This can be easily explained looking at the velocity plot along the centreline for the two cases: the backflow velocity for the isentropic geometry is higher so that a stronger circulating flow is induced. From another point of view, the expansion at the base corner is weaker for the nonaxisimmetric case because the flow undergoes a previous expansion (leaving part of its energy) at the boattail junction.

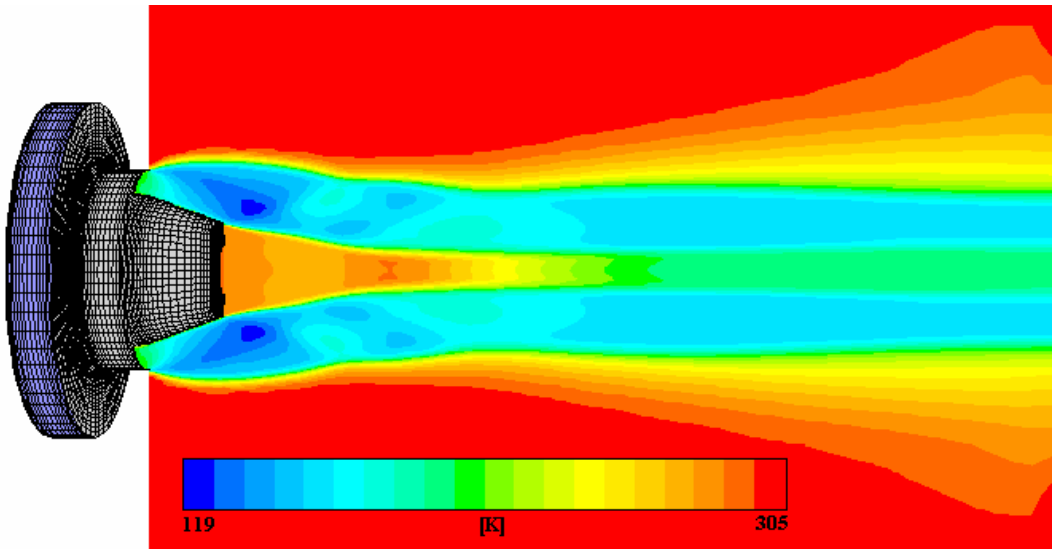


**Figure 4.29: temperature contour for nonaxisymmetric plug**

Figure 4.29 shows that expanded flow reaches very low temperatures, around 120 K: as for the isentropic case, the droplets removed from the melt stream experience extremely rapid cooling, which allows them to reach a suitable microstructure for high performance applications.

## 4.5 Unsteady analysis

Supersonic base flow has been considered until yhr 1990's as steady flow: while the subsonic axisymmetric free shear layer presents vortex shedding phenomena no evidence was found in the supersonic case. The scenario has been clarified by Herrin and Dutton [12]who proved the unsteady nature of the flow at high speed. When Mach number <0.95 the unsteady free shear layer roll-up is driven by Kelvin-Helmholtz instability. The recirculating zone contains small vortices while large coherent structures move downstream in the wake. At the transonic condition, the bi-dimensional instability mode faces the presence of shock waves. When the flow became fully supersonic the scaling parameter became the convective Mach number ($M_c$) defined as:

$$\frac{U_1 - U_2}{c_1 - c_2} \tag{4.1}$$

where U stands for the average velocity, c the speed of sound and subscripts 1-2 indicates the jet and recirculation bubble respectively. According to equation 4.1, for the 12 atm case, $M_c \approx 0.75$. Simon et al. [14] carried out an exhaustive numerical analysis on the compressible mixing layer past an axisymmetric bluff-body: they showed that Kelvin Helmholtz instability is inhibited when $M_c > 0.6$. Simulation schemes are summarized in table 4.3.

| | |
|---|---|
| Solver | Segregated |
| Geometry | 3D – isentropic plug nozzle |
| Time | Unsteady – time step $10^{-6}$ |
| Flow model | Single phase (without melt) |
| Turbulence model | LES |

**Table 4.3: simulation schemes**

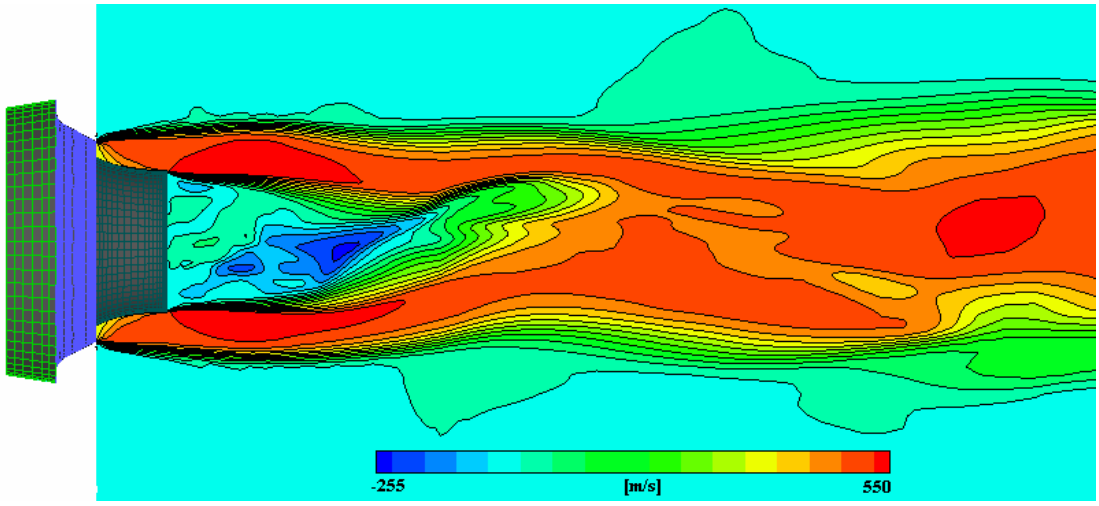


**Figure 4.30: instantaneous velocity contour for isentropic plug.**

Figure 4.30 shows the instantaneous contours of axial velocity for the isentropic geometry. Flow instability is evident compared to figure 4.10. The turbulence model adopted for this simulation is LES, the most appropriate for flow unsteadiness. The end of the recirculation zone experiences ample movement while the flow close to the plug appears almost steady. This can be explained by the particular vortex structure. In fact, when $M_c$ is high, the three dimensional linear stability analysis shows that oblique waves are more amplified than two dimensional (responsible for Kelvin-Helmholtz instability): because of this, the helical pairing is inhibited and the vortex pattern is made up of staggered Λ vortices ( and successively "hairpin vortices").

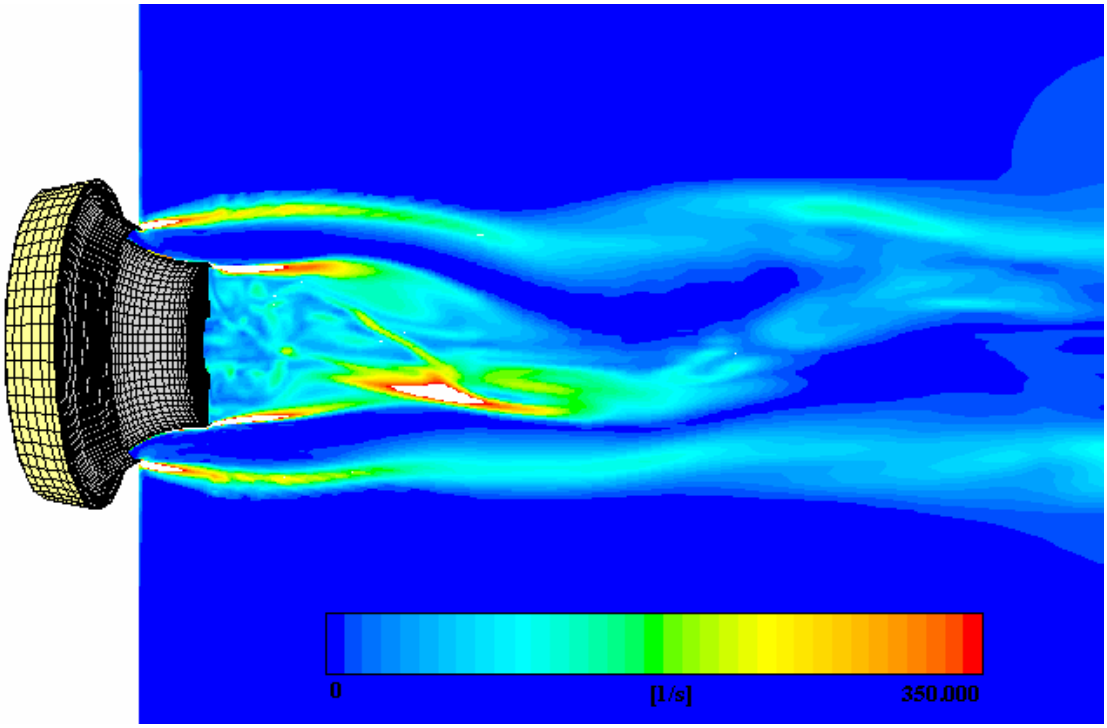


**Figure 4.31: vorticity contour for isentropic plug**

Those eddies are three dimensional and merging does not take place according to the classical pairing scheme, instead, they wrap into braids. It is very hard to visualize a hairpin head because it is not stretched appreciably. As the convective Mach decreases (close to the reattachment point) coherent structures (similar to the shedding pattern for subsonic flow) can be clearly identified. Figure 4.31 illustrates an instantaneous distribution of vorticity. The shear layer becomes unstable at a distance of 1 diameter from the base and successively rolls-up in the downstream region. The shroud mixing layer presents similar behaviour. Small vortices are predicted in the recirculation region: Simon et al. [14] observed similar structures in the experiments past an axisymmetric trailing edge. It is important to note that, for compressible flow, the baroclinic term (Vr X Vp)/$r^2$ plays an important role in vorticity production: in this case, the pressure gradient near to the reattachment point is not aligned with the radial density variation across the shear layer. This term is of the same order of stretching and tilting components.

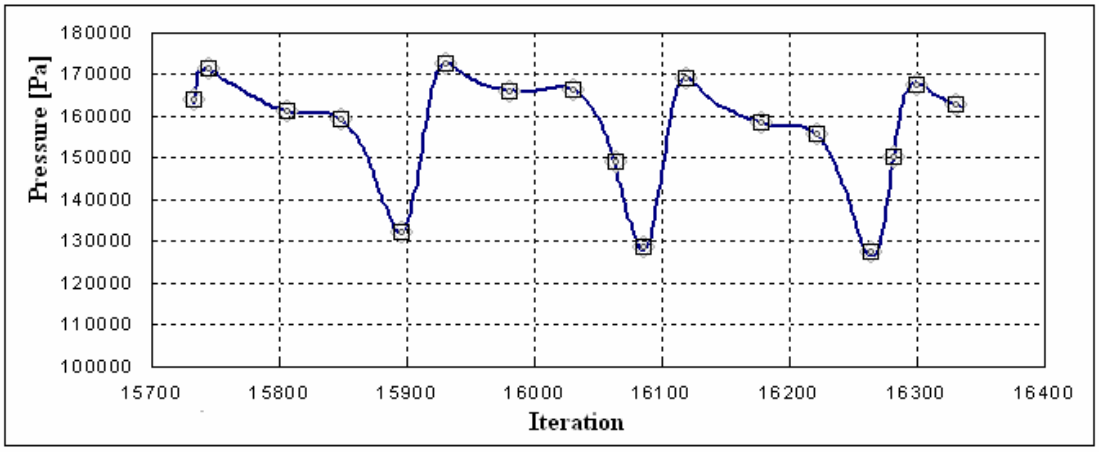


**Figure 4.32: pressure oscillation at reattachment point.**

Pressure was monitored at the reattachment location and the results are reported in figure 4.32. As expected, pressure oscillates following the movement of the separated region. This flapping behaviour has been identified also in [14] and is caused by the convection of large eddies along the mixing layer. Also, for the non axisymmetric geometry, time dependent simulation shows unsteady features. Figure 4.33 demonstrates the asymmetry of velocity contours, especially is the separated bubble. However, the oscillations are also extremely reduced because of the smaller size of mixing layer: the tapering angle of nozzle surface enhance free shear layer interaction. The jet core recovers the velocity defect quite fast so that, immediately after the reattachment, the inner zone velocity is close to the top speed. This might give an important contribution to the atomization of large droplets usually situated near the axis.

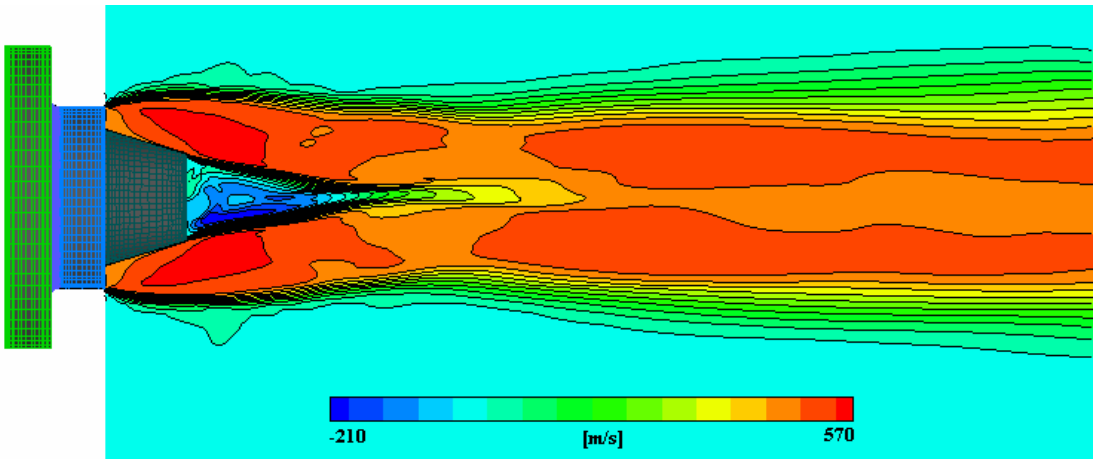


**Figure 4.33: instantaneous velocity contour for non axisymmetric plug.**

Vorticity contours in figure 4.34 resemble the isentropic case. The values are of the same order and both large and small coherent structures are captured. The small vortices seem to have a slightly higher vorticity level close to the base. The external mixing layer (generated by separation at shroud tip) presents a reduced interaction with the plug wake.

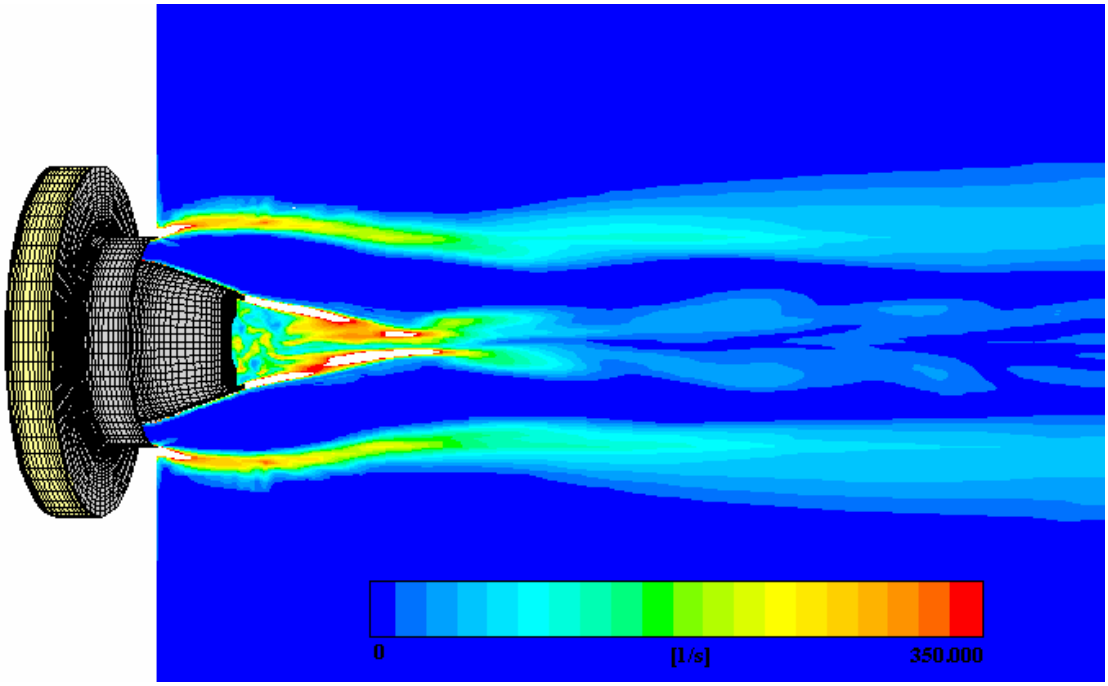


**Figure 4.34: vorticity contours for non axisymmetric plug.**

## 4.6 Multiphase flow

The last effort of this analysis was the simulation of the fully 3D interactions between melt and gas. The initial step was a steady state analysis to evaluate the basic evolution of the flow field. The special approach used to carry out those simulations is an Euler-Euler model (the different phases are treated mathematically as interpenetrating continua) known as VOF, Volume of Fluid [15]: two fluids (gaseous nitrogen and liquid metal) are tracked

into the atomization domain. It is important that the purpose of this model cannot go beyond the primary atomization stage, because the necessary grid resolution involved in secondary atomization is beyond the current computational power. Just, for example, in order to simulate a sphere, it is mandatory to have at least 10 nodes on the diameter: this, for a 20 μm droplet, means grid cell size of microns (100 times smaller than the average cell used in the present grid, in other words a 100 million cells grid). Despite of secondary break-up the primary break-up is not modelled but resolved. The ligaments and large piece of liquid metal (2nd phase) are pinched off by the interaction between the two fluids. Surface tension is reformulated into equivalent volume force and added to the momentum equation while the volume fraction in each cell is determined resolving transport equation (VOF model is available in Fluent). The simulation schemes are summarized in table 4.4.

| | |
|---|---|
| Solver | Segregated |
| Geometry | 3D – isentropic plug nozzle |
| Time | Steady /unsteady $10^{-6}$ |
| Flow model | multiphase – VOF |
| Turbulence model | RSM |

**Table 4.4: simulation schemes**

The liquid melt properties are summarized in table 4.5: they are considered as representative for a wide range of steel.

| property | value |
|---|---|
| Cp | 680 [J/kgK] |
| ϱ | 7000 -0.1T [kg/m$^3$] |
| viscosity | $1.789*10^{-5}$ [kg/m-s] |

**Table 4.5: thermo-physical properties of the melt**

### 4.6.1 Axisymmetric geometry results

Figure 4.35 shows the melt stream shape for a metal flux of 0.20 kg/s (the average value measured on a similar configuration in the BSA plant). The recirculating gases (sketched with the two green arrows) push on the liquid, forming an upside-down mushroom structure (or miniature fountain as stated in [16]): the symmetry is the result of the steady state condition. The melt is "sucked" (in reality, the atmospheric pressure persisting on the melt in the tundish pushes toward the low pressure area) by the sub atmospheric pressure zone. The melt core appears untouched, surrounded by recirculating flow organized in a vortex ring.

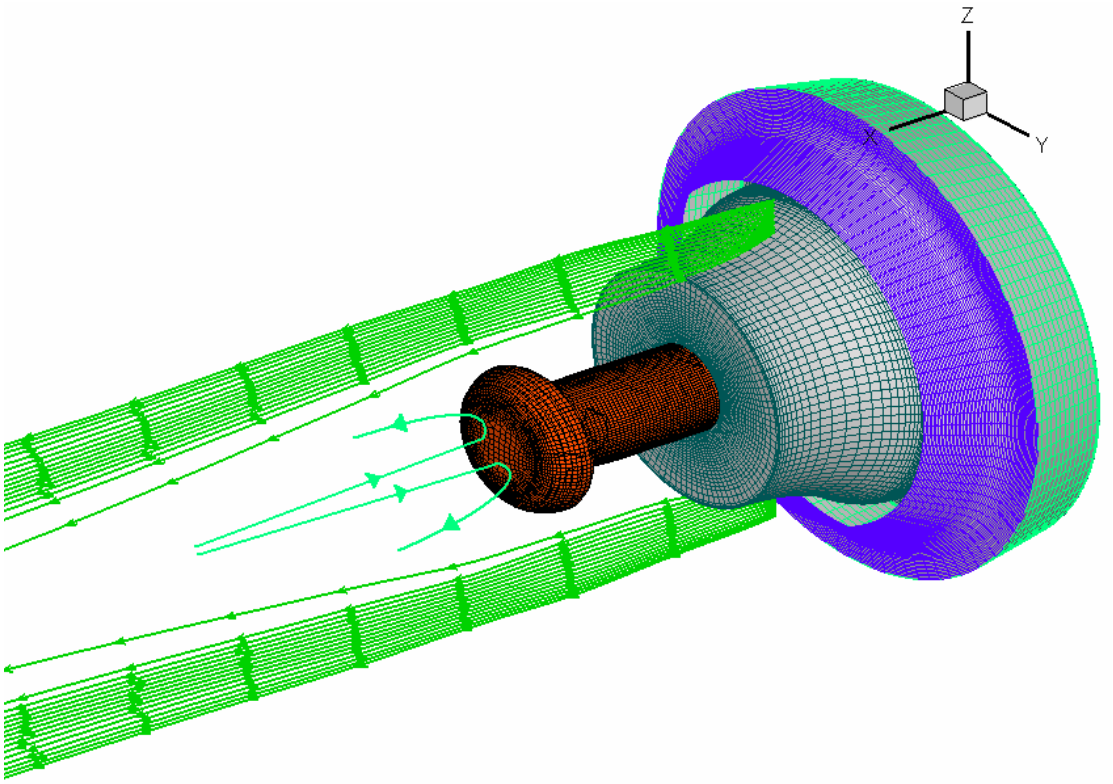


**Figure 4.35: steady melt stream, isosurface volume fraction = 1**

The blow up image in figure 4.36 shows in detail the gas/liquid interaction. The liquid melt turns backwards, driven by separated flow, and part of it reaches the nozzle tip and films radially. The green colour means that the melt fraction content in the grid cell is less than 1. Only a small quantity of melt is pinched off by the expanded gases (the highlighted light blue zone). This has been considered for many years as the perfect working condition.

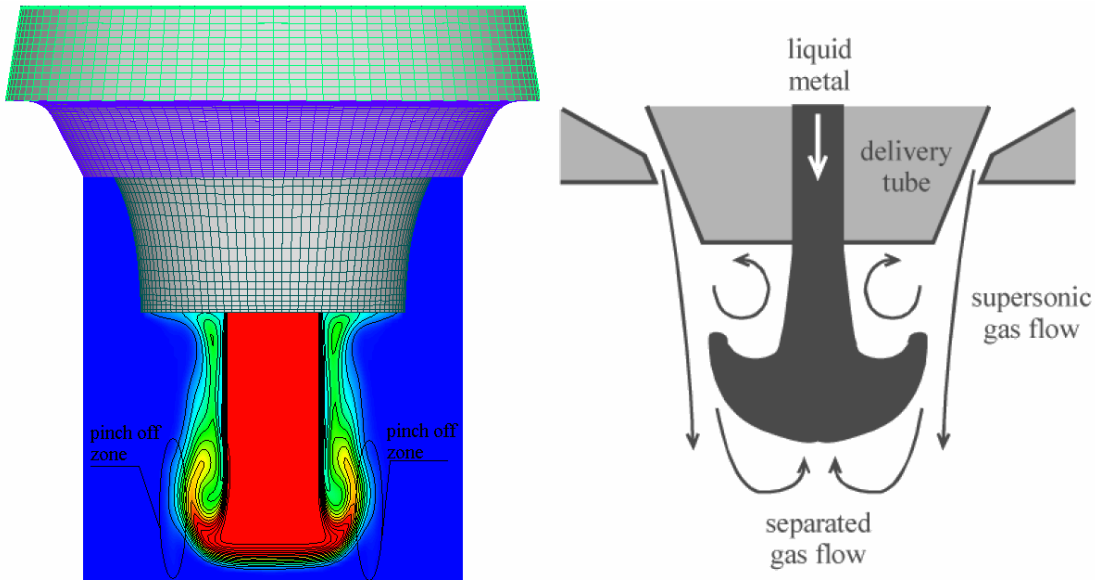


**Figure 4.36: gas- liquid interaction**

The gas flow is deeply affected by the presence of the melt. Figure 4.37 presents the axial velocity contour. The shock structures that characterize figure 4.6 have disappeared: the

trailing shock did not arise because the presence of the melt core works as the nozzle spike thus avoiding the expansion at the truncation edge. The internal shock remains but its position changes. Also the recirculation zone experienced extensive changes.

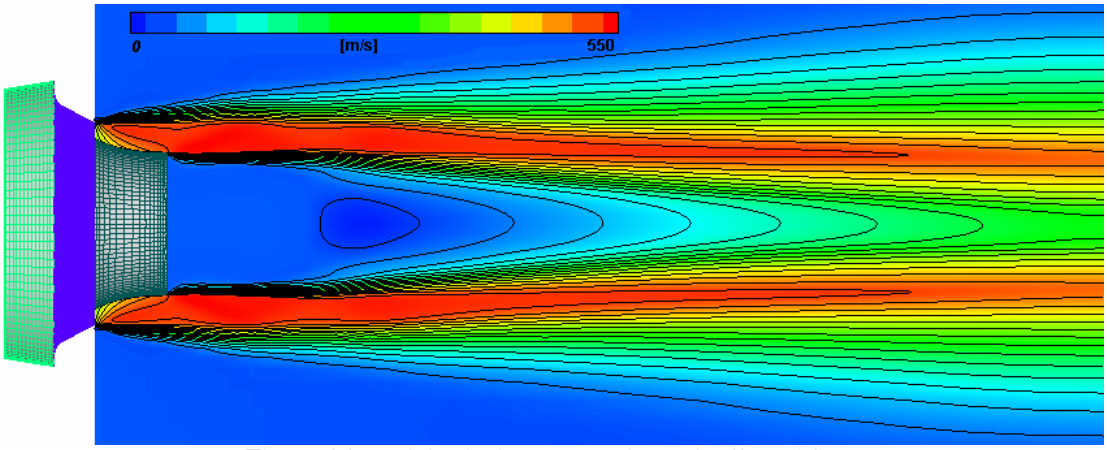


**Figure 4.37: axial velocity contour for melt affected flow**

A useful comparison between gas only and melt affected flow field is given in figure 4.38. The axial velocity along the domain centreline is plotted for both cases. It is evident that the velocity in the wake core is seriously reduced. This important aspect means that a droplet along the centreline would experience low aerodynamic force and consequently inefficient break-up compared to the ones located at a longer distance from the chamber axis. The separated region is also smaller, less than 50%: the maximum backward velocity is about 180 m/s slower. The real momentum that the nitrogen exerts on the melt is much smaller than what could be calculated during measurements on a gas only running tower.

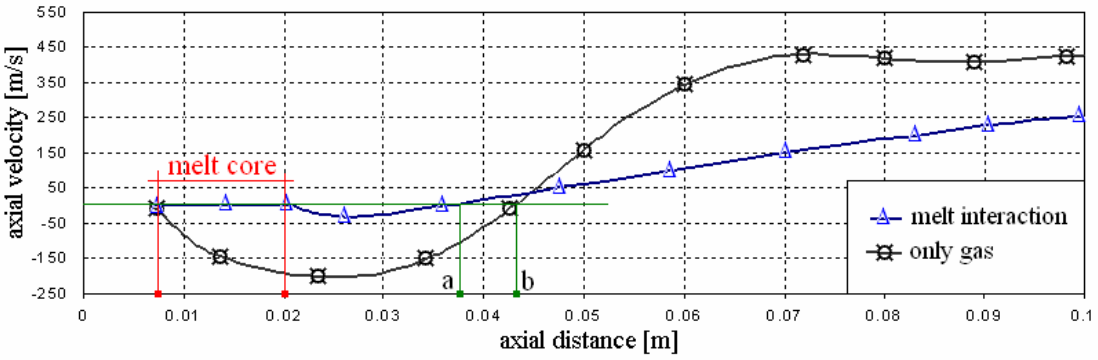


**Figure 4.38: axial velocity plot along domain centerline**

According to the experiments Lasheras et al. [17] obtain the following expression to evaluate liquid core length in a coaxial atomizer:

$$\frac{L}{D} \cong \frac{6}{\sqrt{M}}\left(1-\frac{U_l}{U_g}\right)^{-1} \tag{4.2}$$

where D is the base diameter and M the momentum flux ratio per unit volume defined as:

$$M = \frac{\rho_g U_g^2}{\rho_l U_l^2} \tag{4.3}$$

The simulation result is 12.50 mm core length and this is in good agreement with (4.2), which would giv,e for the current case, 13.20 mm.

The temperature gradient inside the melt is not very high: less than 10 K distinguishes the incoming melt from the filming one. On the contrary, high gradients, are located on the periphery. The stratified black lines in figure 4.39 denote a gradient of 50 K.

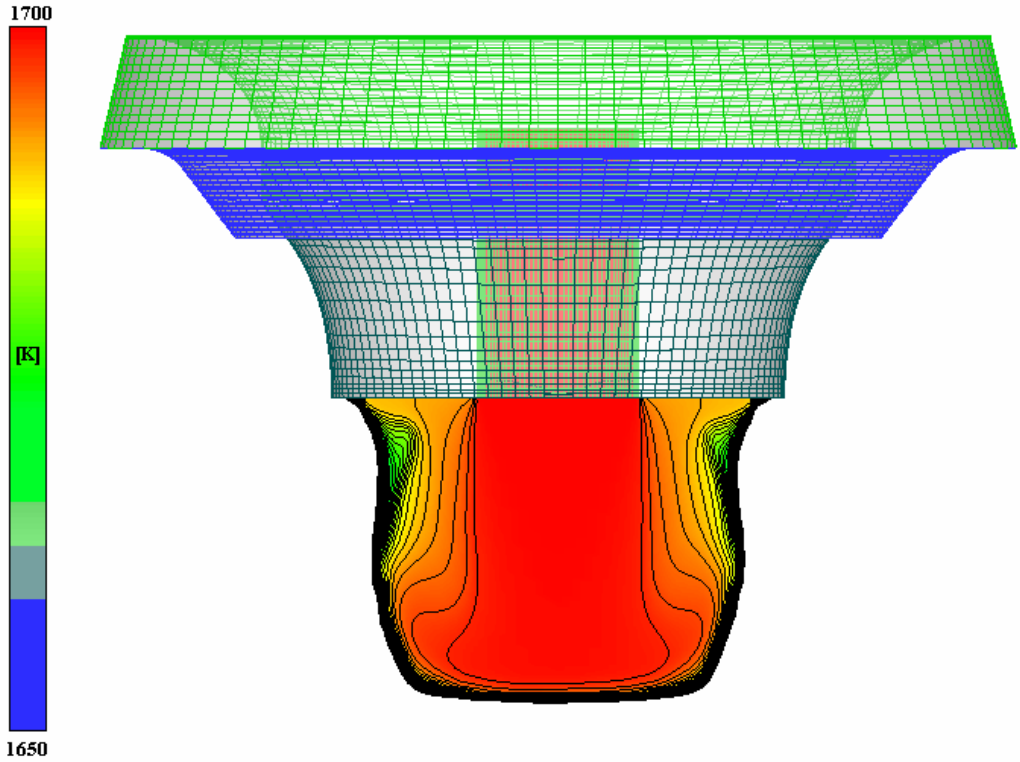


**Figure 4.39: melt temperature contour**

As the melt core is reduced, the cooling process becomes very rapid. However, in the operating conditions showed above, there is no risk of melt freezing near the delivery tube. However, steady results look too different from what is observed (chaotic behaviour) in the atomization tower during process running: unsteady analysis is necessary to evaluate all the phenomena involved in the atomizing process. Three different cases have been simulated, in order to disclose the influence of all key parameters. In the first and second simulation, the melt stream is limited to 0.05 kg/s and 0.1 kg/s respectively. In the third case, the melt flow rate is just the result of pressure boundary conditions: it represents exactly the operating condition of an industrial atomizer.

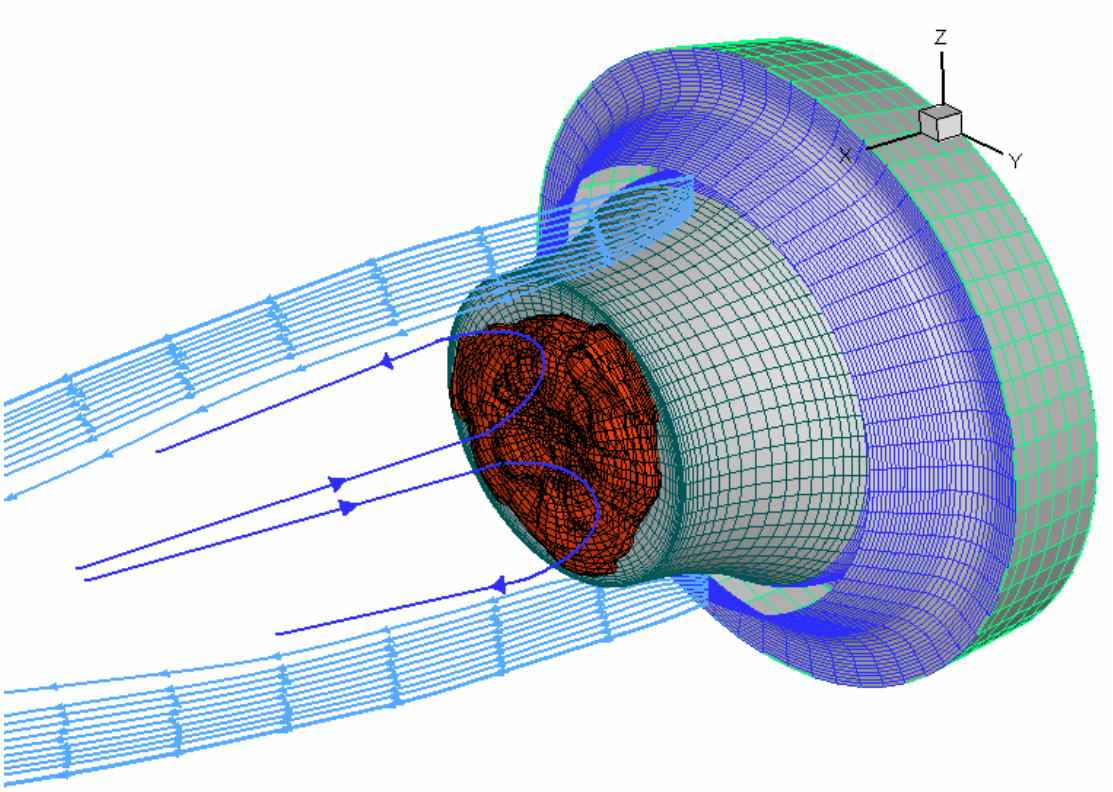


**Figure 4.40: unsteady melt stream for 0.05 kg/s, isosurface volume fraction = 1**

Figure 4.40 shows the melt distribution on the nozzle tip for the 0.05 kg/s case. In this case, the liquid sticks perfectly on the surface and moves radially to meet the high speed gases on the base edge. The momentum of the backward gas flow (sketched with dark blue arrows) is enough to face the melt stream. Considering that the gas flux (sketched as light blue streamlines) is 0.33 kg/s, the gas to liquid mass flow ratio would be 6.6, extremely far from industrial practice (≈ 1-2). The axial velocity contours in figure 4.41 are slightly affected: the shock pattern is the same as for gas only flow.

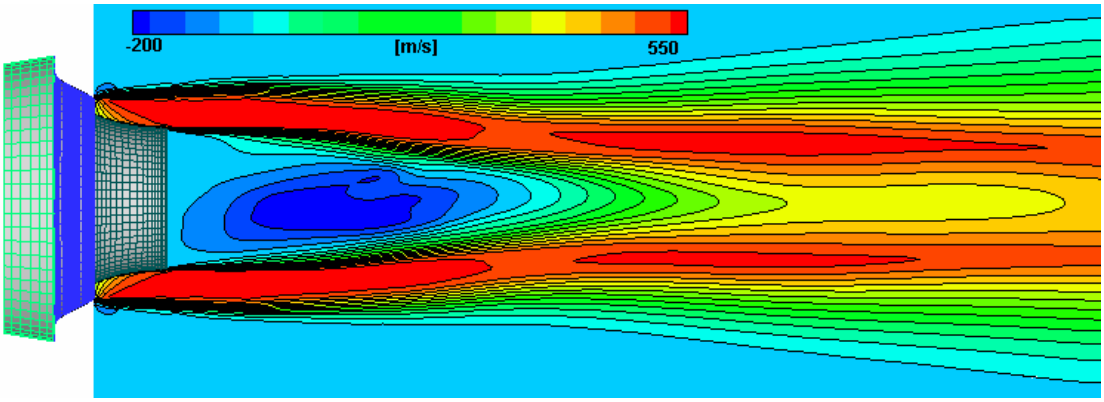


**Figure 4.41: axial velocity contour**

Due to the thin layer, the melt experiences an immediate cooling close to the exit. As reported in Figure 4.42, close to the face edge the temperature decrease is 50 K. It is

commonly accepted practice to overheat the liquid metal by 100K above melting point: in this situation, freeze-off could easily have happened. In terms of process stability, the condition simulated should be avoided. As anticipated, the melt flow rate has been imposed: in order to have it in real scale, we should reduce the inner diameter of the feeding tube. Consequently the melt core would be smaller (as well as its thermal capacity) so that the cooling process would be even faster.

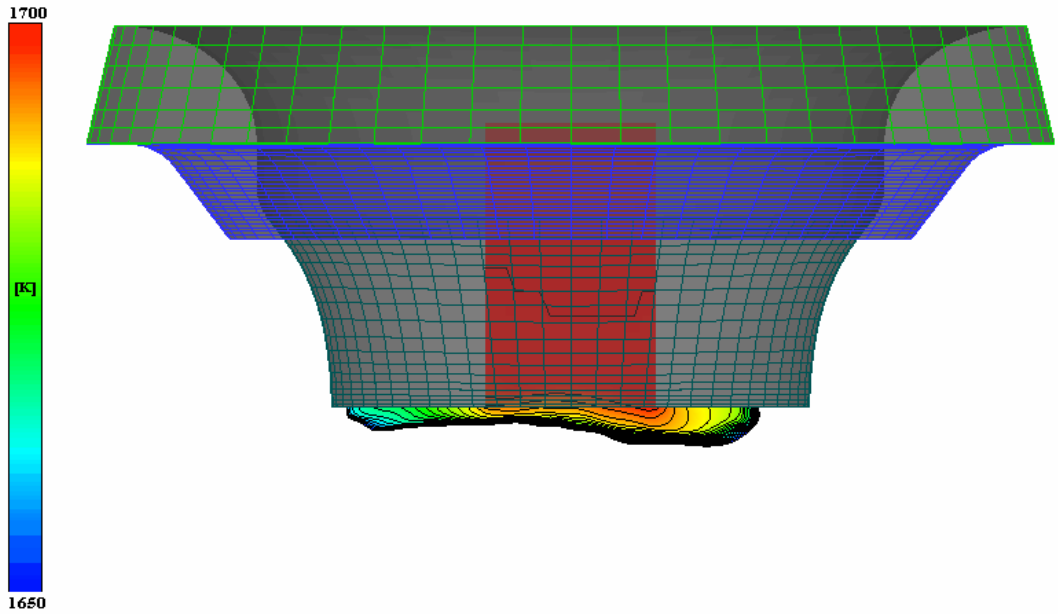


**Figure 4.42: melt temperature contour**

The second unsteady case simulated has a melt flow rate of 0.1 kg/s. the 3D image of liquid configuration is reported in figure 4.43. The melt is still filming on the tip surface but the layer thickness increased. The energy of the reverse flow is still strong compared to the liquid flux. The gas to melt ratio is 3.3, still far from standard application. The melt layer is thicker and presents peaks and valleys. The distribution on the tip is not uniform denoting preferential directions. This is the result of azimuthal pressure gradient generated by unsteady movement in the recirculating zone. The melt begins to turn before reaching the face edge so that liquid tongues are visible inside the mixing layer. The melt is organized in a "crown" structure: this is in good agreement with the shape of frozen material usually found on the ceramic nozzle after the atomization process. Also in this case primary, break-up behaviour is characterized by very short intact liquid core (usually referred to as prompt break-up). The liquid momentum is well below the one of forcing separated gas (sketched as blue arrows). Primary atomization is not caused by the amplification of the most unstable wave but from a direct large pinch off of large liquid droplets: high speed gas impact pulls them out in the jet core. Prompt break up has been visualized by Lasheras

[17] for gas to melt momentum ratio higher than 20: in this 0.1 kg/s simulation, the momentum ratio is 350, so that the results are consistent with experimental findings.

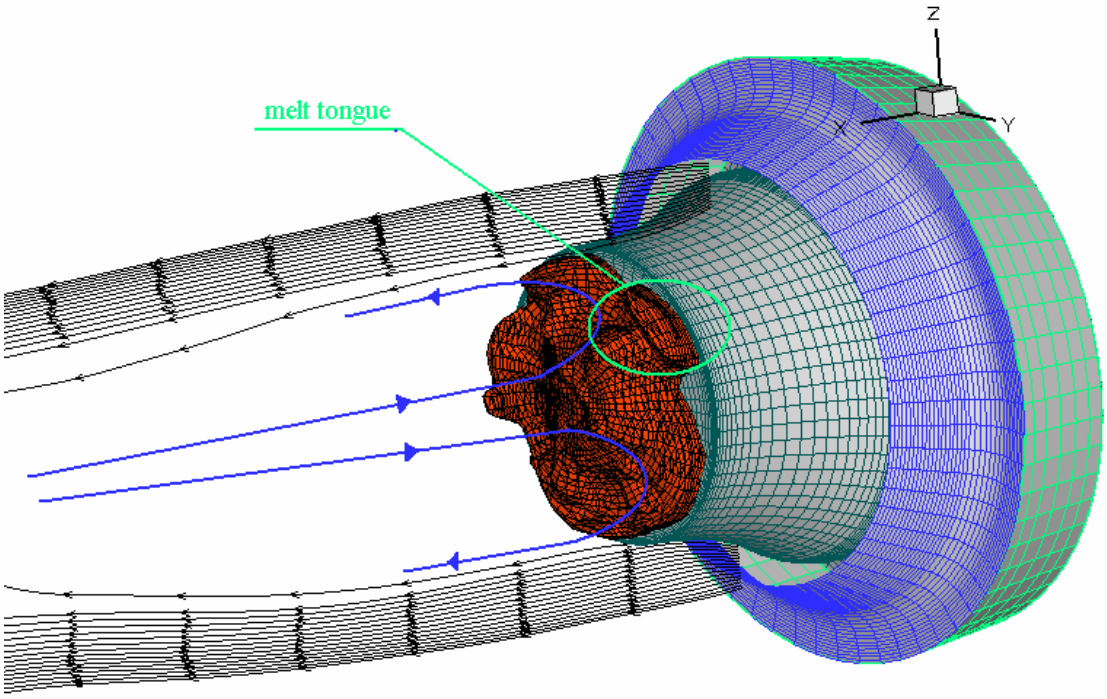


**Figure 4.43: unsteady melt stream, isosurface volume fraction = 1**

The high speed streamlines show weak asymmetry. Looking at the velocity contours in figure 4.44, the flow pattern appears affected by the melt presence. The recirculation zone is elongated and unstable features are evident. However the mixing layer still merges at the rear stagnation point: this means that the mass loading (i.e. ratio of dispersed phase to continuous phase mass flow) effect is not significant.

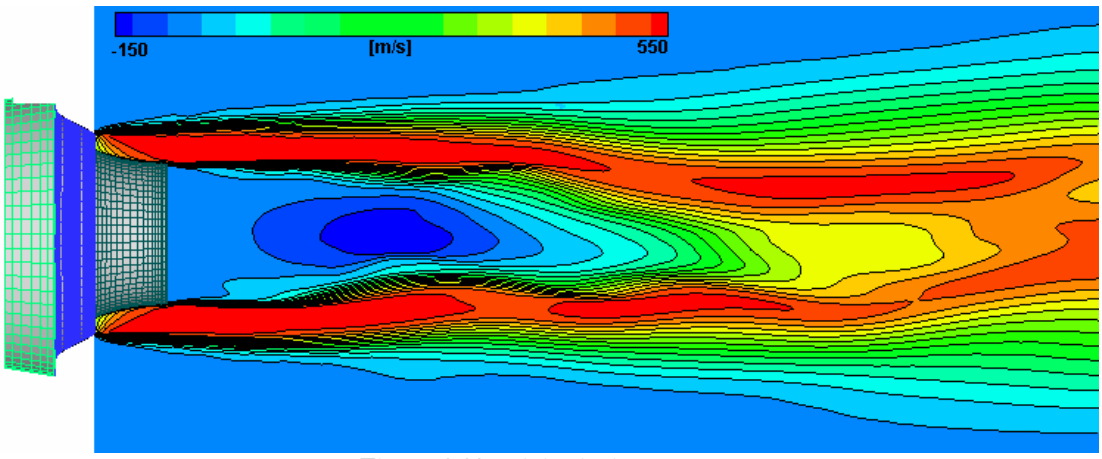


**Figure 4.44: axial velocity contour**

The cooling process is still evident on the radially flowing metal in figure 4.45. The temperature gradient on the tip is almost 25 K: this is reduced compared to the previous

case because of the higher thermal inertia associated with the higher mass flow rate. However, when the process ends, the last layer of melt on the tip is easily frozen, creating the above mentioned crown structure on the circumference of the used ceramic plug.

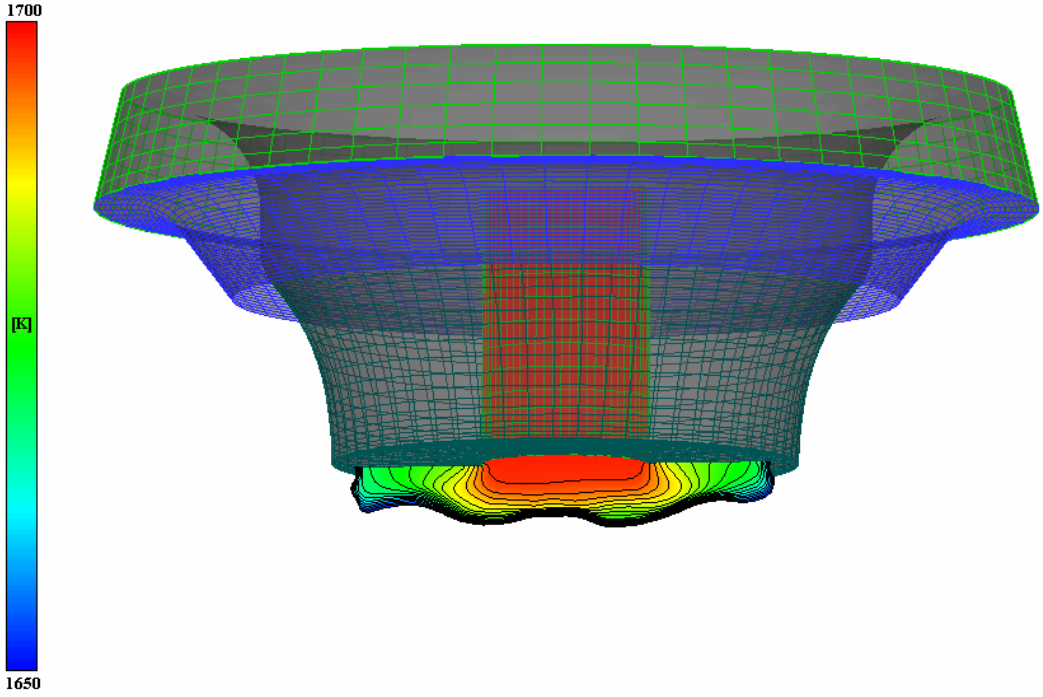


**Figure 4.45: melt temperature contour**

Introducing a pressure boundary condition on melt inlet, the simulation calculates the liquid mass flow. Figure 4.46 shows a completely different scenario compared to the previous case. The melt stream enters the recirculation zone and moves downward. The melt core is stretched by the surrounding gases and melt rims are formed. The liquid metal is not pushed right away toward the tip to create a melt sheet. The gas momentum is not enough to react against the melt: the presence of recirculating gas is demonstrated by the backward orientation of some ribs. Under the influence of unstable recirculating flow, the melt core behaves as a snake. The liquid jet breakup is driven by the aerodynamic force that acts on the surface, exciting the instability waves. Large droplets could be detached in the recirculation bubble and remain there for a long time sheltered from the high speed gas. The ability to survive as a large droplet has a detrimental impact on mass loading effect. Primary breakup ends far away from the tip, confirming that secondary atomization takes place far downstream. Similar conclusions have been deduced by Mates et al. [13], capturing the images of an atomization nozzle working in a similar condition. According to the results mentioned above, break-up model developed in literature and assumed in chapter 3 does not include all the phenomena. Industrial applications (where tip filming

does not take place) cannot be modelled with such scheme: droplets injection points are located everywhere in the domain, without steady distribution of released mass.

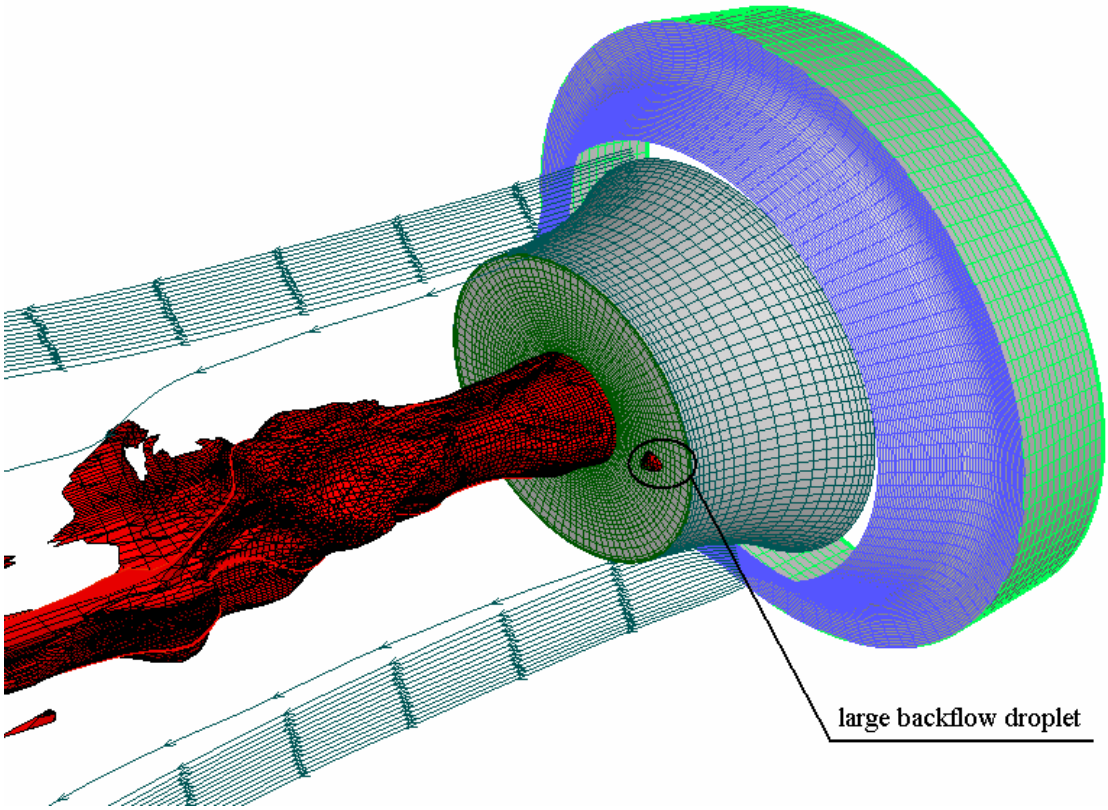


**Figure 4.46: unsteady melt stream, isosurface volume fraction = 1**

Liquid metal flow rate is not constant during the atomization process. Figure 4.47 shows that it moves from 0.37 kg/s to 0.16 kg/s because of the different conditions experienced in the base region.

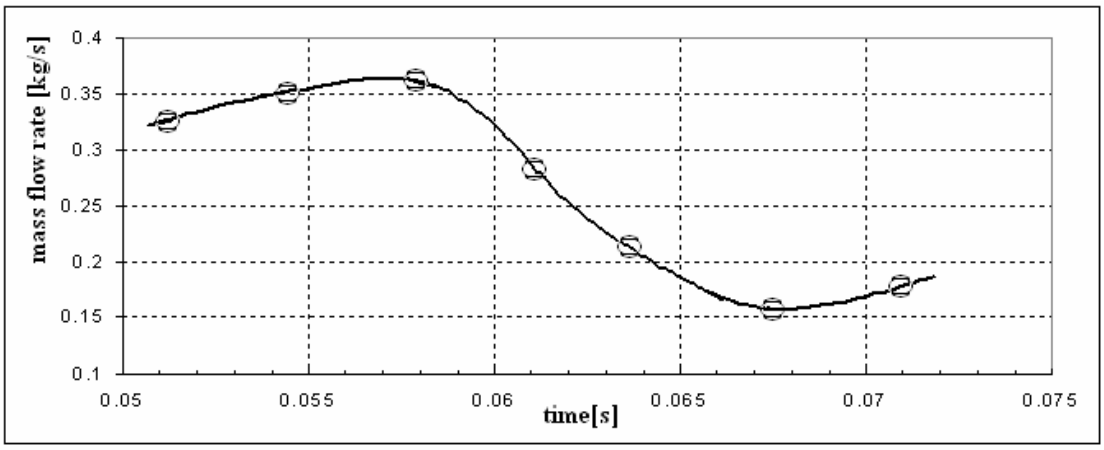


**Figure 4.47: mass flow rate variation**

Previous analysis tends to justify this fluctuation as the passage from open wake to closed wake: however, in this case, closed wake was not reached because of the low operating pressure. This means that the pulsating characteristic is determined by other phenomena. When the mass flow rate reaches the minimum, the melt bending movements are

registered. The large droplet observed on the melt tip is an example of a "wetting" phenomenon: droplets carried by reverse flow stick on the ceramic tip and freeze. The build-up of such droplets may create the freeze off (melt solidification inside the feeding tube). Figure 4.48 contains the axial velocity distribution: it is evident that strong mass loading is present. The velocity vectors along centreline have almost vanished.

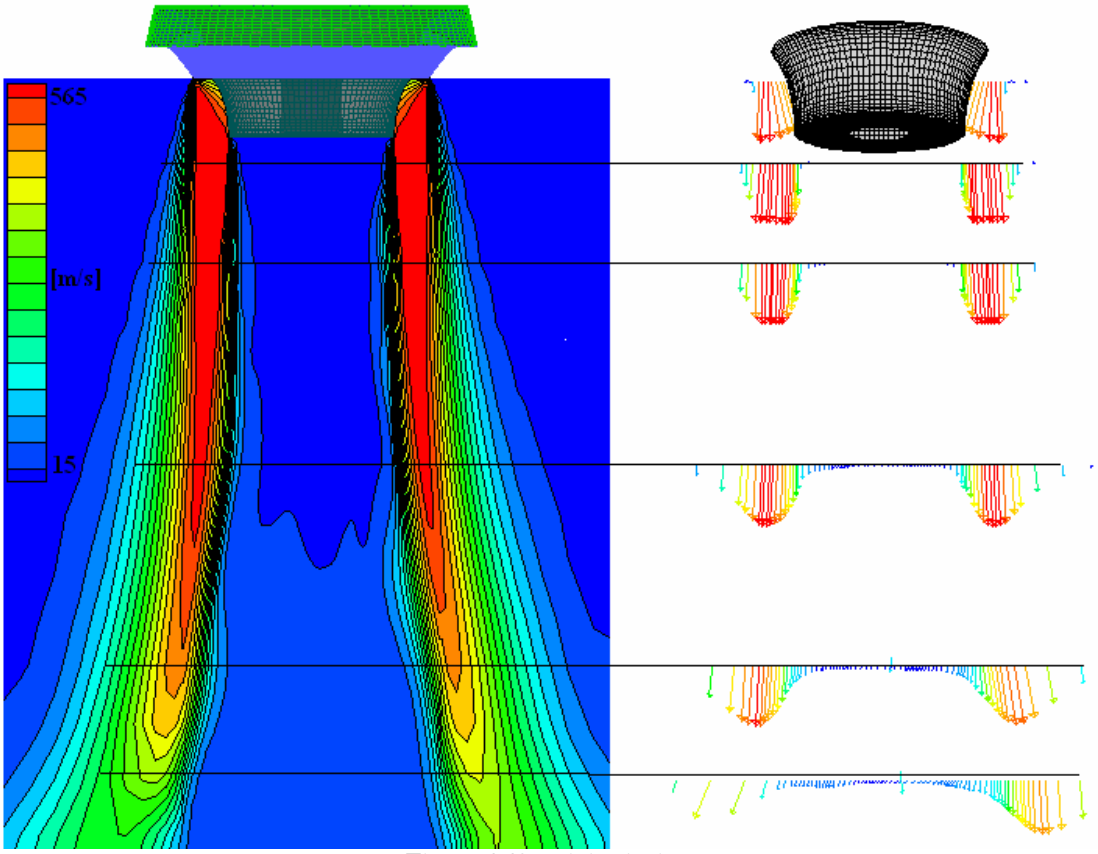


**Figure 4.48: axial velocity**

Figure 4.49 reports a series of images, captured at different simulation time step, describing the sequence from when melt enters the domain until the primary atomization. As the melt stream enters the domain, the strong circulating flow contrasts it and generates a flattened interface.

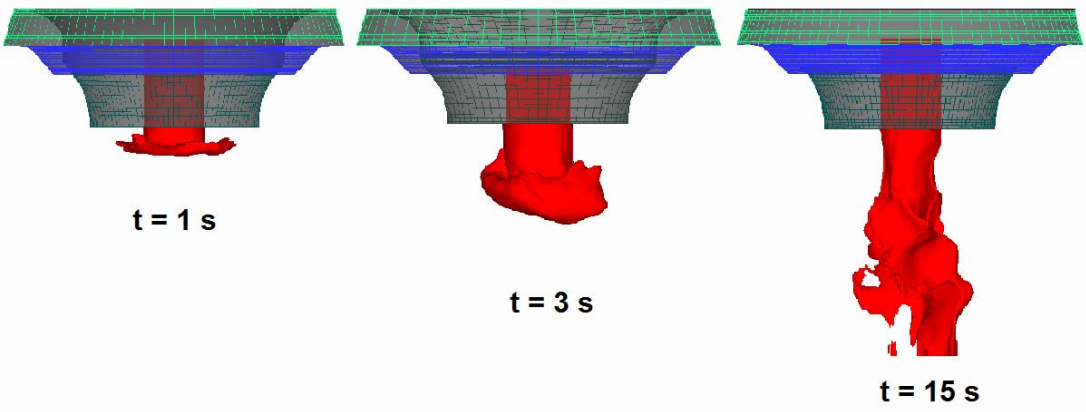


**Figure 4.49: liquid core evolution, isosurface volume fraction = 1**

However ,the melt momentum is higher than the gas one so that the protrusion of liquids in the separated zones extends toward the rear stagnation point. The counter flowing gases pull the metal accumulated on the jet periphery toward the feeding tube, generating an upside-down mushroom shape. At the end, the melt approaches the wake opening the reattachment point and breaks into several liquid sheets/ligaments.

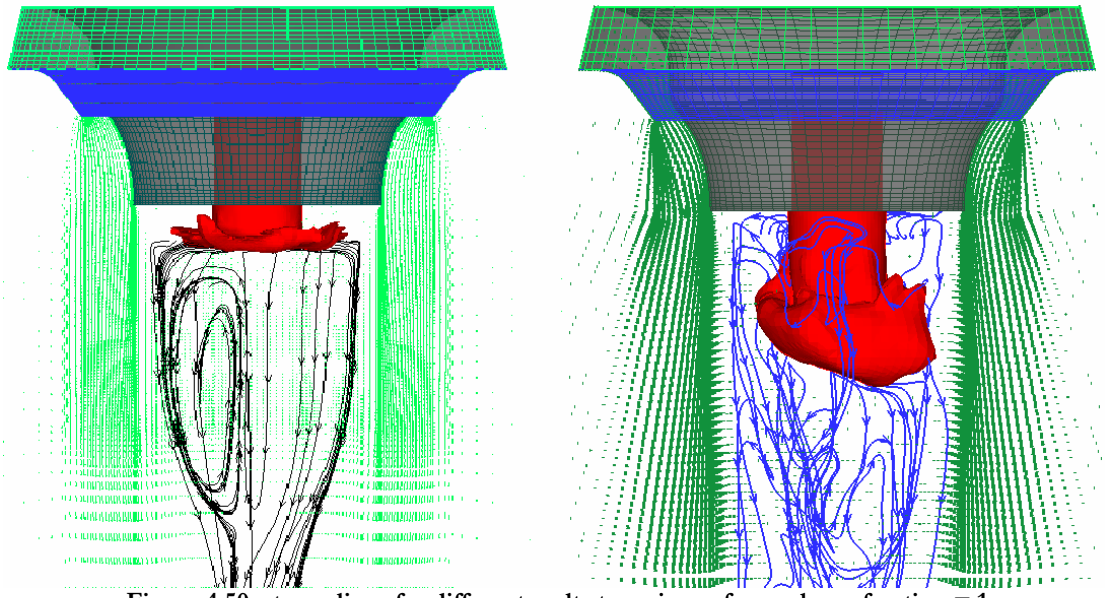

**Figure 4.50: streamlines for different melt stage, isosurface volume fraction = 1**

The streamlines of recirculating flow show in figure 4.50 give an overview of the extreme pattern changes experienced during the transitory liquid core access. Initially the streamlines are positioned only under the melt in a well organized regular distribution. As the melt moves downstream, the streamlines turns around the mushroom with particularly unsteady features and begin to operate against untouched melt core.

Temperature gradients around the melt are steep ,as can be noted by the stratified black lines in figure 4.51. However the liquid core cooling is appreciable far away from the feeding tube exit, avoiding any possibility of freeze off. Figure 4.52 shows the unsteady melt flow for an operating pressure of 30 atm. Basically it presents the same features as the 12 atm case: the melt core opens the recirculation volume and becomes unstable due to the aerodynamic action of side flowing gases. The expanded gas streamlines are not influenced near to the plug. However they seem to depart from the chamber axis. The melt momentum is clearly higher than the circulating gases, even if the detached ligaments look thicker than in figure 4.46. The melt core remains untouched up to one diameter distance from the nozzle tip: this means that the primary atomization zone moves downstream and corresponds with the images recorded during atomization.

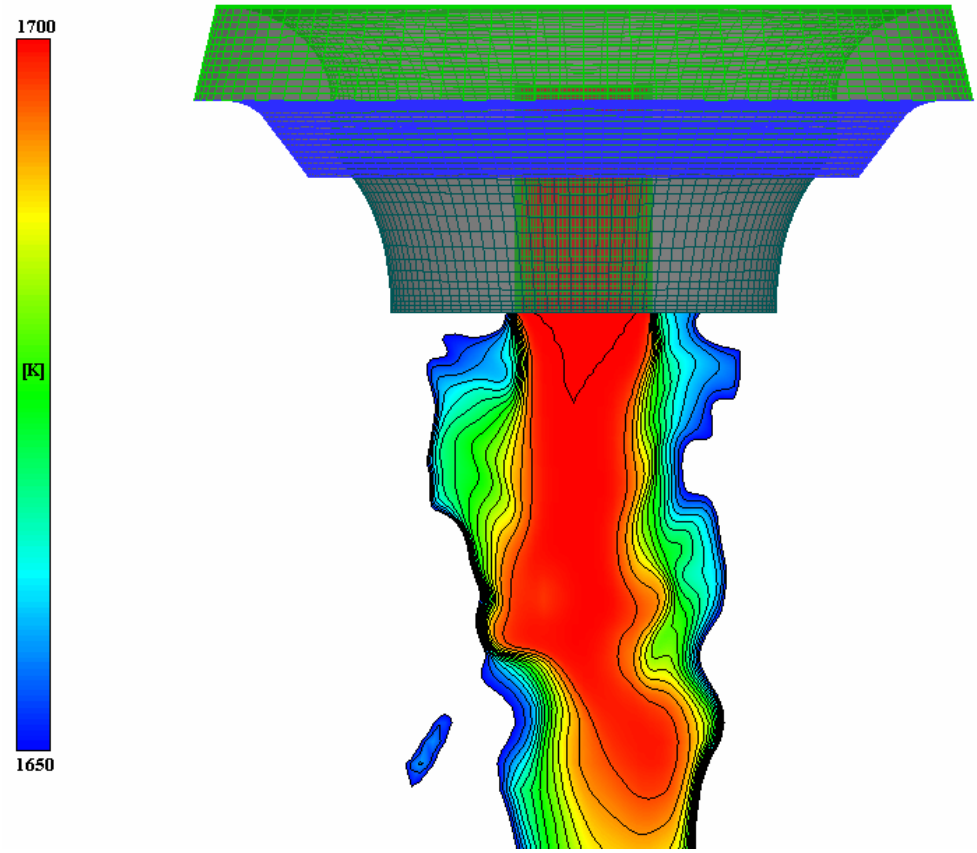


**Figure 4.51: melt temperature contour**

A partial explanation could be that the melt flow rate entering the domain is higher than for 12 atm case and consequently the stream gains momentum and stability.

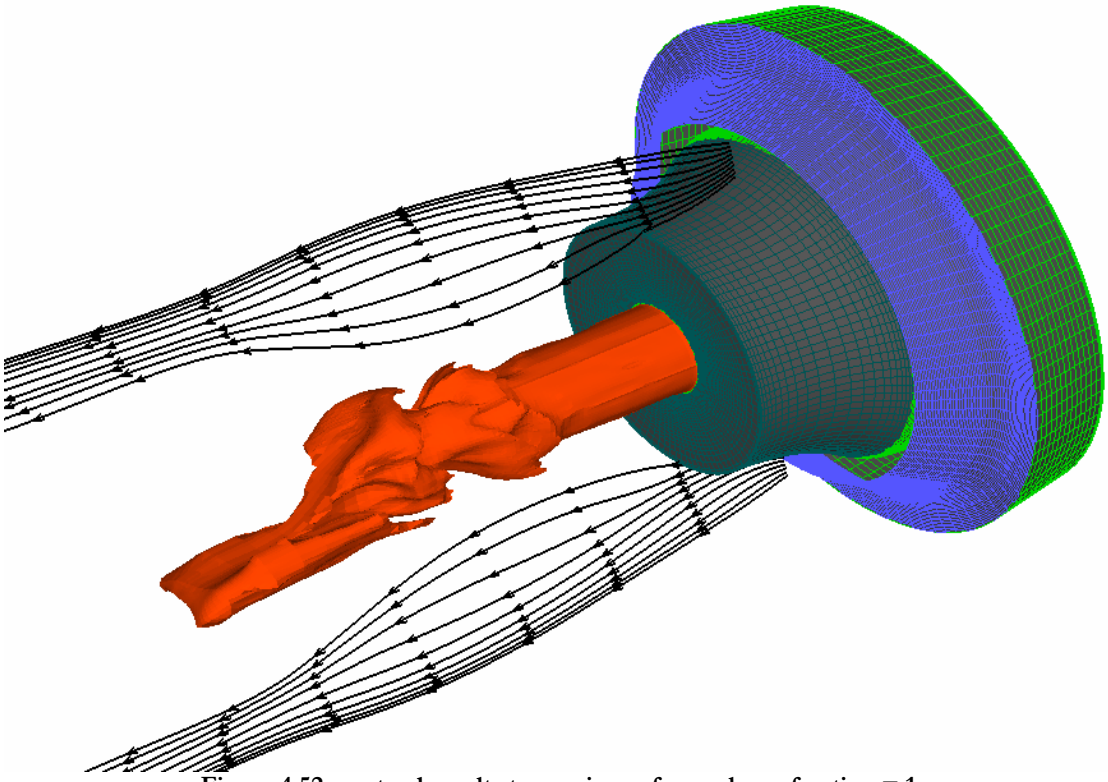

**Figure 4.52: unsteady melt stream, isosurface volume fraction = 1**

The analysis of axial velocity contour in figure 4.53 shows that the Mach disk disappeared in the reason of gas to melt interaction. Velocity distribution along the axis denotes the presence of strong mass loading. The liquid structures (detached from the melt core), travelling along the axis, deflect the high speed gas avoiding the velocity gap recovery.

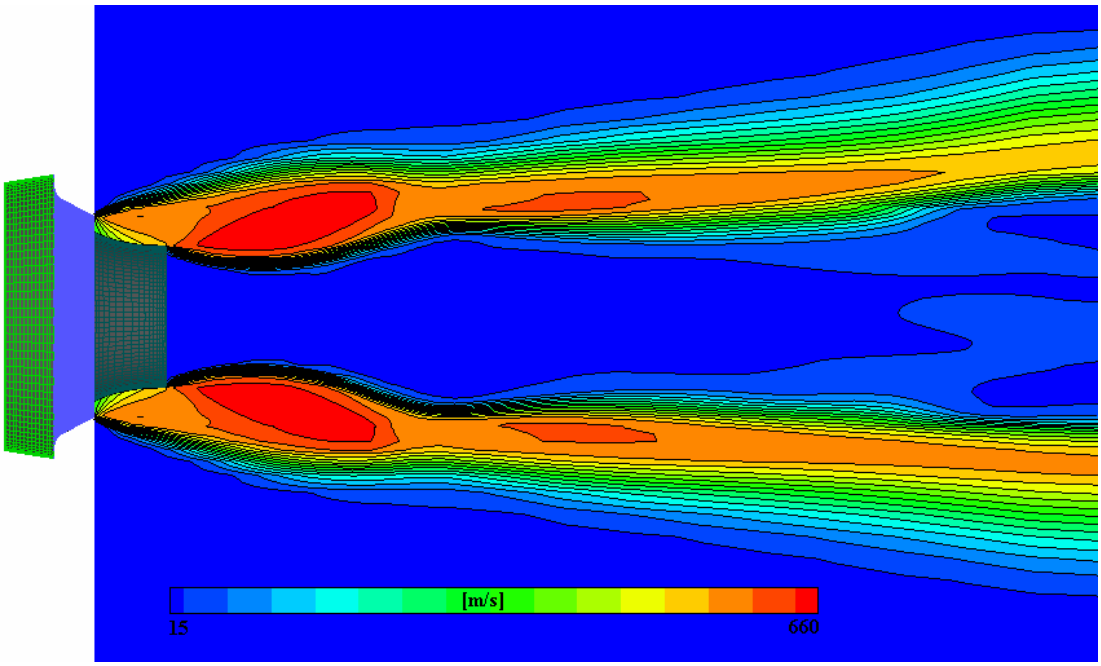


**Figure 4.53: axial velocity contour**

There are clearly 3 different operating conditions that affect deeply the atomization results. The first mode is filming and this works when the gas to melt flow rate ratio is large: very thin sheets are atomized into extremely fine powder. The second mode could be defined as a "mixed" condition: part of the liquid stream films on the nozzle tip and part is pinched off by streamwise expanded nitrogen. As the melt flow rate increases, the quantity of melt removed by stripping the liquid core increases until the condition of no filming at all and this corresponds to the third mode. The first mode is typical of small scale atomizers (such as laboratory prototypes) and could create wrong assumption on the atomization characteristics of high running facilities. The third mode properly represents the usual operating condition of industrial coaxial gas atomizers.

### 4.6.2 Nonaxisymmetric geometry results

As evidenced for the axisymmetric design, the presence of melt along the domain axis pushes the recirculation bubble away from the nozzle tip: this means that a coarser grid can be introduced and computational time reduced. In any case, the resulting $y^+$ was < 5 on the external plug surface. The particular organization of the flow in the non axisymmetric geometry creates preferential directions for the melt leaving the feeding tube. Disregarding the nozzle geometry, two symmetry planes are clearly visible in the melt organization reported in figure 4.54.

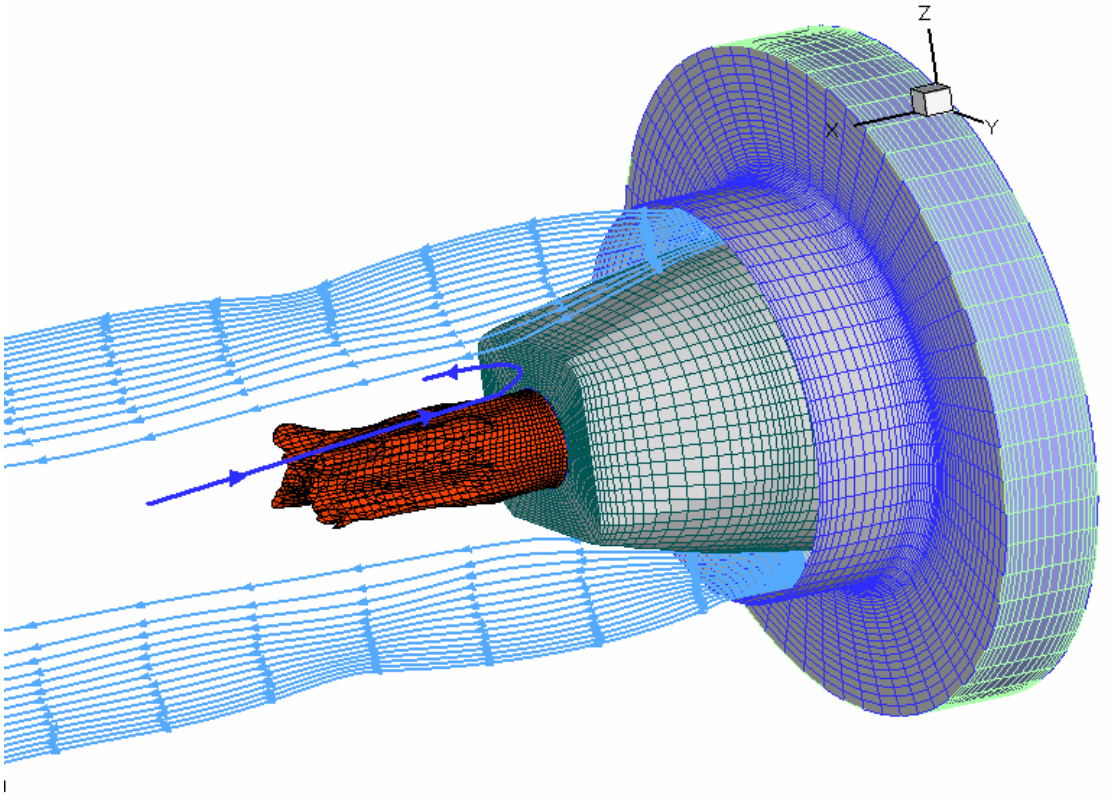


**Figure 4.54: unsteady melt stream, isosurface volume fraction = 1**

The liquid is "squeezed" by the expanded nitrogen (represented by the blue arrows) and moves in the quatrefoil leaves direction following two orthogonal planes inclined at 45 degrees with respect to the vertical symmetry plane. Disregarding the non axisymmetric plug geometry, liquid metal is organized in 4 different cores that are easier to atomize by the supersonic gases (the diameter of each core is smaller than the feeding tube). Furthermore, the departure from the axis in the radial direction avoids or at least makes less probable phenomena such as collision or adhesion of secondary atomized droplets. Mass loading is present but the impact on the flow field is limited, as shown in figure 4.55.

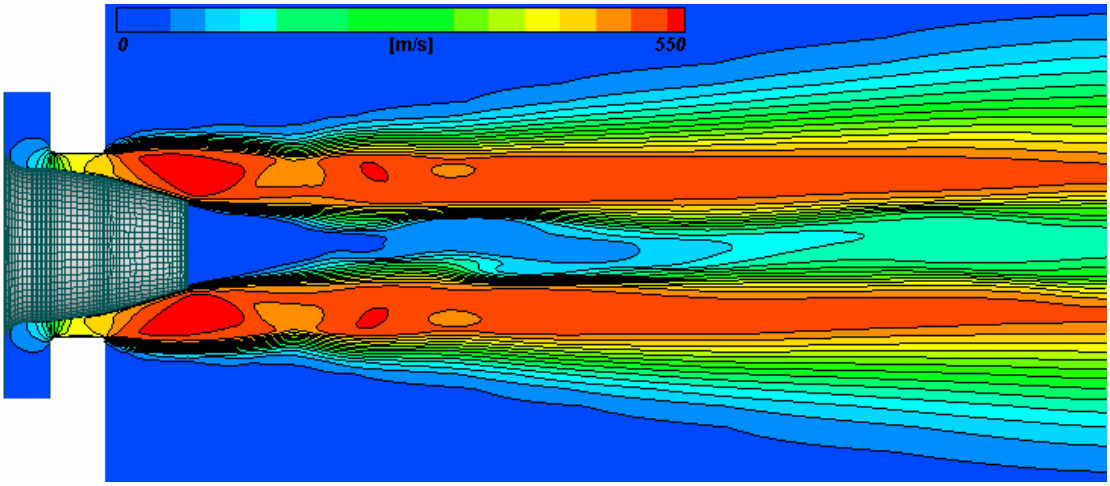


**Figure 4.55: axial velocity contour**

The melt temperature contours in figure 4.56 present a strong gradient on liquid core periphery as for the previous cases. However, due to the quick movement along the symmetry planes, the melt extension on the vertical plane is limited and the gradients at melt tip are less steep than for the axisymmetric cases.

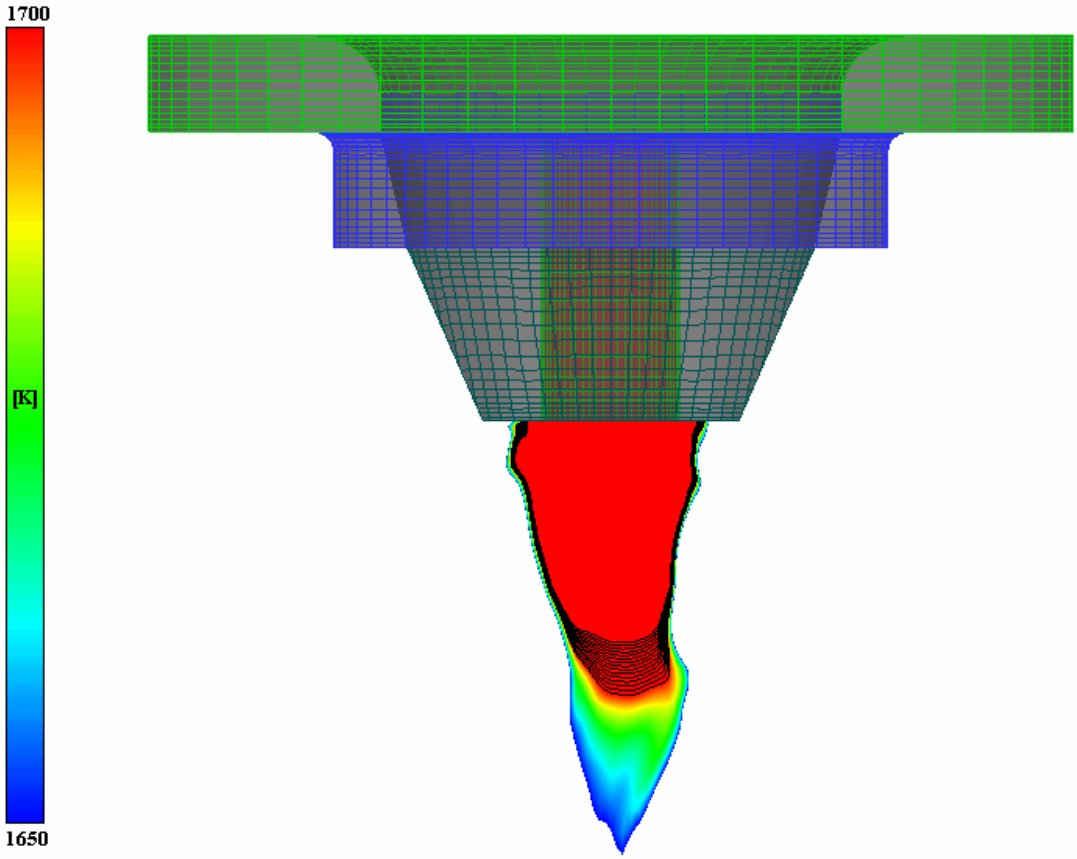


**Figure 4.56: melt temperature contour**

It is extremely interesting to note that the axisymmetric geometry looses the symmetry after gas/metal interaction while in the nonaxisymmetric case the area nearby nozzle tip remains stable. Miller et al. [11] registered a considerable improvement in nickel base

superalloy powder yields when atomized with a nonaxysimmetric nozzle, but they were not able to clearly address the reason of the good performance. Based on the above results, it is evident that initially the gas energy works to divide into multiple components the main stream and only after the aerodynamic forces destabilize (i.e. atomize) the "child" stream. The surface of interaction between the fluids is considerably increased by the splitting operation and the momentum exchange is augmented: as a consequence the break-up becomes extremely effective.

## 4.7 Chapter 4 summary

Chapter 4 was focused on the 3D analysis of gas flow field and primary atomization. Two geometries have been investigated: isentropic plug nozzle and a non axisymmetric geometry (it was not possible to model with 2D scheme). Time dependent gas only simulations revealed the unsteady nature of the high speed plume: especially for the isentropic nozzle coherent structure are clearly visible at a distance of 1 plug diameter from the tip. Unsteadiness means that 2D approach is not able to capture an important aspect of the process because it forces symmetry along the axis of the domain (i.e. atomization chamber). Successively the liquid metal is introduced in the domain to study primary break up on the isentropic geometry. Flow configuration is determined by the gas to melt mass flow ratio: very high value (laboratory scale condition) enhances metal filming at pouring tube tip. When the melt flow rate is increased the filming attitude gradually disappeared and the liquid stream crossed the recirculation bubble. Gas velocity flow field does not change considerably during the filming stage while it is strongly affected by the formation of liquid core along the axis. Very interesting results arose from non axisymmetric design: the liquid core is split outward into four minor streams that are easier to atomize because of the major interaction surface with the gas. Furthermore velocity field is less affected than the isentropic case.

Production plant needs to produce high quantitative of powder at competitive price: this means that melt filming is not possible because the high cost impact of gas consumption. Based on this, the mentioned results brought interesting data to industrial development: in order to improve primary break up it is not sufficient to optimize the gas flow but it is necessary to enhance the momentum/energy exchange between gas and liquid phase increasing the interaction area.

**References**

[1] A. Martinez, Aerodynamic nozzle study, Rocketdyne, NASA- CR- 55891, pp. 1-59, 1963;

[2] S. N. Murthy, J. R. Osborn, Base flow phenomena with and without injection: experimental results, theories, and bibliography, in Aerodynamics of base combustion, Vol. 40 of Progress in astronautics and aeronautics, 7--210, AIAA, New York, 1976;

[3] F.R. Hama, Experimental studies on the lip shock, American Inst of Aeronautics and Astronautics, Aerospace Sciences Meeting, 5th, New York, N.Y., Jan 23-26, 1967;

[4] J. Parker Lamb, W.L. Oberkampf, A Review and Development of Correlations for Base Pressure and Base Heating in Supersonic Flow, SANDIA REPORT SAND93-0280 UC--706, 1993;

[5] D.R. Chapman, D.M. Kuehn, H.K. Larson, Investigation of separated flows in supersonic and subsonic streams with emphasis on the effect of transition, NACA Report 1356, 1958;

[6] N.K. Pui, I.S. Gartshore, Measurements of the growth rate and structure in plane turbulent mixing layers, Journal of Fluid Mechanics, vol. 91, pp. 111-130, 1979;

[7] W.P. Sule, T.J. Mueller, Annular Truncated Plug Nozzle Flowfield and Base Pressure Characteristics, Journal of Spacecraft and Rockets, vol. 10, pp. 689-695, 1973;

[8] J.H. Ruf, P.K. McConnaughey, A Numerical Analysis of a Three Dimensional Aerospike, AIAA Paper 97-3217, 1997;

[9] A. Matesanz, A.Velazquez, M. Rodriguez, Mach disk simulation in jets from convergent-divergent axisymmetric and thrust vectoring nozzles, AIAA-1994-2328, 1994;

[10] T. V. Jr. Giel, T.J. Mueller, The Mach disc in truncated plug nozzle flows, AIAA-1975-886, 1975;

[11] S.A. Miller, R.S. Miller, D.P. Mourer, R.W. Christensen, High yield, nonaxisymmetric atomization of nickel base superalloys, International journal of powder metallurgy, vol. 33, pp. 37-50, 1997;

[12] J.L. Herrin, J.C. Dutton, Supersonic base flow experiments in the near wake of a cylindrical afterbody, AIAA Journal, vol 32, pp. 77–83, 1994;

[13] S.P. Mates, G.S. Settles, A Study of Liquid Metal Atomization Using Close-Coupled Nozzles, Part 1: Gas Dynamic Behavior, Journal of the International Institutes for Liquid Atomization and Spray Systems, vol., issue 1, pp. 19-40, 2005;

[14] F. Simon, S. Deck, P. Guillen, P. Sagaut, A. Merlen, Numerical simulation of the compressible mixing layer past an axisymmetric trailing edge, J Fluid Mech vol 591, pp. 215-253, 2007;

[15] C.W. Hirt, B.D. Nichols, Volume of fluid (VOF) method for the dynamics of free boundaries, Journal of Computational Physics, vol. 39, pp. 201-225, 1981;

[16] J.S. Thompson, A Study of Process Variables in the Production of Aluminium Powder by Atomization, J. Inst. Metal., vol. 74, pp. 101-132, 1948;

[17] J.C. Lasheras, E. Villermaux, E.J. Hopfinger, Break-up and atomization of a round water jet by a high-speed annular air jet, J. Fluid Mech., vol. 357, pp. 351-379, 1998;

# CHAPTER 5

## PROCESS IMPROVEMENT WITH OPTIMIZED DESIGN

The purpose of this chapter is to present possible improvements for the gas atomization process. The main goal is to narrow the range of particles size. Two different geometries (swirled and inner gas jet) will be simulated to evaluate possible benefits. Pressurized systems and swirl nozzles showed good performance in fuel atomization and combustion: additional insight in melt atomization could be given by future research on those technologies. As anticipated in chapter 2, Lagutkin et al. [1] proposed a pressure swirl atomizer for melt, where the liquid metal leaves the nozzle as a hollow cone and is further atomized in a free fall configuration. Usually, in spray technology, the swirling movement is given to the liquid core to improve its disintegration. However, in a coaxial geometry, the flow dynamics is determined by the annular gas. In this case, it is reasonable to investigate the effect of a swirling gas jet on the breakup of the liquid stream as a function of superimposed rotation. In a pressure atomizer, the break up is achieved by means of the pressure difference between melt reservoir ($P_M$) and atomization chamber ($P_C$). The velocity $U_{exit}$ at nozzle exit is given by the Bernoulli relation $U_{exit} = C_D \sqrt{\frac{P_M - P_C}{\rho_l}}$ where $C_D$ is a discharge coefficient that accounts for the losses. Liquid inertia, surface tension and aerodynamic force are involved in determining primary break up features. When the relative velocity becomes significant ,the aerodynamic force overtakes the liquid inertia and promotes the growth of unstable waves on the liquid surface. The introduction of a swirl component involves also the centrifugal force in the initial disruption of the melt and increases the spray cone angle.

### 5.1 Swirled atomization

The geometry used to simulate effect of swirled flow is reported in figure 5.1: the gas enters the atomization nozzle from inlet_1 and inlet_2 faces and moves into the atomization chamber after the expansion over a 15° conical plug. The grid is made of 1.2 million cells and extends 7 base diameters axially and 7 base diameters radially. A structured grid is used to discretize the chamber domain, while an unstructured mesh is applied to the nozzle head. The base diameter D measures 14 mm and protrudes 11.1 mm axially, while the slit width is 2 mm. The nitrogen operating pressure is 12 atm and the

inlets are supposed to be directly connected to the reservoir. Simulation schemes are summarized in table 5.1:

| | |
|---|---|
| Solver | Segregated |
| Geometry | 3D – swirl |
| Time | Gas only - Steady<br>multiphase - unsteady $10^{-6}$ |
| Flow model | multiphase VOF |
| Turbulence model | RSM |

**Table 5.1: simulation schemes**

The liquid metal properties are summarized in table 5.2:

| property | value |
|---|---|
| Cp | 680 [J/kgK] |
| ϱ | 7000 -0.1T [kg/m$^3$] |
| viscosity | 1.789*10$^{-5}$ [kg/m-s] |

**Table 5.2: thermo-physical properties of the melt**

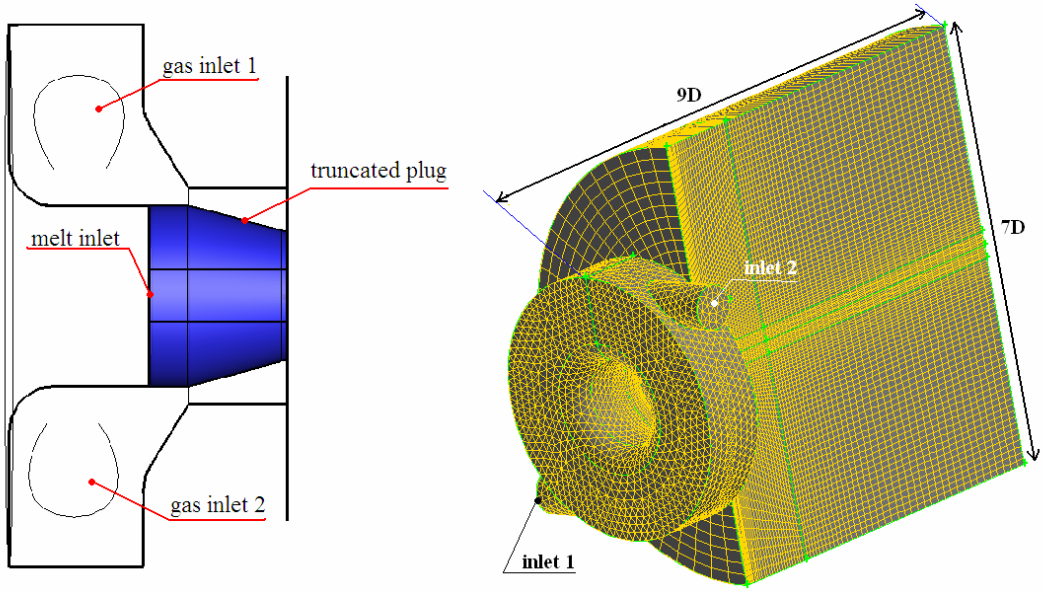


**Figure 5.1: swirling nozzle sketch and atomizer grid**

Flow streamlines are showed in figure 5.2: the expanding gas rotates around the feeding tube and expands after the annular neck reaching a swirl intensity (S) of 0.35 at plug tip. Swirl intensity is a measure of the ratio between angular momentum axial flux and the axial momentum flow: low values indicate reduced turbulent diffusion. Higher S values promote mixing activity and consequently the fast decay of jet velocity: sometimes this takes place in a combustor with a short flame but would be detrimental in metal atomization because it considerably reduces the secondary atomization zone.

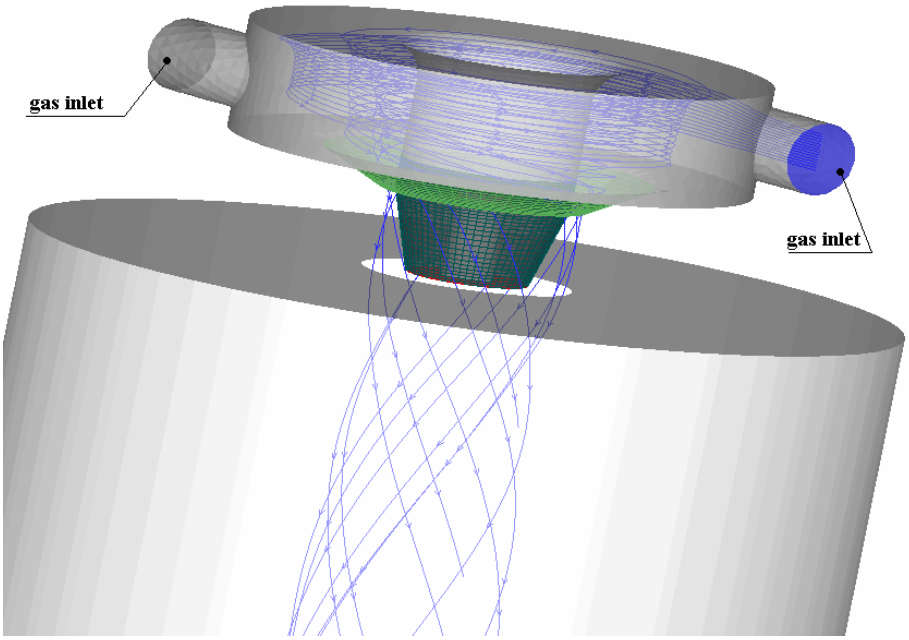


**Figure 5.2: gas only flow streamlines**

Figure 5.3 reports the axial velocity contours: the flow field under the tail base is completely different from all other cases analyzed so far. There is no hourglass shaped recirculation and the free shear layers do not merge axially so that the rear stagnation point is absent. Reverse flow occupies all the volume along the centreline: a negative velocity peak is located close to the nozzle tip (0.017 m).

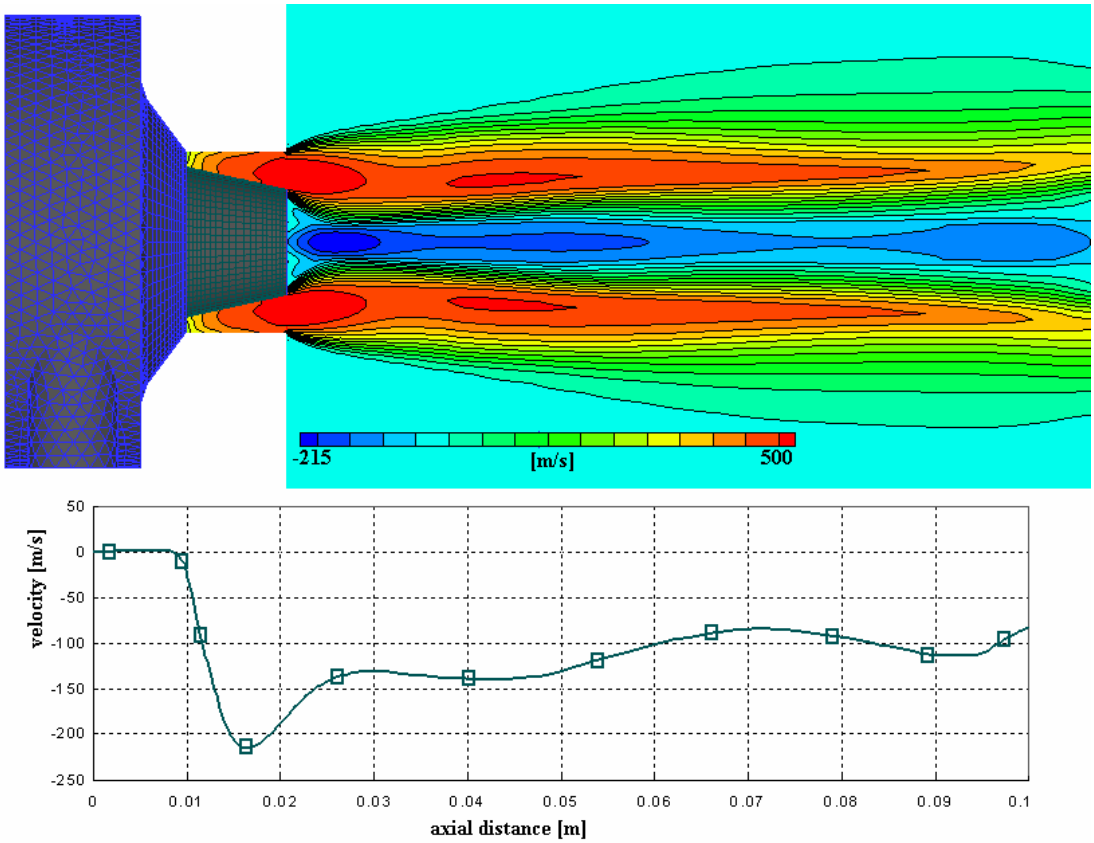


**Figure 5.3: axial velocity component behind swirling atomizer plug**

The fluid in the chamber is captured and moves upward through the wake. Because of the swirled flow also the tangential component of the velocity assumes significant values as shown in figure 5.4: it reaches 53% of the axial component with an axisymmetric distribution.

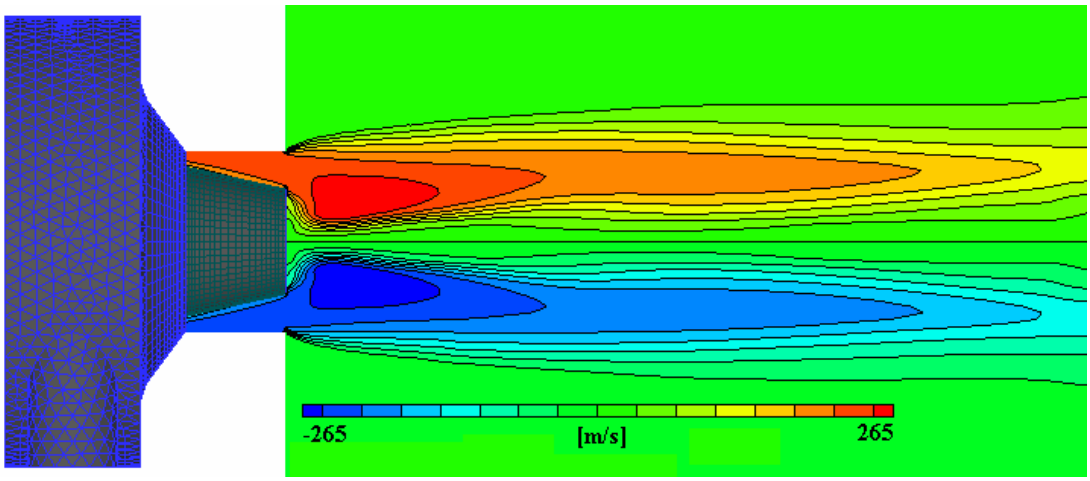


**Figure 5.4: tangential velocity component behind swirling atomizer plug**

The pressure distribution reported in figure 5.5 clearly shows the deep subambient condition existing in the reverse flow zone: the delta pressure is employed to balance centrifugal acceleration.

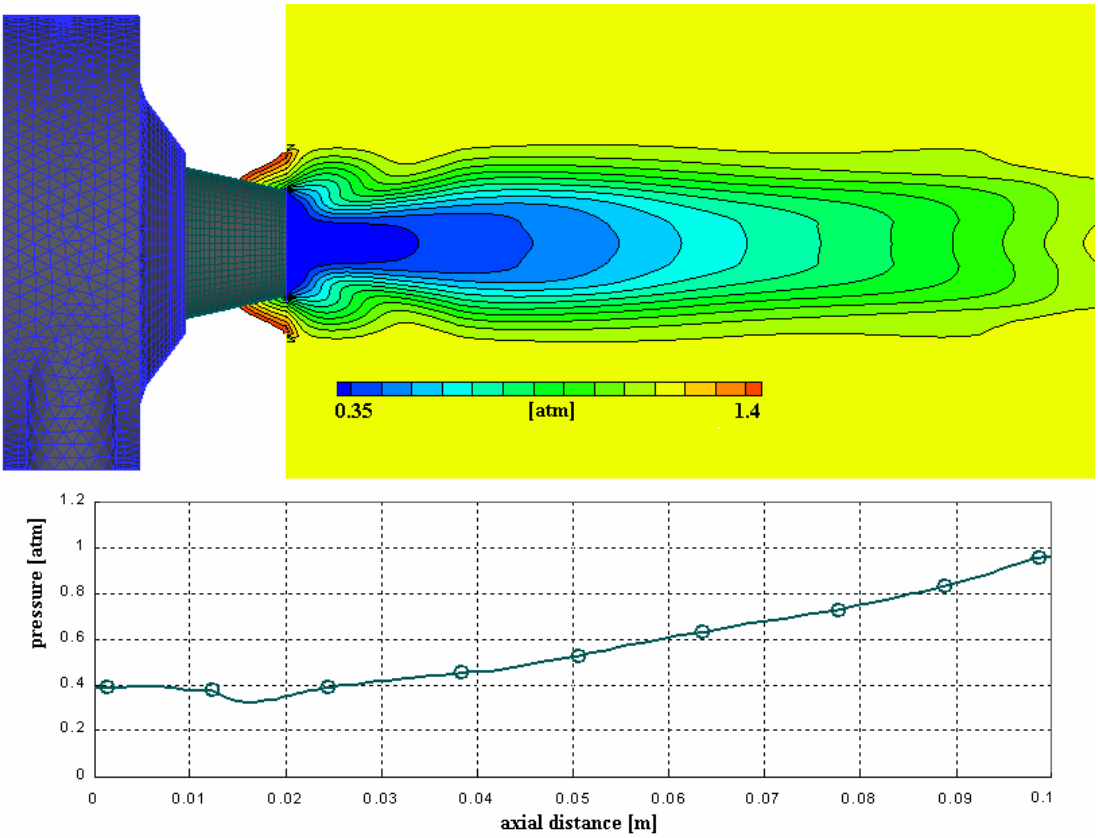


**Figure 5.5: pressure distribution behind plug separation**

Due to the very low pressure close to the feeding tube, a strong aspiration on the incoming melt is expected. Isovalue lines are not stratified: they indicate that there is a radial pressure gradient but no strong shock (as per lip shock in the configuration without swirl). The adverse pressure gradient along the axis promotes recirculating flow. When the second phase enters into the atomization chamber, the flow pattern experiences considerable variations. Figure 5.6 shows the gas streamlines distribution around the melt. The liquid core crosses the chamber relatively untouched: the external surface presents distortions caused by aerodynamic interaction but these are not enough for primary break up. Isosurfaces relative to solid fraction =1 are not visible outside the liquid core: this means that gas flow does not remove ligaments from the metal stream. The grid resolution does not allow us to evaluate if small droplet are pinched-off from the melt jet but, if any, they represent a very small mass amount. The gas trajectory appears wider than in figure 5.2, where the streamlines denote a rather absent radial velocity component. The presence of second phase seems to reflect the incoming gas radially. As expected, the liquid flow rate is very high (driven by the low pressure at the feeding tube exit), almost 0.60 kg/s. On the contrary, the gas flow rate is reduced to 0.22 kg/s (while, in the conventional geometry, it is 0.41 kg/s): one of the effects of swirl introduction is the reduction of mass flow rate and consequently the momentum introduced in the domain. This means that the gas to melt flow rate is well under 1 and the atomization performance is certainly poor.

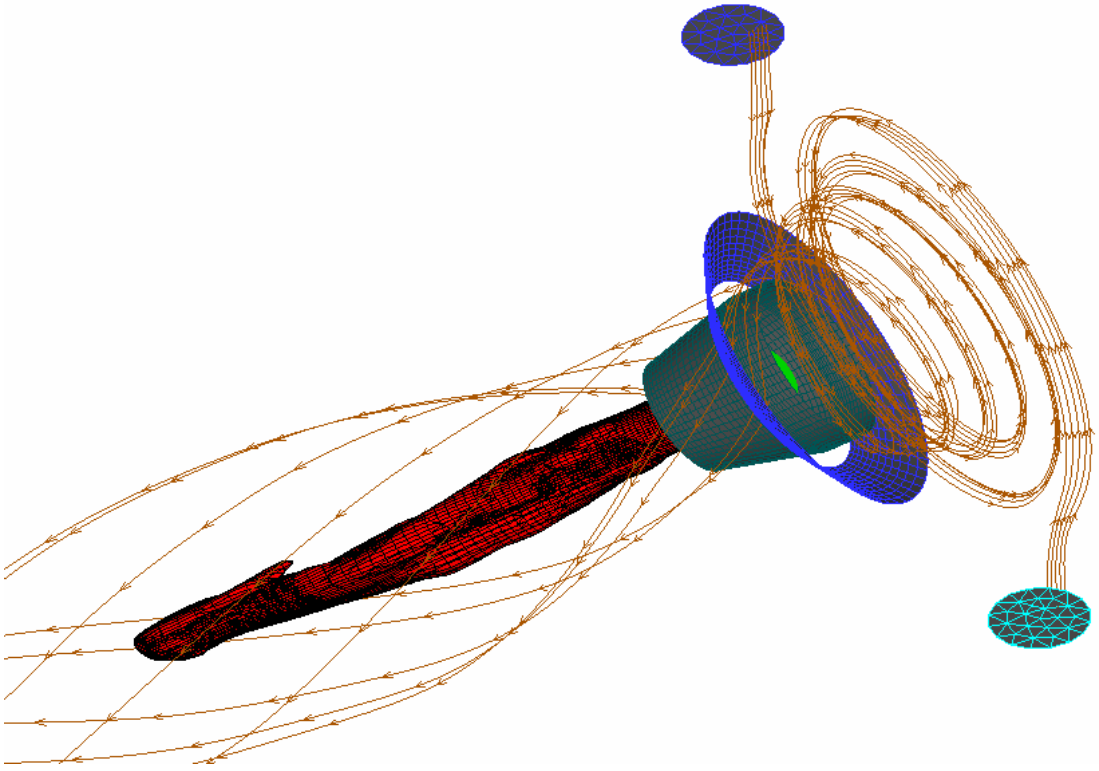

**Figure 5.6: unsteady melt stream, isosurface volume fraction = 1**

Figure 5.7 reports the axial velocity contour on a symmetry plane. The flow is asymmetric and the liquid core determines a severe mass loading effect in the wake. The presence of melt along the centreline and the reduced velocity increases the probability of having large unatomized portions in the yield.

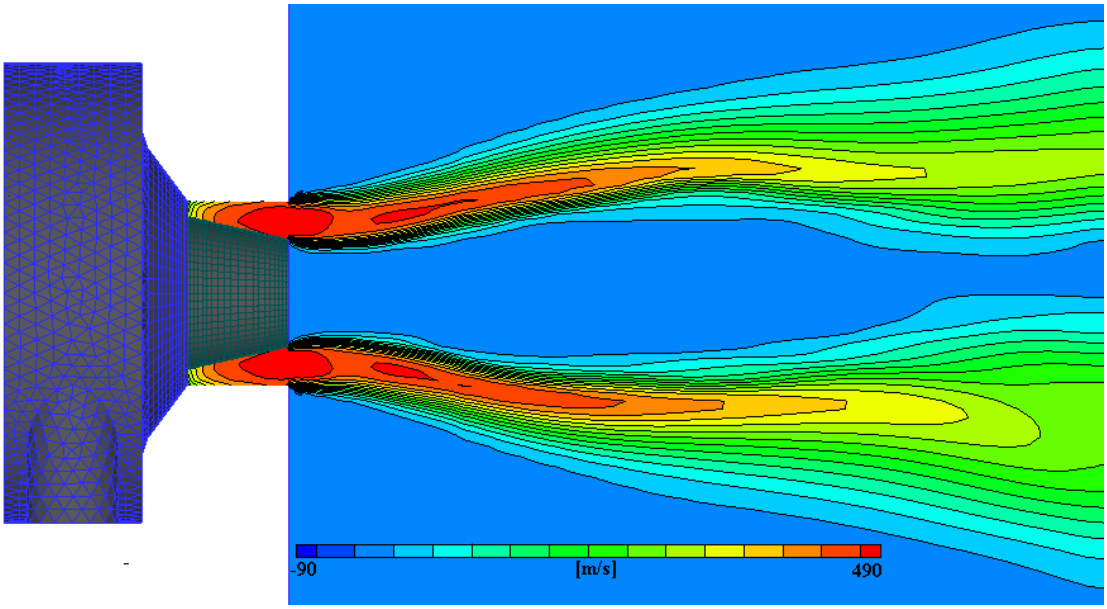


**Figure 5.7: axial velocity distribution behind plug separation**

Jet Velocity decay is faster than in gas only flow, indicative of an even worse secondary atomization attitude. Gas swirl seems to inhibit the atomization process: A possible explanation is that the pressure gradient inside the "swirling curtain" increases radially outward the static pressure: this means that the liquid rib, pulled by the gas, experiences an adverse static pressure that pushes it back to the external surface of the liquid jet. The radial pressure gradient acts as an additional surface tension to damp the disturbances at liquid/gas interface. In other words the helical modes are damped while the axisymmetric mode is enhanced [2]. Finally the temperature contours are reported in figure 5.8. Also, in this case, temperature gradients inside the melt near to the plug base are small and the freeze-off risk is extremely low. According to what has been discussed, a standard nozzle cannot be converted in a straightforward manner to a swirling one without compromising overall performance. In order to have a better view, it is necessary to have a future analysis for gas to melt mass flow ratio higher than 1 and to evaluate the influence of different swirl intensity on the liquid core. Based on the experience done in chapter 4, and considering the very small time step, $10^{-6}$s, this would require at least 6 months investigation.

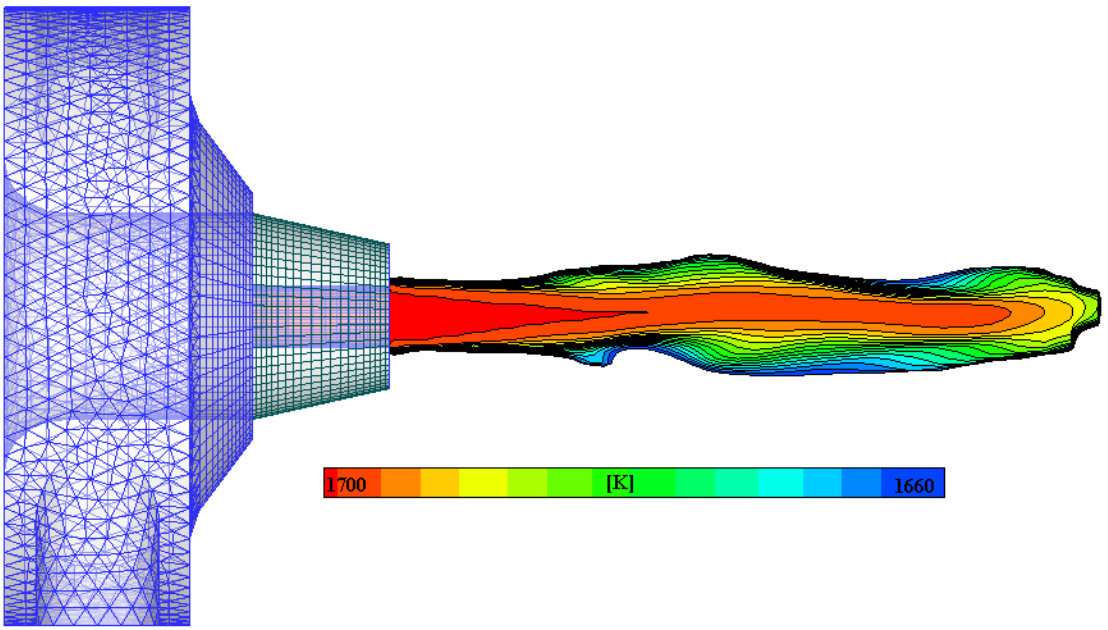


**Figure 5.8: melt stream temperature**

## 5.2 Inner gas jet atomization

As pointed out in chapter 5, the filming mechanism does not take place at the operating condition present in industrial scale equipment. On the other hand, it is evident that the presence of a thin melt layer near the plug tip would enhance primary break up. Furthermore, a large droplets population has been evidenced along domain centreline, causing the well known mass loading effect. The narrow particle size yield of Lagutkin et al. [1] was the result of the better primary atomization of hollow cone liquid sheet.

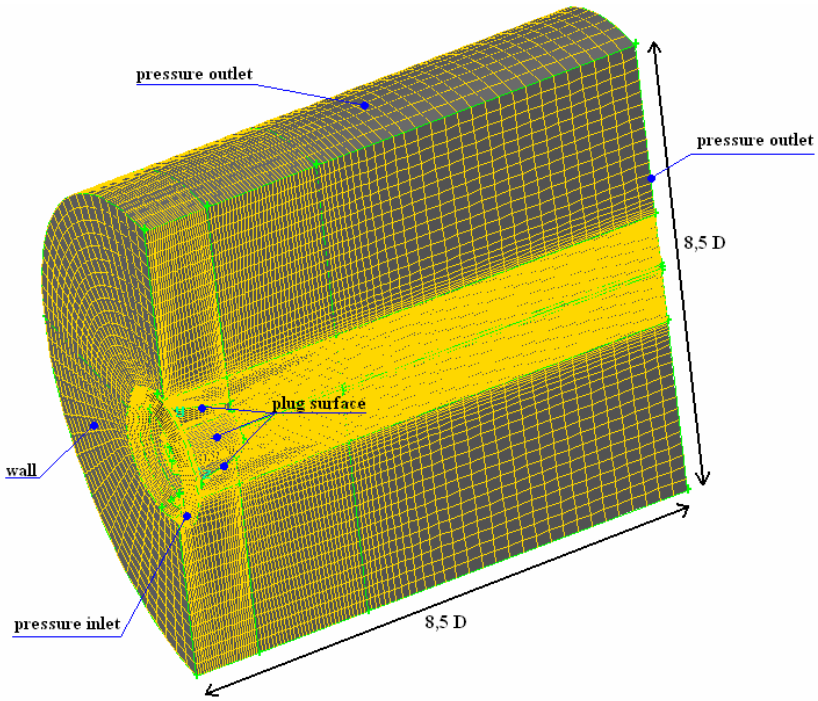


**Figure 5.9: coaxial atomizer grid**

Based on these considerations, the idea of an inner gas jet seemed to represent a good solution. Half domain is shown in figure 5.9: this expands 5.5 plug diameters axially and 8.5 plug diameters radially. The boundary conditions are pressure inlet for the gas coming from the manifold and pressure outlet at the chamber interface. The ideal gas law has been used to model the nitrogen density. The grid has been refined close to the plug nozzle wall in order to capture the boundary layer features. Figure 5.10 illustrates the particular shape and mesh used for the plug. The inner nozzle is a converging-diverging type (necessary to achieve supersonic expansion). Melt is fed into the domain by an annular vane in the standard ceramic plug. The conical plug apex angle is 30°.

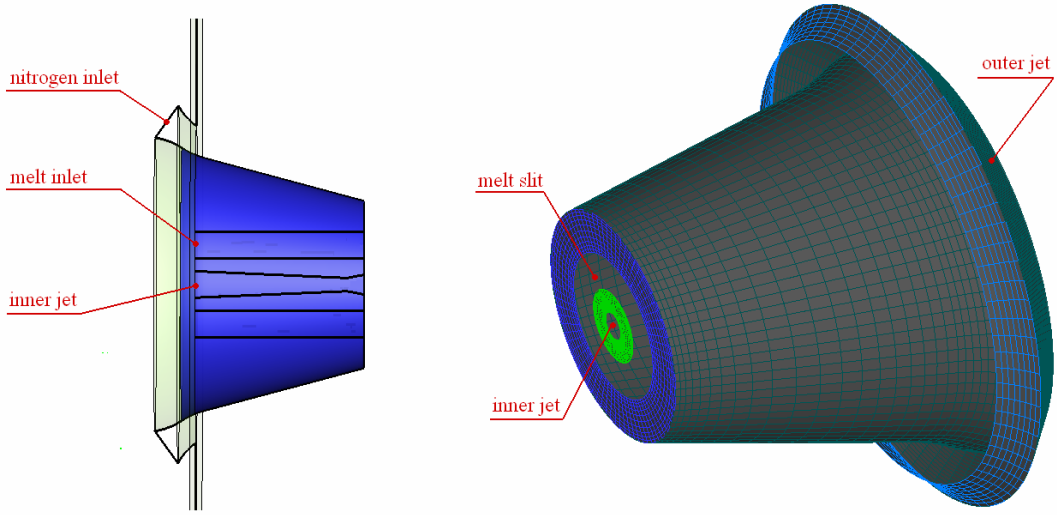


**Figure 5.10: coaxial atomizer plug sketch**

Simulation parameters are the same used for swirled geometry reported in table 5.1 and 5.2. The predicted velocity field is reported in figure 5.11. The shock pattern is clearly visible from the velocity contour. The non isentropic profile generates underexpanded flow with strong internal shock. The flow pattern resembles what has been already discussed in chapters 3 and 4: a recirculation zone is formed behind the plug base and the rear stagnation point is localized at free shear layer reattachment along the axis.

The internal jet crosses the separated bubble along the centreline and pushes the reattachment point downstream: surprisingly, the velocity defect on the chamber axis is still high. Notwithstanding the additional momentum carried by the inner jet, the velocity gap in the radial direction is not recovered at the domain exit and its value is similar to the cases without an inner jet simulated in chapter 4. The rear stagnation point acts as a barrier for the inner jet that spends a lot of energy to overcome it. The recirculating flow is organized in an annular ring squeezed downstream: the free shear layer interacts on both sides of the ring.

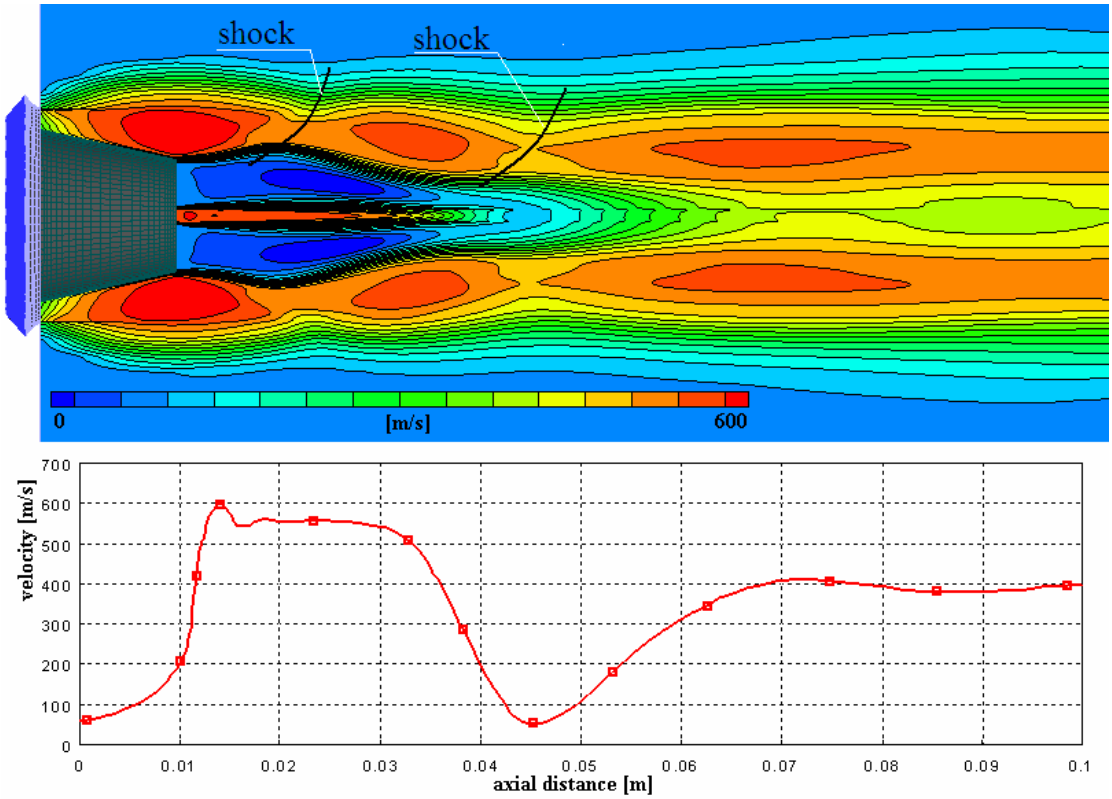


**Figure 5.11: axial velocity component behind plug separation**

Pressure contours are given in figure 5.12: steep gradients (i.e. shocks) denote overexpansion at the base tip.

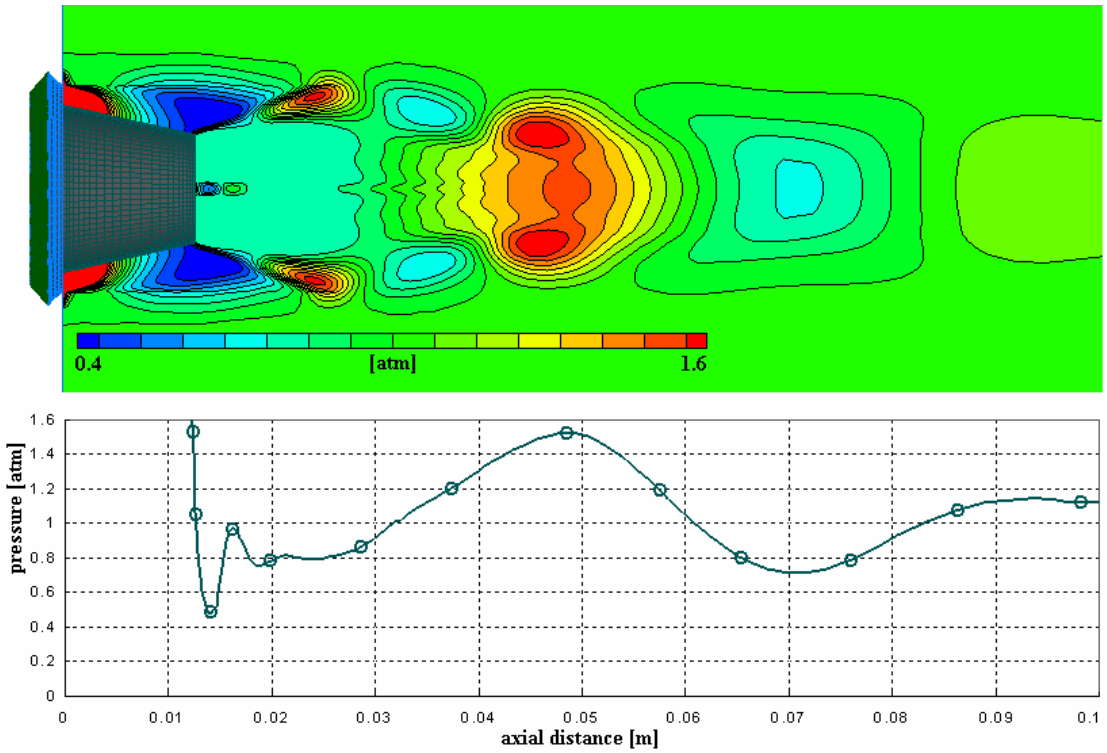


**Figure 5.12: pressure distribution behind plug separation**

Pressure inside the recirculating fluid is constant, confirming the qualitative agreement with experimental observations done on the base flow problem. The supersonic inner nozzle produces an underexpanded jet that continues to expand through a series of Prandtl-Meyer fans and shocks until the bubble pressure is matched. The lower level of pressure reached is the same as for the annular jet after separation on plug corner. At the axial distance 0.045 m, the reattachment point is located clearly marked by the pressure peak: its value is similar to the isentropic plug geometry. The pressure insisting on the base is also sub atmospheric (≈ 0.8 atm) in this case, so that the liquid pouring is encouraged. When the fluid leaves the domain, the pressure is almost equal to the atmospheric condition existing in the atomization tower.

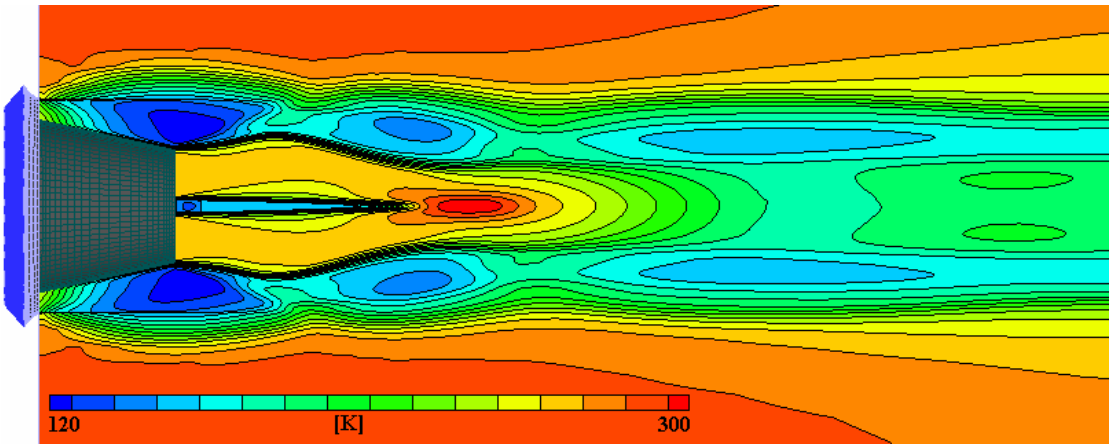


**Figure 5.13: temperature contour**

The temperature distribution is given in figure 5.13: expanded gases reaches 120K around the feeding tube and the same value is achieved by the inner jet. The recirculation zone is slightly affected by the new configuration: apart from the centreline, the temperature maintains the same level as in the absence of a central jet. The spreading of the external isovalue lines denotes strong activity of the free shear layer, while the stratified presence around the recirculation shows a significant gradient. When the melt enters the domain the flow pattern experiences evident changes. As can be seen in figure 5.14 the axial velocity field presents a completely different wake. As already noted in chapter 4, the external jet does not experience reattachment: the melt acts as a tail extension that protects the centreline from converging flow. The amount of shock structures is the same as in the gas only flow but the reattachment shock is reflected off the core region and no longer crosses the middle of the jet. The high speed plume of the central jet has a longer penetration in the wake (almost double): this is a clear effect of the different flow organization in the rear stagnation point. The sudden velocity decay at the axial distance 0.05 m denotes the wake

mixing between the expanded nitrogen of central jet and the low velocity gas coming from the separated zone.

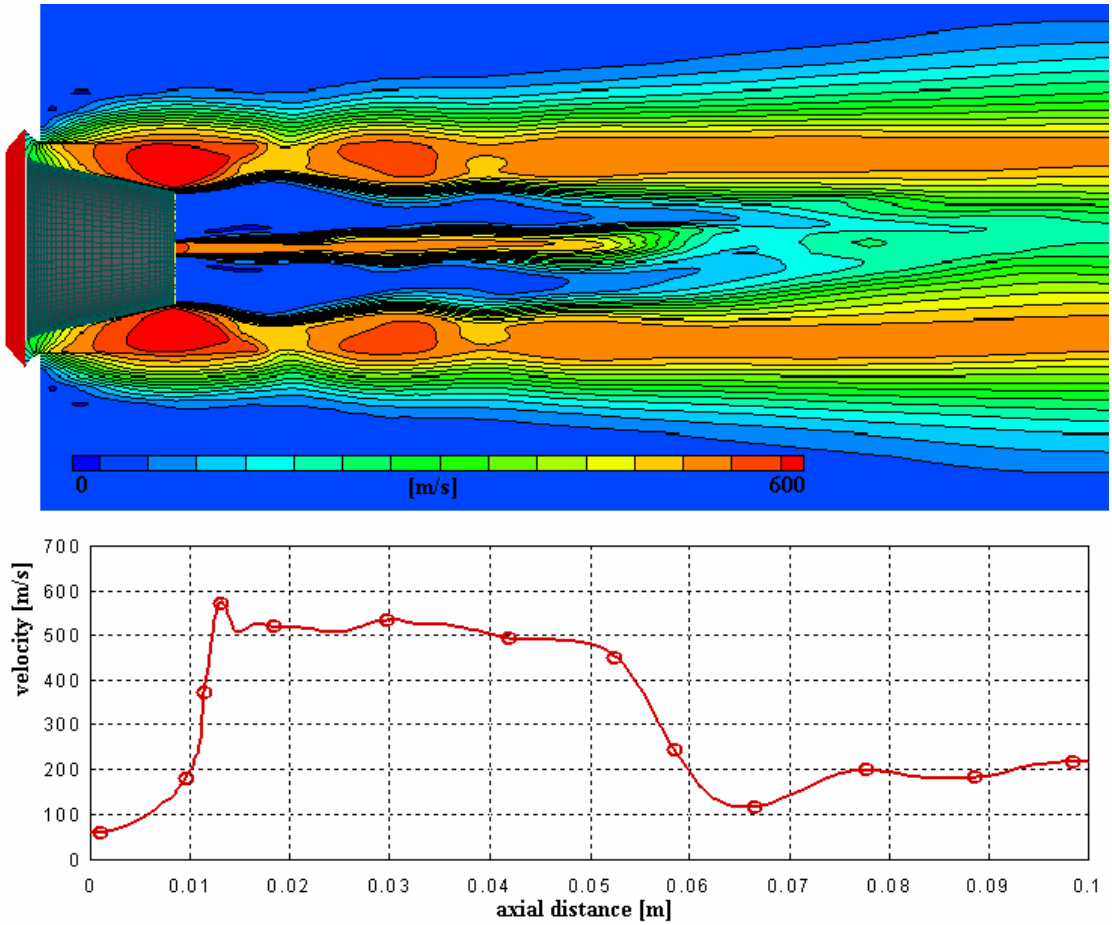


**Figure 5.14: axial velocity component behind plug separation**

Due to this entrapment, the velocity defect along the centreline is considerable (about 300 m/s at the domain exit).

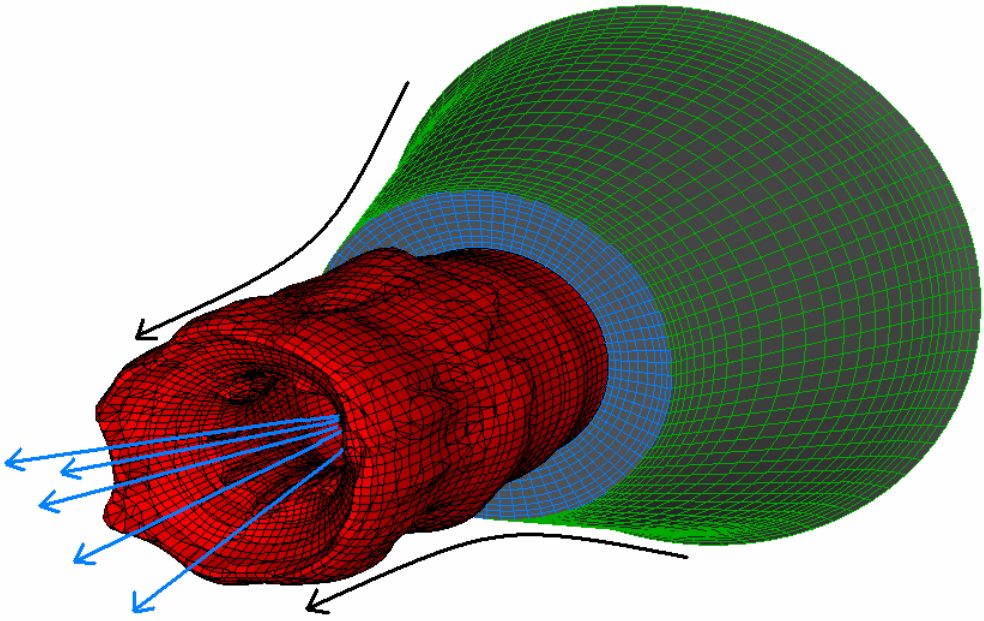

**Figure 5.15: unsteady melt stream, isosurface volume fraction = 1**

The shape of the liquid metal during the atomization is presented in figure 5.15. The inner jet maintains the axial bore inside the melt that moves downstream as a hollow cylinder. The annular jet action is sketched with the black arrows: high speed gas comes into contact with the external side of the melt and exerts an aerodynamic force that destabilizes the liquid sheet (see the sinuous red surface). The unstable liquid layer is squeezed between the internal and external jets until it breaks into small liquid ligaments that undergo secondary break up (as in the Dombrowski and Johns model [3]). In order to have a better understanding, a 2D section is shown in figure 5.16. The light blue stream represents ligaments: due to the computational requirements, it was not possible to capture secondary break up with the VOF model, however the ligament formation phenomena is clearly defined.

Due to the intrinsic limitation of VOF model, the boundary layer around the melt core (solid fraction =1) identifies only a zone where the cell is not full of liquid. Primary break up seems to be a reasonable interpretation, however only simulations on refined grid with large supercomputer could bring more insight in 7 months time. It is important to note that there is no second phase presence along the centreline, so, even if the central jet experiences steep decay, there are no droplets in that area to atomize. Certainly this is a big improvement because, as shown in chapter 4, the big particles moving along the chamber axis experience low atomization level and form process scrap.

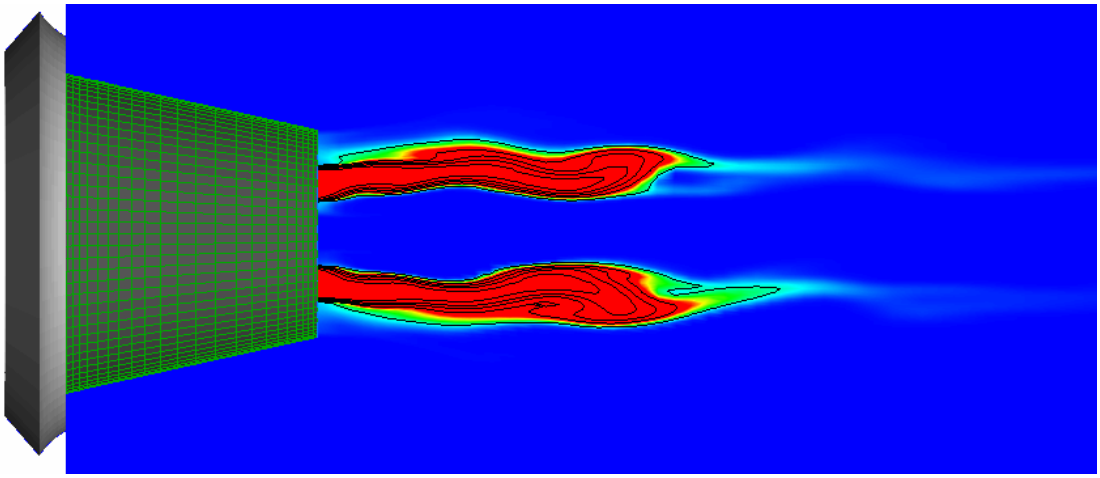

**Figure 5.16: unsteady melt stream section, isosurface volume fraction = 1**

Finally the melt temperature contour is shown in figure 5.17: as expected, strong gradients are localized around the melt core because of the huge temperature difference between metal and gases (about 1600 K). However, the melt temperature remains close to the temperature at injection up to 1 base diameter distance, avoiding freeze-off concerns. As per the solid fraction results, also for the temperature the boundary layer is not accurate,

because cells properties average (according to mass fraction) of 2 fluids very different (nitrogen and liquid steel).

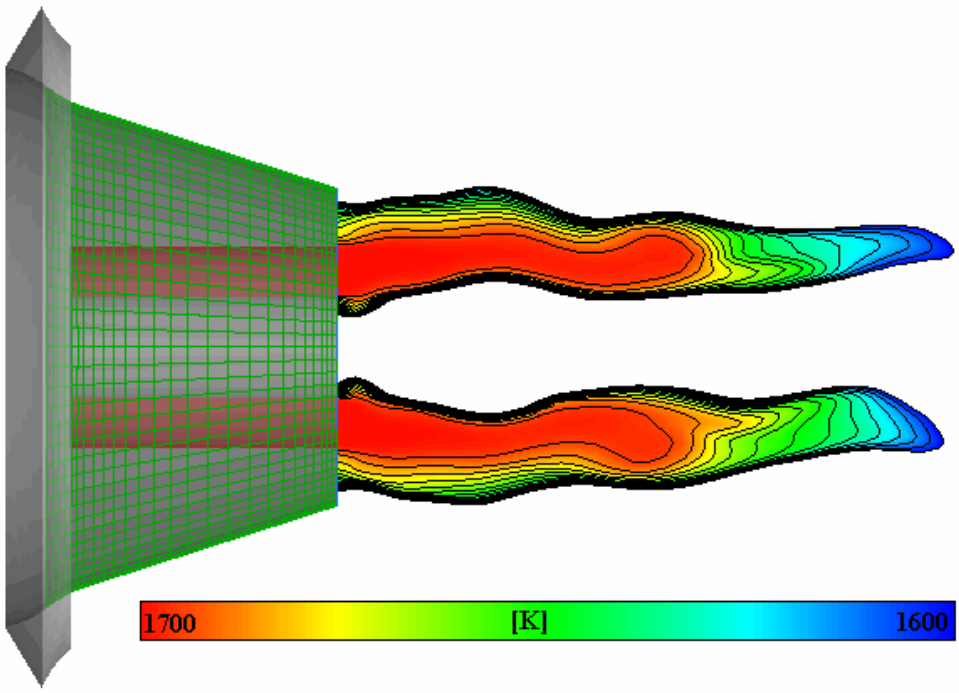


**Figure 5.17: melt stream temperature**

The potential of the inner jet configuration seems to be very high: the hollow liquid stream is created as in a pressurized swirl atomizer but it does not require the complex system of the former. Further tests need to be done in order to optimize this configuration. iIt would also be extremely interesting to investigate the superimposition of swirl on an inner jet.

## Chapter 5 summary

Chapter 5 was focused on possible improvement for primary break up. The first attempt relied on the idea that introducing a swirl component also the centrifugal force would act in the initial disruption of the melt. Furthermore this should have increased the spray cone angle reducing the possibility of droplet merging. The results showed that the swirled flow is characterized by deep aspiration at the nozzle that enhances liquid flow and avoids metal freeze off. Nevertheless this configuration experienced very low disruption of liquid core: tangential velocity component reduces the gas flow rate and, consequently, the momentum available to pinch off the liquid ligaments. The metal stream pass through the domain almost intact: this solution did not provide any benefit.

Based on chapter 4 results, in order enhance the interaction between gas and liquid phase, it was decided to design a nozzle that released liquid sheet (hollow cylinder) instead of round jet. The introduction of inner nozzle creates a barrier that does not allow the liquid

to flow radially inward. Simulation showed the formation of thin metal layer that is easier to destabilize and breakup into ligaments. Initial results seems to be very promising, nevertheless additional work is necessary to introduce this concept in industrial facility.

**References**

[1] S. Lagutkin, L. Achelis, S. Sheikhaliev, V. Uhlenwinkel, V. Srivastava, Atomization process for metal powder, Materials science & engineering. A383, pp. 1-6, 2004;

[2] Y. Liao, S. M. Jeng, M. A Jog, M. A. Benjamin, The effect of air swirl profile on the instability of a viscous liquid jet, Journal of Fluid Mechanics 424, pp. 1-20, 2000;

[3] N. Dombrowski, W.R. Johns, The aerodynamic instability and disintegration of viscous liquid sheet, Chem. Eng. Sci. 18, pp. 203–214, 1963.

# CHAPTER 6

## CONCLUSIONS AND FUTURE WORK

The object of this thesis was to perform a numerical analysis of liquid metal atomization. In order to achieve this purpose, the problem has been subdivided into two main aspects: primary and secondary atomization. Chapter 3 has been dedicated to the analysis of particle laden flow in two dimensional domains, while chapters 4 and 5 deal with three dimensional interactions of gas and liquid near to the feeding tube tip.

Due to the rotational symmetry, the initial 2D simulations were conducted on one half of the axial section of the atomization chamber. Multiphase simulations on close coupled atomization were never performed before. In order to investigate the interaction between fluid and particles during atomization, a self written code was implemented: the algorithm switches dynamically from Taylor analogy breakup to Kelvin-Helmotz instability model depending on the particle Weber number. The discrete phase motion is modeled with the Lagrangian approach and interacts with the continuous phase by means of source and sink terms in Navier Stokes equations. The initial results showed that droplet cooling process became effective when its diameter reached 500 μm.

With the purpose at improving gas expansion and avoiding energy waste in shock cells the isentropic plug nozzle design was introduced. The oblique shock formed on the nozzle shroud was removed, but, because of the truncated spike, the trailing shock was still present. The performance in atomization gave promising results. The resulting size distribution was narrowed: for a 1mm parent droplet, it moved from 30 μm to 20 μm while, for an initial droplet of 3mm, it passed from 40 μm to 30 μm. Based on the secondary break-up results it possible to state that IPN has a superior performance compare to standard converging-diverging geometry.

Hot gas has been addressed in the literature as a possible improvement in fine powder production. So, three different cases were simulated for reservoir nitrogen at 300K, 400K and 500 K respectively.. The break-up results showed that child droplet sizes for 400K and 500K were similar: this means that the additional temperature increase would not have a proportional effect.

In the last section of chapter 3, a more sophisticated solidification model was introduced into the break up function already implemented. The full model allows the designer to determine the in-flight distance before solidification and consequently calculate the

minimum atomization tower height to avoid melt sticking at the bottom (this is one of the major reasons for facility shut-down).

Chapter 4 is dedicated to the three dimensional investigation of the flow field near to the atomization nozzle. Additionally, the interaction between liquid melt and expanded gas during the early atomization stage is simulated with the Eulerian approach (VOF). So far, there is no evidence of similar work in the open literature and also experiments are not totally clear due to the difficulties in capturing the process details inside the atomization tower (high temperature, chaotic movement of droplets and high speed gas). In any case, most of published reports were time averaged, so that a clear picture of primary break-up is still missing..

Gas only and multiphase flowfields show a non axisymmetric behaviour and are characterized by unsteady features (wake shedding and sinusoidal melt flow rate): this means that 2D axisymmetric scheme (basic assumption of all previous work) cannot be used to model this phenomena. The presence of the melt affects significantly the velocity field: previous attempts to gain insight on nozzle performance based on single phase appear inadequate. Primary break-up for high yielding configuration extends into the domain far away from the feeding tube tip and filming mechanism is completely absent. Consequently secondary break-up starts in the wake and not at the base corner: injections points for discrete phase model should be uniformly distributed in the gas plume. Based on this the assumption done in chapter 3 is incorrect: secondary break-up cannot be modelled alone but it has to be linked with primary break-up. It is important to notice that extended primary break-up pushes the secondary break-up away from the nozzle exit so that the mother droplets experience a decayed gas velocity (i.e. aerodynamic force) with poor atomization performance.

. The melt flow rate was monitored in time and showed a fluctuating characteristic: it reduced from 0.37 to 0.16 kg/s. Previous studies of Anderson and Ting explained this as the switch from close to open wake: in our case the wake closure was not achieved in the gas only flow, so we can conclude that the two phenomena are not correlated. As demonstrated the melt flow rate determined the primary break-up mode: low values produced filming (that has been considered for many years as the break-up mechanism of close coupled atomization) but, as the GMR is reduced, the melt core contrasted the reverse flow and overcame the reattachment point.

The presence of nonaxisymmetric tail produced a particular shape of melt stream: this was organized in two orthogonal planes (corresponding to the quatrefoil axes of velocity

defect). Miller registered a superior performance of non-axisymmetric nozzle compared to axisymmetric one but was not able to clearly address the reason. The liquid is squeezed by impinging gas and forms 4 small cores: the reduced dimension and the increased surface area makes the child stream easier to disrupt. It is not unwise to correlate the fine atomization with the enhanced primary break up. Furthermore, the secondary atomization occurred in regions far from the jet core: this means that collision and adhesion are less probable and finer powder is produced. The swirl effect was investigated as a potential improvement for primary break-up but it did not show particularly good result: the low pressure insisting on the tip promoted a very high melt flow rate and, even for an appropriate GMR, it would be hard to produce acceptable powder. Moreover the high velocity field departs outward very close to the base, leaving the inner zone with a complete absence of aerodynamic force: this would enhance the production of completely unatomized flakes. On the contrary the inner jet configuration gave promising results. It was able to produce a uniform liquid sheet (hollow cylinder) suitable for secondary atomization. The axial velocity defect along the domain axis was not improved but this was totally irrelevant in this case because the liquid is concentrated in the periphery. Compared to the hollow swirl atomization proposed by Lagutkin, this geometry appears much more convenient. In fact, it does not require a pressurized system and could be applied to all existing plant without capital investment. This represents a solution with high potential for good yield at industrial scale productivity. In conclusion, the "lessons learned" through this study are:

- 2D axisymmtric model is not adequate to simulate close coupled gas atomizaztion because the flow field is non axisymmetric and unsteady;
- Metal stream deeply affect the flowfield and gas only simulation does not bring any insight on the nozzle performance;
- Liquid metal does not film over the nozzle tip in high yielding facility and consequently primary break-up is performed along the plume;
- Isentropic plug nozzle and hot reservoir gas improve secondary break-up, however further analysis are necessary to evaluate primary break-up outcome;
- Primary break-up plays major role in the atomization process;
- Primary break-up should be confined nearby the nozzle tip so that secondary break-up acts in the high speed portion of the gas plume;
- The goal for new design is to increase the initial surface of metal stream (hollow metal sheet or split into multi cores) to enhance momentum exchange between

liquid and gas phase (i.e. maximize the instability attitude of aerodynamic force) and reduce the primary break-up extension;

## 6.1 Future work

As highlighted in previous chapters, full scale simulation of an industrial atomizer will be impossible to be performed in the near future due to the high computational requirements. However, gas only modelling cannot give valuable infoemation on the atomization process because the flow field is dramatically affected by the presence of the melt. So far, the only viable solution is to model the second phase with a Lagrangian approach. However, it would be necessary to improve the model by introducing the effect of primary atomization. Basically the self implemented udf (see Appendix B) can be used as a starting point. Successively, the following modules should be introduced:

- momentum/energy equation source and sink as a function of distance from the feeding tube exit in order to reproduce the effect of untouched melt core on the flow pattern;
- adhesion scheme to reproduce the sticking phenomena in the cloud of liquid droplets and the build-up on the atomization chamber surface;

The lumped heat capacity assumption in the cooling model is reasonable because of the small Biot number involved ($< 0.1$). Nevertheless, a better description of solidification is achievable by solving the algebraic system of equations at each time step by means of the Gauss Seidel iterative method. The benefit of full scale simulation is that, once the model has been validated, it can be used to set up the process parameters and control the final yield according to the specific needs (i.e. droplet size distribution).

The 3D effects on flowfield unsteadiness presented in chapter 4 have a key role in the initial disruption, because they affect deeply the melt flow rate. A more refined grid ($\approx 4 \div 5$ million cells) allows the use of large eddy turbulence scheme together with VOF: a 24 nodes cluster could give interesting results within 1 year time.

A new atomization nozzle can be designed based on the results of inner jet performance outlined in chapter 6: drawing optimization, full scale simulation and unsteady behaviour is feasible within 2 years (included trials on production plant to validate the theory).

# APPENDIX A

## OVERVIEW OF THE GOVERNING EQUATIONS

This chapter contains the complete description of all the mathematical models used in the current analysis. Based on the assumption of continuum the basics equations of fluid dynamics are derived according to the Reynolds's transport theorem:

$$\begin{bmatrix} rate\ of\ change\ of \\ total\ property\ in\ V \end{bmatrix} = \begin{bmatrix} rate\ of\ property \\ being\ created\ in\ V \end{bmatrix} + \begin{bmatrix} property\ flowing \\ in\ V\ surface \end{bmatrix} + \begin{bmatrix} property\ flowing \\ out\ of\ V\ surface \end{bmatrix}$$

which states the conservation of a flow quantity inside an arbitrary volume. The integral form is given by the following equation:

$$\frac{d}{dt}\int_{V(t)} F(r,t)dV = \int_{V(t)} \frac{\partial F}{\partial t}dV + \int_{S(t)} F(\vec{u}\cdot\vec{n})dS \tag{A.1}$$

The dynamical behaviour of fluid flow is completely described by the conservation of three quantities: mass, momentum and energy. An important (and extremely fascinating!!!) feature of the fluid flow is the turbulence: in the following paragraph the basic description of the approaches employed here is reported.

The presence of the metal phase is represented following a Lagrangian approach that, in fluid dynamics, is referred as discrete particles model (DPM). The thermal metal/gas interaction is governed by the conduction and convection laws. The final part of the chapter gives a description of the numerical schemes necessary to solve the complete set of equations.

### A.1 Flow Description

The complete system (in vector form) made by the integral expressions of the three conservation laws is:

$$\frac{\partial}{\partial t}\int_{\Omega}\vec{W}d\Omega + \int_{S}\left(\vec{F}_c - \vec{F}_v\right)dS = \int_{S}\vec{Q}dS \tag{A.2}$$

where $\Omega$ represents the control volume (fixed in space) and S is the surface that encloses $\Omega$. The first term on the right hand side, $\vec{W}$, has five components and is called the conservative variable vector. In the second surface integral, $\vec{F}_c$ is related to the convective

transport of properties inside the fluid while $\vec{F}_v$ represents the viscous stress work and heat of diffusion: the former is called convective flux vector and the latter viscous flux vector. The vector $\vec{Q}$ includes the contribution of all volume sources (or sinks!) due to external forces $\vec{f}_e$, heat sources $\dot{q}_H$ and work done by the external forces $W_{f_e} = \rho \vec{f}_e \cdot \vec{v}$. If $\vec{n}$ is the unit normal vector to the surface S (pointing outward of the volume) the component V of the flow velocity ($\vec{v}$) normal to the volume boundary can be expressed as:

$$V = \vec{v} \cdot \vec{n} = n_x u + n_y v + n_z w \tag{A.3}$$

The expanded expressions of the column vectors are:

$$\vec{W} = \begin{bmatrix} \rho \\ \rho u \\ \rho v \\ \rho w \\ \rho E \end{bmatrix}; \vec{F}_c = \begin{bmatrix} \rho V \\ \rho u V + n_x p \\ \rho v V + n_y p \\ \rho w V + n_z p \\ \rho H V \end{bmatrix}; \vec{F}_v = \begin{bmatrix} 0 \\ n_x \tau_{xx} + n_y \tau_{xy} + n_z \tau_{xz} \\ n_x \tau_{yx} + n_y \tau_{yy} + n_z \tau_{yz} \\ n_x \tau_{zx} + n_y \tau_{zy} + n_z \tau_{zz} \\ n_x \Theta_x + n_y \Theta_y + n_z \Theta_z \end{bmatrix}; Q = \begin{bmatrix} 0 \\ \rho f_{ex} \\ \rho f_{ey} \\ \rho f_{ez} \\ \rho \vec{f}_e \cdot \vec{v} + \dot{q}_h \end{bmatrix} \tag{A.4}$$

The term $\tau$ is the viscous stress tensor (symmetric) and, for a Newtonian (linear!) viscous fluid, is defined as:

$$\tau_{ij} = -p\delta_{ij} + \mu\left(\frac{\partial u_i}{\partial x_j} + \frac{\partial u_j}{\partial x_i}\right) + \delta_{ij}\lambda\vec{\nabla} \cdot \vec{v} \tag{A.5}$$

It is still not clear how the coefficient of bulk viscosity λ can be considered: it appears to depend on frequency so that should not be a thermodynamic property. However, except for extreme conditions (high temperature or pressure), the hypothesis proposed by Stokes (1845) is widely accepted and explicates the dependence of λ from μ as:

$$\lambda + \frac{2}{3}\mu = 0 \tag{A.6}$$

The first coefficient of viscosity μ (from now on *viscosity*) is calculated with the formula obtain by Sutherland from kinetic theory:

$$\mu \approx \mu_0 \left(\frac{T}{T_0}\right)^{3/5} \frac{T_0 + S}{T + S} \tag{A.7}$$

The constants are reference values (ex. for air $T_0$ =273 K and $\mu_0 = 1.71e-05\ N \cdot s/m^2$ ). The vector $\Theta$ has the following components:

$$\begin{aligned}\Theta_x &= u\tau_{xx} + v\tau_{xy} + w\tau_{xz} + k\frac{\partial T}{\partial x}\\ \Theta_y &= u\tau_{yx} + v\tau_{yy} + w\tau_{yz} + k\frac{\partial T}{\partial y}\\ \Theta_z &= u\tau_{zx} + v\tau_{zy} + w\tau_{zz} + k\frac{\partial T}{\partial z}\end{aligned} \tag{A.8}$$

The external $\bar{f}_e$ forces (also called body forces) represent all the typology acting directly on the mass: examples are gravitational, Coriolis and buoyancy. The total enthalpy H is given by the relation:

$$H = e + \frac{|v|^2}{2} + \frac{p}{\rho} \tag{A.9}$$

where e is the internal energy per unit of mass. For a perfect gas the internal energy is given by the equation:

$$e = \frac{p}{\rho(\gamma - 1)} \tag{A.10}$$

where γ is the specific heats ratio $c_p/c_v$. The equations system (A.2) is known as the Navier-Stokes equations.

## A.2 Turbulent models

The borderline for laminar flow existence is delimited by a dimensionless parameter such as Reynolds number, Taylor number, Grashof number and Richardson number. The complex and chaotic flow that arises outside this range is called turbulent. Even if much is known about turbulence, this is still one of the most difficult and challenging areas for the scientific community. Brilliant monographs are available in the open literature, both for experimental [1,2] and numerical analysis [3-6]. The inherent features of turbulent flow can be summarized as:

a) Three dimensional random fluctuation in the values assumed by the flowfield variables (velocity, pressure, temperature);

b) Presence of eddies of different size, from a characteristic dimension δ (ex: in the free shear flow δ = shear layer thickness) to the Kolmogorov length scale $L = \left(\mu^3 \delta / \rho^3 v^3\right)^{1/4}$;

c) The small eddies dissipated by viscosity are replaced by the production of new ones, in a self sustaining mode.

An immediate effect of turbulence is the strong increase in the mixing behaviour (i.e. transport of mass, momentum and energy) of the flow compared to the solely molecular diffusion acting in the laminar state. This means also that due to the higher rate of interaction of molecules with the wall the heat transfer and skin friction (at the same conditions) are increased. From a mathematical point of view, the mixing activity is directly related to the presence of gradients (transport!!!) in the time-averaged flow.

The equation (A.2) is a complete description of the turbulent flow but unfortunately does not have an analytical solution: the only way to obtain a complete description of the flow field (velocity and pressure as function of time and space) is to solve numerically the Navier-Stokes equations. This approach is called direct numerical simulation (DNS) and, as indicated in [7], "is a research tool, and not a brute-force solution to the Navier-Stokes equations for engineering problems". The main concern about DNS is related to the rapid increase in the instantaneous range of length and timescale with the Reynolds number, so that, for usual engineering application, the range of scales to solve directly is too wide. Let us consider the flow of air at 3.3 m/s past a flat plate: the smallest eddy has a diameter of about 0.04 mm, consequently, to solve a shear layer of 10 cm over a 2.9 $m^2$ plate it is necessary to employ a grid with 5 trillion points (the size of the biggest mesh realized is around 100 million nodes). As a rule of thumb, the number of grid points required for a DNS is proportional to $Re^{9/4}$ while the CPU-time scales as $Re^3$. For such a reason, the common approach for turbulent flow does not solve the instantaneous flowfield but is based on its statistical description (≈ approximate solution). It is possible to subdivide the entire turbulence models in three main groups: the so called first order closure (algebraic, one equation and multiple equations), second order closure (Reynolds-stress model, RSM) and Large eddy simulation (LES). As it will be pointed out, closure is the main drawback of statistical description: the equations derived for this method contain some terms absent in (A.2), so they need to be modelled. The first order closure models are based on the linear eddy viscosity hypothesis introduced by Boussinesq or the non linear extension proposed

by Lumley. RSM models employ the exact equations for the Reynolds-stresses $\overline{v_i' v_j'}$ while the closure is necessary for higher order correlation terms $\overline{v_i' v_j' v_k'}$ . Those two classes of model belong to a more general approach, called RANS (Reynolds Averaged Navier Stokes equations). Finally, the Large Eddy Simulation solves the large structure (vortex with high energy content) while modelling the influence of small structure (based on the observation they have a more homogeneous and universal character).

### A.2.1 RANS Equation

In order to explain the determinant aspects of turbulence, the differential form of the system (A.2) is used. Assuming that there are no sources or sinks, the differential Navier Stokes equations are:

$$\begin{aligned}
&\frac{\partial \rho}{\partial t} + \frac{\partial}{\partial x_i}(\rho v_i) = 0 \\
&\frac{\partial}{\partial t}(\rho v_i) + \frac{\partial}{\partial x_i}(\rho v_j v_i) = -\frac{\partial p}{\partial x_i} + \frac{\partial \tau_{ij}}{\partial x_j} \\
&\frac{\partial}{\partial t}(\rho E) + \frac{\partial}{\partial x_j}(\rho v_j H) = \frac{\partial}{\partial x_j}(v_i \tau_{ij}) + \frac{\partial}{\partial x_j}\left(k \frac{\partial T}{\partial x_j}\right)
\end{aligned} \tag{A.11}$$

where *i* and *j* are two indices denoting the components of the tensor. The compact notation for the viscous stress tensor (according to the Stokes hypothesis) is:

$$\tau_{ij} = 2\mu S_{ij} - \left(\frac{2\mu}{3}\right)\frac{\partial v_k}{\partial x_k}\delta_{ij} \tag{A.12}$$

According to the mass conservation in (A.11), the last term on the lhs disappears for incompressible flow. The strain rate tensor and the rotation rate tensor become:

$$S_{ij} = \frac{1}{2}\left(\frac{\partial v_i}{\partial x_j} + \frac{\partial v_j}{\partial x_i}\right); \quad \Omega_{ij} = \frac{1}{2}\left(\frac{\partial v_i}{\partial x_j} - \frac{\partial v_j}{\partial x_i}\right) \tag{A.13}$$

The basic concept in the statistical analysis is to decompose the flow u variables in a fluctuating $u'$ part and its mean value $\bar{u}$ :

$$u = \bar{u} + u' \tag{A.14}$$

In order to obtain the mean value, there are 4 possible averaging procedures:

a) time averaging (appropriate for statistically steady turbulence, the mean $\overline{u}$ value varies only in space and not in time);
b) spatial averaging ($\overline{u}$ varies only in time);
c) ensemble averaging ($\overline{u}$ varies with both time and space);
d) density weighted averaging (known also as Favre decomposition, designed for compressible flow).

The first three methods are also known as Reynolds averaging: when the turbulent flow is stationary and homogeneous they are equivalent (ergodic hypothesis). The Favre method is necessary because, when density is fluctuating, an additional correlation between the variables arises: usually (for compressible flow) density and pressure are decomposed using the Reynolds approach while the other variables (velocity, temperature, enthalpy, internal energy…) undergo the density weighted procedure. The analytical expression of the four methods is respectively:

$$\begin{aligned} &a)\quad \overline{u}_i = \lim_{\Delta t\to\infty}\frac{1}{\Delta t}\int_t^{t+\Delta t} u_i dt; \qquad b)\quad \overline{u}_i = \lim_{\Omega\to\infty}\frac{1}{\Omega}\int_\Omega u_i d\Omega; \\ &c)\quad \overline{u}_i = \lim_{N\to\infty}\frac{1}{N}\sum_{n=1}^{N} u_i; \qquad d)\quad \overline{\overline{u_i}} = \frac{1}{\overline{\rho}}\lim_{\Delta t\to\infty}\frac{1}{\Delta t}\int_t^{t+\Delta t}\rho u_i dt; \end{aligned} \tag{A.15}$$

It is important to note that the main fluctuation term is zero, $\overline{u_i'} = 0$, while the average product of two fluctuating term is not zero, $\overline{u_i'u_j'} \neq 0$. In case of the Favre decomposition $\overline{\overline{\rho u_i}} = \overline{\rho}\,\overline{\overline{u_i}}$ and $\overline{\overline{\rho u_i''}} = 0$. The application of the Favre averaging to the equations (A.11) yields the so called RANS system:

$$\begin{aligned} &\frac{\partial\overline{\rho}}{\partial t} + \frac{\partial}{\partial x_i}\left(\overline{\rho}\,\overline{\overline{v_i}}\right) = 0 \\ &\frac{\partial}{\partial t}\left(\overline{\rho}\,\overline{\overline{v_i}}\right) + \frac{\partial}{\partial x_i}\left(\overline{\rho}\,\overline{\overline{v_j}}\,\overline{\overline{v_i}}\right) = -\frac{\partial\overline{p}}{\partial x_i} + \frac{\partial}{\partial x_j}\left(\overline{\overline{\tau_{ij}}} - \overline{\rho}\,\overline{\overline{v_i''v_j''}}\right) \\ &\frac{\partial}{\partial t}\left(\overline{\rho}\,\overline{\overline{E}}\right) + \frac{\partial}{\partial x_j}\left(\overline{\rho}\,\overline{\overline{v_j}}\,\overline{\overline{H}}\right) = \frac{\partial}{\partial x_j}\left[\overline{\overline{v_i}}\left(\overline{\overline{\tau_{ij}}} - \overline{\rho}\,\overline{\overline{v_i''v_j''}}\right)\right] + \frac{\partial}{\partial x_j}\left(k\frac{\partial\overline{\overline{T}}}{\partial x_j} - \overline{\rho}\,\overline{\overline{v_j''h''}} + \overline{\overline{\tau_{ij}v_i''}} - \overline{\rho}\,\overline{\overline{v_j''K}}\right) \end{aligned} \tag{A.16}$$

The equations in (A.16) have the same terms as (A.11) plus a new unknown quantity, called Reynolds-stress tensor:

$$\tau_{ij}^{R} = -\bar{\rho}\,\overline{\overline{v_i''v_j''}} \tag{A.17}$$

The turbulent kinetic energy is given by the sum of the normal stresses:

$$\bar{\rho}\,\overline{\overline{K}} = \frac{1}{2}\bar{\rho}\,\overline{\overline{v_i''v_i''}} \tag{A.18}$$

Usually, in transonic and supersonic flow, the terms expressing the molecular diffusion, $\frac{\partial}{\partial x_j}\left(\overline{\overline{\tau_{ij}v_i''}}\right)$, and turbulent transport of K, $\frac{\partial}{\partial x_j}\left(\bar{\rho}\,\overline{\overline{v_j''K}}\right)$, are neglected. The Reynolds-stress tensor is symmetrical, so that, after the averaging procedure, we introduce six more unknown terms in the equations describing the flow. Furthermore, there are three other unknowns coming from the components of the turbulent heat-flux vector $\frac{\partial}{\partial x_j}\left(\bar{\rho}\,\overline{\overline{v_j''h''}}\right)$. In conclusion, 9 more relations are necessary to close the problem.

## A.2.2 Boussinesq hypothesis

The basic approach to solve the closure problem belongs to Boussinesq. After noticing that the momentum transport in turbulent flow is enhanced by the mixing activity of the big energetic vortices, he theorized a linear relation between turbulent shear stress and mean rate of strain:

$$\tau_{ij}^{R} = -\bar{\rho}\,\overline{\overline{v_i''v_j''}} = 2\mu_T\,\overline{\overline{S_{ij}}} - \left(\frac{2\mu_T}{3}\right)\frac{\partial\overline{\overline{v_k}}}{\partial x_k}\delta_{ij} - \frac{2}{3}\bar{\rho}\,\overline{\overline{K}}\delta_{ij} \tag{A.19}$$

The proportionality $\mu_T$ coefficient is called turbulent viscosity. This is not a physical property of the fluid (like molecular viscosity), but it is function of the local flow condition. Especially in the simplest models, like the algebraic ones, the last term on the right hand side is removed. According to the Reynolds analogy [8], the turbulent heat-flux vector can be modelled as:

$$\bar{\rho}\,\overline{\overline{v_j''h''}} = -k_T\,\frac{\partial\overline{\overline{T}}}{\partial x_j} \tag{A.20}$$

The turbulent thermal conductivity coefficient is given as a function of the turbulent Prandtl number (generally considered constant in the flow, ≈ 0.9 for air) ant turbulent viscosity:

$$k_T = c_p \frac{\mu_T}{\mathrm{Pr}_T} \tag{A.21}$$

It is now clear that, when the value of the turbulent viscosity is known, the equations (A.16) are ready to be solved (the value of $\overline{\overline{K}}$ in the last term on the rhs of A.19 is usually neglected or deducted as a product of the specific model). However, although the simplest formulation, the Boussinesq hypothesis is not generally valid. It is not accurate in cases such as sudden variation in the mean strain rate, secondary flows, separated flow, rotating and stratified flows. The limit of this approach relies on the assumptions of local equilibrium between turbulence and main strain and of system rotation independence.

### A.2.3 Reynolds stress transport

The exact Reynolds stress transport description can be derived averaging the product of the second equation in (A.11) and fluctuating quantity. As described in [9] the result is:

$$\begin{aligned}\frac{\partial \tau_{ij}^R}{\partial t} + \frac{\partial}{\partial x_k}\left(\overline{\overline{v_k}}\,\tau_{ij}^R\right) = &-\tau_{ik}^R \frac{\partial \overline{\overline{v}}_j}{\partial x_k} - \tau_{jk}^R \frac{\partial \overline{\overline{v}}_i}{\partial x_k} + \varepsilon_{ij} - \Pi_{ij} + \frac{\partial}{\partial x_k}\left[-\overline{\tau_{kj} v_i'' + \tau_{ki} v_j''} + C_{ijk}\right] \\ &+ \overline{v}_i'' \frac{\partial \overline{p}}{\partial x_j} + \overline{v}_j'' \frac{\partial \overline{p}}{\partial x_i}\end{aligned} \tag{A.22}$$

where

$$\begin{aligned}&\Pi_{ij} = \overline{p'\left(\frac{\partial v_i''}{\partial x_j} + \frac{\partial v_j''}{\partial x_i}\right)}; \quad \varepsilon_{ij} = \overline{\tau_{kj}\frac{\partial v_i''}{\partial x_k} + \tau_{ki}\frac{\partial v_j''}{\partial x_k}} \\ &C_{ijk} = \overline{\rho}\,\overline{\overline{v_i'' v_j'' v_k''}} + \overline{p' v_i''}\delta_{jk} + \overline{p' v_j''}\delta_{ik}\end{aligned} \tag{A.23}$$

Because of the nonlinearity of the momentum conservation equation, additional unknowns (e.g. $\overline{\overline{v_i'' v_j'' v_k''}}$) are generated every time a higher moment (averaging level) is taken. The closure of equation (A.22) is done using an empirical model.

### A.2.4 Standard k-ε

This is the most commonly used 2 equations model: a detailed description can be found in [10]. It relies on the solution of two additional transport equations, one for the turbulent kinetic energy $\overline{\overline{K}}$ and the other for its dissipation rate ε. For high values of the Reynolds number, the transport of the turbulent kinetic energy can be written as:

$$\overline{\rho}\frac{\partial\overline{\overline{K}}}{\partial t}+\overline{\overline{\rho}}\overline{v}_j\frac{\partial\overline{\overline{K}}}{\partial x_j}=\tau_{ij}^R\frac{\partial\overline{\overline{v}_i}}{\partial x_j}-\overline{\tau_{ji}\frac{\partial v_i''}{\partial x_j}}+\frac{\partial}{\partial x_j}\left[\overline{\tau_{ji}v_i''}-\frac{1}{2}\overline{\rho v_j''v_i''v_i''}-\overline{p'v_j''}\right]$$
$$-\overline{v}_i''\frac{\partial\overline{p}}{\partial x_i}+\overline{p'\frac{\partial v_i''}{\partial x_i}} \tag{A.24}$$

However, in the standard K-ε a modelled expression is implemented, instead of (A.24):

$$\frac{\partial\overline{\rho}\overline{\overline{K}}}{\partial t}+\frac{\partial}{\partial x_j}\left(\overline{\overline{K}}\overline{\rho}\overline{\overline{v}}_j\right)=\frac{\partial}{\partial x_j}\left[\left(\mu+\frac{\mu_T}{\mathrm{Pr}_K}\right)\frac{\partial\overline{\overline{K}}}{\partial x_j}\right]-\overline{\rho}\varepsilon-P_K-P_b-2\overline{\rho}\varepsilon M_T^2$$
$$P_K=\overline{\rho}\overline{\overline{v_i''v_j''}}\frac{\partial\overline{\overline{v}_i}}{\partial x_j};\quad P_b=g_i\frac{\mu_T}{\overline{\rho}\,\mathrm{Pr}_T}\frac{\partial\overline{\rho}}{\partial x_i};\quad M_T=\sqrt{\frac{\overline{\overline{K}}}{a^2}} \tag{A.25}$$

where $P_K$ and $P_b$ are the production of turbulent kinetic energy due to main velocity gradients and buoyancy, respectively. The mass averaged dissipation rate is given by:

$$\overline{\rho}\varepsilon=\overline{\tau_{ji}\frac{\partial u_i''}{\partial x_j}} \tag{A.26}$$

The exact equation that expresses the dissipation rate transport is extremely complicated and would introduce new terms with double and triple correlation between the fluctuating parts of the flow variables. Furthermore, those quantities are almost impossible to measure at any level of accuracy, so that a closure model would be impossible. In order to overcome this difficulty, an approximate expression for ε is used:

$$\frac{\partial\overline{\rho}\varepsilon}{\partial t}+\frac{\partial\overline{\rho}\varepsilon\overline{\overline{v}}_j}{\partial x_j}=\frac{\partial}{\partial x_j}\left[\left(\mu+\frac{\mu_T}{\mathrm{Pr}_\varepsilon}\right)\frac{\partial\varepsilon}{\partial x_j}\right]-\left(C_{\varepsilon1}P_K+C_{\varepsilon2}\overline{\rho}\varepsilon+C_{\varepsilon3}P_b\right)\frac{\varepsilon}{\overline{\overline{K}}} \tag{A.27}$$

The quantities $\mathrm{Pr}_K$ and $\mathrm{Pr}_\varepsilon$ are the Prandtl numbers for $\overline{\overline{K}}$ and $\varepsilon$: the respective values are 1.0 and 1.3. The eddy viscosity is:

$$\mu_T=C_\mu\overline{\rho}f_\mu\frac{\overline{\overline{K^2}}}{\varepsilon} \tag{A.28}$$

The function $f_\mu$ depends on Reynolds number: its role is to damp the turbulent diffusion mechanism close to the wall (boundary layer) and becomes important only for low Reynolds numbers. The closure coefficients are [11]:

$$C_{\varepsilon 1}=1.44;\ C_{\varepsilon 2}=1.92;\ C_{\mu}=0.09; \tag{A.29}$$

The value of the constant $C_{\varepsilon 3}$ determines the influence of buoyancy on the dissipation rate. Its value can be expressed as a function of the ratio between the velocity component aligned ($v_n$) to the gravity direction and the normal one ($v_t$), with the following relation [12]:

$$C_{\varepsilon 3}=\tanh\left|\frac{v_t}{v_n}\right| \tag{A.30}$$

## A.2.5 Reynolds stress model

In this approach [13-14] the Reynolds stresses $\overline{\overline{v_i''v_j''}}$ are not modelled but are obtained as the solution of the transport equation (A.22). In order to give a better description of the model closure, a brief description of the different terms in (A.22) is given in the following. The turbulent diffusivity term $d_T$ is approximated as:

$$d_T=\frac{\partial}{\partial x_k}\left(\overline{\rho}\,\overline{\overline{v_i''v_j''v_k''}}+\overline{p'v_i''}\delta_{jk}+\overline{p'v_j''}\delta_{ik}\right)\approx\frac{\partial}{\partial x_k}\left(\frac{\mu_T}{\mathrm{Pr}_k}\frac{\partial\overline{\overline{v_j''v_k''}}}{\partial x_k}\right) \tag{A.31}$$

The value of $\mathrm{Pr}_k$ is different from the one used in the standard k- ε and is $\mathrm{Pr}_k = 0.82$. The pressure strain correlation term $\Pi_{ij}$ is responsible for the redistribution mechanism between Reynolds stresses and is written as:

$$\begin{aligned}\Pi_{ij}=\overline{p'\left(\frac{\partial v_i''}{\partial x_j}+\frac{\partial v_j''}{\partial x_i}\right)}\approx&-\frac{C_2+8}{11}\left(P_{ij}-\frac{2}{3}\delta_{ij}P_k\right)-\frac{8C_2-2}{11}\left(D_{ij}-\frac{2}{3}\delta_{ij}D_k\right)\\&-\frac{30C_2-2}{55}\overline{\rho}\,\overline{\overline{K}}\,\overline{\overline{S_{ij}}}-C_1f_1\overline{\rho}\left(\overline{\overline{v_i''v_j''}}-\frac{2}{3}\delta_{ij}\overline{\overline{K}}\right)\\&+\frac{\overline{\overline{K}}^{\frac{3}{2}}}{\varepsilon h}\left[C_3\overline{\rho}\,\frac{\varepsilon}{\overline{\overline{K}}}\left(\overline{\overline{v_i''v_j''}}-\frac{2}{3}\delta_{ij}\overline{\overline{K}}\right)+C_4\left(P_{ij}-D_{ij}\right)\right.\\&\left.+C_5\overline{\rho}\,\overline{\overline{K}}\left(\frac{\partial v_i''}{\partial x_j}+\frac{\partial v_j''}{\partial x_i}-\frac{2}{3}\delta_{ij}\frac{\partial v_k''}{\partial x_k}\right)\right]\end{aligned} \tag{A.32}$$

$$P_{ij}=\tau_{ik}^R\frac{\partial\overline{\overline{v}}_j}{\partial x_k}-\tau_{jk}^R\frac{\partial\overline{\overline{v}}_i}{\partial x_k};\ D_{ij}=\tau_{ik}^R\frac{\partial\overline{\overline{v}}_k}{\partial x_j}-\tau_{jk}^R\frac{\partial\overline{\overline{v}}_k}{\partial x_i};P_k=D_k=-\tau_{ij}^R\frac{\partial\overline{\overline{v}}_j}{\partial x_j}$$

The turbulent kinetic energy and the dissipation rate are calculated from modelled equations having the same structure as the ones used in the standard k-ε:

$$\frac{\partial \overline{\rho}\,\overline{\overline{K}}}{\partial t}+\frac{\partial \overline{\rho}\,\overline{\overline{K}}\,\overline{\overline{v_j}}}{\partial x_j}=\frac{\partial}{\partial x_j}\left[\left(\mu+\frac{\mu_T}{\mathrm{Pr}_\varepsilon}\right)\frac{\partial \overline{\overline{K}}}{\partial x_j}\right]-\left(P_k+G_k\right)-\overline{\rho}\varepsilon\left(1+2M_T^2\right)$$
$$\frac{\partial \overline{\rho}\varepsilon}{\partial t}+\frac{\partial \overline{\rho}\varepsilon\,\overline{\overline{v_j}}}{\partial x_j}=\frac{\partial}{\partial x_j}\left[\left(\mu+\frac{\mu_T}{\mathrm{Pr}_\varepsilon}\right)\frac{\partial \varepsilon}{\partial x_j}\right]-\left(C_{\varepsilon 1}P_k+C_{\varepsilon 2}\overline{\rho}\varepsilon+C_{\varepsilon 3}G_k\right)\frac{\varepsilon}{\overline{\overline{K}}} \qquad \text{(A.33)}$$
$$G_{ij}=\overline{\rho}\beta\left(g_i\overline{u_j'T}+g_j\overline{u_i'T}\right)$$

The values of the constants are $\mathrm{Pr}_k$ =0.82 and $\mathrm{Pr}_\varepsilon$ =1.It is important to note that the values of $\overline{\overline{K}}$ obtained from the solution of the turbulent kinetic energy are used only for as boundary condition while, for the rest of the calculation, k is derived directly from the Reynolds stresses $\overline{\overline{K}}=\frac{1}{2}\overline{\overline{v_i''v_i''}}$. The buoyancy influence term is modelled as:

$$G_{ij}=\frac{\mu_T}{\overline{\rho}\,\mathrm{Pr}_T}\left(g_i\frac{\partial \overline{\rho}}{\partial x_i}+g_j\frac{\partial \overline{\rho}}{\partial x_j}\right) \qquad \text{(A.34)}$$

where the constant Pr = 0.85. The turbulent viscosity is calculated following the same approach of k-ε:

$$\mu_T=C_\mu\overline{\rho}\frac{\overline{\overline{K^2}}}{\varepsilon} \qquad \text{(A.35)}$$

with the constant $C_\mu$=0.09.

the last term that needs to be modelled to give closure to the problem is the viscous dissipation tensor $\varepsilon_{ij}$:

$$\varepsilon_{ij}=\overline{\tau_{kj}\frac{\partial v_i''}{\partial x_k}+\tau_{ki}\frac{\partial v_j''}{\partial x_k}}\approx\frac{\varepsilon}{\overline{\overline{K}}}\left[\overline{\overline{v_i''v_j''}}f_s+\left(1-f_s\right)\frac{2}{3}\delta_{ij}\overline{\overline{K}}\right]$$
$$f_s=\frac{1}{1+\frac{\mathrm{Re}_t}{10}};\quad \mathrm{Re}_t=\frac{\overline{\overline{K}}^2}{\nu\varepsilon} \qquad \text{(A.36)}$$

## A.2.6 Large eddy

The large eddy simulation (LES) is actually the most powerful method of numerical analysis for turbulent flow. The principal theoretical concept behind LES is that the small

scales (high wave number) have, according to Kolmogorov, a more "*universal character*" compared to large scale structures (low wave numbers): for this reason they could be modelled in lieu of being resolved. Hence the large scales, that are strongly affected by the flow boundary conditions and contain a large amount of energy, are resolved directly. A complete description of LES methodology can be found in [4, 15]. The small scales are called the subgrid-scales and are the subject of study for many researchers. In order to separate the small scales from the resolvable scales, the Navier-Stokes equations undergo a process of spatial filtering. In this manner, any flow variables can be decomposed into large scale part and small scale part as follows:

$$u = \bar{u} + u' \tag{A37}$$

where the spatial filter of u is given by:

$$\bar{u} = \int_D G\left(x - x^*, \Delta\right) u\left(x^*\right) d^3 x^* \tag{A.38}$$

G is the filter function, while $\Delta$ is the filter width and, in the current analysis they have the form:

$$G = \begin{cases} \dfrac{1}{\Delta^3} & if \quad \left|x_i - x_i^*\right| < \dfrac{\Delta x_i}{2} \quad i = 1,2,3 \\ 0 & otherwise \end{cases} \tag{A.39}$$
$$\Delta = \left(\Delta x_1 \Delta x_2 \Delta x_3\right)^{1/3}$$

The dimensions $(\Delta x_1; \Delta x_2; \Delta x_3)$ define the volume D of the cells over which the flow equations are discretized: this kind of filter is also called a volume-average box. Many other filters are available in the literature and all of them are normalized, i.e.:

$$\int_D G\left(x - x^*, \Delta\right) d^3 x^* = 1 \tag{A.40}$$

The Favre averaged variables are now obtained as:

$$\tilde{u} = \frac{\overline{\rho u}}{\bar{\rho}} \tag{A.41}$$

The spatial filtered and Favre averaged flow equations become:

$$
\begin{aligned}
&\frac{\partial \overline{\rho}}{\partial t}+\frac{\partial \overline{\rho}\overline{\overline{v}}_k}{\partial x_k}=0\\
&\frac{\partial \overline{\rho}\overline{\overline{v}}_i}{\partial t}+\frac{\partial \overline{\rho}\overline{\overline{v}}_i\overline{\overline{v}}_k}{\partial x_k}=-\frac{\partial \overline{p}}{\partial x_i}+\frac{\partial \Lambda_{ik}}{\partial x_k}\\
&\frac{\partial \overline{\rho}\overline{\overline{e}}}{\partial t}+\frac{\partial}{\partial x_k}\left(\overline{\rho}\overline{\overline{e}}+\overline{\overline{p}}\right)\overline{\overline{v}}_k=\frac{\partial \mathrm{H}_k}{\partial x_k}+\frac{\partial}{\partial x_k}\left(\Lambda_{ik}\overline{\overline{v}}_i\right)\\
&\overline{p}=\overline{\rho}R\overline{\overline{T}}
\end{aligned}
\tag{A.42}
$$

The total stress tensor $\Lambda_{ik}$ is the sum of the subgrid scale (SGS) $\tau_{ij}$ stress and the viscous stress $\overline{\sigma}_{ij}$:

$$
\begin{aligned}
&\Lambda_{ik}=\tau_{ij}+\overline{\sigma}_{ij}\\
&\tau_{ij}=-\overline{\rho}\left(\overline{\overline{v_i v_j}}-\overline{\overline{v}}_i\overline{\overline{v}}_j\right)\\
&\overline{\sigma}_{ij}=\mu\left(\overline{\overline{T}}\right)\left(-\frac{2}{3}\frac{\partial \overline{\overline{v}}_k}{\partial x_k}\delta_{ij}+\frac{\partial \overline{\overline{v}}_i}{\partial x_j}+\frac{\partial \overline{\overline{v}}_j}{\partial x_i}\right)
\end{aligned}
\tag{A.43}
$$

The SGS (Q) and molecular (q) heat fluxes are:

$$
\begin{aligned}
&\mathrm{H}_j=Q_j+q_j\\
&Q_j=-c_p\overline{\rho}\left(\overline{\overline{v_j T}}-\overline{\overline{v}}_j\overline{\overline{T}}\right)\\
&\overline{q}_j=k\left(\overline{\overline{T}}\right)\left(\frac{\partial \overline{\overline{T}}}{\partial x_j}\right)
\end{aligned}
\tag{A.44}
$$

The total energy $\overline{\overline{e}}$ and the SGS turbulence kinetic energy ($k$) are given by:

$$
\begin{aligned}
&\overline{\rho}\overline{\overline{e}}=\overline{\rho}c_v\overline{\overline{T}}+\frac{1}{2}\overline{\rho}\overline{\overline{v}}_i\overline{\overline{v}}_i+\overline{\rho}k\\
&\overline{\rho}k=\frac{1}{2}\overline{\rho}\left(\overline{\overline{v_i v_i}}-\overline{\overline{v}}_i\overline{\overline{v}}_i\right)
\end{aligned}
\tag{A.45}
$$

The closure of system (A.36) requires a modelled equation for the subgrid scale stress $\tau_{ij}$ and heat flux $Q_j$. The subgrid-scale models implemented in the solver used in this study relies on the Boussinesq hypothesis:

$$
\tau_{ij}-\frac{1}{3}\tau_{kk}\delta_{ij}=-2\mu_T\overline{\overline{S}}_{ij}
\tag{A.46}
$$

where $\mu_T$ is the SGS turbulent viscosity and $\overline{\overline{S_{ij}}}$ is the rate of strain tensor of the resolved scales:

$$\overline{\overline{S_{ij}}} = \frac{1}{2}\left( \frac{\partial \overline{\overline{v_i}}}{\partial x_j} + \frac{\partial \overline{\overline{v_j}}}{\partial x_i} \right) \tag{A.47}$$

Many models for the turbulent viscosity have been developed: here the classical Lilly-Smagorinsky model is used [16]. The eddy viscosity is:

$$\mu_T = \overline{\rho} C_S^2 \Delta^2 \sqrt{2\overline{\overline{S}}_{mn}\overline{\overline{S}}_{mn}} \tag{A.48}$$

The value of constant $C_S$ is in the range 0.065-0.1. The SGS stress and heat flux modelled expressions are:

$$\begin{aligned} \tau_{ij} &= 2\overline{\rho} C_S^2 \Delta^2 \sqrt{2\overline{\overline{S}}_{mn}\overline{\overline{S}}_{mn}} \left( \overline{\overline{S}}_{ij} - \frac{1}{3}\overline{\overline{S}}_{kk}\delta_{ij} \right) \\ Q_j &= \overline{\rho} c_P \frac{C_S^2}{\mathrm{Pr}_T} \Delta^2 \sqrt{2\overline{\overline{S}}_{mn}\overline{\overline{S}}_{mn}} \frac{\partial \overline{\overline{T}}}{\partial x_j} \end{aligned} \tag{A.49}$$

The small scales have a reduced growth close to the wall, so that the turbulent viscosity needs to be reduced in the boundary layer by the Van Driest damping factor:

$$\mu_T = \overline{\rho}\left[ C_S \Delta \left( 1 - e^{\frac{-y^+}{25}} \right)^2 \right] \sqrt{2\overline{\overline{S}}_{mn}\overline{\overline{S}}_{mn}} \tag{A.50}$$

where $y^+$ is the dimensionless cell distance from the wall.

## A.2.7 Standard Wall Functions

There is a vast amount of literature on the statistics and structure of turbulence near solid boundaries [17]. The present discussion aims to describe turbulent flow in the near-wall region and to introduce some basic terminology describing the near-wall velocity and temperature profiles. At the beginning of 1930, Ludwig Prandtl and Theodore von Karman determined, through experimental analysis, that the velocity profile close to the boundary consists of three different layers:

- Inner layer dominated by viscous shear (molecular origin);
- Outer layer dominated by turbulent shear (eddy origin);
- Overlapping layer where eddy and molecular viscosity have the same weight;

As shown in A.2.7.1, the overlapping profile is well reproduced by a logarithmic function. Figure A.1 represents a sketch of the boundary layer profile zones: the logarithmic law matches the linear law coming from the wall at $y^+ \approx 30$, through the buffer layer.

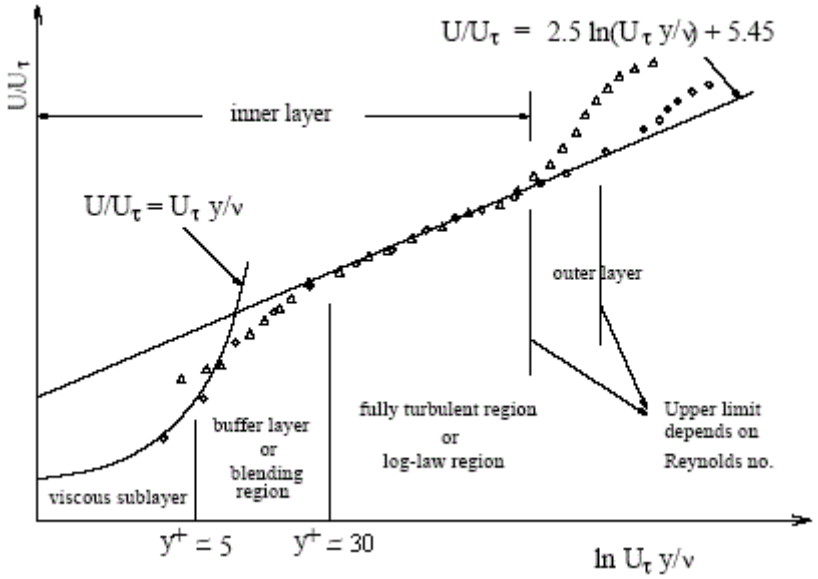


**Figure A.1 Schematic subdivision of near wall region for a smooth wall.**

The distance from the wall is specified in terms of $y^+$ values and is defined as:

$$y^+ = \frac{U_\tau y}{\nu}$$
$$U_\tau = \sqrt{\frac{\tau_{wall}}{\rho}} \qquad \text{(A.51)}$$

where $U_\tau$ is the "friction velocity", $\tau_{wall}$ is the wall shear stress and $y$ is the distance from the wall.

### A.2.7.1 Law of the Wall for Velocity

For zero pressure gradient, fully developed flow, in which there are no streamwise gradients of velocity or stress, the wall normal velocity is zero (according to continuity equation) and the equation for the mean streamwise velocity U simplifies to:

$$\frac{\partial}{\partial y}\left(\mu\frac{\partial U}{\partial y} - \rho\overline{uv}\right) = 0 \qquad \text{(A.52)}$$

Appendix A

Near the wall, the viscous effects are dominating the flow so, by integrating with boundary conditions $\overline{\rho uv}=0$ and $\mu\frac{\partial U}{\partial y}=\tau_{wall}$ at y = 0, the expression for the near-wall shear stress becomes:

$$\mu\frac{\partial U}{\partial y}-\overline{\rho uv}=\tau_{wall} \tag{A.53}$$

In this region immediately adjacent to the wall ($y^+<5$), termed the "viscous sub-layer", the Reynolds stress ($\overline{\rho uv}$) is negligible compared to the viscous stress ($\mu\frac{\partial U}{\partial y}$). According to these assumptions, integrating equation (A.10) leads to an expression in which the U velocity is a linear function of the wall normal distance and is written as:

$$U^+=y^+ \tag{A.54}$$

where $U^+$ is the dimensionless streamwise velocity given by $U^+=\frac{U}{U_\tau}$. Moving further away from the wall, viscous effects diminish and the turbulent stress dominates. In the fully turbulent region, from $y^+\approx 30$ to $y/\delta\approx 0.1$ (where $\delta$ is the boundary layer thickness0, viscous stresses are negligible in comparison to the turbulent stresses and equation (1.10) simplifies to:

$$-\overline{\rho uv}=\tau_{wall} \tag{A.55}$$

Applying the mixing length hypothesis:

$$-\overline{\rho uv}=\rho l_m^2\left(\frac{\partial U}{\partial y}\right)^2 \tag{A.56}$$
$$l_m=ky$$

Integrating leads to the following expression:

$$U^+=\frac{1}{k}\ln y^+ + C \tag{A.57}$$

The above formula is known as the "log-law". The two constants $k$ and $C$ are usually assigned the values $k$ = 0.41 and $C$ = 5.0. When the flow separates, $U_\tau$ approaches zero

and consequently $U^+$ becomes very large: the scaling with wall shear stress is inconsistent for this case.

### A.2.7.2 Law of the Wall for Temperature

Similarly to velocity, there is a law for temperature. The temperature, $T$, is made dimensionless by the "friction" temperature, $T_\tau$, and wall temperature $T_{wall}$:

$$T^+ = \frac{(T_{wall} - T)}{T_\tau}$$
$$T_\tau = \frac{q_{wall}}{\rho c_p U_\tau} \tag{A.58}$$

In the viscous sublayer, the relationship between $T^+$ and $y^+$ is given by Fourier's heat-conduction law:

$$q_{wall} = -\lambda \frac{\partial T}{\partial y} \tag{A.59}$$

which can be written as:

$$T^+ = y^+ \sigma \tag{A.60}$$

where $\sigma$ is the molecular Prandtl number ($\sigma = \mu c_p / \lambda$), which physically represents the ratio between the ability to diffuse momentum and the ability of diffusing heat. A log-law for temperature can be derived as follows [18].

$$T^+ = \frac{1}{k_h} \ln(y^+) + c_h \tag{A.61}$$

where the constants are:

$$k_h = \frac{k}{\sigma_t}$$
$$c_h = \frac{1}{k_h} \ln(E) + P\left(\frac{\sigma}{\sigma_t}\right) \tag{A.62}$$

## A.2.8 Near-Wall Reynolds Stress Behaviour

Close to the wall, the behaviour of Reynolds stresses, $k$ and ε can be obtained from the asymptotic behaviour of the fluctuating velocity components, as follows:

$$\begin{aligned}
\overline{u^2} &= \overline{\alpha_1^2}y^2 + 2\overline{\alpha_1\alpha_2}y^3 + \left(\overline{\alpha_2^2} + 2\overline{\alpha_1\alpha_3}\right)y^4 + \ldots \\
\overline{v^2} &= \overline{\beta_1^2}y^4 + \ldots \\
\overline{w^2} &= \overline{c_1^2}y^2 + 2\overline{c_1c_2}y^3 + \left(\overline{c_2^2} + 2\overline{c_1c_3}\right)y^4 + \ldots \\
\overline{uv} &= \overline{\alpha_1 b_2}y^3 + \left(\overline{a_1b_3} + \overline{a_2b_2}\right)y^4 + \ldots
\end{aligned} \tag{A.63}$$

where the α's, b's and c's are functions of x,z and time but not of y. From continuity, the wall-normal fluctuating velocity component, v, is small compared to the wall-parallel components, u and w, so the wall-normal stress $\overline{v^2}$ increases with $y^4$ whilst the two wall-parallel components $\overline{u^2}$ and $\overline{w^2}$ increase as $y^2$. The turbulent kinetic energy, k is given by:

$$k = \frac{1}{2}\left(\overline{u^2} + \overline{v^2} + \overline{w^2}\right) = \frac{1}{2}\left[\left(\overline{a_1^2} + \overline{c_1^2}\right)y^2 + 2\left(\overline{a_1a_2} + \overline{c_1c_2}\right)y^3 + \ldots\right] \tag{A.64}$$

and the dissipation rate ε:

$$\varepsilon = \nu\overline{\left(\frac{\partial u}{\partial y}\right)^2} + \nu\overline{\left(\frac{\partial v}{\partial y}\right)^2} + \nu\overline{\left(\frac{\partial w}{\partial y}\right)^2} = \nu\left[\left(\overline{a_1^2} + \overline{c_1^2}\right)y^2 + 4\left(\overline{a_1a_2} + \overline{c_1c_2}\right)y + \ldots\right] \tag{A.65}$$

The dissipation rate is finite at the wall ($\varepsilon = \nu\left(\overline{a_1^2} + \overline{c_1^2}\right)$ when y = 0). Referring back to the expression for $k$ at the wall (equation A.26), the first-order terms result in the following expression for ε in terms of $k$:

$$\varepsilon = \nu\left(\overline{a_1^2} + \overline{c_1^2}\right) = \frac{2\nu k}{y^2} \tag{A.66}$$

At the wall surface, the dissipation rate of turbulence energy is balanced by viscous diffusion of kinetic energy towards the wall, which can be expressed:

$$\frac{2\nu k}{y^2} = \nu\frac{\partial^2 k}{\partial y^2} \tag{A.67}$$

## A.3 Discrete phase model

The equation of motion for particles can be written as a force balance that equates the droplet inertia with forces acting on the droplet as:

$$\frac{d\vec{v}_p}{dt} = F_D\left(\vec{v} - \vec{v}_p\right) + \frac{\vec{g}\left(\rho_p - \rho\right)}{\rho_p} + \vec{F} \tag{A.68}$$

The drag force per unit particle mass is:

$$F_D = \frac{18\mu}{\rho_p d_p^2}\frac{C_D\,Re}{24} \tag{A.69}$$

The drag coefficient $C_D$ given by [19]:

$$C_D = \frac{24}{Re_p}\left(1 + b_1\,Re_p^{\,b_2}\right) + \frac{b_3\,Re_p}{b_4 + Re_p} \tag{A.70}$$

The coefficients in the equation stand for:

$$\begin{aligned} b_1 &= \exp\left(2.3288 - 6.4581\phi + 2.4486\phi^2\right) \\ b_2 &= 0.0964 + 0.5565\phi \\ b_3 &= \exp(4.905 - 13.8944\phi + 18.4222\phi^2 - 10.2599\phi^3) \\ b_4 &= \exp\left(1.4681 + 12.2584\phi - 20.7322\phi^2 + 15.8855\phi^3\right) \end{aligned} \tag{A.71}$$

the shape factor Φ is given by

$$\phi = \frac{s}{S} \tag{A.72}$$

where s is the surface area of a sphere having the same volume as the particle, and S is the actual surface area of the particle.

## A.4 Numerical scheme

The discretization scheme adopted for the numerical solution of equations (A.16) is Finite Volume [20]. This scheme is the state of the art in computational fluid dynamics: if compared with finite elements or finite differences, the main features are the intrinsic local conservation of the numerical scheme and its robustness (through the discrete maximum principle). The analyzed domain is subdivided into a finite number of small volumes, usually called control volumes (CVs): however the grid does not define the computational nodes but the boundaries of each control volume (in this study, the cell centred version is

used, specifically the values of computational variables are stored in the centre of the CV). The discretization procedure takes place applying equations (A.16) to each single CV of the grid. The integrals of quantity *f* (in general the component of the convective or diffusive flux vector) on the surfaces $S_i$ defining a CV are, approximated as follows:

$$\int_S f dS = \sum_{i=1}^{n} \int_{S_i} f dS \approx \sum_{i=1}^{n} f_i S_i \tag{A.73}$$

where $f_i$ is the value of *f* on the centre of the face S and $S_i$ is its area: this expression has second order accuracy. However the value of f is not known a priori (variables are stored in the CV centre) and it needs to be interpolated from the values of *f* at the centres of the contiguous CVs. The gradient in the diffusive term is discretized with a central difference scheme. A complete review of the different interpolation schemes is given in [21]. Volume integral approximation is given by:

$$\int_V q dV \approx q_C V \tag{A.74}$$

where $q_C$ is the value of the q at the centre of CV and V stands for its volume. This approximation is second order accurate: if higher order accuracy is desired, the value $q_C$ has to be determined as an interpolation of values in the surrounding CVs. After all terms are discretized the system (A.16) becomes an algebraic system and is solved by iterative methods, like Gauss-Seidel.

## A.4.1 Implicit pressure-correction Method

A common procedure for the iterative solution of flow field equation systems is the segregated method, which is based on the successive solution of equations for velocity components, pressure correction, temperature and scalar variables. After the discretization process, the momentum equations become:

$$v_{i,P}^{*} = \frac{Q_{v_i}^{m-1} - \sum_l A_l^{v_i} v_{i,l}^{*}}{A_P^{v_i}} - \frac{\Delta V}{A_P^{v_i}} \left( \frac{\delta p^{m-1}}{\delta x_i} \right)_P \tag{A.75}$$

where the symbol $\frac{\delta}{\delta x_i}$ represents a discretized spatial derivative and Q is the source term without the contribution of pressure. The values carrying the asterisk are the predicted (but not yet the correct!) quantity for the time step m, while the superscript m-1 indicates a value coming from the previous time step. Basically the velocity field obtained from the

solution of equations (A.75) do not satisfy the continuity law (this is the reason why they are called predicted and not new value). The target is to find a guest value for the pressure field in order to predict a value for the velocity that progressively matches the continuity. For compressible flows, the mass flux is determined not only by the normal velocity component, but also by the density. Assuming that the correct values are obtained from the predicted ones with a small correction term, it is possible to write them as:

$$v_n^m = v_n^{m*} + v_n' ; \quad \rho^m = \rho^{m-1} + \rho'; \quad p^m = p^{m-1} + p' \tag{A.76}$$

where the subscript n indicates the normal component of velocity on the control surface. The real mass flux through a surface e of the control volume can be expressed as:

$$\dot{m}_e^m = \left(\rho^{m-1} + \rho'\right)_e \left(v_n^{m*} + v_n'\right)_e S_e \tag{A.77}$$

Introducing the A.76 in A.78, the mass correction is:

$$\dot{m}_e' = \left(\rho^{m-1} S v_n'\right)_e + \left(v_n^{m*} S\, \rho'\right)_e + \left(\rho' v_n' S\right)_e \tag{A.78}$$

The third term on the right hand side of the latter expression is usually neglected because it is second order and tends to zero faster than the other terms. For the colocated method, the first term can be approximated as:

$$\left(\rho^{m-1} S v_n'\right)_e = \left(\rho^{m-1} S \Delta V\right)_e \overline{\left(\frac{1}{A_P^{v_n}}\right)} \left(\frac{\delta p'}{\delta n}\right)_e \tag{A.79}$$

The over-bar means interpolated from the values of neighbouring cells. The density correction is:

$$\rho' \approx \left(\frac{\partial \rho}{\partial p}\right)_T p' = C_p p' \tag{A.80}$$

and, for ideal gas, $C_p = 1/RT$. Considering all the faces of the control volume, the continuity equation in term of mass correction, becomes:

$$\frac{\rho_P' \Delta V}{\Delta t} + \sum_l \dot{m}_l' + Q_m^* = 0 \tag{A.81}$$

where Q is the unbalance of continuity due to the use of non correct values of velocity and density field. Rearranging the equation (A.81) with equations (A.79) ÷ (A.80) the pressure correction equation system for the node P is obtained:

$$A_P p'_P + \sum_l A_l p'_l = -Q^*_m \tag{A.82}$$

The algorithm for the calculation of the correct flow field is:

a) guess a value for the pressure $p^*$ and density $\varrho^*$ (usually the values at the previous iteration m-1);

b) solve the momentum equation (A75) for $v_i^*$ ;

c) solve pressure correction (A.82) for $p'$ and update the pressure field $p$ ;

d) update the density by means of (A.76) and (A.80);

e) update the velocities $v_i$ using (A.76) and (A.79);

f) repeat a) to e) until the convergence is fulfilled;

g) move to the next time step (or assume that steady state is reached in a stationary calculation)

**References**

[1] M. Van Dyke, Album of Fluid Motion, Parabolic Press Inc, 1982;

[2] A. J. Smits, T.T. Lim, Flow Visualization: Techniques and Examples, World Scientific Publishing, 2000;

[3] J.O. Hinze, Turbulence, McGraw-Hill Companies, 1975;

[4] S.B. Pope, Turbulent Flows, Cambridge University Press, 2000;

[5] P.S. Bernard, J.M. Wallace, Turbulent Flow: Analysis, Measurement and Prediction, Wiley, 2002;

[6] B.E. Launder, N.D. Sandham, Closure Strategies for Turbulent and Transitional Flows, Cambridge University Press, 2002;

[7] P. Moin, K. Mahesh, Direct Numerical Simulation: A Tool in Turbulence Research, Annu. Rev. Fluid Mech., vol. 30, pp. 539-578, 1998;

[8] O. Reynolds, On the Extent and Action of the Heating Surface for Steam Boilers. Proc. Manchester Lit. Phil. SOC., vol. 14, pp. 7-12, 1874;

[9] D.C. Wilcox, Turbulence Modeling for CFD,DCW Industries Inc., La Cafiada, California, USA, 1993;

[10] W.P. Jones, B.E. Launder, The Prediction of Laminarization with a Two-Equation Model of Turbulence. Int. Journal of Heat and Mass Transfer, vol.5, pp. 301-314, 1972;

[11] B.E. Launder, D.B. Spalding, Lectures in Mathematical Models of Turbulence, Academic Press, England, 1972;

[12] R.A.W.M. Henkes, F.F. Van der Flugt, C.J. Hoogendoorn, Natural Convection Flow in a Square Cavity Calculated with Low-Reynolds-Number Turbulence Models, Int. Journal Heat Mass Transfer, vol.34, pp. 1543-1557, 1991;

[13] B.E. Launder, G.J. Reece, W. Rodi, Progress in the Development of a Reynolds-Stress Turbulence Closure, J. Fluid Mech., vol. 68, pp. 537-566, 1975;

[14] B.E. Launder, Second-Moment Closure and Its Use in Modeling Turbulent Industrial Flows, International Journal for Numerical Methods in Fluids, vol. 9, pp. 963-985, 1989;

[15] M. Lesieur, O. Metais, P. Comte, Large-Eddy Simulations of Turbulence, Cambridge University Press, 2005;

[16] J. Smagorinsky, General Circulation Experiments with the Primitive Equations. I. The Basic Experiment, Month. Wea. Rev., vol. 91, pp. 99-164, 1963;

[17] F.M. White, Viscous Fluid Flow, McGraw-Hill Education, pp. 411-417, 2005;

[18] T. Cebeci, P. Bradshaw, Physical and computational aspects of convective heat transfer, Springer-Verlag, 1984;

[19] A. Haider, O. Levenspiel, Drag Coefficient and Terminal Velocity of Spherical an Nonspherical Particles, Powder Technology, vol. 58, pp. 63-70, 1989;

[20] H.K. Versteeg, W. Malalasekera, An introduction to computational fluid dynamics The finite volume method, Longman Scientific & Technical, 1995;

[21] J. Blazek, Computational Fluid Dynamics: Principles and Applications, Elsevier, 2001;

# APPENDIX B

## BREAK-UP & COOLING UDF FUNCTION

```
#include "udf.h"
#include "dpm.h"
#include "surf.h"
#define UDF_FILENAME "udf_check"
static void
write_check(real loc, real velo, real omega, real timep, real cassio,
real puzo, real zora,real zaza)
{
FILE*fp=fopen(UDF_FILENAME,"a");
if(fp!=NULL)
{
fprintf(fp,"(%e%e%e%e%e%e%e%e)\n",loc,velo,omega,timep,cassio,puzo,zo
ra,zaza);
fclose(fp);
}
}

DEFINE_DPM_OUTPUT(child_droplet,header,fp,p,thread,plane)
{
  char name[100];

  if (header)
   {
   if (NNULLP(thread))
     fprintf(fp,"(%s %d)\n",thread->head-
>dpm_summary.sort_file_name,11);
   else
     fprintf(fp,"(%s %d)\n",plane->sort_file_name,11);
     fprintf(fp,"(%10s %10s  %10s  %10s  %10s  %10s  %10s"
               " %10s  %10s  %10s  %10s  %s)\n",
                 "X","Y","Z","U","V","W","diameter","T","mass-flow",
                 "time","childnumber","name");
    }

  else
    {
      sprintf(name,"%s:%d",p->injection->name,p->part_id);
      fprintf(fp,
           "((%10.6g  %10.6g  %10.6g  %10.6g  %10.6g  %10.6g  "
           "%10.6g  %10.6g  %10.6g  %10.6g %10.6g) %s)\n",
           p->state.pos[0], p->state.pos[1], p->state.pos[2],
           p->state.V[0], p->state.V[1], p->state.V[2],
           p->state.diam, p->state.temp, p->flow_rate, p->state.time,
           p->user[1], name);
    }
}
                                    /*NICOLA ZEOLI BREAKUP MODEL*/
                                         /*13 APRILE 2005*/

DEFINE_DPM_LAW(BreakupLaw2, p, ci)
{
real y;
real x;
real T_KH;
```

```
real RHO;
real RE;
real RE_d;
real WE;
real WE_d;
real WE_T;
real Oh;
real Ta;
real Akh;
real DEN;
real RAD;
real D_K_MIN;
real V_DIFF;
real X_VEL;
real Y_VEL;
real Z_VEL;
real Om;           /*omega KH*/
real N_new;
real Req;
real rtd;
real omsq;
real om;           /*omega TAB*/
real webte;
real yweb1;
real yweb2;
real Asq;
real A;
real recipA;
real phicos;
real phite;
real quad;
real phi;
real radius;
real tsubb;
real coste;
real theta;
real awetrans;
real sqrtweb;
real omsqrtweb;
real rwebte;
real cosdtbu;
real dtbu;
real decay_factor;
real radp_n;
real part_n;
real ex;
real Dr;

real T_liq;
real Cp_s;
real Cp_l;
real T_under;
real dT_hom;
real dT_act;
real H_f; /* [J/mol] --> divide by 0.102 to have [J/kg]*/
real de_T;
real AV; /*atomic volume [m3/mol]*/
real SL; /*solid liquid interface*/
real tu;
real T_rate;
real espo1;
```

```
real espo2;
real Cp;
real k_inf; /*thermal conductivity of cotinuous phase*/
real h_conv;
real T_rec;
real T_per; /*peritectic temperature*/
real df_dt; /*solid fraction rate of change stored in
P_USER_REAL(p,12)*/
real k_e;
real T_M;
real peritec;
real f_per;
real f_rec;
real Pr_h;
real Re_h;
real ratio;
real f_max;


real df;
real H;
real temp;
real Raggio;
real cosodt;
real sinodt;
cell_t c =P_CELL(p);
Thread *t =P_CELL_THREAD(p);



                              /*P_USER_REAL(p,0) droplet break time*/

     if (P_USER_REAL(p,1)<1)  /* number child droplets*/
        {
        P_USER_REAL(p,1)=1;
        }
                              /*P_USER_REAL(p,2) Volume Shed KH*/

                              /* (P_USER_REAL(p,3)Volume 3% KH*/



                             /*P_USER_REAL(p,4) y0p(n)TAB*/
                             /*P_USER_REAL(p,5) y0pdot(n)TAB*/

                                        /* Weber number
calculation*/
y = (2/3);
RHO = C_R(c,t);
X_VEL=P_VEL(p)[0]-C_U(c,t);
Y_VEL=P_VEL(p)[1]-C_V(c,t);
Z_VEL=P_VEL(p)[2]-C_W(c,t);
V_DIFF=pow(X_VEL,2)+pow(Y_VEL,2)+pow(Z_VEL,2);
WE=0.83*RHO*P_DIAM(p)*0.5*V_DIFF;
P_USER_REAL(p,2)=WE;
WE_d=0.83*P_RHO(p)*P_DIAM(p)*0.5*V_DIFF;
RE=RHO*sqrt(V_DIFF)*P_DIAM(p)*0.5/C_MU_L(c,t);
RE_d=P_RHO(p)*sqrt(V_DIFF)*P_DIAM(p)*167*0.5;
```

```
                                        /* Ohnesorge number
calculation*/
Oh=(sqrt(WE_d))/RE_d;
                                        /* Taylor number
calculation*/
Ta=Oh*sqrt(WE);
                                        /* main disturbance
wavelength */
DEN=1+0.865*pow(WE,1.67);
Akh=9.02*P_DIAM(p)*0.5*(1+0.45*sqrt(Oh))*(1+0.4*pow(Ta,0.7))/pow(DEN,
0.6);

                                        /* main disturbance
wavelength's growth rate */
RAD=sqrt(1.2/(P_RHO(p)*pow(0.5*P_DIAM(p),3)));
Om=(0.34+0.385*pow(WE,1.5))*RAD/((1+Oh)*(1+1.4*pow(Ta,0.6)));

                                          /* KH breakup time */
T_KH=37.26*P_DIAM(p)/(Akh*Om);
Req=0.61*Akh;
temp=P_T(p);

/*set material properties*/
T_liq= 1785;
Cp_s= 727;
Cp_l= 829;
SL=0.2034;
AV=0.0000208;
H_f=28270;
Cp=(1-P_USER_REAL(p,8))*Cp_l + P_USER_REAL(p,8)*Cp_s;
k_inf=0.01636;
T_per=1764;
k_e=0.74;
T_M=2016;
f_per=0.67;

/* reynolds and prandtl values for convection calculation*/
Re_h=RHO*sqrt(V_DIFF)*P_DIAM(p)/C_MU_L(c,t);
Pr_h=C_MU_L(c,t)*C_CP(c,t)/k_inf;
h_conv= (k_inf/P_DIAM(p))*(2+0.6*pow(Re_h,0.5)*pow(Pr_h,0.333));

 if (temp>T_liq)
 {

  InertHeatingLaw(p);


if (WE >= 90)                                        /* KH Breakup*/
     {
       P_USER_REAL(p,3)=0.03*pow((0.5*P_DIAM(p)),3);
         Raggio=0.5*P_DIAM(p);
         if (Raggio>Req)
         {
         Dr=(Raggio-Req)*(P_USER_REAL(p,0)/T_KH);
       P_USER_REAL(p,7)=pow((0.5*P_DIAM(p)),3)-pow((Raggio-Dr),3);

        if(P_USER_REAL(p,7)>=P_USER_REAL(p,3))
              {
           P_DIAM(p)=2*(Raggio-Dr);
           P_MASS0(p)=P_RHO(p)*pow((0.5*P_DIAM(p)),3)*4.187;
```

```
            P_N(p)=P_N(p)*(P_MASS(p)/P_MASS0(p));

                P_MASS(p)=P_MASS0(p);
            P_USER_REAL(p,0)=0;
            }
          }
       }
else
     {
      if(WE<90 && WE>6)
      {

/* TAB Breakup*/
             radius=0.5*P_DIAM(p);
             rtd=0.5*5*0.006/(P_RHO(p)*pow(radius,2)); /*1/Td*/
             omsq=8*1.2/(P_RHO(p)*pow(radius,3))-pow(rtd,2);
                   if(omsq<=0.0)
                  {
                   P_USER_REAL(p,4)=0.0;
                   P_USER_REAL(p,5)=0.0;
                   goto timeincrease;
                   }
                   else
                  {
                   om=sqrt(omsq);
                   webte=WE*0.33/(8*0.5);
                   yweb1=P_USER_REAL(p,4)-webte;
                   yweb2=P_USER_REAL(p,5)/om;
                   }

/*calcolo ampiezza oscillazione*/
              Asq=pow(yweb1,2)+pow(yweb2,2);
              A=sqrt(Asq);
                        if(A+webte<=1.0)
                        {
                        goto ZEOLIagg;
                        }
              recipA=1.0/A;

/*breakup time*/
                       if (yweb1*recipA<1.0)
                       {
                        phicos=yweb1*recipA;
                        }
                        else
                       {
                        phicos=1.0;
                        }
                        if(phicos<-1.0)
                       {
                        phicos=-1.0;
                        }
               phite=acos(phicos);
               quad=-yweb2*recipA; /*sin(phi)*/
               phi=phite;
                        if(quad<0.0)
                        {
                        phi=6.28-phite;
                         }
               tsubb=P_USER_REAL(p,0);
                        if(fabs(P_USER_REAL(p,4)>=1.0))
```

```
                        {
                         goto ZEOLIrad; /*go to sauter diameter
calculation*/
                         }
               coste=1.0;
                        if ((webte-A)<-1.0 && P_USER_REAL(p,5)<0.0)
                        {
                        coste=-1.0;
                         }
              theta=acos((coste-webte)*recipA);
                         if(theta>=phi)
                         {
                          tsubb=P_USER_REAL(p,0)+(theta-phi)*(1/om);
                          }
                          else
                          {
                                      if((6.28-theta)>=phi)
                                      {
                                       theta=-theta;
                                       }
                           theta=6.28+theta;
                           tsubb=P_USER_REAL(p,0)+(theta-phi)*(1/om);
                           }
                           if((P_DT(p)+P_USER_REAL(p,0))<tsubb)
                          {
                           goto ZEOLIagg;
                           }
                           else
                          {
                           goto ZEOLIrad;
                           }
          ZEOLIrad: awetrans=(sqrt(81)*1-1)/pow(81,4.0);
                             sqrtweb=awetrans*pow(WE,4)+1.0;
                             omsqrtweb=0.22222*om*sqrtweb;
                             rwebte=1.0/webte;
                             if(1.0-rwebte<1.0)
                             {
                              cosdtbu=1.0-rwebte;
                              }
                              else
                             {
                              cosdtbu=1.0;
                              }
                               if(cosdtbu<-1.0)
                              {
                               cosdtbu=-1.0;
                               }
                              dtbu=(1/om)*acos(cosdtbu);
                              decay_factor=exp(-omsqrtweb*(dtbu));
                              radp_n=radius*decay_factor; /*child
droplets radius*/
                              part_n=
pow(0.5*P_DIAM(p),3)/pow(radp_n,3); /*number of child droplets for
each parent one*/
                             P_DIAM(p)=2*radp_n;

P_MASS0(p)=P_RHO(p)*pow((0.5*P_DIAM(p)),3)*4.187;


       P_N(p)=P_N(p)*(P_MASS(p)/P_MASS0(p));
```

```
                              P_MASS(p)=P_MASS0(p);
                              P_USER_REAL(p,1)=P_USER_REAL(p,1)*part_n;
                              P_USER_REAL(p,4)=0;
                              P_USER_REAL(p,5)=0;
                              P_USER_REAL(p,0)=0;
                                          P_USER_REAL(p,6)=8;
                              goto timeincrease;
       ZEOLIagg: cosodt=cos(om*P_DT(p));
                           sinodt=sin(om*P_DT(p));
                           ex=exp(-P_DT(p)*rtd);
                           yweb2=(1/om)*(P_USER_REAL(p,5)+yweb1*rtd);

P_USER_REAL(p,4)=webte+ex*(yweb1*cosodt+yweb2*sinodt);
                           P_USER_REAL(p,5)=(webte-
P_USER_REAL(p,4))*rtd+ex*om*(yweb2*cosodt-yweb1*sinodt);
                           }
}
}

/* P_USER_REAL(p,9) is a check value, while P_USER_REAL(p,8) is the
solid fraction*/

else
{
      if (P_T(p)<T_liq && P_USER_REAL(p,9)!=1)/*undercooling
modeling*/
      {
            tu=1;
            dT_hom=2;
            de_T=-6*((h_conv/(P_DIAM(p)*P_RHO(p)*Cp))*(P_T(p)-
C_T(c,t))*P_DT(p));
            P_T(p)=P_T(p)+de_T;
            T_rate=-(de_T)/P_DT(p);
            while (((dT_hom-tu)/tu)>0.001)
            {
                  tu=dT_hom;
                  espo1=pow(10,44)*4.187*pow(0.5*P_DIAM(p),3);
                  espo2=pow(10,23);

      dT_hom=sqrt(12.135*espo2*SL*SL*SL*AV*AV*T_liq*T_liq/(H_f*H_f*(T
_liq-dT_hom)*log(espo1*dT_hom/T_rate)));
            }
            dT_act=dT_hom*exp(-
2.2*pow(10,12)*pow(0.5*P_DIAM(p),3)*4.187);
            T_under=T_liq-dT_act;
            P_USER_REAL(p,9)=1;
            P_USER_REAL(p,10)=T_under;

      }
      else
      {
            if (P_T(p)>P_USER_REAL(p,10) && P_USER_REAL(p,8)<=0 )
            {
                  de_T=-6*((h_conv/(P_DIAM(p)*P_RHO(p)*Cp))*(P_T(p)-
C_T(c,t))*P_DT(p));
                  P_T(p)=P_T(p)+de_T;
            }/*end undercooling*/
            else
            {
                  if (P_T(p)<=P_USER_REAL(p,10) &&
P_USER_REAL(p,11)==0 )/*recalescence modeling*/
```

```
                  {
                        ratio=6*h_conv*0.102/(P_RHO(p)*H_f*0.01);
                        T_rec=(T_liq+(ratio*C_T(c,t)))/(ratio+1);
                        P_USER_REAL(p,13)=T_rec;
                        df_dt=0.01*(T_liq-P_T(p))/P_DIAM(p);
                        de_T= (H_f/(0.102*Cp_l))*df_dt*P_DT(p)-
6*((h_conv/(P_DIAM(p)*P_RHO(p)*Cp_l))*(P_T(p)-C_T(c,t))*P_DT(p));
                        P_T(p)=P_T(p)+de_T;
                        P_T0(p)=P_T(p);
                        P_USER_REAL(p,8)=df_dt*P_DT(p);
                        P_USER_REAL(p,11)=1;


                  }
                  else
                  {
                        if ( P_USER_REAL(p,14)==0 &&
P_USER_REAL(p,8)<=1)
                        {
                              P_USER_REAL(p,12)=0.01*(T_liq-
P_T(p))/P_DIAM(p);/*it is equal to df_dt*/

      de_T=(9.8*H_f/Cp)*P_USER_REAL(p,12)*P_DT(p)-
6*((h_conv/(P_DIAM(p)*P_RHO(p)*Cp))*(P_T(p)-C_T(c,t))*P_DT(p));
                              P_T(p)=P_T(p)+de_T;
                              P_T0(p)=P_T(p);
                              P_USER_REAL(p,8)=P_USER_REAL(p,8)+
P_DT(p)*P_USER_REAL(p,12);
                              f_max=(T_liq-
P_USER_REAL(p,10))*Cp_l/(9.8*H_f);
                              if (P_USER_REAL(p,8)>=f_max ||
P_USER_REAL(p,8)>=1 || P_T(p)>=P_USER_REAL(p,13))
                              {
                                    P_USER_REAL(p,14)=1;

      P_USER_REAL(p,17)=P_USER_REAL(p,8);
                              }
                        }/*end recalescence*/
                        else
                        {
                              if(P_T(p)>T_per && P_USER_REAL(p,15)==0
&& P_USER_REAL(p,8)<=1 )/*segregated solidification stage 1*/
                              {
                                    espo1=(2-k_e)/(k_e-1);
                                    espo2=(1-
P_USER_REAL(p,17))/((k_e-1)*(T_M-P_USER_REAL(p,13)));
                                    P_USER_REAL(p,12)=espo2*pow((T_M-
P_T(p))/(T_M-P_USER_REAL(p,13)),espo1);
                                    peritec=Cp-
(9.8*H_f*P_USER_REAL(p,12));

      de_T=6*((h_conv/(P_DIAM(p)*P_RHO(p)*peritec))*(P_T(p)-
C_T(c,t))*P_DT(p));
                                    P_T(p)=P_T(p)-de_T;

      P_USER_REAL(p,8)=P_USER_REAL(p,8)-P_USER_REAL(p,12)*de_T;
                                    if (P_T(p)<=T_per)
                                    {
                                          P_USER_REAL(p,15)=1;
                                          P_T(p)=T_per;
```

```
                                    }
                              }
                              else
                              {
                                    if (P_T(p)==T_per &&
P_USER_REAL(p,8)<=f_per)/*peritectic solidification*/
                                    {

      P_USER_REAL(p,12)=6*((h_conv/(P_DIAM(p)*P_RHO(p)*9.8*H_f))*(P_T
(p)-C_T(c,t))*P_DT(p));

      P_USER_REAL(p,8)=P_USER_REAL(p,8)+P_USER_REAL(p,12);

                                    }
                                    else
                                    {
                                          if
(P_USER_REAL(p,8)<1)/*segregated solidification stage 2*/
                                          {
                                                espo1=(2-k_e)/(k_e-
1);
                                                espo2=(1-
P_USER_REAL(p,17))/((k_e-1)*(T_M-P_USER_REAL(p,13)));

      P_USER_REAL(p,12)=espo2*pow((T_M-P_T(p))/(T_M-
P_USER_REAL(p,13)),espo1);
                                                peritec=Cp-
(9.8*H_f*P_USER_REAL(p,12));

      de_T=6*((h_conv/(P_DIAM(p)*P_RHO(p)*peritec))*(P_T(p)-
C_T(c,t))*P_DT(p));
                                                P_T(p)=P_T(p)-de_T;

      P_USER_REAL(p,8)=P_USER_REAL(p,8)-P_USER_REAL(p,12)*de_T;
                                                P_USER_REAL(p,16)=25;
                                          }
                                          else
                                          {
                                                InertHeatingLaw(p);
                                          }
                                    }
                              }
                        }
                  }
            }
      }
}


timeincrease: P_USER_REAL(p,0)= P_USER_REAL(p,0)+P_DT(p);
write_check(P_TIME(p),      P_USER_REAL(p,8),      P_T(p),      de_T,
P_USER_REAL(p,12), P_USER_REAL(p,14),P_USER_REAL(p,15),h_conv);
```